TECHNISCHE UNIVERSITÄT MÜNCHEN

Walter Schottky Institut

Zentralinstitut für physikalische Grundlagen der
Halbleiterelektronik

Nitride Nanowire Heterostructures

Florian Georg Josef Furtmayr

Vollständiger Abdruck der von der Fakultät für Physik der Technischen
Universität München zur Erlangung des akademischen Grades eines

Doktors der Naturwissenschaften
(Dr. rer. nat.)

genehmigten Dissertation.

Vorsitzender:	Univ.-Prof. Dr. Norbert Kaiser
Prüfer der Dissertation:	1. Univ.-Prof. Dr. Martin Stutzmann
	2. Univ.-Prof. Dr. Martin Eickhoff Justus-Liebig-Universität Gießen

Die Dissertation wurde am 11.09.2013 bei der Technischen Universität München
eingereicht und durch die Fakultät für Physik am 10.12.2013 angenommen.

Contents

Abstract **5**

1. Introduction **7**
  1.1. The nitride material system . . . 8
  1.2. Introduction to the DOTSENSE project . . . 15
  1.3. Outline of this thesis . . . 15

2. Nanowire growth and experimental techniques **19**
  2.1. Different growth techniques for nanowires . . . 19
  2.2. The MBE system . . . 22
  2.3. Experimental techniques . . . 26
    2.3.1. Scanning electron microscopy (SEM) . . . 26
    2.3.2. Transmission electron microscopy (TEM) . . . 26
    2.3.3. X-ray diffraction . . . 29
    2.3.4. Photoluminescence spectroscopy (PL) . . . 30
    2.3.5. Raman scattering . . . 31

3. GaN nanowire growth on different substrates **33**
  3.1. Growth window for nanowires . . . 34
  3.2. Si substrates . . . 36
    3.2.1. Interface properties and nucleation behavior . . . 38
    3.2.2. Time-dependence of the nucleation process . . . 40
  3.3. Sapphire substrates . . . 45
  3.4. Diamond substrates . . . 52
  3.5. Summarized growth model . . . 57

4. Impact of doping of GaN NWs on the morphology **61**
  4.1. Influence of silicon . . . 61
  4.2. Influence of magnesium . . . 66
    4.2.1. TEM analysis of highly Mg-doped NWs . . . 69

5. Optical properties of doped and undoped GaN NWs **71**
  5.1. Raman scattering . . . 71
  5.2. Low-temperature PL . . . 72
    5.2.1. Near band edge PL for undoped and Si-doped samples . . . 73
    5.2.2. Near band edge regime in Mg-doped samples . . . 79
    5.2.3. DAP region (below 3.4 eV) . . . 80
    5.2.4. Deep yellow luminescence . . . 82
  5.3. Conclusions . . . 83

6. Electrical properties of GaN NWs 85
6.1. Surface band bending . . . 85
6.2. Sample preparation . . . 86
6.3. Si-doped GaN NWs for single wire measurements . . . 88
    6.3.1. NWs with short contact regions . . . 89
    6.3.2. NWs with long contact regions . . . 96
6.4. E-beam assisted contacting . . . 98
6.5. Conclusions . . . 100

7. GaN nanodisks embedded in AlGaN/GaN NWs 103
7.1. Sample design . . . 104
7.2. Structural characterization . . . 106
7.3. Optical characterization . . . 113
    7.3.1. Influence of nanodisk thickness . . . 114
    7.3.2. Influence of barrier composition . . . 118
    7.3.3. Temperature dependence . . . 118
7.4. Discussion and comparison with 3D simulations . . . 120
7.5. Conclusions . . . 124

8. InGaN nanodisks embedded in GaN NWs 125
8.1. Design of the samples and growth parameters . . . 126
8.2. Morphological properties . . . 128
    8.2.1. Morphology and defects of low-temperature GaN . . . 128
    8.2.2. Structural characterization of nanodisk samples . . . 131
8.3. Optical investigation . . . 136
8.4. Conclusions . . . 143

9. Conclusions 145

A. Appendix 147
A.1. Sample processing for single NW contacts . . . 147

Bibliography 153

List of publications 171

Acknowledgements 174

Abstract

This work reports on the optical and structural properties of self-assembled group III-nitride nanowires (NWs) and nanowire heterostructures and their growth by molecular beam epitaxy (MBE). These NWs are single crystals with typical diameters of 10 nm - 100 nm and lengths (controlled by growth duration) up to 2 μm.

Mainly Si is used as substrate, but also sapphire and diamond in different crystallographic orientations are investigated. The best results for GaN NW growth are obtained on Si(111) substrates, where the growth of matrix-free single domain NWs is possible without substrate pretreatment. In the case of sapphire substrates, different buffer layers are evaluated and it is shown that by employing an approx. 20 nm thin Si buffer layer GaN NW growth on sapphire is possible.

In general, GaN NWs are formed under highly nitrogen-rich growth conditions and for high substrate temperatures. GaN NW nucleation shows a delay up to 60 min for high substrate temperatures (around 790°C), whereas for slightly lower temperatures (770°C) instantaneous nucleation is observed. It is shown by transmission electron microscopy (TEM) and Raman measurements that these GaN NWs are strain-free single crystals which are practically free of structural defects except for the case of high Mg doping levels where basal plane stacking faults (BSF) form cubic inclusions inside the otherwise wurtzite crystal. These BSFs also strongly affect the photoluminescence properties by decreasing the band edge emission and enhancing emission below 3.27 eV.

The impact of doping on the NW morphology and their photoluminescence properties is analyzed over a wide range of doping levels, both p-type with Mg and n-type with Si. The presence of Mg leads to lateral growth which is not present for not intentionally doped (n.i.d.) GaN NWs and, accordingly, to reduced axial growth rate. For Si doping a conical widening of the the NWs is observed. The Mg concentration determined by secondary ion mass spectroscopy (SIMS) ranges up to $1\times10^{20}\,\mathrm{cm}^{-3}$. The near band edge photoluminescence (PL) emission of undoped or slightly Si-doped material is dominated by the narrow D^0X recombination at 3.4715 eV with a full width at half maximum (FWHM) of 1.5 meV at 4K. For moderate Mg fluxes the acceptor-bound exciton recombination was detected at 3.4665 eV. Point defects due to the N-rich growth conditions are discussed as the origin of the emission band at 3.45 eV.

A special design for long GaN:Si NWs (typical length 2 μm) with highly n-type doped end regions is developed to facilitate ohmic contacts to the NWs. Current-voltage measurements on single NWs show that the conductivity can be varied

over several orders of magnitude by changing the doping level of the center part of the NWs. However, contacting individual NWs is technically challenging and not yet mastered reproducibly.

Additionally, GaN/AlGaN heterostructure NWs with embedded GaN nanodisks were grown (NDs, thin insertions of the lower bandgap material inside the NW in the analogy to quantum wells or quantum dots in thin films). By changing the composition of the $Al_xGa_{x-1}N$ barrier throughout the whole composition range or the thickness of the GaN NDs in the range of 1.2 nm to 3.5 nm, the PL emission energy is modified. For low and moderate Al concentrations, the luminescence emission energies increase with increasing Al content due to better confinement. The temperature stability improves which makes these structures usable as optical sensors for gas detection at room temperature or elevated temperatures, exploiting the higher sensitivity of nanowire heterostructures for gases like oxygen, hydrogen or hydrocarbons compared to thin films. However, for high Al concentrations (above 30% – 35%) the emission energy decreases again mainly due to internal electric fields (quantum-confined Stark effect). Furthermore, the temperature stability decreases. Generally, the emission properties are strongly affected by the strain state of the structures. Lateral growth of the barrier material for samples with AlN or $Al_xGa_{x-1}N$ with high Al content leads to the formation of a shell. The variation of the shell thickness along a stack of NDs (i.e. the shell thickness is increased for the lower NDs due to the deposition of the subsequent Al(Ga)N barriers) is identified as the main source of PL emission broadening in these structures. The experimental results are compared to 3D simulations modeling the real structures according to dimensions determined by high resolution TEM imaging. These simulations reveal that the maximum in the emission energy for an Al content of approx. 30% is assigned to the smallest lateral strain gradient and, consequently, the lowest radial internal electric fields in the NDs. Higher Al concentrations in the barrier cause high radial electric fields that can overcome the exciton binding energy and result in substantially reduced emission intensities.

Finally, the growth and PL properties of InGaN/GaN NW heterostructures, both with several thin InGaN NDs as well as with a single large InGaN segment are discussed. Due to the relatively low growth temperatures which are necessary to avoid InGaN decomposition, these heterostructures suffer from stacking faults. The temperature dependence of PL emission points towards the formation of In-rich clusters. InGaN/GaN heterostructures exhibit luminescence emission in the visible range, with highest intensities around 2.0 eV to 2.5 eV.

1. Introduction

This work reports on the growth as well as on the optical and structural properties of self-assembled group III-nitride nanowires and nanowire heterostructures grown by molecular beam epitaxy (MBE). Nanowires (NWs) are small filamentary single crystals (typical diameter in the range 10 nm – 100 nm) that can be successfully grown on different substrates (like silicon, sapphire or diamond in different crystallographic orientations) with or without the use of catalysts [Cal00, Cal07b]. Sometimes they are also called "whiskers", "nanorods", or "nanocolumns". Nanowires are almost free of structural defects which are present at high density in heteroepitaxially grown thin films. In contrast to Si or GaAs, bulk nitride crystals are not available in satisfying quality and quantity [Ima12]. The main problems are high impurity concentrations, high costs, and small substrate sizes. This creates a demand for new approaches to heteroepitaxy. Here, one solution is provided by nanowire growth.

First reports from the groups of E. Calleja [Cal97, SG98, Cal99], and K. Kishino [Yos97] showed that the self-assembled catalyst-free growth of GaN nanowires by molecular beam epitaxy is feasible. The precisely controlled layer-by-layer growth in MBE allows to form well-defined thin inclusions (quantum wells) of the lower bandgap material within barriers of the higher bandgap material. This principle can be transferred to nanowire growth. These so-called nanodisks (NDs) inside NWs exhibit different properties compared to quantum wells (QWs) in thin films. Unlike pure GaN NWs, nanowire heterostructures (like GaN/AlGaN or InGaN/GaN) are no longer strain-free due to pseudomorphic growth of the different layers in the quantum well stack [Ris05a, Riv07]. Strain inhomogeneities [Riv07] and small size effects [Cal05] become dominant.

The group III-nitride material system(1) covers a bandgap range (at room temperature) from the infrared ($E_{gap} = 0.7\,eV$ for InN [Dav02]) throughout the whole visible range ($E_{gap} = 3.4\,eV$ for GaN) into the UV region ($E_{gap} = 6.1\,eV$ for AlN(2)).

---

(1) Detailed reviews of nitride properties and suitable substrates can be found in [Amb98, Liu02, Vur01, Vur03].

(2) The bandgap value for AlN differs by ±0.1 eV in the literature. Ref. [Guo94] reports 6.03 eV (onset of optical absorption), [Bru97] reports 6.13 eV (determined at an absorption coefficient of $10^{4.8}\,cm^{-1}$), [Yam79] reports 6.2 eV (determined at approx. $10^5\,cm^{-1}$).

The bandgap is direct throughout the whole alloy system, allowing the application in optical devices. InGaN/GaN quantum well structures are currently used as active regions in blue or white light emitting diodes (LEDs), which is a huge and rapidly growing market(1).

Light emission from GaN NWs with InGaN quantum wells throughout the visible range has already been demonstrated [Kik04, Kik06]. Later, also UV emission from GaN/AlGaN NWs was reported [Sek08a], proving the potential of NWs for solid state lighting [Li12].

Another benefit of III-nitrides lies in their chemical and thermal stability which makes device operation possible even in harsh environments. Since it is possible to achieve a sensitivity towards certain surface conditions like the pH value of a surrounding liquid [Wal12a, Wal12b] or concentration of gases like O_2, NO_2, H_2 or various hydrocarbons [Sch02b, Sch02a, Eic03, Teu11, Pau12], the nitrides are suitable for chemical sensing applications. The strongly increased surface-to-volume ratio of NWs drastically increases this sensitivity [Jun08]. For MBE-grown Pt-coated GaN quantum dots embedded in AlN layers hydrogen detection down to 500 ppm could be shown by measuring the change in photoluminescence intensity [Wei09]. In comparison, for GaN NDs inside Pt-coated GaN/AlGaN NWs, a hydrogen detection limit around 5 ppm has been reported recently [Teu11]. Uncoated NWs exhibited an oxygen sensitivity in the same order of magnitude. Thus, NWs present a promising approach for the realization of improved chemical sensors e.g. for pH measurements in liquids or gas detection.

For a reproducible utilization of NWs in applications, the control of the growth mechanism in general, the formation of heterostructures with well-defined interfaces, and doping has to be mastered.

1.1. The nitride material system

Crystal structure The group III-nitrides normally crystallize in the hexagonal wurtzite structure which is thermodynamically favored over the cubic zincblende structure(2). The basal plane of the hexagonal wurtzite lattice, which is spanned

---

(1) The compound annual growth rate between 2009 and 2015 is expected to be 28% according to a study published by Yole Developpment, France (http://www.i-micronews.com/reports/Status-LED-Industry/182/). The revenues of packaged LEDs are reported to be 8.9 billion USD in 2010 with the main sources of general lighting (light bulb replacement) and displays and display backlighting. More than 60 companies involved in the epitaxy of GaN-based LEDs are listed.

(2) The name is derived from the mineral zincblende (α-ZnS, cubic zinc sulphide), which is also called sphalerite structure after the second mineralogical name of zincblende. The hexagonal modification of ZnS, which is called wurtzite (β-ZnS), can also be found in nature.

Table 1.1: *Bandgap and lattice parameters a and c of the III-nitrides at 300K.*

	E_{gap} [eV]	a [Å]	c [Å]
InN	0.7 [Dav02]	3.533	5.693 [Zub01]
GaN	3.43 [Vur01]	3.188	5.185 [Les94]
AlN	6.13 [Bru97]	3.112	4.982 [Gol01]

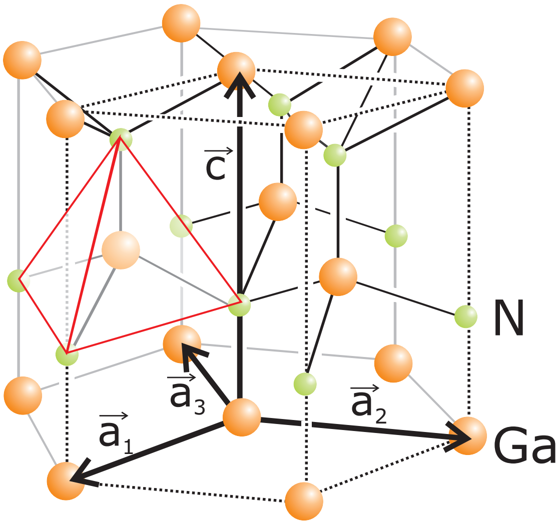

Figure 1.1: *The wurtzite lattice. The hexagonal cell is shown which is built by the lattice vectors $\vec{a_i}$ $(i = 1..3)$ and $\vec{c}$. The black dashed lines indicate the primitive unit cell. Each atom has four bonds to its neighbors, which are tetragonally coordinated. One tetrahedron is outlined in red.*

by the $\vec{a_i}$ lattice vectors, is called *c-plane* (0001), the sides of the hexagonal prism are called *m-planes* $(10\bar{1}0)$ (for further information see e.g. [Amb98] or [Kle90]). These form the sidewalls of the investigated nanowires (**Fig. 1.1**). The a and c lattice parameters of InN, GaN, and AlN are listed in **Tab. 1.1**.

One layer of N atoms together with one adjacent layer of Ga(Al,In)-Atoms (connected by bonds that are not along the *c-axis*) form one *bilayer*. One has to discern between N-face (N atoms on top of a bilayer) and metal face (metal atom on top of a bilayer) of the *c-plane* surfaces. The properties of the two orientations differ, since the III-nitride unit cell does not show inversion symmetry. Furthermore, the chemical stability of these two surfaces is different [Amb98].

Wurtzite vs. zincblende structure These two crystal structures differ only in the stacking sequence of the lattice planes, which is A-B-A-B along the *c-direction* [0001] for wurtzite (WZ) and A-B-C-A-B-C along the cubic [111] direction for

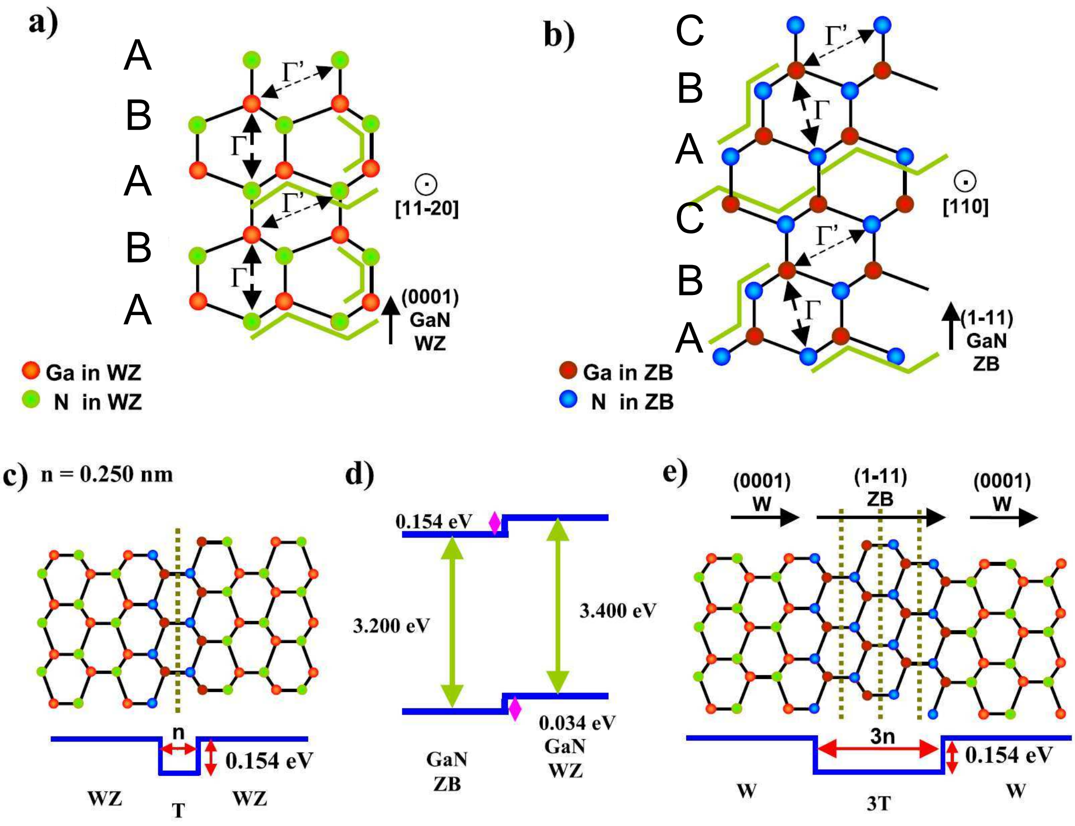

Figure 1.2: *(a) Scheme of the Wurtzite (WZ) structure with A-B-A-B stacking viewed along the [11$\bar{2}$0] direction. (b) Zincblende phase (ZB) with A-B-C-A-B-C stacking viewed along the [110] direction. (c) Atomic arrangement and conduction band profile for a single GaN ZB unit inside WZ GaN (quantum well of a thickness of 0.25 nm). (d) Possible band alignment between GaN WZ and GaN ZB according to [Mur94]. (e) Atomic scheme and conduction band profile for a QW equivalent to three ZB cells (3T). Figure taken from [Arb09].*

zincblende (ZB). One lattice structure can be transferred into the other by changing the stacking order.

All NWs presented in this work are of wurtzite crystal structure. In some cases like high Mg doping (see Sec. 4.2 or Ref. [Arb09]) or growth at low substrate temperatures (p. 53 and Sec. 8.2.1, p. 128), basal plane stacking faults (BSFs) can be generated, leading to cubic inclusions (**Fig. 1.2 a,b**). The bandgap of ZB GaN (3.27 eV) is smaller than for WZ GaN. It is not fully clear whether the band alignment between WZ and ZB is of type I or type II (staggered) [Bel11, Mur94]. Type II leads to a confinement of electrons (formation of a quantum well) in the ZB part, whereas holes are confined in the WZ region. For type I, both electrons and holes are confined in the ZB region. In **Fig. 1.2 c,e** it is schematically shown how quantum wells can be formed by ZB inclusions.

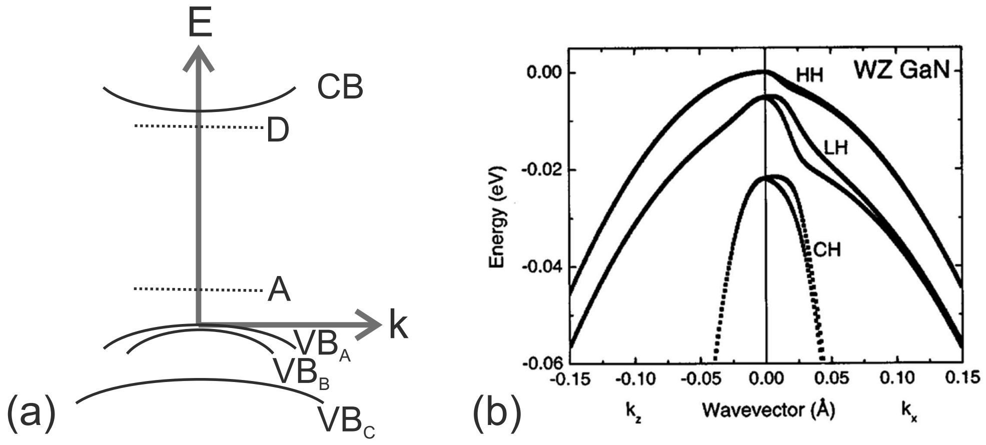

Figure 1.3: *(a) Band structure of GaN around the* Γ*-point (center of the Brillouin zone). The conduction band (CB), the valence band which is split in three components (VB*$_A$*, VB*$_B$*, and VB*$_C$*), an exemplary donor level (D) and an acceptor level (A) are shown. k: wave vector, E: energy; (b) Detail of the valence band splitting around* Γ*-point according to Ref. [Vur03] with the three valence bands that can be attributed to the heavy hole (HH), light hole (LH), and crystal field splitting (crystal hole, CH) valence bands.*

Bandgap The bandgap varies from 0.7 eV (InN) over 3.4 eV (GaN) to 6.1 eV (AlN) i.e. from the near infrared through the whole visible range into the UV (see **Fig. 1.4**). Since the bandgap is direct for the whole alloy range, the III-nitrides are a suitable system for light emitters. A schematic picture of the band structure at the Γ-point is shown in **Fig. 1.3**. The valence band (VB) is split into three sub bands. Therefore, the free exciton energies are split into three components as it can be observed e.g. in low-temperature PL measurements (see e.g. **Fig. 5.3** on p. 73). At low temperatures, holes are only found in VB$_A$ and VB$_B$, while holes in the VB$_C$ need a higher thermal energy to by excited. Therefore, only the free exciton A and B recombinations are visible at 4K.

The bandgap of a ternary nitride alloy can be calculated from the standard bowing equation [Wu03].

$$E_g^{Al_xGa_{1-x}N} = E_g^{GaN} \cdot (1-x) + E_g^{AlN} \cdot x - b \cdot x(1-x) \tag{1.1}$$

This equation can be used in analogy for the other alloy combinations. Experimental values for the bowing parameter b are 1.3 eV for AlGaN [Ang97], 2.5 eV [Dav02] or 2.8 eV [Mor09] for InGaN , and 3.0 eV for InAlN [Wu03].

Polarity Due to the difference in electronegativity between nitrogen (N) and the respective metal cations (In, Ga, or Al), their bonds are not purely covalent, but have a strong ionic component, which leads to a dipole moment along the *c-axis*.

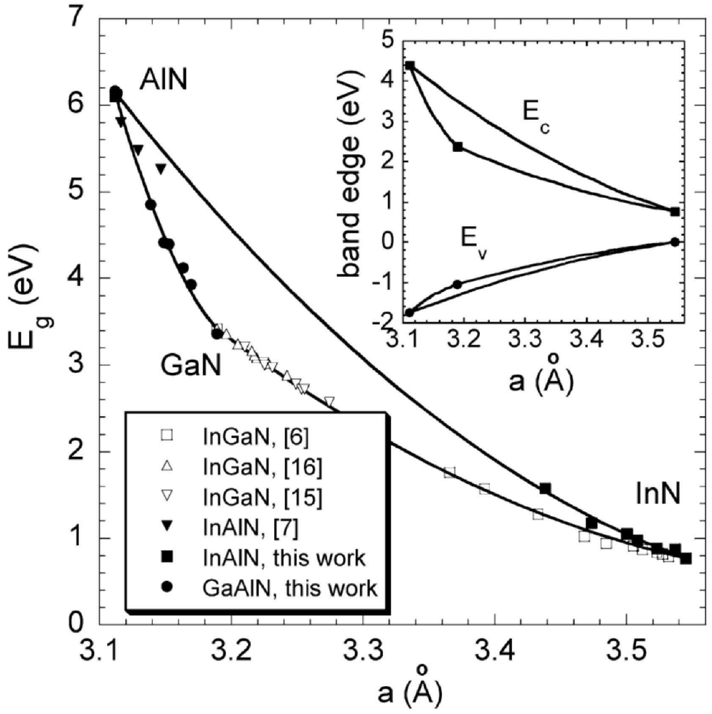

Figure 1.4: *Bandgaps of group III-nitride alloys as a function of in-plane lattice constant. The curves for the bandgap of the ternary alloys were calculated using Eq. 1.1. Inset: The calculated valence and conduction band edges of group III-nitride ternary alloys as a function of the* a *lattice parameter. The points at 3.11, 3.19, and 3.54 Å represent AlN, GaN, and InN, respectively. All the band edge energy values are referenced to the valence band maximum of InN. Graph from [Wu03].*

In an ideal wurtzite crystal the resulting dipole moment would be zero. However, in the real crystal (due to different bond lengths and bond angles of the four bonds of each atom) a net dipole moment remains. This leads to a spontaneous polarization generating an electric field inside the crystal. An additional piezoelectric polarization can be introduced by applying pressure. For pseudomorphical growth of e.g. a thin layer of AlGaN on a thick (relaxed) GaN template, the different lattice parameters lead to strain at the GaN/AlGaN interface and inside the AlGaN layer. This can be observed as a shift in the emission peak position or reduction in luminescence intensity (due to reduced overlap between electron and hole wave functions) of a quantum well. A schematic band diagram of a GaN quantum well is shown in **Fig. 1.5**. The polarization can generate carrier accumulation at the interface (the so-called 2-dimensional electron or hole gas, 2DEG or 2DHG), allowing high carrier densities without doping [Amb99, Amb03]. This effect is used for high electron mobility transistors (HEMTs) in high power and high frequency electronics.

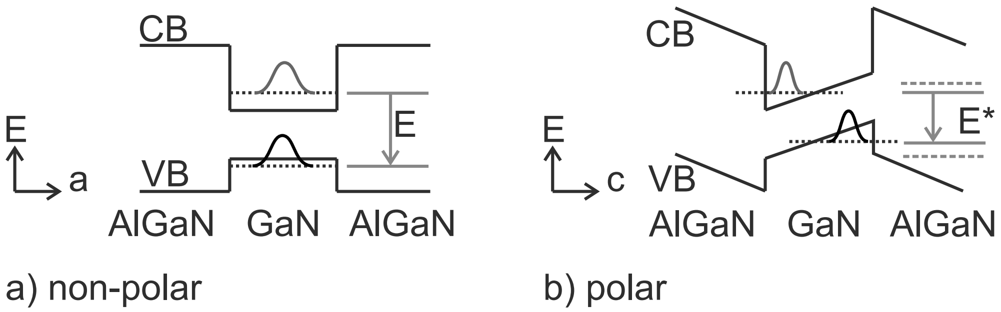

Figure 1.5: *Schematic band diagram (CB: conduction band, VB: valence band) of an AlGaN/GaN quantum well. The first bound state for the electron and the hole is depicted with a dashed line and the respective wave function is shown. (a) Non-polar material (growth along the* a-axis*). (b) Polar material (growth along the* c-axis*). The hole and electron wave functions are spatially separated and the transition energy* E *is reduced to* E^* *(quantum-confined Stark effect, red-shift of the optical emission).*

When polarization effects shall be avoided, the structures must be grown along a non-polar direction (*a-axis* $[11\bar{2}0]$ or *m-axis* $[10\bar{1}0]$). All NWs presented here are grown along the *c axis* [0001] and, therefore, are subjected to these effects, as discussed for GaN/Al(Ga)N heterostructures in Chapter 7.

GaN layers on *c-plane* sapphire grown by molecular beam epitaxy (MBE) usually exhibit N-face polarity [Kaz98]. The GaN nanowires on Si presented here also exhibit N-face polarity (see Section 3.2.1 or Ref. [Mat12]). AlN layers on sapphire substrates show Al-face polarity [Fel98, Dim00]. The polarity of GaN layers on sapphire can be switched to Ga-face by a thin AlN buffer layer (with a thickness of e.g. 5 nm) [Amb99, Stu01]. N-face polarity of GaN layers grown by MBE was also reported for growth on Si(111) by Palacios et. al. [Pal00]. However, a 10 nm to 20 nm AlN buffer was not sufficient to change the polarity, only samples with a 20 nm to 30 nm thick AlN buffer showed Ga-face polarity, according to wet etching experiments with KOH. Long nitridation of *c-plane* sapphire (100 min at growth temperatures) is reported to favor Ga-face polarity (but with reduced crystal quality) [Geo01]. However, GaN on *c-plane* sapphire grown by metal-organic chemical vapor deposition (MOCVD) is reported to exhibit Ga-face polarity (see [Amb98]). It is assumed that under conditions present in MOCVD (higher growth temperatures, N-rich conditions) the surface becomes nitridated (i.e. an AlN layer is formed).

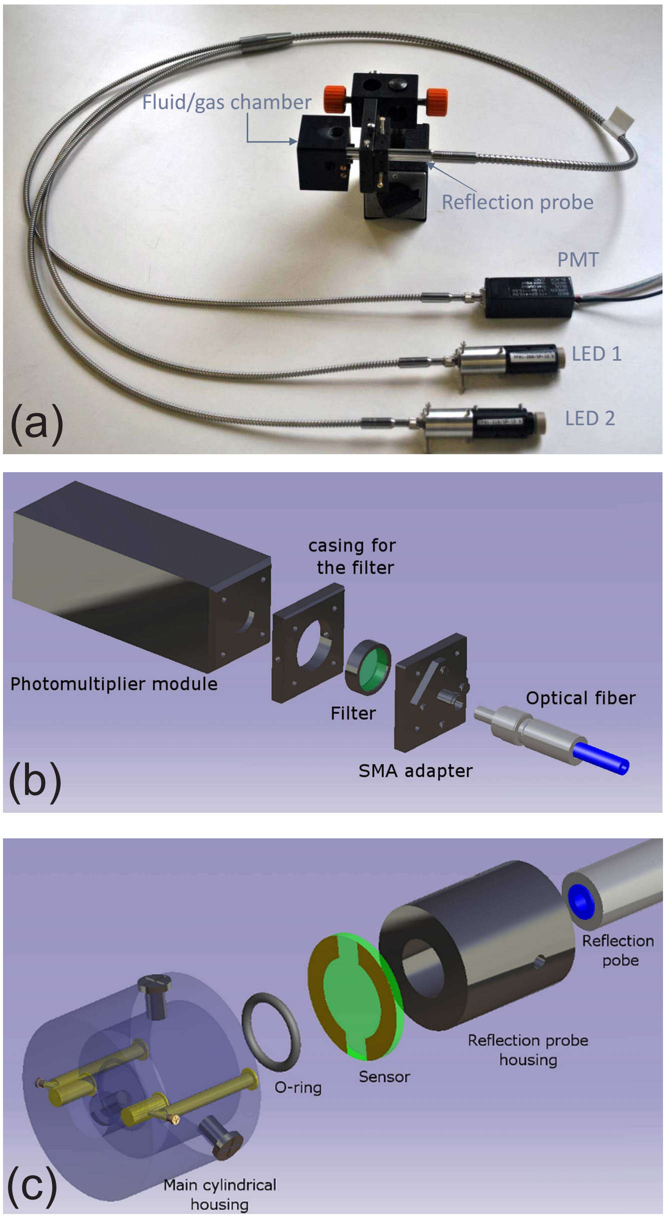

Figure 1.6: *(a) Photograph of a DOTSENSE demonstrator built by the company EADS. A commercially available LED is used as the light source for PL excitation. This demonstrator has two LED ports to either use two LEDs with different wavelengths ((i)*$\lambda = 275\,nm$*; optical output power: P=0.5* mW*, (ii)*$\lambda = 365\,nm$*; P=80* mW *or (iii)* $\lambda = 365\,nm$*; P=330* mW*) or two equal ones for higher light intensity. Both excitation and PL light is collected via fiber optics. The emitted light is detected by a photomultiplier tube (PMT). (b) Explosion drawing of the detector unit. A suitable filter prevents light from the LED to pass. The PMT could be replaced by a semiconductor photo-detector. (c) Explosion drawing of the fluid/gas chamber. The transducer ("sensor", GaN/InGaN QDots in layers or NDs in NWs) is mounted as a window and sealed with an o-ring. The sample area which is not in contact with the fluid/gas (outside the o-ring) can be electrically contacted and, thereby, the sample can be biased for measurements in fluids.*

1.2. Introduction to the DOTSENSE project

The work on GaN/InGaN heterostructures was carried out within th EU-funded project DOTSENSE⁽¹⁾. The aim of this project was to utilize GaN/InGaN quantum dots and nanodisks in nanowires as opto-chemical transducers for sensor units. The photoluminescence intensity of such structures is changed when different molecules come in contact with the surface and alter the surface potential. One application is detection of small concentrations of gases like H_2 or hydrocarbons [Sch02b, Sch02a, Teu11, Pau12], another is fluid monitoring (pH measurements) [Wal12b]. The sensor will be operated in harsh environments (corrosive media, high temperatures) and, therefore, the transducer must withstand these conditions. The idea is to use transparent substrates (like sapphire) and perform excitation and detection of the GaN/InGaN photoluminescence through the substrate. Alternatively, the transducer could also be illuminated from the front side through a window in the fluid/gas chamber. Whereas the first design also works with substances (fluids or gases) in which the light would be absorbed, the latter demands transparency in the used wavelength regime. Therefore, illumination through the substrate is preferred. Only the transducer itself is in contact with the gas or liquid and no electrical contacts to it are necessary. A demonstrator of a sensor assembly is shown in **Fig. 1.6**.

This work is performed in collaboration of the Walter-Schottky-Institut and the Justus-Liebig-University Giessen(2) together with EADS Innovation Works(3), the CEA (Commissariat a l'Energie Atomique)4), and the Aristotle University of Thessaloniki(5).

1.3. Outline of this thesis

Goal of the present thesis is the understanding of self-assembled III-nitride nanowire growth by molecular beam epitaxy. The main focus is on GaN NWs. The be-

---

(1) Funded under 7th FWP (Seventh Framework Programme) of the European commission; Grant No. 224212; Research area: ICT-2007.3.5 Photonic components and subsystems; www.dotsense.eu

(2) Project leader: Prof. Dr. Martin Eickhoff; I. Physikalisches Institut; Justus-Liebig-Universität; Heinrich-Buff-Ring 16; D-35392 Gießen

(3) Workpackage leader: Dr. Andreas Helwig; EADS Innovation Works, Dept. Sensors, Electronics & Systems Integration; D-81663 München (Ottobrunn)

4) Workpackage leader: Dr. Eva Monroy; Commissariat a l'Energie Atomique (CEA); INAC/SP2M/PSC; 17 rue des Martyrs; 38054 Grenoble, France

(5) Workpackage leader: Prof. Dr. Philomela Komninou; Nanostructured Materials Microscopy Group; Department of Physics; Aristotle University of Thessaloniki; GR-54124 Thessaloniki (Greece)

havior of GaN NWs on different substrates, mainly Si(111), but also sapphire and diamond in different crystallographic orientations is investigated. Doping of GaN NWs with Si and Mg is studied, which procures deeper understanding of the growth process itself and is also of great importance for electrical applications. Based on the experience obtained from GaN NW growth, AlGaN/GaN and GaN/InGaN heterostructure NWs were grown and analyzed. By specific insertion of thin regions of the lower bandgap material, quantum well- or quantum dot-like structures are formed. These heterostructures are suitable as transducers for various sensing applications.

In Chapter 2 an overview of the different nanowire growth techniques used by various groups is given. The MBE system and important experimental techniques used in this work are introduced.

In Chapter 3 the self-assembled GaN nanowire growth on different substrates like silicon, sapphire with various surface orientations, and diamond is compared. It is shown that Si(111) is the most suitable substrate material since NWs without wetting layer can be grown directly on untreated wafers. The dependence on various growth parameters like Ga flux and substrate temperature as well as a study of the nucleation behavior and the substrate-to-nanowire interface are presented.

In Chapters 4 and 5 doped GaN nanowires grown on Si(111) are discussed in detail. In Chapter 4, the impact of doping with Si and Mg on the NW structure is investigated by scanning electron microscopy (SEM) and transmission electron microscopy (TEM). This is completed by optical studies on the same samples (Chapter 5). Results from Raman scattering and temperature-dependent photoluminescence are discussed.

In Chapter 6 the results of electrical measurements on single GaN:Si nanowires are presented and methods of contact formation by photolithography and e-beam-assisted metal deposition are explained and evaluated.

In Chapters 7 and 8 NW heterostructures of III-nitrides are investigated. In Chapter 7, GaN nanodisks inserted in NWs between Al(Ga)N barriers are studied by TEM and PL. The emission properties as a function of ND thickness and barrier composition are discussed. It is shown that the temperature stability of the PL emission has its maximum at a certain Al concentration where it is comparable to that of quantum dots. One important point in these structures is the strain distribution that will be analyzed by TEM and theoretical modeling.

In Chapter 8 InGaN NDs inside GaN NWs are discussed. These samples were grown in analogy to the GaN/AlGaN structures. Additional samples with thick InGaN sections are used for comparison. As in the previous chapter, the optical properties are analyzed by temperature-dependent PL spectroscopy. Structural analysis is provided by TEM.

In Chapter 9 the main conclusions of this thesis are summarized and a brief outlook is given.

2. Nanowire growth and experimental techniques

In this chapter, different methods for NW growth are presented. In general, NWs can be grown with or without the use of metal catalysts (like Au or Ni), on untreated or on pre-patterned substrates (selective area growth). The growth method used in this work is catalyst-free and self-assembled. The avoidance of catalysts does not only simplify the process, but avoids detrimental effects of incorporated catalyst atoms [Chè10]. Furthermore, the MBE system is described and experimental techniques are briefly introduced. For optical characterization, photoluminescence spectroscopy (PL) at temperatures between 4K and room temperature was performed. The NW morphology was assessed by scanning electron microscopy (SEM) and transmission electron microscopy (TEM).

2.1. Different growth techniques for nanowires

The intentional growth of semiconductor wires has been reported first in 1964 by Wagner and Ellis [Wag64] for Si wires (or so-called “whiskers”) using Au droplets as catalysts in a vapor-liquid-solid (VLS) growth mode. Hereby, Si is accumulated in a liquid Au droplet. When the Au droplet becomes super-saturated with Si, a solid Si crystal grows under the droplet (**Fig. 2.1**).

Self-assembled growth Nitride nanowire growth without the use of foreign catalysts by MBE – the method employed in this work – has been first reported independently by the groups of E. Calleja [Cal97, SG98, Cal99] and K. Kishino in 1997 [Yos97]. The latter also proposed the idea of growing GaN/AlGaN multilayer structures to form GaN quantum disks in analogy to quantum wells in thin films [Yos98]. We investigate this topic in detail in Chapter 7. In earlier publications, the NW formation has been assumed to be driven by “Ga-balling” [Cal00, Ris02, Mei06], similar to the above-mentioned VLS process. However, further experiments including results presented in this work disprove this.

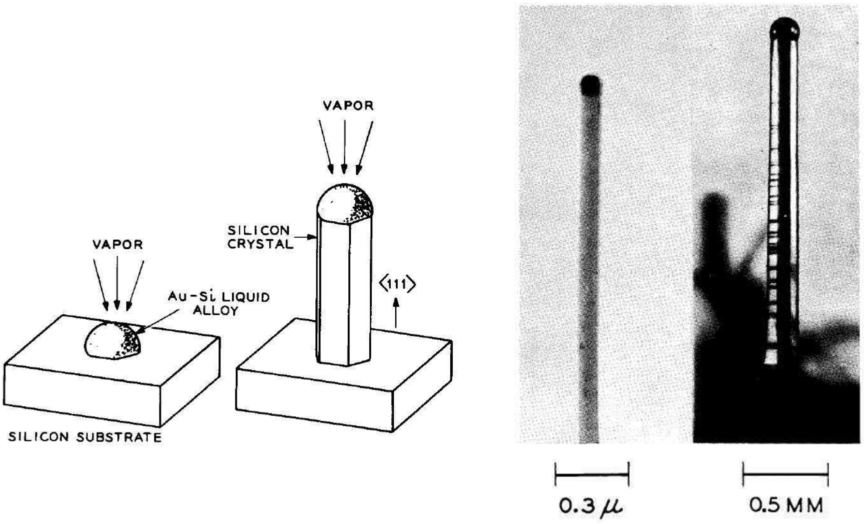

(a) (b) (c) (d)

Figure 2.1: *Left: Schematic illustration: Growth of a silicon crystal by VLS growth. (a): Initial condition with liquid Au droplet on the substrate. (b): Growing crystal with liquid droplet at the tip. Right: Silicon wire showing solidified gold-silicon alloy at the tip. (c): Transmission electron micrograph of a 100 nm thick whisker. (d): Photograph of a crystal seeded on a {111} substrate. This is a twelve-sided needle with alternating {211} and {110} faces. Images from [Wag64].*

Catalyst-assisted growth GaN NWs can be grown by MBE using a catalyst, which is deposited on the substrate before growth. For GaN NWs, nickel is used [Chè10], whereas for Si or GaAs/GaP NWs typically gold is used [Wag64, Gud02]. The deposited Ni forms droplets that act as nucleation sites. However, it was shown that this technique leads to a high density of structural defects (stacking faults) most likely due to the incorporation of catalyst atoms [Gee07, Keh08]. The solid GaNi droplet which has cubic structure may promote the introduction of stacking faults [Chè10]. NW growth on sapphire substrates was only observed under nitrogen rich growth conditions. The growth is explained by the VLS model by accumulation of the group III element inside the Ni catalyst droplet. This accumulation leads to a blurring of the interfaces in heterostructures since even for an abrupt change of the impinging species only a gradual transition of the concentrations of the different group III atoms in the droplet is achieved [Gud02]. Direct comparison of low temperature PL exhibits that Ni-catalyzed NWs have a weaker near band edge emission intensity than catalyst-free grown NWs (by a factor of 25) [Chè10] although the samples featured similar morphology in SEM. Therefore, this approach is not suitable for optical applications.

Heteroepitaxial growth on pre-patterned substrates Self-assembled growth lacks the possibility to freely control diameter, density, and position of the NWs. This can be overcome by the use of pre-patterned substrates. One approach for self-assembled heteroepitaxial growth was presented in Ref. [Cal07a]. In this case, a SiO_2 layer was grown onto the Si substrate and holes defining the NW nucleation spots were generated by e-beam lithography and reactive ion etching. Although this concept is straightforward, its practical implementation is not free of problems and peculiarities: No selectivity in GaN growth is achieved between the untreated Si and the SiO_2 mask. Hence, it is necessary to remove the NWs grown on the oxide, e.g. by wet chemical etching with hydrofluoric acid (HF). Furthermore, if the holes are wider than typical NW diameters (20 nm – 50 nm) not a single NW, but a bundle of NWs grows in each hole. This demonstrates that the NW diameter is still determined by the self-assembly process itself (like on an unpatterned substrate) rather than by the hole diameter. Recently, selective area growth (SAG) using a SiO_2 mask was demonstrated for AlN-buffered Si(111) substrates [Sch11]. At high substrate temperatures ($T \geq 835°C$) nucleation on the oxide mask could be inhibited whereas GaN NW growth inside the holes was observed. Nucleation of single NWs was observed for holes with a diameter of 50 nm. NW bundles nucleated inside larger holes.

Kishino *et al.* [Kis08] demonstrated that a selective area growth is possible on Si(111) substrates patterned with Ti masks when the growth temperature is high enough. At temperatures above a threshold of approx. 900°C, nucleation was observed only on the Si areas, whereas GaN NWs were found both on the Ti mask and the Si substrate at growth temperatures below. These growth temperatures are considerably higher than those reported by other groups or those used in this work.

Homoepitaxial growth on pre-patterned substrates Alternatively, GaN NWs can be grown homoepitaxially on GaN templates with different growth masks such as Ti (see Ref. [Sek08b] for MBE growth) or Si_xN_y (Ref. [Her06] for metal organic chemical vapor deposition, MOCVD). It should be noted that this can lead to different properties than those of self-assembled NWs since the NW growth adopts the morphology of the GaN template which normally suffers from structural defects. However, it could be shown that the optical properties in case of PL emission intensity and defect luminescence are superior to unpatterned thin films [Her06]. Furthermore, threading dislocations were only found within the template, but not in the NWs. Hence, this method allows the growth of regular arrays of individual nanopillars with diameters that are controlled by the mask hole diameter. For

MOCVD GaN growth, no catalyst-free self-assembled method is known. Thus, *ex situ* patterning, the use of (metal) catalysts, or special nucleation steps involving $\mathrm{Si_xN_y}$ deposition [Koe10] are required to promote NW growth.

Growing NWs in a well-ordered array is not necessary e.g. for application as an optical sensor in the DOTSENSE project. The high NW area density of our structures facilitates intense signal response.

Other techniques All methods described above lead to NWs which grow along the *c-axis* and which are aligned perpendicular to the substrate (partially with a few degrees misorientation). GaN NWs growing along either the *c-* or *a-axis* with different morphologies can be produced by direct nitridation and vapor transport of Ga in dissociated ammonia [Li06]. Catalytic growth in a furnace leads to the deposition of randomly orientated NWs [Che01]. However, such a technique does not yield high quality NWs and does not allow the formation of well-defined heterostructures.

In summary, self-assembled NW growth offers many advantages:

- Contamination by catalysts is avoided
- The density of structural defects is drastically reduced compared to heteroepitaxial films
- Different substrates – including Si – can be used
- No pre-patterning steps are required
- Nanowire growth on the whole substrate wafer, not confined to a small area
- Relatively inexpensive compared to other approaches

2.2. The MBE system

Plasma-Assisted Molecular Beam Epitaxy (PAMBE) was used for the growth of all samples investigated in this work. An overview of the setup is given in **Fig. 2.2**. In the UHV growth chamber (manufactured by *TecTra*, Frankfurt) thermal effusion cells are used to supply the group III metals Ga, Al, In, as well as the dopants Si and Mg. For Ga, a hot lip cell is used to avoid precipitation of Ga droplets at the crucible opening. Al is evaporated by a cold lip cell. These cells were manufactured by *Dr. Eberl MBE Komponenten GmbH* (Weil der Stadt, Germany; www.mbe-components.com). Each cell is equipped with a computer-controlled shutter. Nitrogen (purity 7N) is fed through a gas purifier (*Entegris*) and a UHV needle valve to ensure constant flux. Since molecular nitrogen is too inert to react, active (atomic) nitrogen is produced by an *Oxford Applied Re-*

search CARS 25 radio frequency plasma source which is driven by a 13.56 MHz RF generator operated at 425 W output power. The nitrogen pressure is monitored by a spinning rotor gauge [Fre85] manufactured by *MKS Instruments Deutschland GmbH, München* (model: SRG-2) and a Bayard-Alpert (ionization) pressure gauge [Bay50] manufactured by *Arun Microelectronics Ltd. (AML), England.* The chamber is equipped with a second Bayard-Alpert gauge that can be moved to the substrate position to measure the flux (beam equivalent pressure, BEP) of each effusion cell. Flux measurements both for the group III metals and for the dopants are shown in **Fig. 2.3**. All effusion cells show the expected thermally activated behavior. No element-specific correction was performed. The values are therefore nitrogen equivalent pressures, since the gauge has been calibrated for nitrogen by the manufacturer. As a guideline it can be said that a change of the effusion cell temperature by 35°C (for Ga), 36°C (for Al), 30°C (for In), 33°C (for Si), 13°C (for Mg) changes the flux by a factor of two. Furthermore, the chamber is equipped with a quadrupole mass spectrometer (*Leda Mass Spectra Physics*, model: Vacscan) for residual gas analysis.

During growth, the substrates are heated by thermal radiation of a tungsten wire heater and are constantly rotated (typically at 15 rpm). The maximum substrate size is 2" (50.8 mm). For Si, the samples were grown on 1" × 1" pieces. The pieces were cut from 4" wafers (thickness 525 μm, single side polished, n-type doped with As, specific resistance of $\rho = 0.003 - 0.007\,\Omega$cm unless otherwise noted). While 2" wafers can be mounted directly into a ring cartridge, tantalum holders with the size of a 2" wafer (thickness 1 mm) are used as adapters for smaller substrates. These holders have exactly sized holes and the substrates can be clamped at their edges with thin tantalum foil (thickness 0.1 mm). The substrate temperature is monitored by a pyrometer looking through a viewport (manufacturer: *Dr. Georg Maurer GmbH*, model: TMP-85d, measuring range of 550°C to 1100°C). A reproducible substrate temperature is crucial, as will be shown in Sec. 3.2.2 (p. 40).

The substrates are introduced into the system via the load lock chamber, which is also used for storage of several HF-etched Si substrates and which is pumped at least over night before one substrate is transferred into an intermediate chamber (preparation chamber with a background pressure comparable to the growth chamber) and further into the growth chamber. The growth chamber is pumped with a turbo molecular pump. Additionally, a cryopanel is permanently refilled with liquid nitrogen (T = 77K) to adsorb residual gases and provide cell cooling. The typical chamber background pressure is 3×10^{-10} mbar, mainly limited by the presence of nitrogen from previous growth runs.

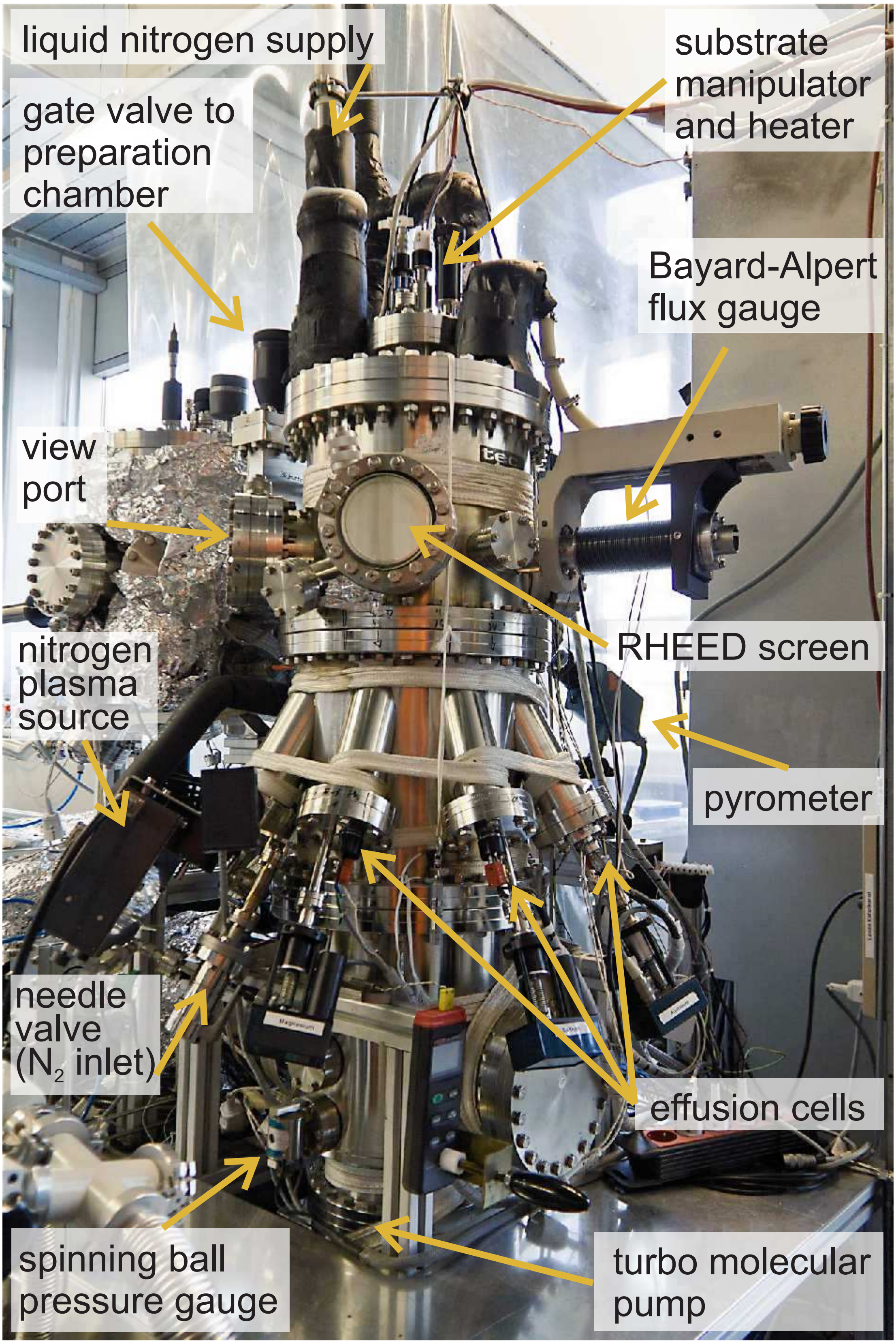

Figure 2.2: *Photograph of the MBE system with important components marked.*

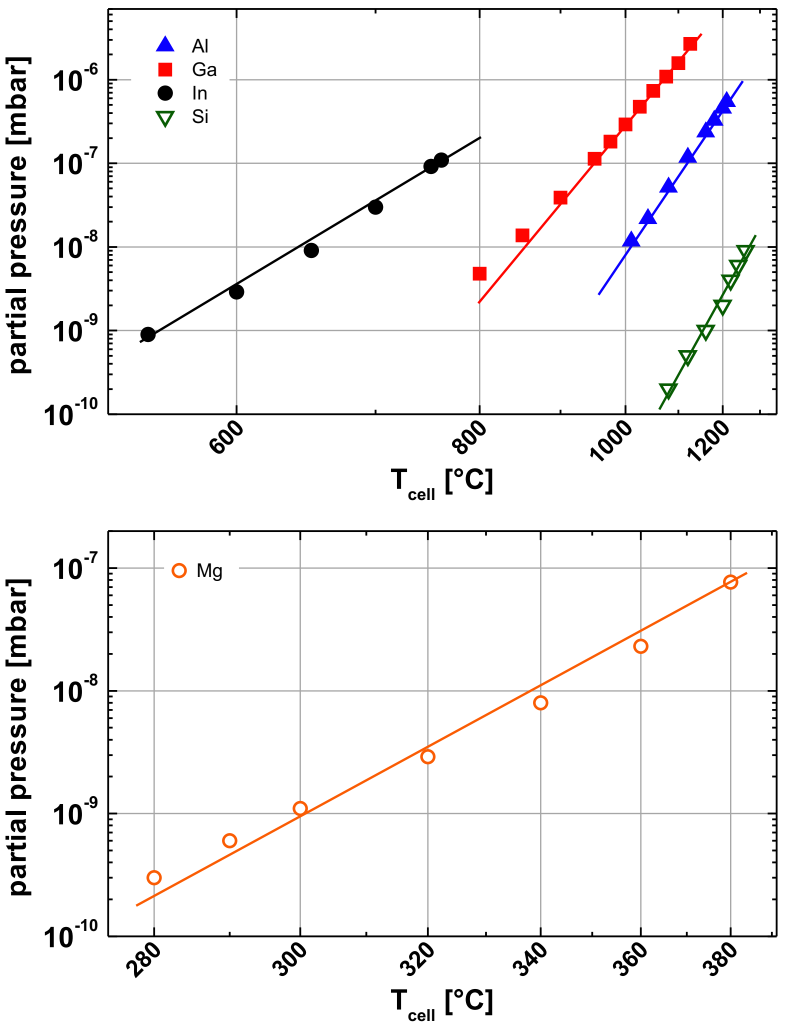

Figure 2.3: *BEP of the different effusion cells as a function of temperature.*

The typical NW growth rate is 7 nm/min. With 0.25 nm per monolayer (ML) this is equivalent to 0.5 ML/sec. The rate w_i of gas particles (atoms or molecules) of the species i that impinge on an area of 1 m^2 per second is [Umr]:

$$w_i = p_i \sqrt{\frac{N_a}{2\pi k_B M_i T}} \tag{2.1}$$

p_i is the partial pressure, N_A the Avogadro constant, k_B the Boltzmann constant, M_i the molar mass of the particles, and T the absolute temperature. For nitrogen at room temperature, this leads to $2.87 \times 10^{20} \cdot p$ molecules per (cm$^2\cdot$ sec) with p the pressure in mbar. For comparison, a Si surface has a density of surface atoms of the order of 10^{15} atoms per cm^2. Further information on the MBE growth technique can be found in [Her89].

2.3. Experimental techniques

The morphological and structural analysis was performed by electron microscopy. Due to their small size, the NW structures cannot be imaged with optical microscopy. In contrast, accelerated electrons exhibit a much smaller wavelength. The de-Broglie-wavelength of a 20 keV electron is 0.086 nm, whereas visible light is in the range of 400 nm to 800 nm.

2.3.1. Scanning electron microscopy (SEM)

Nanowire dimensions (heights and diameters) and area densities were analyzed in a *Hitachi* field emission scanning electron microscope (model S4000), which was operated at 20 kV accelerating voltage and 10 μA emission current. For SEM, no specimen pretreatment is necessary (unless the sample is highly insulating) allowing a fast analysis of the NW morphology. To assess the NW height, edge views of cleaved samples were taken.

2.3.2. Transmission electron microscopy (TEM)

SEM is not capable of reaching atomic resolution and imaging the nanodisks. Therefore, TEM analysis was performed(1). With different TEM techniques as explained below it is possible to extract a variety of valuable information like crystal structure, epitaxial relation, lattice parameters, defect density, quality of the hetero-interfaces, polarity, and element composition.

Sample pretreatment For Cross section TEM (XTEM) and high resolution TEM (HRTEM), a slice of the specimen (cut along a certain crystallographic direction) has to be thinned by mechanical grinding and polishing followed by Ar ion milling until it is sufficiently transparent to the incident electron beam (thickness in the range of 10 nm – 30 nm). Since the NWs remain on their substrate it is possible to determine the epitaxial relationship between the NW and the substrate.

Alternately, the NWs can be "harvested" by removing them from the growth substrate by scraping and/or ultrasonic agitation in a solvent like acetone or n-hexane. A drop of this suspension is transferred onto a TEM grid. After drying

---

(1) The TEM analysis of the GaN NWs and the GaN/AlGaN NW heterostructures was done at the University of Barcelona (Dept. Electrònica) in the groups of Prof. Joan Ramon Morante and Prof. Jordi Arbiol i Cobos (currently at the Institució Catalana de Recerca i Estudis Avançats (ICREA); Institut de Ciència de Materials de Barcelona (ICMAB-CSIC). All InGaN samples were analyzed at the University of Thessaloniki in the group of Profs. Philomela Komninou and George Dimitrakopulos.

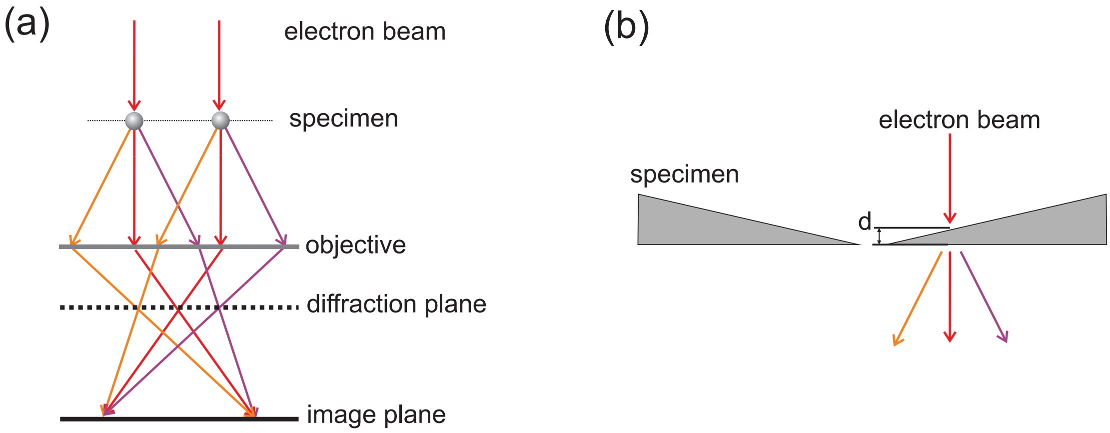

Figure 2.4: *(a) Schematic view of the electron beam path inside a TEM. See text for further explanation. (b) Schematic drawing of a specimen after milling which is done with a conical profile to ensure the preparation of a region with suitable thickness. The thickness* d *is typically 10 nm to 30 nm.*

of the solvent, the NWs can be imaged without a thinning procedure since their diameter is small enough for electron transmission. However, due to the arbitrary NW orientation and the missing substrate, less information can be extracted than from XTEM samples.

TEM operation modes A TEM can be used to obtain both images and diffraction patterns. In **Fig. 2.4** the beam path inside a TEM is sketched. After being scattered by the specimen, the electrons pass through the objective lens. All electrons scattered from one point in the specimen are collected in one point in the image plane generating an image of the specimen. It is also possible to obtain a diffraction pattern where electrons scattered in the same direction from different positions in the specimen are collected in one point. This is observed with a detector placed in the diffraction plane (back focal plane) [Ben01].

Imaging modes For standard imaging, the contrast is obtained by absorption of electrons in the specimen. The strength of the interaction between the electrons and the atoms in the specimen is proportional to the square of the atomic number ($\propto Z^2$) which makes imaging of light elements like nitrogen difficult(1). Therefore, in most TEM images of III-nitrides only the metal atoms can be seen. Only carefully aberration-corrected TEM images allow visualizing the nitrogen atoms (see e.g. [Mat12]).

A higher contrast between different elements is achieved when the high angular

---

(1) The atomic numbers (proton numbers) of the elements involved are: 7 (N), 13 (Al), 31 (Ga), 49 (In)

annular dark field (HAADF) mode is used. For this TEM imaging technique, a ring-shaped detector is utilized that only collects electrons which are scattered under high angles. In this case, the image contrast is highly sensitive to the atomic number. Therefore, this technique is also called Z-contrast mode due to the sensitivity to the atomic number Z. For high resolution TEM (HRTEM), contrast is generated by the phase difference of the electron wave.

When using an energy-dispersive detector, the energy loss of the electrons due to scattering by the specimens' atoms can be measured. This technique is used to determine the chemical elements by their specific absorption edges and is called electron energy loss spectroscopy (EELS) [Ege09, Mai09].

Selective area electron diffraction (SAED) For SAED measurements, a sufficiently monochromatic parallel electron beam passes through the TEM specimen. Using small apertures, only a selected area of the specimen is analyzed giving this technique its name. A diffraction pattern similar to X-ray diffraction is generated. This allows to determine the orientation of the lattice planes and the lattice parameters. For cross section specimens where the NWs are still on their growth substrate, also the epitaxial relationship between substrate and NW can be determined.

Convergent beam electron diffraction (CBED) For the previously explained techniques, a parallel electron beam is used which is necessary to obtain sharp images and diffraction patterns. CBED uses converging beams coming from different angles which are directed on a single spot of the specimen. This leads to a broadening of the diffraction spots into disks with the disk diameter given by the convergence angle. In this case, dynamic scattering effects (interactions between the electromagnetic field distribution of the electrons in the sample and the electron beam) become visible as variations in brightness within the diffraction disks. These effects are sensitive to the polarity of the GaN crystal, i.e. the pattern is different for the (0001) and $(000\bar{1})$ orientations. The obtained patterns are compared to simulations. Whereas this technique allows reliable polarity determination in nitride layers it can lead to false results for NWs. Therefore, contradictory results have been reported for GaN NWs grown at similar conditions (compare e.g. [Fur08a] and [Hes11]).

Equipment The not intentionally doped (n.i.d.) GaN NWs and GaN/AlGaN heterostructures were characterized by HRTEM and scanning transmission electron microscopy (STEM) in bright-field (BFSTEM) and high angular annular dark-field (HAADF or Z-STEM) modes in a *Jeol* JEM2010F field emission gun (FEG) microscope with a 0.19 nm point to point resolution. Electron energy loss spectroscopy (EELS) was carried out by using a GIF2001 spectrometer coupled to the JEM2010F microscope. For TEM sample preparation the GaN NWs were mechanically removed from the substrate and a suspension in n-hexane was prepared. A drop of the suspension was then deposited on a holey carbon copper grid. In order to study in more detail the substrate interface of the GaN NWs, cross-sectional TEM (XTEM) samples were prepared by conventional ion milling.

For all the GaN/InGaN samples, specimens for conventional TEM and HRTEM observations were prepared in cross-sectional geometry (XTEM). Tripod or conventional polishing techniques followed by Ar^+ ion milling up to electron transparency were implemented for specimen preparation. TEM/HRTEM images were recorded on photographic plates and/or saved as digital images through a CCD camera connected to the microscopes. Observations were performed using a HRTEM JEOL2011 (200KV, resolution 0.19 nm) microscope and two TEM microscopes JEM2000FX (200KV, resolution 0.28 nm) and JEOL 100CX (100KV, resolution better than 0.5 nm).

2.3.3. X-ray diffraction

X-ray diffraction was used to determine crystallographic orientation of the NWs with respect to their substrate. A *Philips* (now: *PANalytical*) X'Pert high resolution diffractometer equipped with an Eulerian Cradle was used. X-rays were generated by a ceramic tube with copper anode operating at 40 mA emission current and 40 kV acceleration voltage. The $Cu_{K\alpha}$ radiation (wavelength λ=1.5406 Å) was selected by a Bartels monochromator consisting of four Ge(220) crystals.

The incident beam is diffracted at the crystal lattice planes. The lattice plane distance d can be determined by the maxima of the intensity of the diffracted beam at diffraction angles Θ according to Bragg's law [Kle90]

$$n\lambda = 2d\sin\Theta \tag{2.2}$$

with the diffraction order n.

The standard scan mode is the $2\Theta-\Omega$ scan, where the sample stage and detector arm are moved in a way, that the incidence angle of the X-ray beam with respect to the sample surface is kept equal to the scattering / detector angle ($\Omega = \Theta$, **Fig. 2.5**). This allows to determine the distances of the lattice planes parallel to the sample surface, and thereby to identify the growth direction.

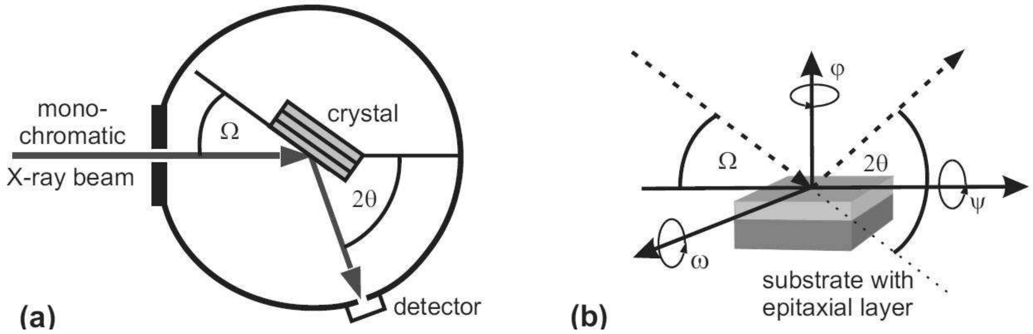

Figure 2.5: *(a) Schematic view of the HRXRD diffractometer. (b) Illustration of the Euler angles.*

NWs can grow tilted with respect to the substrate surface normal. This tilt angle can be evaluated by the width (FWHM) of a symmetrical reflex recorded in the Ω-scan mode (rocking curve). For this, the sample is rotated around the ω axis, whereas the X-ray source and the detector stay at a fixed position.

The epitaxial relation of the NWs with respect to the substrate can by probed by rotating the sample around its surface normal (φ-scan). For a symmetric reflex (i.e. scattering at lattice planes that are parallel to the sample surface), a signal can by detected independently of the value of φ. However, for an asymmetric reflex (i.e. scattering at lattice planes are not parallel to the sample surface) the reflex can be observed only for certain φ angles. For example, the (20.5) reflex of GaN ($2\Theta = 136.4716°$, offset$= -36.9022°$) exhibits a six-fold symmetry due to the hexagonal wurtzite crystal structure and will therefore only be detected for $\varphi = m \cdot 60°$ ($m = 0 \ldots 5$). Further details on X-ray diffraction and the used system can be found in [Kle90, Her09, Höp97, Met97].

2.3.4. Photoluminescence spectroscopy (PL)

Photoluminescence spectroscopy (PL) is an important tool to study basic semiconductor properties like bandgap, excitonic states, quantum confinement in heterostructures, incorporation of dopants, and unwanted impurities. It also allows to assess the crystal quality due to its high sensitivity towards various defects. For PL, the sample is illuminated by light whose energy is above the bandgap to excite electrons from the valence band into the conduction band. Electron-hole pairs are generated inside the semiconductor. These photo-generated carriers thermalize to the lowest available energy state by phonon emission. This process is much faster than the electron-hole recombination. The electron-hole pairs can recombine either non-radiatively by emission of phonons or radiatively by light emission. When they recombine radiatively, light with a certain wavelength is emitted.

An electron and a hole can form a bound state, the exciton. The near band edge emission regime is dominated by excitonic emission. The exciton can either be free (FX^A, FX^B, FX^C, depending on the contributing valence band, **Fig. 1.3** on p. 11) or bound to an impurity (donor or acceptor). The latter is typically the more dominant emission. At slightly lower energies, donor-acceptor pair recombination emission becomes dominant.

The recombination energy can be reduced by the additional emission of a longitudinal optical (LO) phonon, whose energy is 92 meV in GaN. This leads to a replication of the peak at an energy redshifted by $n{\cdot}92$ meV (n=1,2,. . .). The intensity of the replica is lower than that of the original peak and decreases with the order of n. The ratio between the original intensity and the replica intensities can be described by the Huang-Rhys factor, which is a measure for the strength of the electron-phonon coupling.

For confined systems (quantum wells, quantum dots, nanodisks) the transition energy is higher than the bandgap in the bulk due to quantum confinement. However, strain effects and electric fields (see **Fig. 1.5** on p. 13) can reduce the transition energy and intensity. Therefore, the emission peak position of GaN nanodisks is different than of bulk GaN nanowires as will be discussed in Chapter 7.

Photoluminescence was excited using an Ar^{++} ion laser (*Spectra Physics*) with a frequency-doubler (using a β-barium-borate crystal, BBO, *GWU Lasertechnik Vertriebsgesellschaft mbH, Germany*) operating at 244 nm (5.08 eV) with a downstream monochromator. The samples were illuminated in backscattering geometry. The PL emission light was focused onto a *Dilor* triple axis spectrometer (focal length 800 nm) and detected by a Peltier-cooled photomultiplier. Suitable low-pass filter (transparent for $\lambda > 290$ nm or $\lambda > 475$ nm) were used to select only one diffraction order and to block the excitation wavelength. For low-temperature measurements down to 4K the samples were mounted in a *Oxford Instruments* liquid helium flow cryostat (**Fig. 2.6**).

2.3.5. Raman scattering

Raman scattering is inelastic photon scattering. The photons loose (gain) energy by generation (absorption) of phonons. The energy shift is called Stokes (anti-Stokes) shift. The magnitude of the shift depends on the material and its strain state.

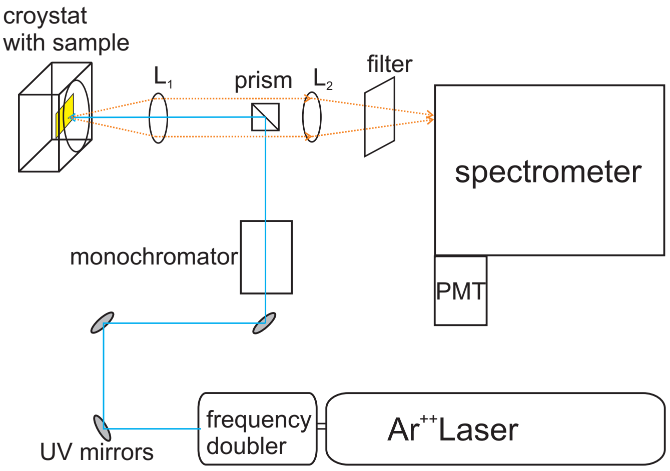

Figure 2.6: *Sketch of the PL setup. The excitation source is a* Ar^{++} *ion laser with a frequency-doubler. The light is monochromatized and directed onto the sample in the cryostat using mirrors and a prism. The PL emission light is collected using lens* L_1 ($f = 150$ mm) *and directed into the spectrometer by* L_2 ($f = 500$ mm). *The light is spectrally dispersed by diffraction gratings inside the spectrometer and recorded by a single channel photomultiplier (PMT). Filters are used to block the 244 nm laser line and - if needed - to avoid higher diffraction orders.*

Raman measurements were performed in backscattering geometry at room temperature, using the 514 nm line of an Ar^{++} ion laser for excitation. The light was focused onto the sample by a 100× microscope objective, the scattered light was analyzed by a DILOR triple axis spectrometer and a liquid nitrogen cooled multichannel charge coupled device (CCD) detector with pixel resolution of 0.7 cm^{-1}. The system was calibrated to the Si substrate mode at 520.0 cm^{-1}.

3. GaN nanowire growth on different substrates

In this chapter, the growth conditions for NW formation on different substrate materials (Si, sapphire, diamond) are comparatively discussed and the substrates are assessed with respect to their suitability for NW growth.

Generally, various substrates can be used for nanowire growth. However, the preferred substrate material is silicon on which GaN NWs can be grown without the need of a buffer layer. It is also the most cost efficient material. Due to the hexagonal symmetry of the (111) surface orientation, a fixed in-plane epitaxial relationship with only one domain is achieved. On the cubic Si(100) surface, a double domain orientation is formed since two equivalent possibilities to orientate the wurtzite *c-plane* on the Si(100) plane exist, which are rotated by 30° with respect to each other. The majority of the samples analyzed in this work were grown on Si(111). The silicon substrate-nanowire interface properties, the formation of a thin Si nitride layer, the time dependence of the nucleation behavior, and suitable parameters for growth on Si substrates will be discussed in detail.

A different substrate is sapphire (single crystalline aluminum oxide, Al_2O_3) which is also commercially available in different crystal orientations (see e.g. [Amb98]). However, for none of these orientations NW formation could be directly achieved. With a suitable buffer layer this problem can be overcome as it will be shown in Sec. 3.3. Finally, diamond was studied in both a polycrystalline, and a single crystalline modification. In contrast to Si or sapphire, it is highly unlikely that diamond surfaces get nitridated(1). Therefore the NW nucleation process on diamond is expected to be different.

---

(1) Carbon nitride C_3N_4 exists and can crystallize in WZ structure (β-C_3N_4). However, the synthesis is difficult and several groups failed with their attempts [Niu93, MG97]. Nitridation of diamond is therefore not expected to happen under the growth conditions employed here.

3.1. Growth window for nanowires

The main difference between the growth processes of thin films and nanowires is the applied ratio of the fluxes of the group III elements like Ga, Al, or In and the group-V element nitrogen (III-V ratio). Whereas for thin films a slight Ga excess has to be maintained [Mou01], the III-V ratio is strongly shifted to nitrogen-rich conditions for NW growth (typically by reducing the Ga flux by a factor of 3 to 4 compared to layer growth). The substrate temperature is chosen relatively high to guarantee a high adatom mobility. The increase of the growth temperature is limited by increased Ga desorption and GaN decomposition. It must be pointed out that the effective III-V ratio is not only determined by the incoming fluxes, but also by the substrate temperature (T_{sub}). A higher T_{sub} leads to a stronger Ga desorption and therefore to more N-rich conditions. Since the temperature also effects the adatom mobility, raising the substrate temperature is not strictly equal to lowering the incoming Ga flux.

The typical dependence of the GaN growth rate as a function of the Ga flux for three different substrate temperatures according to Ref. [SG98] is shown in **Fig. 3.1**. The active nitrogen flux was kept constant and monitored by the optical emission of the nitrogen plasma (optical emission detection, OED). For a given T_{sub} the growth rate first rises with increasing Ga flux (N-rich conditions) and saturates for stoichiometric GaN conditions (III-V ratio equal to 1). For much higher Ga fluxes (metal-rich conditions) Ga droplets are formed on the surface. The growth rate cannot increase further since nitrogen is now the rate-limiting species. The actual Ga flux which is necessary to reach saturation of the growth rate (i.e. stoichiometric conditions) depends on the substrate temperature since a higher T_{sub} leads to higher Ga desorption from the substrate, i.e a lower effective Ga flux.

The influence of the III-V ratio and the substrate temperature on the morphology of GaN NWs grown for this work is shown in **Fig. 3.2**. Image (a) shows an undoped GaN NW sample grown for 90 min on Si(111) at reference conditions (T_{sub} = 780°C, T_{Ga} = 1055°C). For sample (b), the fluxes were the same as for (a), but a 10°C lower substrate temperature was chosen. For samples (c) and (d), the Ga flux was raised by selecting a Gallium effusion cell temperature of T_{Ga} = 1075°C and T_{Ga} = 1123°C, respectively. The substrate temperature was the same for samples (b) to (d). The nitrogen flux was the same for all four samples.

A high substrate temperature is reported as beneficial for the luminescence intensity. In Ref. [Mei06] GaN NWs grown at different substrate temperatures

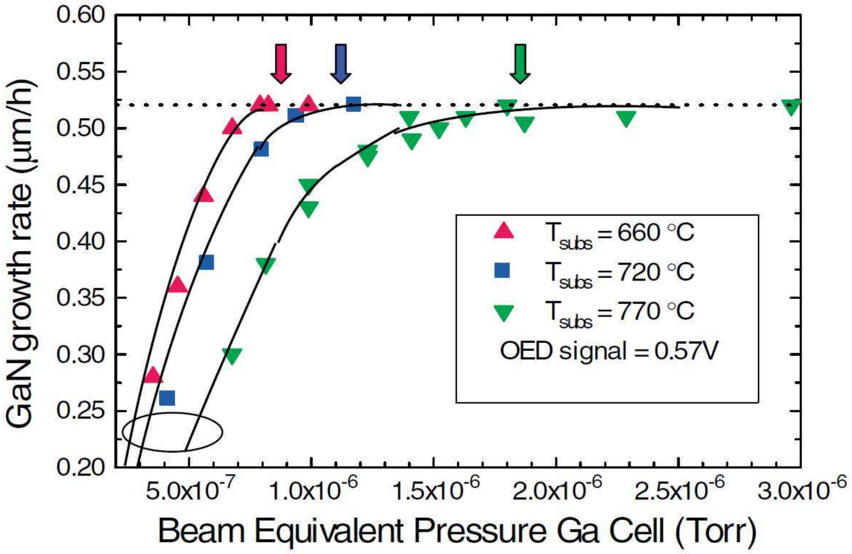

Figure 3.1: *GaN layer growth rate versus Ga flux (beam equivalent pressure, BEP) for different growth temperatures. Arrows indicate the saturation points corresponding to stoichiometric conditions, while the circle at the bottom-left side represents highly nitrogen-rich conditions. Graph taken from Ref. [Cal07b].*

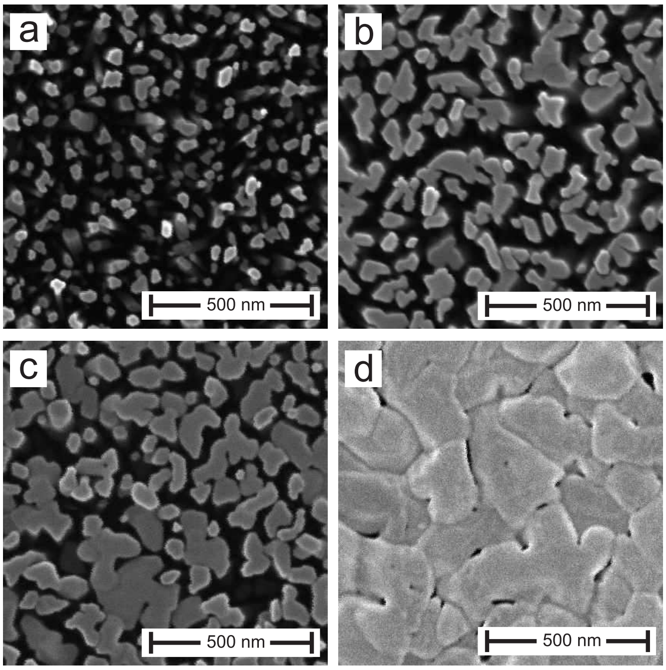

Figure 3.2: *SEM top view micrographs of four undoped GaN NW samples with increasing degree of coalescence from (a) to (d). Sample* ***(a)*** *grown under standard NW conditions (T_{Ga}=1055°C, T_{sub}=780°C).* ***(b)*** *Same as in (a), but with a 10°C lower substrate temperature.* ***(c)*** *Same T_{sub} as in (b), but T_{Ga}=1075°C.* ***(d)*** *Same T_{sub} as (b), but T_{Ga}=1123°C. An almost coalesced GaN layer is formed.*

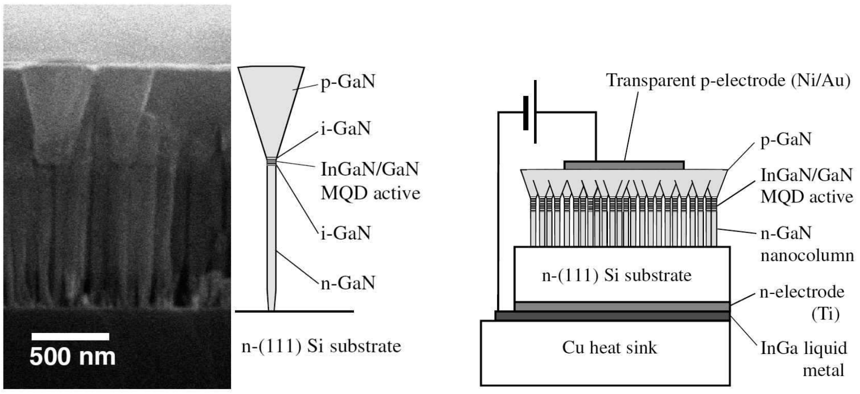

Figure 3.3: *left: Cross-sectional SEM image of InGaN/GaN MQD nanocolumn LEDs grown on (111) Si substrate and schematic diagram of a single nanocolumn LED. right: Cross-sectional diagram of InGaN/GaN MQD nanocolumn LED with semitransparent p-electrodes. Images from [Kik04].*

are compared with respect to their low temperature (10K) cathodoluminescence spectrum. Samples grown at a low T_{sub} ($\Delta T = -30°C$ from the optimum conditions) show the typical defect-related yellow luminescence (a broad emission band around 2.2 eV) that is not present for the optimized samples. The emission band at 3.28 eV is also stronger for the low-temperature samples. It can originate both from donor-acceptor pair (DAP) recombination and from band-to-band transitions in cubic GaN. The ratio between the intensity of the excitonic emission band (3.4 eV – 3.5 eV) and 3.0 eV – 3.3 eV region is increasing with increasing growth temperature. In that report, a two-step growth method was used. The Ga flux was increased by a factor of 1.3 to 2.5 after the nucleation stage to avoid an abrupt reduction of the NW diameter. However, in the work presented here, no such thinning was observed and therefore no such two-step method was used. We optimized the growth parameters for a relatively high substrate temperature accompanied with a higher Ga flux to compensate the elevated desorption.

Coalescence can be enhanced in a later stage of growth by increasing the flux and decreasing T_{sub}. A closed layer is formed, which can be contacted using a large top contact. With this technique, MBE-grown InGaN/GaN nanowire LEDs were demonstrated by Kikuchi *et al.* [Kik04] (**Fig. 3.3**).

3.2. Si substrates

Si(111) vs. Si(100) On Si(100) substrates GaN NWs grow in two domains, which are rotated by 30° around the *c-axis* with respect to each other. This leads to a high density of domain boundaries for coalescing NWs. Si(100) surfaces

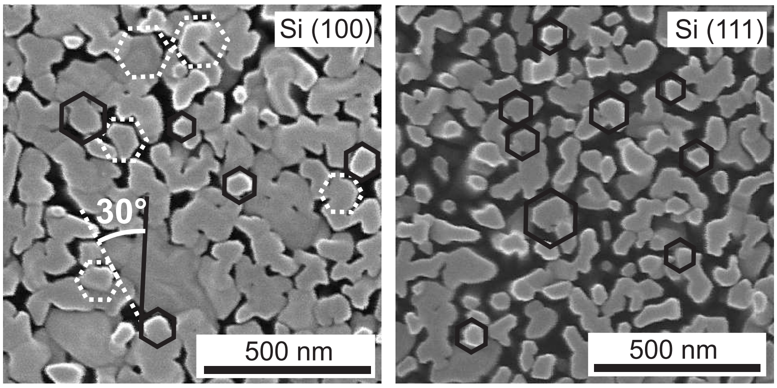

Figure 3.4: *Top-view SEM images of GaN NWs grown on Si(100) and Si(111). On Si(100) substrates two domains rotated by 30° are found (some wires of each domain are highlighted with dashed white hexagons or black hexagons, respectively), whereas on Si(111) NWs grow only in one domain.*

exhibit a cubic symmetry, which allows two equivalent in-plane orientations of the wurtzite basal plane hexagon. On Si(111) substrates only one domain is found (**Fig. 3.4**). This is due to the hexagonal symmetry of the Si(111) surface. These results are in agreement with other reports, see e.g. [Ber08]. We confirmed the domain structure by XRD. A φ-scan for the asymmetric GaN (20.5) reflex, where the sample is rotated around its surface normal in the range of 360° showed the expected six-fold symmetry on Si(111). (Data not shown. φ-scans of GaN samples grown on sapphire and diamond are shown in **Fig. 3.16** and **Fig. 3.21**, respectively.)

Direct growth vs. growth with a buffer layer A direct growth approach was used throughout this work. However, other groups deposit a thin (approx. 10 nm) AlN buffer layer before NW growth. In the case of AlN-buffered Si(111) substrates, a matrix layer with a high density of defects (threading dislocations) with hexagonal pits with $(\bar{1}102)$ side facets is formed from which NWs protrude. This technique has been reported in Refs. [Ber06a, Ber06b, Ber07, Ber08, San05]. It leads to a reduction of NW density in comparison to the growth on bare Si. The density of nanowires can be controlled by the thickness of the AlN layer and the flux of atomic nitrogen [Ber07]. NW growth on AlN buffer layers is possible for a substrate temperature in the range of 810°C to 830°C which does not lead to nucleation on untreated Si, since the critical nucleation temperature for GaN on Si is lower than on AlN [Ber06b, Tan06]. For AlGaN NWs this matrix effect is more pronounced than for pure GaN NWs (**Fig. 3.5**). A better NW orientation is reported when growing on AlN-buffered substrates [Son07]. In this work, we show that prolonged wafer nitridation helped to improve the NW orientation by

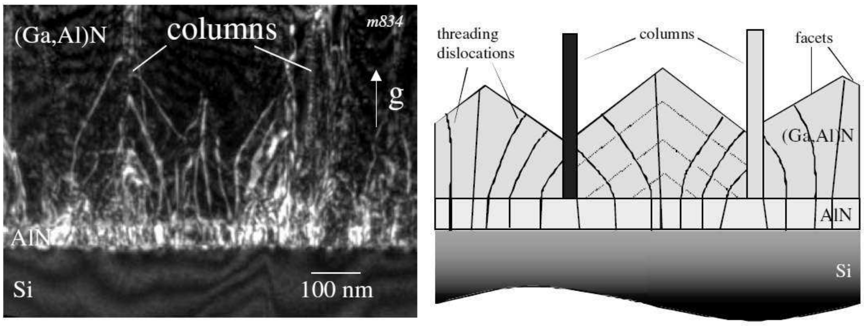

Figure 3.5: *Left: Dark-field cross-sectional TEM (XTEM) of (Al,Ga)N nanocolumns surrounded by compact (Al,Ga)N. Right: Schematic illustration of the growth process, in which columnar and compact material coexist. Image from [Cal07b].*

reducing the maximum tilt and twist angles (see Section 3.2.1). Another possibility to grow on AlN-buffered Si(111) without wetting layer was shown in [Con10]. In that case, initially Al was deposited, followed by a nitridation which led to a relaxed AlN film. According to Ref. [Son07], a closed GaN wetting layer can be suppressed by high substrate temperatures (above 765°C). In that case, only well separated GaN islands were formed on the AlN-buffered Si(111) substrates.

3.2.1. Interface properties and nucleation behavior

Spontaneous formation of a Si nitride interlayer For NW growth on Si, the substrates were etched in 5% hydrofluoric acid (HF) for 30 s before subsequent transfer into the UHV system in order to remove the natural oxide. In the first growth stage the surface is nitridated. Molecular nitrogen is introduced into the growth chamber through the plasma cell, while the radio frequency (RF) power is gradually increased up to 425 W within approximately 2 min. The NWs are found to nucleate on a $\mathrm{Si_xN_y}$ layer and not on bare silicon, even when the Ga cell shutter is opened instantly after finishing the ramp for the RF power.

Prior to nucleation of the NWs, a thin amorphous silicon nitride layer with a thickness of 1.5 nm to 2 nm is formed spontaneously on the Si(111) surface. On samples with long nitridation times, the NWs are better oriented, both in terms of tilt angle (angle towards the substrate normal) as well as twist angle distribution (rotation angle around the substrate normal). This is shown by the Selected Area Electron Diffraction (SAED) patterns (**Figs. 3.6c, d**) for samples with nitridation times of 0 min and 15 min. The epitaxial relationship of the GaN NWs with respect to the Si(111) surface was found to be $(0002)[0\bar{1}10]\mathrm{GaN} \parallel (111)[\bar{1}\bar{1}2]\mathrm{Si}$. This relationship was also reported by [Lar08].

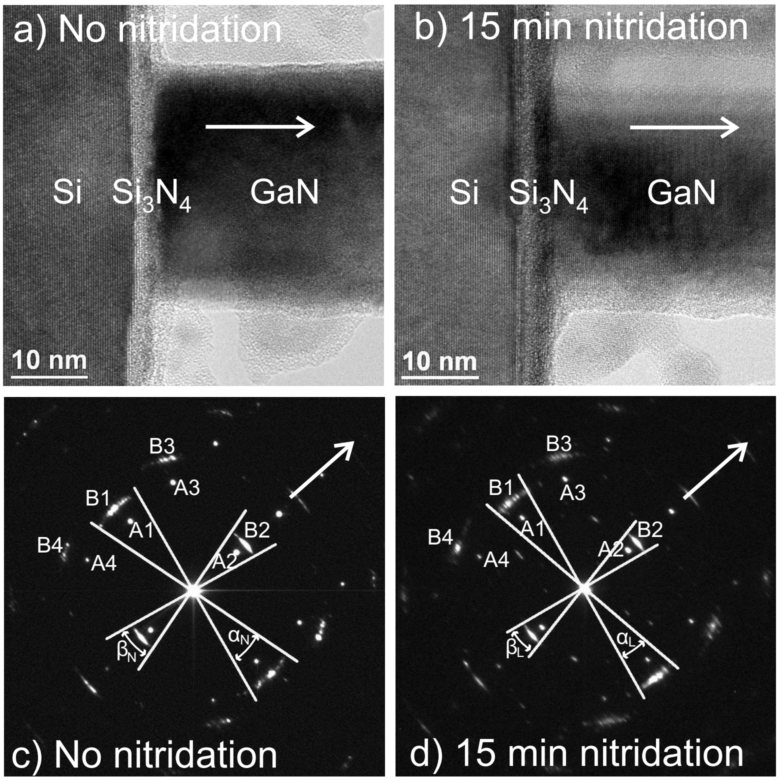

Spot	° vs. Spot A$_1$	Indexing
A$_1$	—	$(2\bar{2}0)$ Si
A$_2$	90	(111) Si
A$_3$	31	$(3\bar{1}1)$ Si
A$_4$	31	$(1\bar{3}\bar{1})$ Si
B$_1$	0	$(\bar{2}110)$ GaN
B$_2$	90	(0002) GaN
B$_3$	32	$(\bar{2}112)$ GaN
B$_4$	32	$(\bar{2}11\bar{2})$ GaN

Figure 3.6: *(a) XTEM image of the GaN nanowire/Si(111) interface region after 90 min growth of nominally undoped nanowires without intentional nitridation. (b) XTEM image after 15 min additional nitridation in the initial stage of growth. (c) SAED pattern obtained for the sample without intentional nitridation. (d) SAED pattern of the 15 min nitridated sample. Arrows indicate the growth direction (c axis). The diffraction spot indexing is given in the table below.*

Most of the GaN NWs remain epitaxially related to the Si substrate. However, some of the NWs present a certain degree of twist or tilt with respect to the normal direction, as indicated by the presence of faint arcs around the (0002) and ($\overline{2}$110) main spots in **Figs. 3.6c, d**. The maximum tilt angle was evaluated for ($\overline{2}$110) (α) and (0002) (β) planes. For the non-nitridated sample $\alpha_N = 26°$ and $\beta_N = 27°$ were obtained, and $\alpha_L = 20°$ and $\beta_L = 21°$ for the sample with a nitridation time of 15 min. These results can be used to explain the differences found between both samples: In general, we observe more homogeneous growth of NWs with reduced tilting angles for longer nitridation times, i.e. the surface nitridation has a beneficial role. An inhomogeneous silicon nitride layer might also be responsible for inhomogeneous orientation of GaN NWs reported by Songmuang *et al.* [Son07]. The silicon nitride layer is formed in a self-passivating manner during the initial stage of NW growth, when the heated substrate is exposed to the nitrogen plasma. From these results it is evident that NW growth and the related surface processes take place on a silicon nitride surface. In contrast to reports on GaN NW growth on AlN-buffered Si substrates [Ber06a], no GaN wetting layer was formed at the applied growth temperature. This indicates that the sticking coefficient for Ga adatoms on the nitridated Si(111) surface is low. This behavior was also described in Ref. [Tan06], where Si(111) surfaces are used as pseudomasks for selective area growth of GaN by ammonia MBE.

Polarity The polarity of the NWs cannot be revealed by SAED or conventional TEM. Convergent beam electron diffraction (CBED, see Sec. 2.3.2) is not reliable for NWs and led to contradictory results (compare e.g. [Fox09, Che08, Fur08b, Hes11]). Recently, it could be shown by direct imaging of both Ga and N atoms by aberration-corrected scanning transmission electron microscopy (STEM) together with high angle annular dark field (HAADF) imaging that the GaN NWs presented in this work are N-polar (see Fig. 4 in [Mat12]).

3.2.2. Time-dependence of the nucleation process

To further investigate the nucleation process, the nucleation density as a function of growth time was analyzed by top-view SEM imaging. After 30 min of growth a low NW density of approximately 5 NW/μm^2 is found (**Fig. 3.7a**). If the growth time is increased, a strong increase of the NW density from 85 NW/μm^2 at 37 min (**Fig. 3.7b**) to 150 NW/μm^2 at 45 min (**Fig. 3.7c**) and to 450 NW/μm^2 at 60 min is found, followed by an apparent decrease to 275 NW/μm^2 at 90 min (**Fig. 3.7d**) and 75 NW/μm^2 at 300 min, caused by an increasing degree of coalescence of neighboring NWs as growth proceeds. In **Fig. 3.8**, the measured nucleation density is shown as a function of growth time for a substrate temperature of 790°C (solid triangles). The nucleation time t_{nucl}, which represents the onset of nucleation, sensitively depends on the substrate temperature.

For the edges of the investigated samples a lower substrate temperature by approx. 10°C is assumed, due to thermal shielding of the tantalum foil which clamps the sample. The lower temperature leads to a decrease in nucleation time (**Fig. 3.8**, open triangles). An increase of the substrate temperature further delays the nucleation. For a substrate temperature of T_{sub} = 795°C (**Fig. 3.8**, open circle) the NW density was equal to zero after 45 min of growth. For T_{sub} = 790°C, the maximum nucleation density of approximately 450 NWs/μm^2 was found for a growth duration of 60 min. It should be mentioned that the density of tilted NWs and thus the resulting density of joints is reduced in the case of Si-doped NWs (see Chapter 4). In addition, we have observed that an increase of the nitridation time does not accelerate the nucleation process, demonstrated by the same nucleation density of samples with no additional nitridation and additional nitridation times of 15 min and 45 min, measured after 30 min of growth (**Fig. 3.8a**, open diamond).

The long nucleation times observed here cannot be explained by "Ga-balling" as the responsible nucleation mechanism, as suggested in [Cal00]. Instead, the initial nitridation of the Si(111) surface is assumed to create nucleation sites under the growth conditions applied here. During the nitridation process, nitrogen atoms penetrate the silicon surface and form Si-N bonds. As these are longer compared to the Si-Si bond, this process generates local compressive strain fields. In addition, interstitial silicon atoms are generated which can diffuse to the surface, enhancing the local nucleation of GaN. Indeed, we have observed the diffusion of Si into the GaN NW by spatially resolved electron energy loss spectroscopy (EELS) measurements (**Fig. 3.9**). The Si-signal is detectable up to several nanometers into the GaN NW, whereas the Ga signal disappears abruptly in the silicon nitride layer, demonstrating that the observed result is not an effect of electron beam spreading in the sample.

Summarizing the results presented above, we found that the applied growth conditions result in nucleation times of more than 30 min and inhibit the formation of a wetting layer. The conclusion that this delayed nucleation is caused by the high growth temperatures, is strongly supported by similar findings in [Mei06]. In contrast to the standard NW samples in that paper, one sample was grown at a substrate temperature approximately 20°C higher than the other samples (Fig. 4b in [Mei06]), exhibiting a strongly decreased NW density. Consequently,

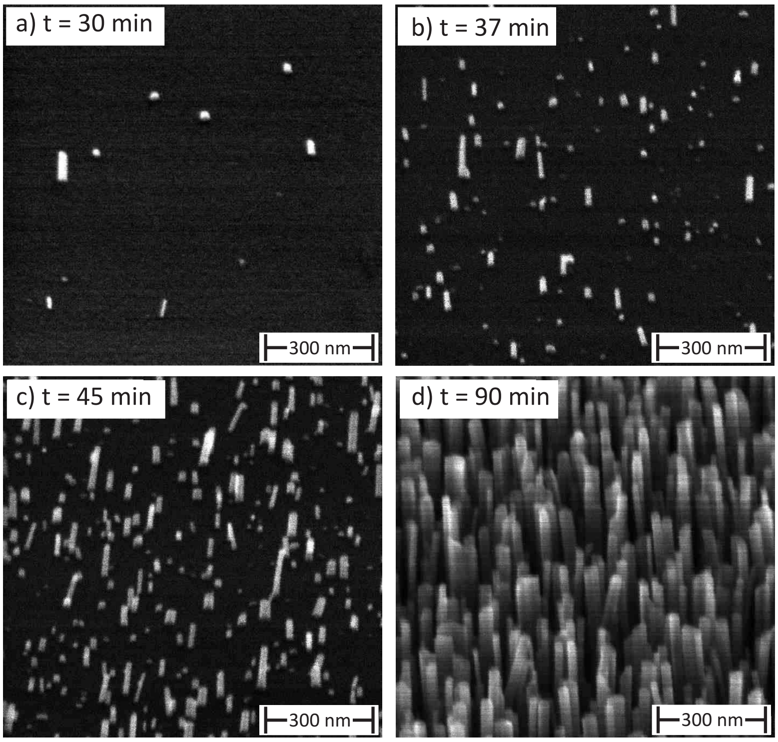

Figure 3.7: *SEM images of GaN NW samples grown on a Si(111) substrate for different growth durations, taken under a inclination angle of 45°. Nucleated nanowires were observed for growth times above 30 min. Nucleation proceeded up to a growth time of 60 min. For longer growth durations, the density of nanowires decreased due to coalescence.*

the nucleation time could be decreased by reducing the substrate temperature, leading to similar results as in Ref. [Mei06].

NW heights The dependence of the NW height on the growth time is shown in **Figure 3.10a**. No NWs are present for growth times shorter than t_{nucl}. After the nucleation phase is completed, we observed a constant growth rate of (8.5 ± 2.2) nm/min up to a NW length of 2.4 µm (**Fig. 3.10a**, solid line).

These results differ from earlier reports on catalyst-free NW growth by PAMBE. In particular we have not observed the strong dependence of the NW length on the diameter as it was reported in Ref. [Deb07]. In that report a linear dependence of the NW length on the inverse diameter was found, meaning that thinner NWs grow faster. This was explained by a diffusion-induced process according to a mass transport model which has been developed for metal particle assisted growth and was presented by Johansson *et al.* [Joh05, Joh06].

On the contrary, the variation of NW lengths observed here is due to different nucleation times for individual NWs (**Fig. 3.7**) and remains almost constant

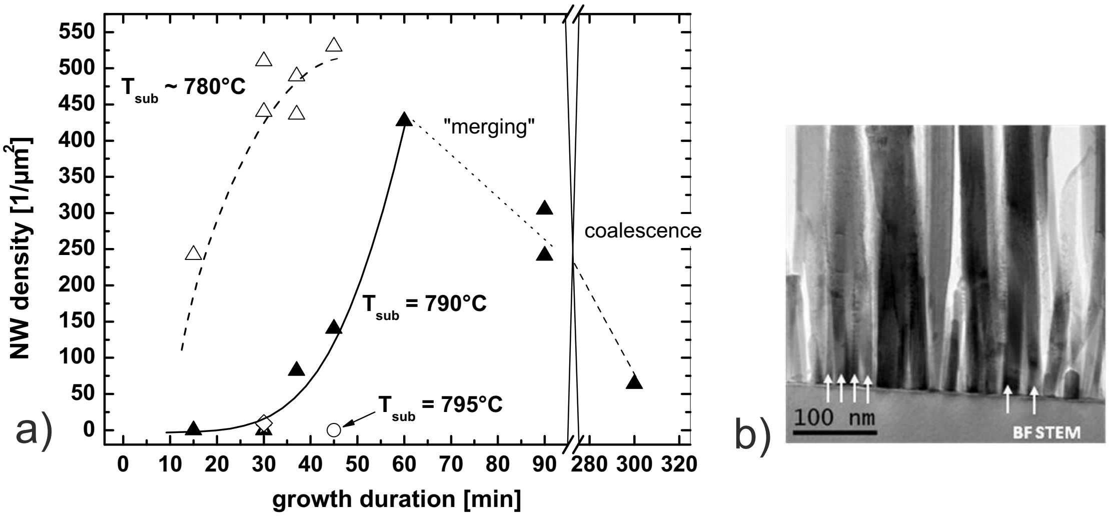

Figure 3.8: *(a) Nanowire density as a function of growth time for different substrate temperatures. For a substrate temperature of 790°C, two different additional nitridation times (0 min, 45 min) besides the standard nitridation time of 15 min were evaluated after 30 min growth, yielding almost identical values (open diamond). (b) Bright field scanning TEM image showing the merging of tilted and adjacent straight nanowires, leading to an apparent decrease of the nanowire density.*

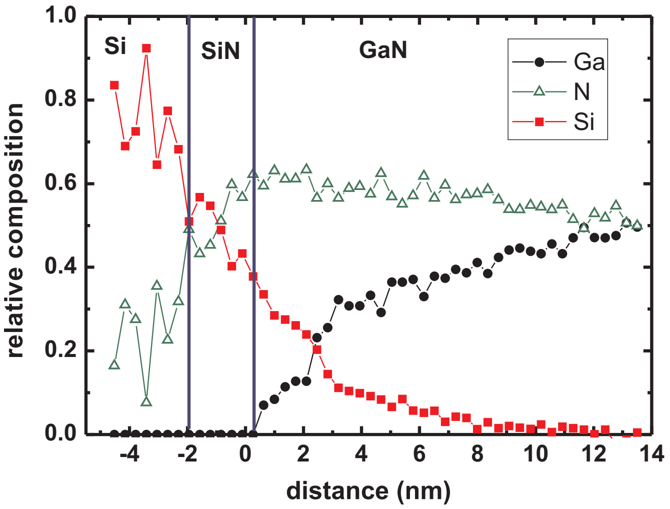

Figure 3.9: *Spatially resolved electron energy loss spectroscopy (EELS) measurement of the GaN/Si interface region. A silicon nitride interfacial layer is observed as well as diffusion of silicon atoms into the GaN nanowires.*

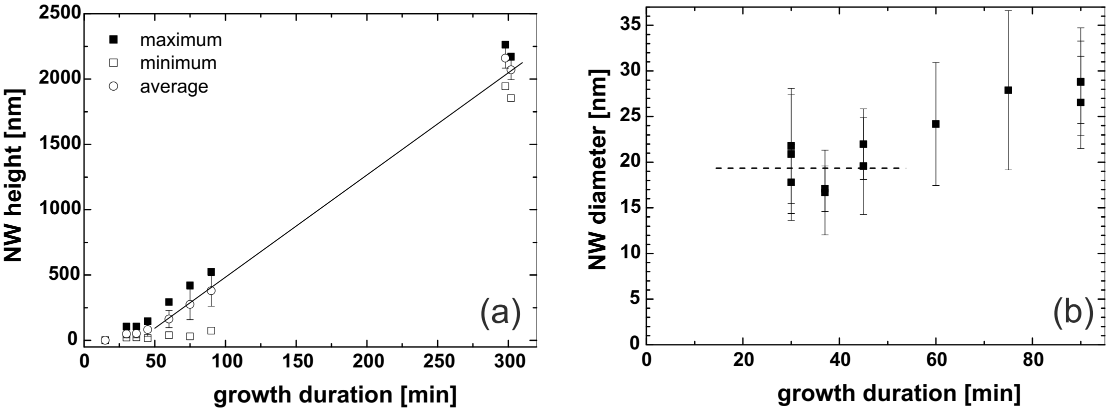

Figure 3.10: *(a) Dependence of the nanowire height on the growth duration. After nucleation, a constant growth rate of (8.5 ± 2.2) nm/min is obtained. (b) Dependence of the nanowire diameter on the growth duration. A real radial growth rate cannot be extracted as the apparent increase of the diameter at t = 60 min is due to merging nanowires (**Fig. 3.8b**).*

during the growth process. For a NW sample with a growth time of 90 min the distribution of NW heights (450 nm ± 28 nm) is the same as for an 180 min grown sample (1090nm ± 23 nm) and 300 min grown sample (2400 nm ± 25 nm) within the measurement uncertainty.

Radial growth The dependence of the NW diameter on the growth duration is shown in **Fig. 3.10b**, as it was evaluated from top-view SEM images. As a general trend the diameter increases with increasing growth time. A linear fit (not shown in the graph) of the NW diameter as function of the growth duration could be considered as the upper limit for the radial growth rate and is 1.7 Å/min. However, the determination of a radial growth rate from the displayed data is not reasonable: For growth times below 60 min the NW diameter is constant, allowing the determination of a minimum diameter (i.e. nucleation diameter) of 19 nm. The apparent increase for longer growth durations can be attributed to merging and coalescence of neighboring NWs (**Fig. 3.8**).

Nanowire Coalescence The high NW density and slight tilting of the NWs causes adjacent NWs to come in contact with each other. In **Fig. 3.11** the coalescence region of two adjacent nanowires is studied in detail. Although the two coalescing NWs are tilted by about 5° with respect to each other, they merge into one crystal within 10 nm to 15 nm beyond the coalescence point. This adaption is facilitated by the formation of dislocation defects, which are visualized by Fourier filtering of the HRTEM image (**Fig. 3.11d**).

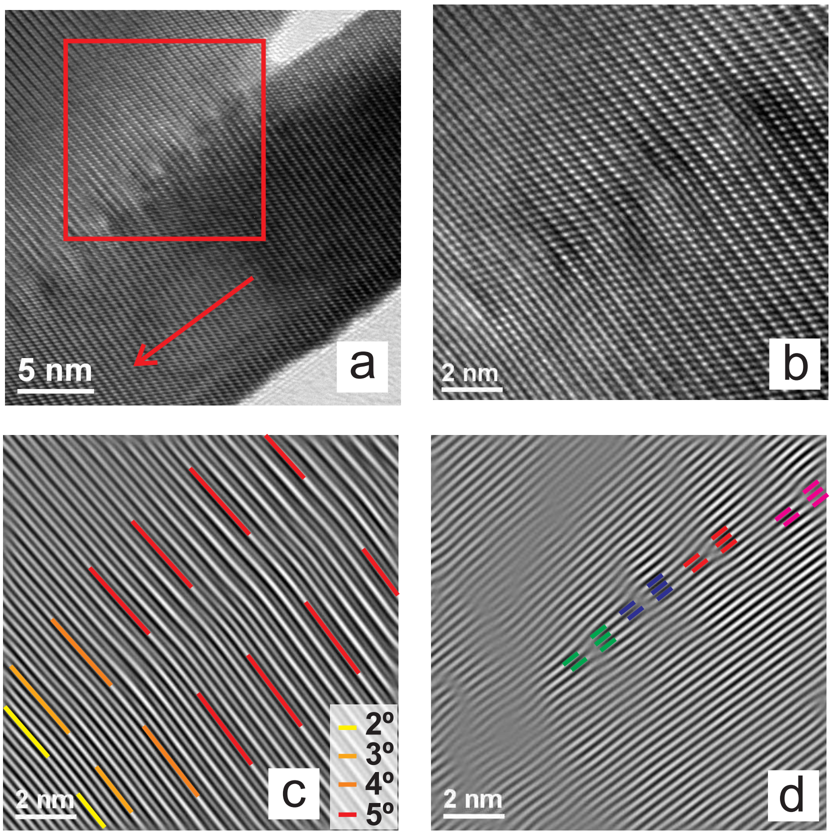

Figure 3.11: *HRTEM micrographs of the coalescence region of two nanowires. (a): Wider view of coalescence region. The arrow indicates the growth direction. (b): Detailed view of the area marked with a red rectangle in image a. (c): Fourier filtered version of image b showing the two basal planes re-adjust quickly, lowering their tilt angle and fusing into a perfect structure just 10 – 15 nm beyond from the coalescence point. (d) Fourier-filtered version of image b showing that in the case of* $\{1\bar{1}00\}$ *planes, they fuse by using dislocation defects until the material becomes relaxed and can grow like a monocrystal.*

3.3. Sapphire substrates

Although Si substrates are favored for most applications, special requirements raise the need for other substrate materials. For using NW samples as transducers in a DOTSENSE device (see Sec. 1.2), a substrate is needed which is transparent in the wavelength regime that is used for excitation and detection of NW PL emission since the structures shall be illuminated from the backside. Si absorbs light with energies above its bandgap of 1.1 eV and can therefore not be used. Additionally, a high chemical, thermal, and mechanical stability is demanded.

Sapphire (the common name for crystalline aluminum oxide, Al_2O_3) has a rhom-

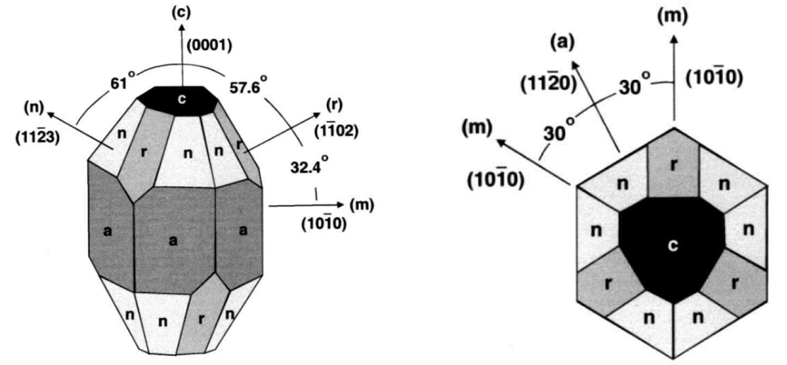

Figure 3.12: *Rhombohedral lattice of sapphire indicating the different planes. Image from [Amb98].*

bohedral lattice(1). Sapphire is available in different surface orientations (see e.g. [Amb98]). When the crystal is cut along the *c-plane*, a hexagonal lattice at the surface is obtained, which makes this orientation suitable for nitride growth along their *c-axis* despite the large lattice mismatch. On *a-plane* sapphire (11$\bar{2}$0), which is orientated perpendicular to the *c-plane*, the III-nitrides also grow in *c-plane* orientation, but the nitride layer will exhibit uniaxial in-plane strain. In contrast to this, *r-plane* (1$\bar{1}$02) sapphire leads to the growth of *a-plane* III-nitride films. The structural quality is generally inferior to *c-plane* films since the *c-axis* is the preferred growth direction for III-nitrides in MBE. The orientations of the sapphire planes are shown in **Fig. 3.12**.

Since sapphire is transparent in the range of 170 nm to 6 µm, it cannot be heated by thermal radiation during growth. Therefore, the unpolished backside of the wafers was metalized with 200 nm Ti and 70 nm Pt. This metal combination is stable at the growth temperature and provides absorption of radiation.

Fig. 3.13 shows SEM images of GaN NWs grown for 90 min at nominally identical conditions (T_{Ga} = 1012°C, T_{sub} = 874°C, $p_{\mathrm{MBE}} = 2.7\times10^{-5}$ mbar) on sapphire substrates of different orientations and on Si(111) for comparison(2).

All substrates were nitridated for 10 min at the growth temperature. Whereas for Si(111) the NWs start growing directly from the substrate interface, for sapphire always a rough matrix layer is formed. The actual morphology on sapphire depends on the substrate surface orientation. On *r-plane* sapphire a GaN wetting layer and nanocrystals with low aspect ratio (height/diameter) are formed. Their

---

(1) The lattice according to the Bravais lattice classification is called rhombohedral, the space group is R$\bar{3}$c, the crystal system is called trigonal.

(2) Even with the metalization applied here, the absorption of radiation by the sapphire substrates is lower than by Si. Therefore, the effective surface temperature is lower for the sapphire substrates. Lower temperatures enhance coalescence. Due to the small substrate size of 10 mm × 10 mm, a measurement of the surface temperature by a pyrometer was not possible.

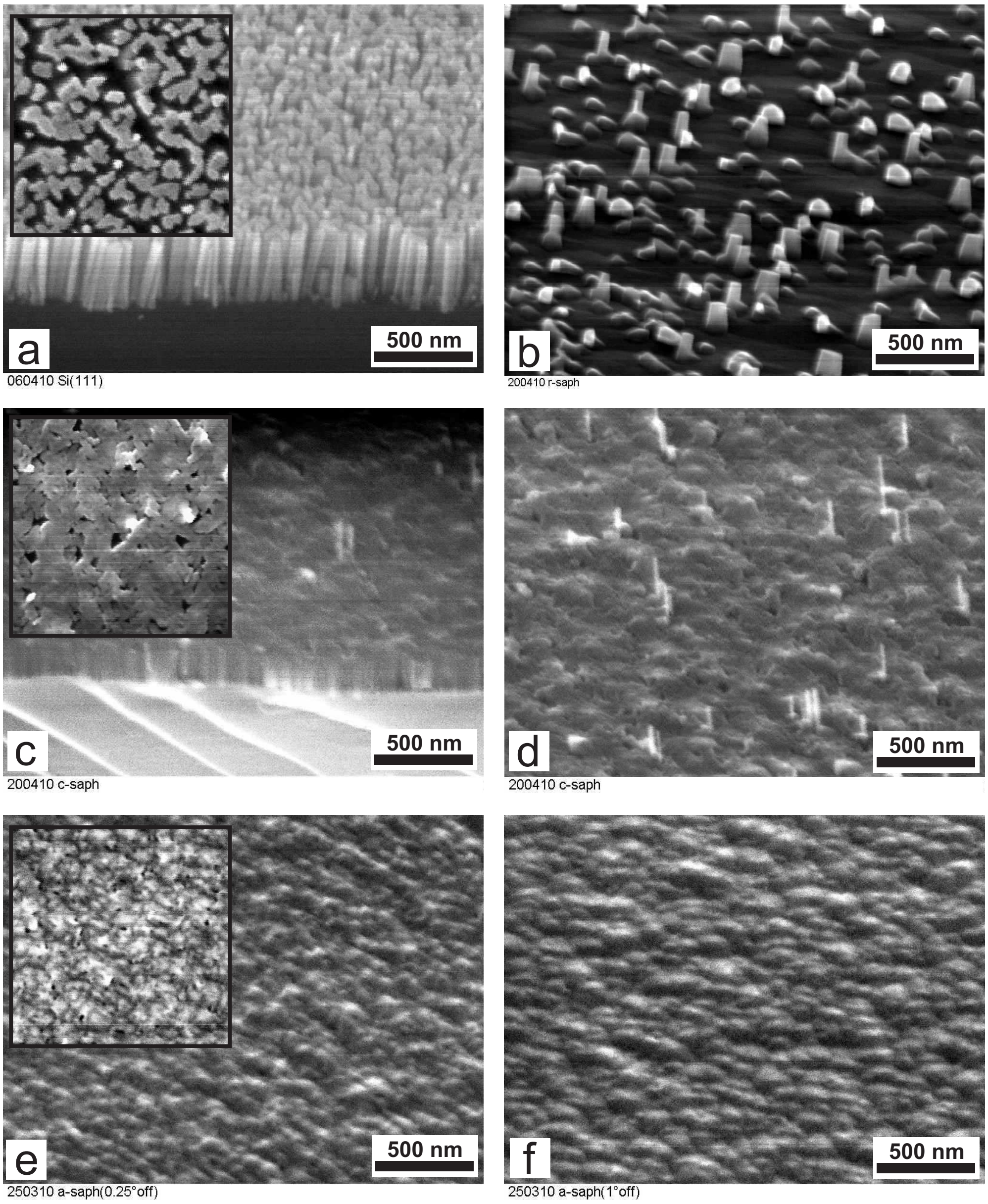

Figure 3.13: *SEM micrographs taken at 45° viewing angle (insets showing top views at the same scale) of GaN NW grown at the same parameters on different substrates. All scale bars are 500 nm.* **(a)** *Cleaved edge view of Si(111); NWs without wetting layer are present.* **(b)** *r-plane sapphire; wetting layer and nano crystals with low aspect ratio.* **(c)** *and* **(d)** *c-plane sapphire; columnar growth (see Fig. (c) which shows cleaved edge), but leading to a coalesced layer with a low density of thin NWs protruding from it.* **(e)** *and* **(f)** *a-plane sapphire with different off-cut angles of 0.25° and 1°, respectively.*

average diameter is 190 nm, their average height 300 nm. The aspect ratio is between 0.7 and 3, the density is approx. 5 µm^{-2}. On *c-plane* sapphire columnar growth was observed (see **Fig. 3.13 c**), forming an almost coalesced layer with a low density of thin NWs protruding from it (approx. 4 µm^{-2}). On *a-plane* sapphire a rough layer is formed (**Fig. 3.13 e** and **Fig. 3.13 f**). No significant difference was observed between specimens of 0.25° and 1° off-cut towards (0001), respectively.

This is in contrast to the growth of ZnO nanoneedles (ZnO does not form prismatic columns like the nitrides, but thin pyramidal structures with sharp tips) on off-cut sapphire. At higher off-cut angles, nanoneedle formation is strongly enhanced [Was]. This was explained by the higher density of atomic steps on the off-cut surface that act as nucleation sites. For MOCVD growth it is reported that a forced nitridation of sapphire wafers [Asc09] using a NH_3/H_2 ambient at high temperatures (1050°C) modifies the surface. AlN islands are formed that can act as nucleation sites for MBE NW growth. In Ref. [Kik06] it is shown that a thin AlN nucleation layer allows the formation of NWs. In this work, a different approach employing a Si interlayer was chosen. This could be performed *in situ* in the MBE chamber without external processing steps.

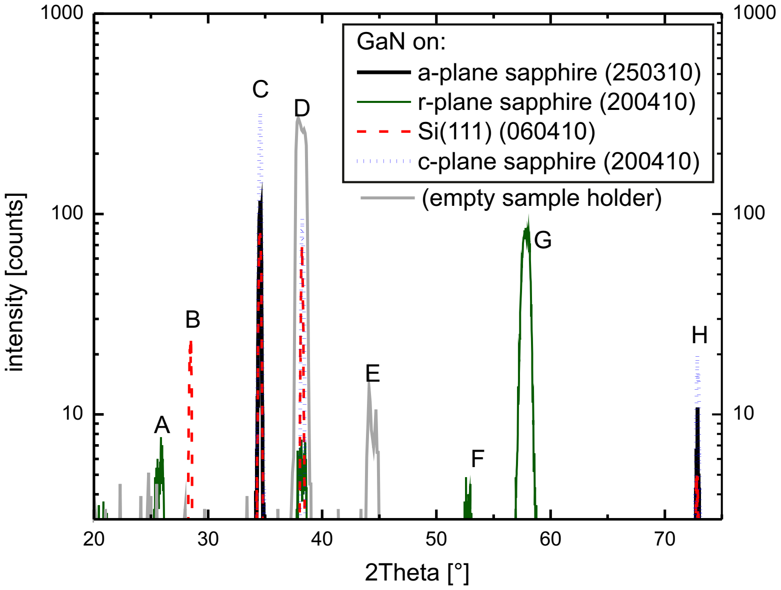

Figure 3.14: *$2\Theta - \Omega$ XRD scans of the samples presented in Fig. 3.13. The peak indexing is given in Tab. 3.1.*

The GaN growth direction was verified by X-ray diffraction (see **Fig. 3.14** and **Tab. 3.1**). GaN NWs on Si(111), *c*-plane sapphire, and *a*-plane sapphire were found to grow along the GaN *c*-axis. In contrast, GaN NWs on *r*-plane sapphire

Table 3.1: *Indexing of the XRD-peaks in Fig. 3.14. The Al reflexes originate from the sample holder.*

Peak index	2Θ [°]	Origin
A	25.6	sapphire $(10.\bar{2})$
B	28.45	Si (111)
C	34.26	GaN (00.2)
D	38.24	Al (111)
E	44.4	Al (200)
F	52.58	sapphire $(20.\bar{4})$
G	57.78	GaN $(2\bar{1}.0)$
H	72.86	GaN (00.4)

were found to grow along the non-polar GaN *a*-axis. These findings are in agreement with reports for GaN layer growth [Amb98].

NW formation on sapphire using a Si interlayer In the following, three different strategies are compared: First, direct growth on a nitridated sapphire wafer as shown in the previous paragraph. Second, the deposition of a thin Si nitride layer prior to GaN growth. Third, the deposition of Si under high vacuum conditions. The Si and Si nitride deposition was done *in situ* prior to growth, thereby avoiding surface contamination.

A comparison of GaN NWs grown by the three methods on 2" *c-plane* sapphire wafers is shown in **Fig. 3.15**. Growth directly on sapphire (after 10 min wafer nitridation at growth temperature) leads to an inhomogeneous GaN layer (see **Figs. 3.15a and b**). The results vary from a layer with rough surface at the wafer center and a columnar and largely coalesced growth at the wafer edge.

Improvement is achieved by the deposition of a thin Si nitride layer (see **Fig. 3.15c**) directly prior to the GaN growth. Si is evaporated for 40 min at an effusion cell temperature of 1240°C ($\mathrm{BEP}_{\mathrm{Si}} = 6\mathrm{x}10^{-9}$ mbar) under standard N flux ($p_{\mathrm{MBE}} = 2.7 \times 10^{-5}$ mbar) at growth temperature. NW formation is observed. However, the degree of coalescence is still high. Furthermore, the NW morphology and optical properties differ between center and edge of the wafer. The thickness of the Si nitride layer was determined to 5 nm by HRTEM (**Fig. 3.17**). The NW morphology can be further improved when the Si deposition is performed without nitrogen being present. Si was deposited for 40 min at T_{Si}=1240°C at growth temperature, resulting in an estimated layer thickness of 5 nm. Nitrogen was not introduced until GaN growth. In this case, the morphology is homogeneous

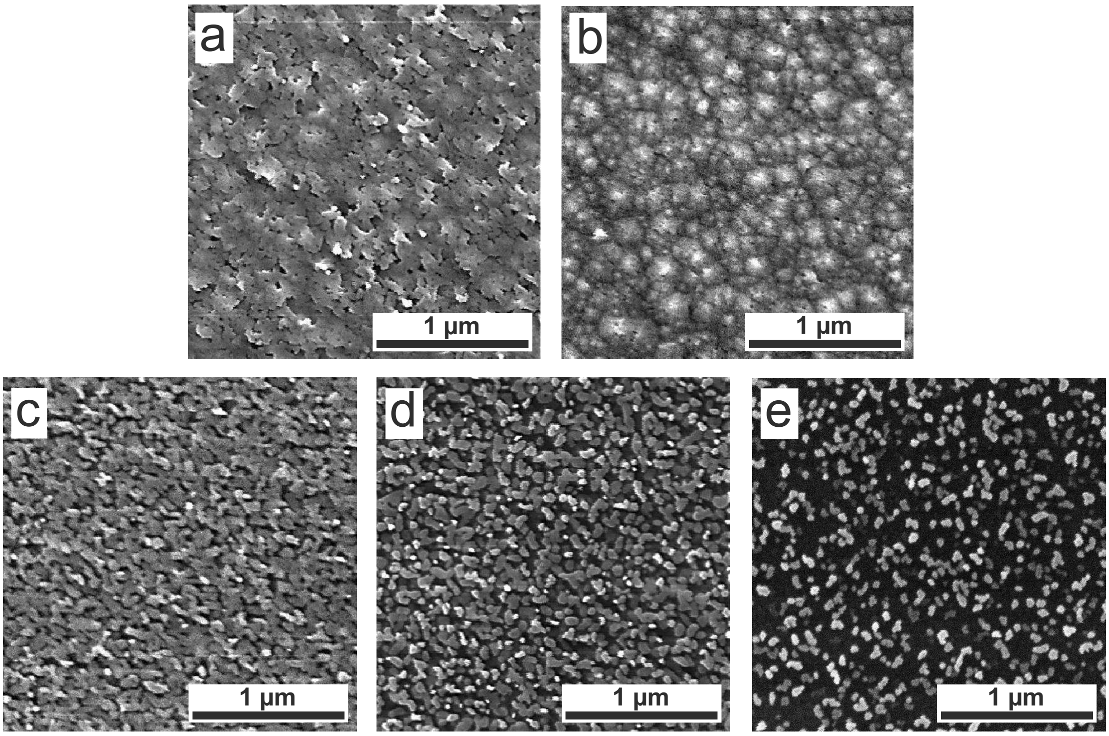

Figure 3.15: *SEM top view micrographs of GaN NW growth on c-plane sapphire wafers. (a) and (b): Directly grown on nitridated wafers (sample 050710). A pronounced inhomogeneity between the wafers' center regions (image a) and edge regions (image b) is observed. (c): with Si nitride interlayer (070710). (d): with approx. 5 nm thick Si interlayer (080710). (e): with approx. 20 nm thick Si interlayer and elevated substrate temperature of* $T_{\mathrm{sub}} = 790°C$ *(210411) instead of* $T_{\mathrm{sub}} = 695°C$ *as for the three other samples.*

throughout the wafer (**Fig. 3.15d**). Coalescence can be fully suppressed by optimizing the buffer layer and growth temperature. After 60 min of Si deposition at T_{Si}=1290°C (estimated layer thickness of 20 nm) and increase of the substrate temperature from 695°C to 790°C, well separated NWs are observed (**Fig. 3.15e**)

The alignment of the GaN wires with respect to the substrate was tested by X-ray diffraction (**Tab. 3.2**). The full width at half maximum (FWHM) of the Ω-scan (rocking curve) of the symmetrical (00.2) reflex of GaN is a measure of the NW tilt (angle between the nanowire axis and the surface normal), whereas the FWHM of the φ-scan on the (20.5) reflex indicates the in-plane alignment (the twist i.e. rotation of the NWs around their growth axis). The (20.5) reflex has a six-fold symmetry for all samples proving that only one domain is grown (**Fig. 3.16**). The tilt angle FWHM is the smallest for the sample grown on sapphire without interlayer. However, this sample shows a high degree of coalescence which suppresses a large variation of tilt angles. Comparison between the sapphire sample with Si interlayer and a reference Si sample shows that the twist

Table 3.2: *Alignment of the GaN wires grown on c-plane sapphire substrates or Si(111) with respect to the substrate measured by XRD.*

Substrate	interlayer	FWHM Ω-scan (00.2) [°]	FWHM φ-scan (20.5) [°]	sample number
sapphire	10 min nitridation	0.78	3.28	050710
sapphire	10 min nitridation + 40 min Si nitride	1.55	3.47	070710
sapphire	40 min Si, no nitridation	2.00	4.2	080710
Si(111)	10 min nitridation	4.2	4.4	191109

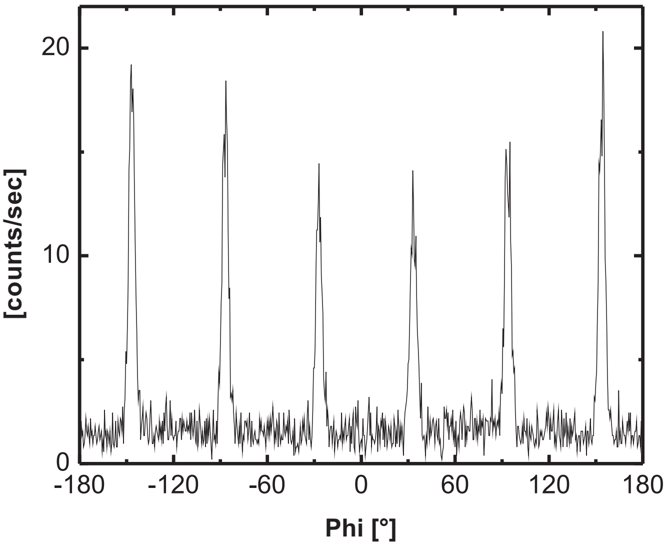

Figure 3.16: *φ-scan of the GaN (20.5) reflex for GaN NWs grown on c-plane sapphire with Si interlayer (sample 080710).*

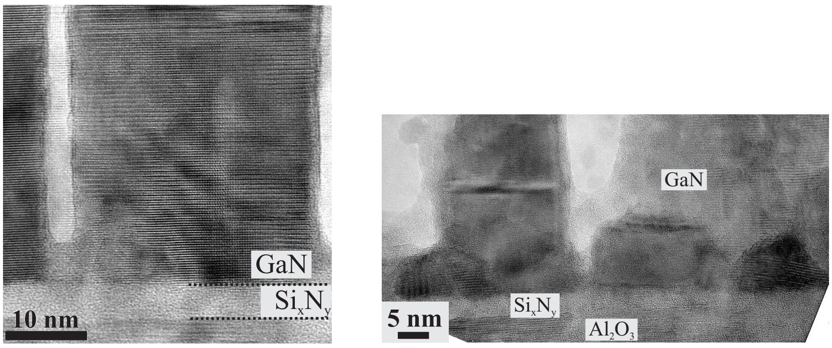

Figure 3.17: *HRTEM images of GaN NWs on sapphire taken along the GaN* $[11\overline{2}0]$ *direction.*

angle distribution is almost identical, but the tilt is reduced when growing on sapphire.

The clear NW morphology of the sample with the Si interlayer (080710), however, does not ensure high structural quality. High resolution TEM images revealed a high density of basal plane stacking faults in these NWs. Their formation is attributed to a lower substrate temperature compared to the Si substrates. Although the substrate heater was at the same temperature set-point (and same heater current of 10.4 A) as for growth on Si(111) the substrate surface is colder due to the lower heat absorption of the sapphire (even with backside metallization). According to the pyrometer, $T_{sub} = 695°C$ was reached compared to 772°C for the same heater temperature setting on a Si wafer. A lower substrate temperature decreases the Ga adatom mobility and thereby facilitates the formation of structural defects.

The near band edge (NBE) PL intensity is strongly reduced in this sample (**Fig. 3.18**). Since stacking faults are radiative defects, this sample has a stronger intensity in the range of 3.0 eV - 3.2 eV compared to the GaN on Si(111). Results for NWs grown on Si exhibit the same trend: In Ref. [Mei06] it was shown by cathodoluminescence measurements that a reduced substrate temperature leads to a relative increase of the 3.2 eV emission band with respect to the NBE region. A discussion of the origin of the different PL emission bands is given in Chapter 5. An increase of the substrate temperature increases the NBE intensity, especially the donor-bound exciton D^0X emission at 3.47 eV. For the sample with the highest heater temperature of 1000°C (this corresponds to a substrate temperature of 785°C as measured by pyrometer) the FWHM of the 3.47 eV emission is 17 meV.

3.4. Diamond substrates

Today, diamond is not widely used as a semiconductor material, although it has unique properties. Recent interest is drawn to it, since the combination of a substitutional nitrogen atom and a vacancy (NV center) forms a defect center in diamond, that is promising for room temperature quantum information processing [Jel06, Wra10]. NWs might be able to address single NV centers in diamond.

Diamond has a bandgap of 5.4 eV (indirect gap) and can be p-type doped with boron. AlN/diamond heterojunction diodes grown by PAMBE exhibiting rectifying properties and light emission were already demonstrated [Mis03]. Both diamond and the group III-nitrides are biocompatible and highly chemically stable. Details on diamond as a substrate material and results from nitride film growth on single crystalline diamond can be found in Refs. [Her09, Wei12]. Like Si, dia-

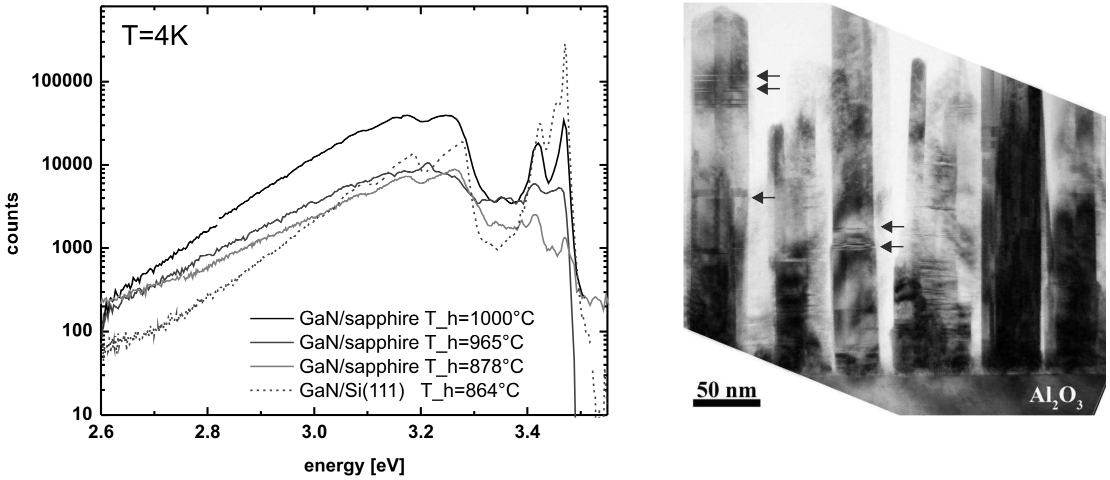

Figure 3.18: *Left: Low-temperature PL spectra for GaN NWs on Si(111) and c-plane sapphire. The temperature of the substrate heater* (T_h) *is given. For growth on sapphire, a higher heater temperature is needed to achieve a good crystalline quality. Right: Cross section TEM image of the sample grown at a heater temperature of 878°C showing a high density of basal plane stacking faults (some are marked with arrows). The NW height is* 258 ± 32 *nm.*

mond crystallizes in the cubic zincblende structure. The most common substrate orientations are (100) and (111). Similar to the growth on Si substrates, the (100) orientation leads to a double domain structure of the Al(Ga)N film, whereas the (111) orientation facilitates single domain layers. In contrast to silicon, diamond cannot be nitridated.

Polycrystalline diamond A polycrystalline boron-doped diamond substrate of the size of 3.0 mm × 3.0 mm was cleaned and treated with an oxygen plasma to ensure a reproducible oxygen-terminated surface (sample 300709). The backside was metalized with Ti/Pt in the same way as sapphire substrates. The substrate was then mounted in a tantalum sample holder. **Fig. 3.19** shows SEM micrographs before **(a)**, and after GaN growth **(b)**. The surface morphology and polycrystalline structure of the substrate is transferred to the GaN. Two distinct regions can be discerned, one with a rough layer (darker region), and one with nanowires (brighter region). The NWs exhibit a slightly higher degree of coalescence than a sample simultaneously grown on Si. However, this could be caused by different heat absorption of the different substrates.

To analyze the orientation of the diamond surface, a 2Θ-Ω-scan was performed by XRD(1). The following surface orientations were found: (110) as the strongest reflex, (311), and (331). No trace of (100) and only a weak signal of (111) was

---

(1) Measurement performed by Jürgen Bläsing, University of Magdeburg

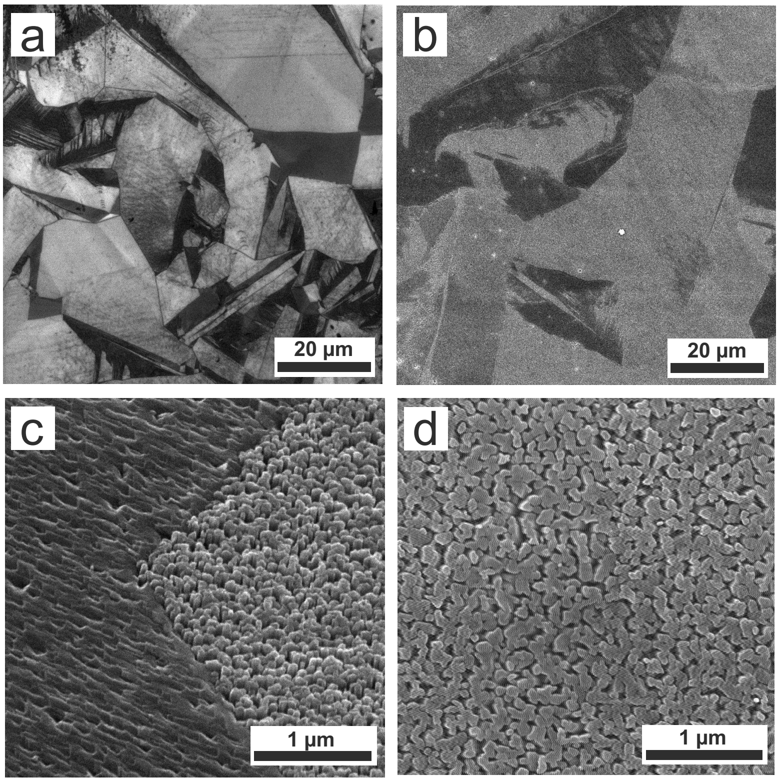

Figure 3.19: *SEM micrographs: (a) Polycrystalline diamond substrate after oxygen plasma treatment. (b) Same substrate after GaN NW growth. (c) 45° view showing a boundary between NW and layer region. (d) Top view of nanowire region.*

found. Unfortunately, it remains unclear which surface orientation favors NW growth and which layer growth. However, this result proves that GaN NW growth on diamond is possible and selective towards specific surface orientations. According to the GaN XRD reflexes, the GaN NWs grow along the *c-axis*, but without preferred in-plane alignment.

Single Crystalline Diamond (SCD) To obtain more detailed information on the crystal orientation dependence, growth experiments on single crystalline diamond in (100) and (111) orientation were performed. The diamond substrates were supplied by *Element Six Ltd., UK*. They were 300 µm thick high quality diamonds of type Ib (i.e. impurity concentration of substitutional nitrogen < 500 ppm, color yellow, resistivity $\rho > 10^{15}$ Ωcm) grown by a high pressure high temperature (HPHT) method. The substrates were not intentionally doped. Further information on these substrates can be found in [Wei12]. The (100) substrates were 3.6 mm × 3.6 mm, the (111) substrates 3.0 mm × 3.0 mm in size. They were treated with hydrogen plasma to achieve a reproducible surface state. The backside was

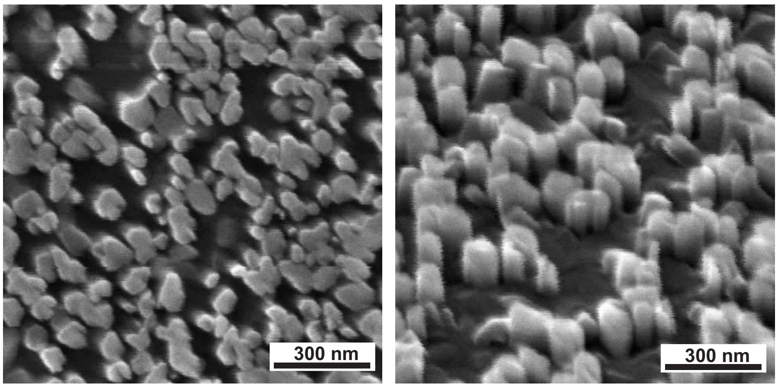

Figure 3.20: *SEM micrographs of GaN NWs on diamond (100). Left: Top-view, Right: 45° tilted view*

metalized with Ti/Pt as described previously. The diamond surfaces were polished for epitaxy by the manufacturer. The surface roughness was checked by atomic force microscopy (AFM) prior to growth. The root meas square (rms) roughness of a 1 µm × 1 µm area was 0.45 nm and 0.44 nm for the (111) and (100) orientation, respectively. The formation of nanowires was observed (**Fig. 3.20**). In contrast to samples grown on Si, a matrix layer was formed and the aspect ratio was relatively low. This might be due to a relatively low substrate temperature. Further optimization of the growth parameters is necessary.

On (100) diamond a double-domain structure is observed. Two GaN domains rotated by 30° with respect to each other are present without a preference (same intensity) according to an XRD area scan of the GaN (10.5) reflex (**Fig. 3.21**). In contrast to this, only a single GaN domain is recorded for growth on (111) diamond.

In **Fig. 3.22**, the low temperature PL emission from NWs grown on diamond (111) (sample 230810) and on Si(111) (sample 150306) are compared. For both samples, the strongest contribution arises from the near band edge region (3.4 eV to 3.5 eV). However, the intensity is higher in the Si case. For the sample on Si, a clear three-peak structure is resolved here. The FWHM of the 3.47 eV emission (donor-bound exciton recombination) is 4 meV for the sample on Si and 16 meV for the sample on diamond. The broadening is attributed to a higher degree of coalescence on the diamond substrate. Generally, a higher degree of coalescence leads to a PL emission broadening for GaN NWs on Si(111) as it is shown on p. 76. Furthermore, the 3.45 eV emission intensity is strongly reduced with rising degree of coalescence (compare **Fig. 5.5**, p. 76).

It shall be noted that the growth parameters were optimized for growth on Si rather than on diamond. Additionally, it was not possible to measure the substrate

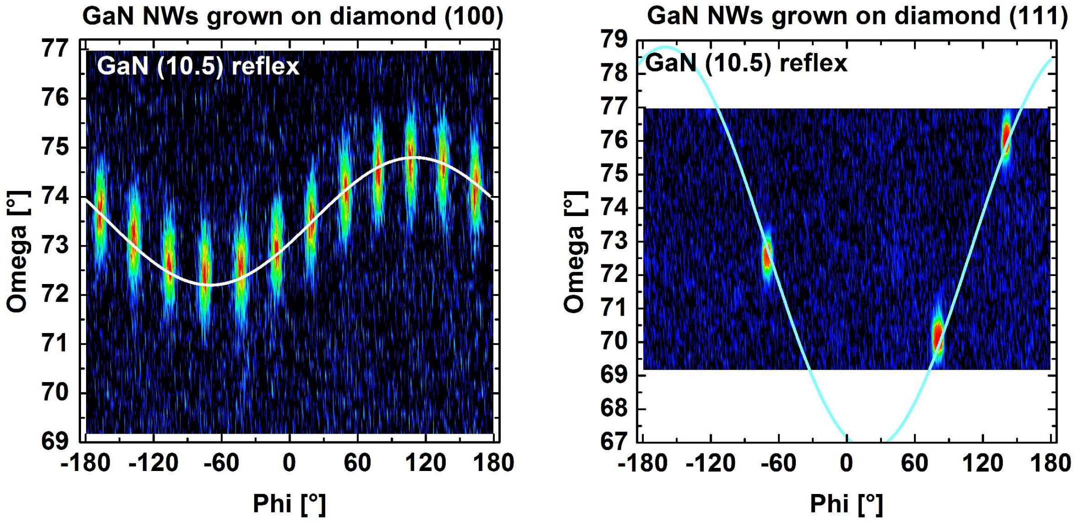

Figure 3.21: *XRD area scan for the asymmetric GaN (10.5) reflex ($2\Theta = 104.99°$, $\Omega = 73.07°$) with a scan area of $\Delta\varphi = 360°$ and $\Delta\Omega = 8°$. Left: Growth on (100) diamond. A twelve-fold symmetry is recorded, indicating two GaN domains. Right: A six-fold symmetry is recorded, indicating a single GaN domain. The light cyan or white curves (sine curves) indicate possible positions for reflexes. The (111) diamond exhibits a large offcut (5°). Therefore not all of the six possible reflexes are located within the scan area.*

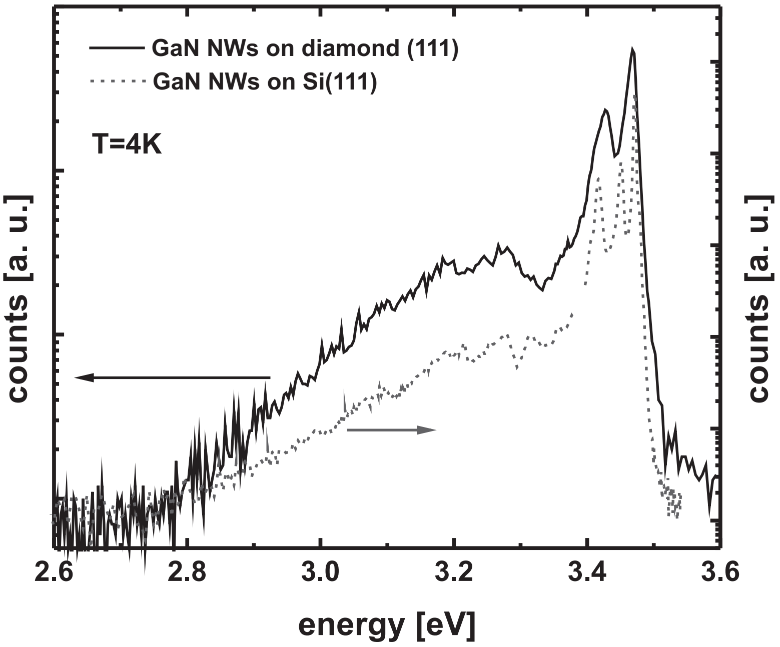

Figure 3.22: *PL spectrum (4K) for comparison between GaN NWs grown on diamond (111) and Si(111).*

temperature by pyrometer due to the small sample size. The following growth parameters were used: $T_h = 875°C$, $I_{sub} = 10.8\,A$, and $T_{Ga} = 982°C$. For comparison, the parameters for growth on 1" × 1" Si(111) substrates are $T_h = 860°C$, $I_{sub} = 10.5\,A$, and $T_{Ga} = 1012°C$. The latter parameters led to a high degree of coalescence on the diamond substrates. Therefore, the Ga flux was reduced and the substrate heater temperature was raised. The morphology might be optimized by increasing the substrate temperature further.

3.5. Summarized growth model

In this section, the results on the growth mechanism are summarized and compared to the results of other groups. A growth model is established, taking into account different effects like desorption and diffusion of adatoms on the substrate surface and the NW sidewalls as well as shading effects of neighboring NWs.

Fig. 3.23 schematically summarizes those effects playing a role in NW formation. The different growth stages are discussed in the following.

Nucleation stage Possible initiators for nucleation are surface steps on the substrate or Si out-diffusion, inhomogeneities in the Si nitride, or local strain variations in the Si nitride layer. The high amount of slightly tilted NWs (see Sec. 3.2.1, p. 38) supports this. Attempts to initiate GaN NW growth by Ga droplets have not been successful [Ris08, Cal07b]. In these studies, Si(111) substrates were pretreated by forming Ga droplets with sizes of 340 nm, 90 nm, and 0 nm (i.e. no droplets). The GaN NW morphology and diameter was unaffected by this pretreatment. However, small areas without NWs were found which feature the same diameter and density as the droplets. These results suggest, that Ga droplets on the surface can even inhibit NW nucleation (see Fig. 19 in Ref. [Cal07b]). This result contradicts the VLS mechanism. Additional counter-evidence was provided by [Ber08], who performed fast cooling of the samples after growth under Ga flux and could not observe any Ga droplets on top. Furthermore it should be noted, that sharp interfaces in GaN/Al(Ga)N NW heterostructures (see Chapter 7) were found in HRTEM images. This abruptness would not be possible with a metal (Ga, GaAl alloy) drop on top of the NW. In Contrast to this, EELS analysis on GaAs/GaP NWs which were grown by a VLS mechanism revealed no sharp interfaces but a transition zone of 15 nm – 20 nm when switching from GaAs to GaP growth [Gud02].

A minimum initial diameter of 19 nm is found (see **Fig. 3.10**, p. 44). This initial diameter seems to be determined by strain relaxation: A nucleation study

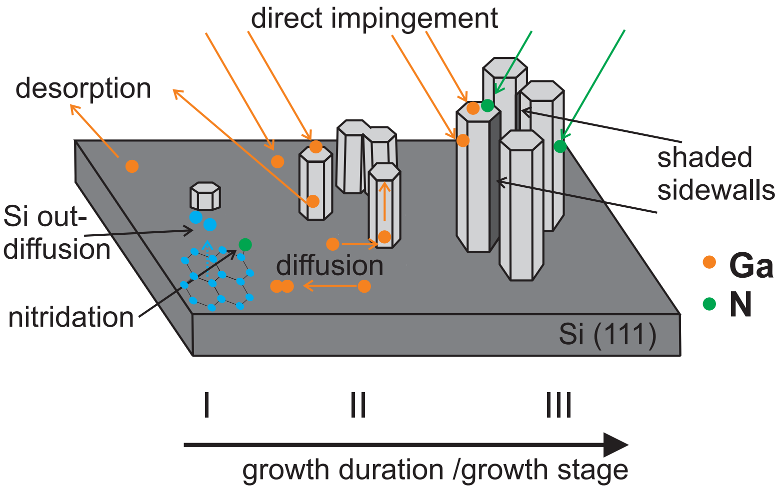

Figure 3.23: *Schematic of effects which determine the growth. The nucleation stage (I), an early growth stage (II), and a long growth stage (III) is depicted.*

by TEM and RHEED [Kne10, Con10] has revealed a 3D nucleation of pyramidal GaN islands on AlN-buffered Si(111) without wetting layer (Volmer-Weber growth mode). These islands undergo plastic relaxation and finally elastic relaxation to form prismatic NWs. The initial NW diameter is the critical diameter at which a misfit dislocation is formed inside the GaN island [Con10]. Hence, the amount of lattice mismatch should determine the critical NW diameter. Landé et al. [Lan09] additionally point out that the granular character of the AlN buffer layer may support the plastic relaxation of the GaN islands.

Early growth stage At this stage, the already nucleated NWs grow in axial direction. New NWs can still nucleate. Bertness *et al.* have assumed a much lower sticking coefficient for Ga adatoms on the *m-plane* sidewalls compared to the *c-plane* top facet to explain the highly anisotropic growth rate between radial and axial direction [Ber08]. Contribution to the growth could then either be given by direct impingement of atoms, or from atoms that impinge on the substrate or at the NW sidewall and diffuse to the NW top. However, it was calculated by Lymperakis *et al.*, that the diffusion barrier for Ga adatoms parallel to the *c-direction* is considerably higher than perpendicular to it on *m-plane* GaN surfaces which form the NW sidewalls ($\Delta E_{\|[0001]}^{m-plane} = 0.93\,\text{eV}$ and $\Delta E_{\perp[0001]}^{m-plane} = 0.21\,\text{eV}$). This reduces the probability of a contribution from Ga diffusion to the axial growth rate [Lym09].

The contribution to NW growth by diffusion along the sidewalls is considered to be of different importance in the literature. This can be understood by the different utilized techniques, substrates, and especially substrate temperatures.

For example, Songmuang *et al.* report that the axial growth rate of GaN NWs is higher than it would be for a 2D-layer grown under the same Ga flux [Son07] showing the presence of a contribution from diffusion. However, for the relatively high growth temperatures used in this work, Ga desorbs strongly either from the Si substrate or from the GaN itself. Therefore, at high growth temperatures it is more likely for Ga adatoms to desorb than to diffuse to the NW top surface and being incorporated. However, the increase of the NW diameter and decrease of the NW height for highly Mg-doped NWs (**Fig. 4.9**, p. 68) points to a contribution from diffusion. Contribution to the growth rate by a diffusion-induced process was derived from statistical analysis of heights and diameters of GaN NWs (thinner NWs grow faster) in Ref. [Deb07]. The contribution from diffusion depends strongly on the substrate temperature and can be more pronounced in the early stage and might be reduced in a later growth stage due to shading effects.

Later growth stage At a later growth stage, the NW density saturates. Coalescence of adjacent NWs which are slightly tilted towards each other apparently reduces the NW density. A complementary geometrical model was suggested by Foxon *et al.* to explain effects like suppressed lateral growth [Fox09]. This model does not rule out a contribution of diffusion, however is shows that the reduced radial growth (but not its complete absence) can be explained by geometrical considerations alone. They state that the lower part of the NW sidewalls are shaded from direct impingement. This originates in the high NW density and the fact that the adatoms do not impinge perpendicularly to the substrate but under an angle given by the geometrical arrangement of the effusion cells in the particular MBE system (in our case approx. 30°). Also the substrate surface is shaded (see p. 112 for details). Additionally, the different species (Ga and N) impinge from different directions. For the NW top surface or a flat layer this is of no importance. In contrast, for NW sidewalls a Ga adatom may desorb before the section of the sample is rotated far enough to meet the nitrogen beam. In Ref. [Fox09] it has been shown that NW samples grown without sample rotation exhibit a higher degree of inhomogeneity, a lower NW density, and sometimes long and thin inclined tips instead of a flat *c-plane* top surface. However, our studies on Mg-doped GaN nanowires (see p. 69) revealed lateral GaN growth for high Mg fluxes, proving that the suppression of lateral GaN growth is rather caused by the different adatom kinetics for Ga rather than by the limited availability of nitrogen alone.

These shading effects are even more important for GaN/Al(Ga)N heterostructures, since Al adatoms have a high sticking coefficient (Chapter 7). In contrast to GaN growth, lateral growth was observed for AlN and $\mathrm{Al}_x\mathrm{Ga}_{x-1}\mathrm{N}$ with high Al fraction. A reduction of the axial growth rate of the Al(Ga)N barriers, but not of the GaN nanodisks was observed. This means that there is a contribution by diffusion from the sidewalls for AlGaN barrier growth present (p. 109). Additionally, a slight reduction of the axial GaN growth rate was observed for the InGaN/GaN samples (p. 133) which can be explained by a reduced Ga adatom mobility due to the lower growth temperature. The different adatom kinetics between Al and Ga are obvious in the cross-section TEM analysis presented in **Fig. 7.3** (p. 108) where it is shown that the AlN shell is cylindrical whereas the GaN core is hexagonal.

4. Impact of doping of GaN NWs on the morphology

For the realization of nano-optical or nano-electronic devices, n- and p-type doping of GaN NWs with silicon and magnesium is a crucial issue that has only been addressed in a few publications ([Nos06] for Si doping, and [Par06, Lim10] for Mg doping). Besides their impact on the optical and electronic properties, the influence of these impurities on the growth process is of importance, as they have been reported to affect the growth kinetics of GaN films [Ros02, Mon04, Mon04, Neu03]. In addition, the simultaneous exposure of polar and nonpolar GaN surfaces during MBE growth of NWs allows to study the impurity effects on both types of surfaces and to obtain additional insight into the NW growth process.

For high doping concentrations, both for Si-doped and for Mg-doped NWs, the NW morphology is altered in a characteristic way (**Fig. 4.1**). Si doping leads to a conical widening of the NWs towards the top, whereas Mg enhances lateral growth. The influence of Si and Mg incorporation is investigated in detail in the following sections.

4.1. Influence of silicon

To achieve n-type conductivity in GaN, silicon is used as a shallow donor. This group IV element substitutes Ga atoms (group III) in the GaN lattice. For our samples, Si was supplied by an effusion cell operating between 900°C and 1160°C ($\mathrm{BEP}_{\mathrm{Si}} = 4 \times 10^{-12}$ mbar to $\mathrm{BEP}_{\mathrm{Si}} = 7 \times 10^{-10}$ mbar) (**Tab. 4.1**).

The presence of silicon is known to influence the surface kinetics during GaN growth. Theoretical investigations have revealed that GaN growth on GaN (0001) surfaces is unstable against the formation of Si_3N_4 under nitrogen-rich and silicon-rich growth conditions which is due to Si-induced surface reconstructions [Ros02]. **Fig. 4.2** shows a XTEM micrograph of NW-substrate interface for a highly Si-doped GaN NW ($\mathrm{BEP}_{\mathrm{Si}} = 7 \times 10^{-10}$ mbar). As also for the nominally undoped NWs (see **Fig. 3.6**, p. 39), a silicon nitride layer with a thickness between 1.5 nm

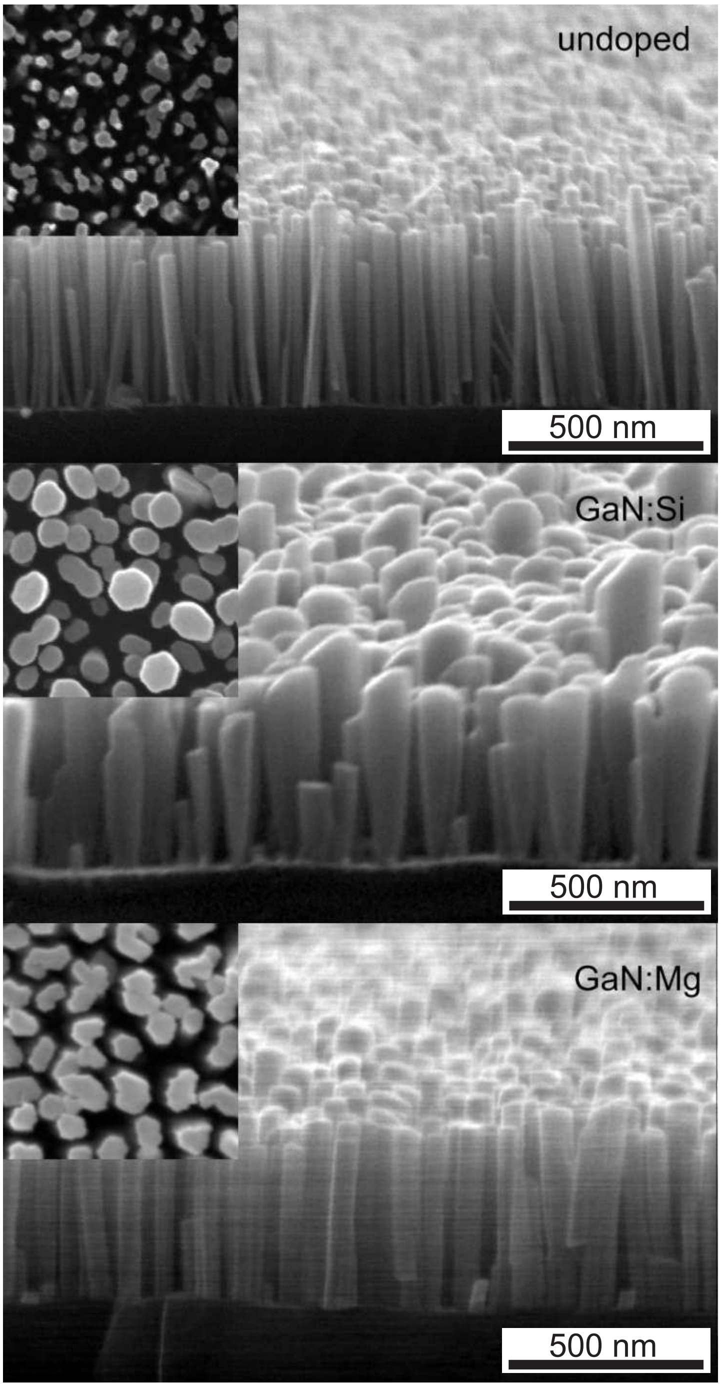

Figure 4.1: *SEM images of cleaved edges taken under 85° inclination and top views (insets) for undoped, heavily Si-doped (T_{Si} = 1160°C), and Mg-doped ($T_{Mg} = 320°C$) GaN NWs. All images are at the same scale.*

Table 4.1: *Si effusion cell temperatures, corresponding* BEP_{Si}*, and numbers of corresponding samples.*

T_{Si} [°C]	BEP_{Si} [mbar]	sample number
0	0	150306
900	4.0×10^{-12}	170306
980	1.8×10^{-11}	030406
1060	9.0×10^{-11}	040406
1120	3.0×10^{-10}	160306
1160	7.0×10^{-10}	050406

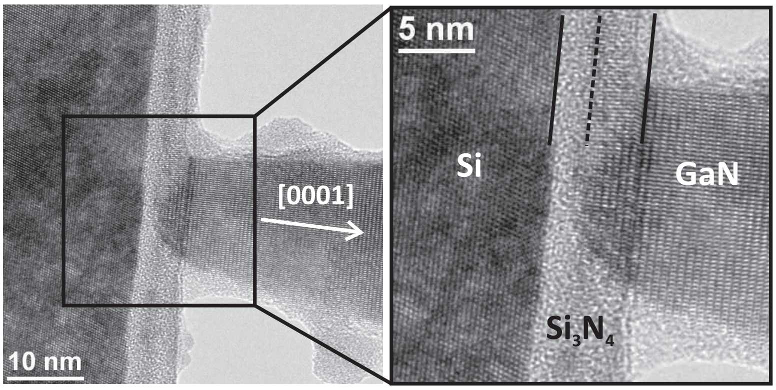

Figure 4.2: *XTEM image of the GaN nanowire / Si(111) interface region for a highly silicon-doped GaN nanowire (*$BEP_{Si} = 7 \times 10^{-10}$ *mbar). The formation of an additional silicon nitride layer between the NWs is observed. The amorphous material on the sidewalls of the NW is part of the glue used for XTEM sample preparation.*

and 2 nm is formed in the initial stage of growth, visible between the NW and the Si-substrate. In addition, a second layer of silicon nitride with a thickness of approximately 3 nm is formed between the NWs. This demonstrates that the formation of silicon nitride on the nitridated silicon surface is favored compared to the growth of GaN under Si- and N-rich growth conditions.

For high Si doping a decrease in the NW density was observed. This is attributed to the enhanced growth of an amorphous silicon nitride layer, which inhibits further nucleation of GaN NWs. Simultaneously, the density of tilted NWs due to nucleation directly on the Si(111) surface is significantly reduced, which also leads to a suppression of NW merging.

Further information about the influence of Si on NW growth was extracted by analyzing the NW diameter and height as a function of the BEP_{Si} during growth (**Fig. 4.3**). For low and medium BEP_{Si}, a continuous decrease of the NW

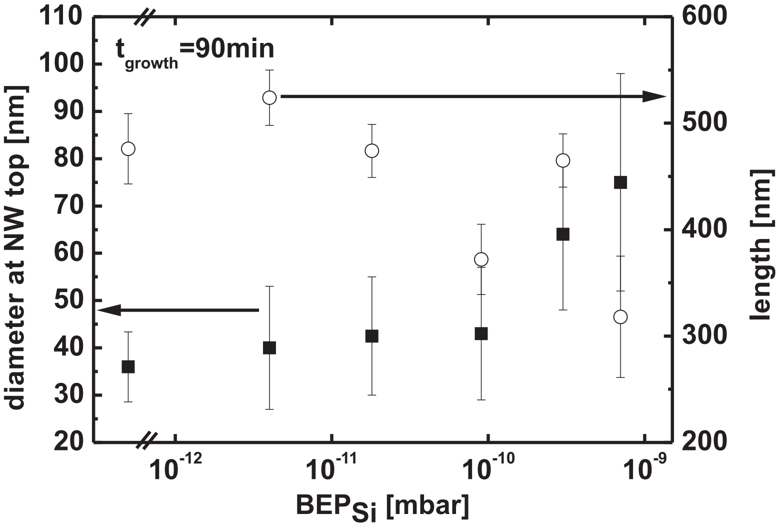

Figure 4.3: *Dependence of the NW diameter (left axis) and length (right axis) on the BEP$_{Si}$. An increase in diameter due to tapering is accompanied by a decrease in height.*

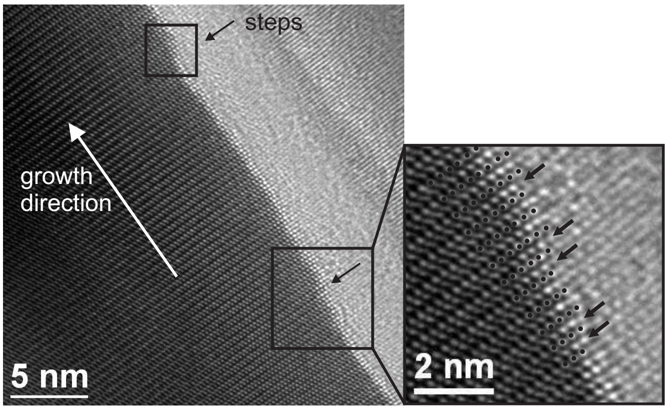

Figure 4.4: *High resolution TEM image of a silicon-doped GaN nanowire (BEP$_{Si}$ = 1.8×10^{-11} mbar). The tapering effect is caused by a gradual increase of the NW diameter due to the formation of monoatomic steps on the sidewall (black arrows).*

length with increasing BEP$_{\mathrm{Si}}$ is observed (i.e. the axial growth rate decreases with increased Si flux). This is accompanied by an increasing NW diameter (measured at the NW top), which is caused by conical widening (tapering) of the NWs (**Fig. 4.4**). For BEP$_{\mathrm{Si}}$ $> 3 \times 10^{-10}$ mbar, both effects are more pronounced.

TEM analysis reveals that this gradual increase of the NW diameter is caused by the formation of bunches of consecutive monoatomic steps along the NWs, which were observed for BEP$_{\mathrm{Si}}$ $\geq 2 \times 10^{-11}$ mbar (**Fig. 4.4**). The distance between such step bunches is decreased when the BEP$_{\mathrm{Si}}$ is increased, leading to a more pronounced conical widening. The NW sidewalls can no longer be defined by

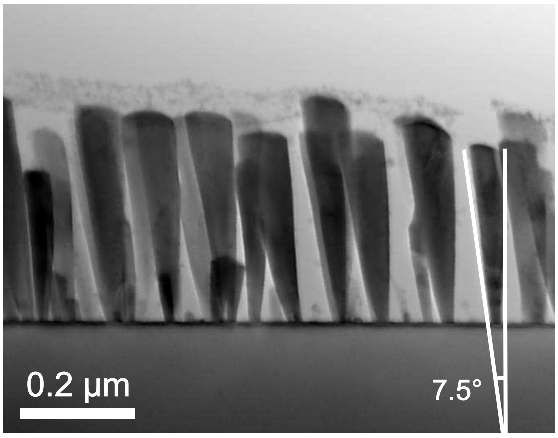

Figure 4.5: *BFSTEM image of highly Si-doped GaN NWs ($T_{Si} = 1160°C$). The angle between two opposing NW sidewalls (approx. 7.5°) is highlighted.*

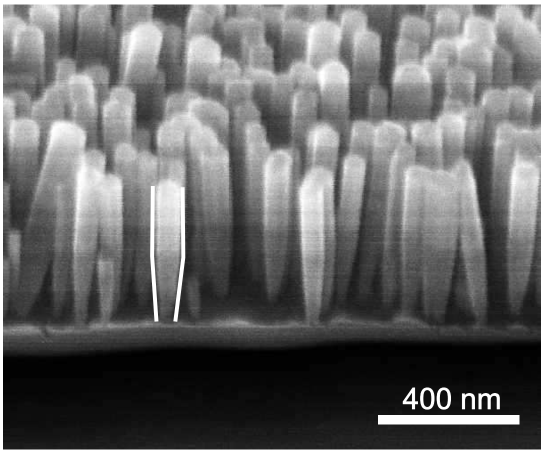

Figure 4.6: *SEM image (45° view) of a sample where first 75 min of GaN:Si (T_{Si}=1160°C) were grown, followed by 40 min of n.i.d. GaN. Widening of the NW diameter is only observed in the lower part.*

one crystallographic plane. For the highest investigated Si flux, the angle formed between two opposing sidewalls was approx. 7.5° (**Fig. 4.5**).

The mechanism leading to this step formation is not clarified yet. For a possible explanation it has to be taken into account that a reduction of the $\mathrm{BEP}_{\mathrm{Si}}$ below 2×10^{-11} mbar during NW-growth results in growth continuation with a constant diameter (see **Fig. 4.6**). Thus, the tapering effect does not originate in the nucleation stage but depends on the Si flux during growth. As this phenomenon is accompanied by a strong decrease in the axial growth rate (**Fig. 4.3**), we assume that it is caused by nucleation of diffusing adatoms at steps on the nonpolar sidewalls, which are present due to slight NW tilt with respect to the growth axis (**Fig. 4.4**). The decrease of the axial growth rate is attributed to the incorporation of diffusing Ga adatoms on the NW sidewalls as a competing process. This

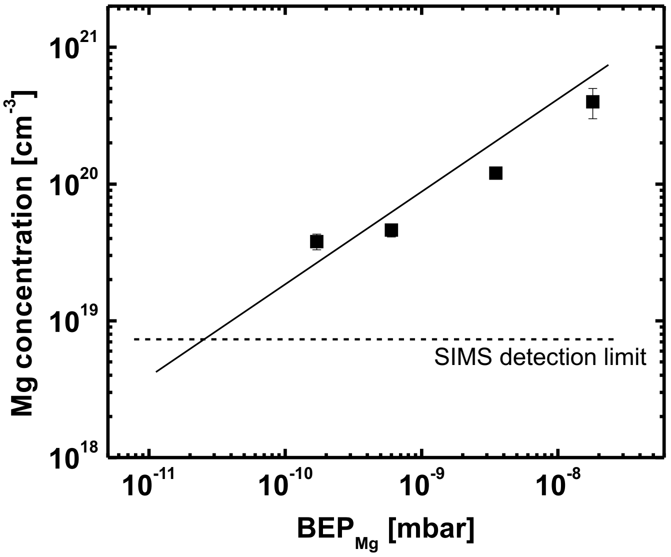

Figure 4.7: *Magnesium concentration of the investigated GaN NWs as a function of Mg beam equivalent pressure measured by secondary ion mass spectroscopy.*

effect supports the conclusions in Refs. [Son07, Gee07, Deb07], stating that Ga adatom diffusion along the NW sidewalls contributes to the axial growth rate.

For high doping levels (when tapering becomes apparent), additionally a change of the NW top surface is found. Whereas undoped NWs are terminated by the *c-plane* (0001), highly Si-doped NWs exhibit $(10\bar{1}n)$ planes with n = 1, 2, 3. Discrete angles of the top surfaces are found, with mainly 32° for the $(10\bar{1}3)$ and 43° for the $(10\bar{1}2)$, but also 62° for the $(10\bar{1}1)$ plane (**Fig. 4.1**). These observations indicate that high Si fluxes change the preferred growth surfaces.

4.2. Influence of magnesium

In analogy to Si incorporation for n-type doping, Mg incorporation for p-type doping was investigated. Mg was supplied by a Mg effusion cell operated between 205°C an 355°C ($\mathrm{BEP_{Mg}} = 1 \times 10^{-11}$ mbar to $\mathrm{BEP_{Mg}} = 1.8 \times 10^{-8}$ mbar).

The Mg concentration was determined by secondary ion mass spectroscopy (SIMS) on as-grown samples(1). These measurements were performed at the University of Gießen. A Duoplasmatron was used as ion beam source with O^{2+} as primary ions (with an energy of 6 keV, a primary ion current of 40 nA, and 250 µm × 250 µm scanning area). The secondary ions were detected with a quadrupole

---

(1) A similar analysis for the GaN:Si samples (previous section) was not possible, since the background originating from the Si wafer was too high.

Table 4.2: *Mg effusion cell temperatures, corresponding* BEP_{Mg}*, Mg concentration measured by SIMS, and corresponding sample numbers. For the weakly doped samples, the Mg concentration was below the detection limit of approximately* 7×10^{-18} cm^{-3}.

$\mathrm{T_{Mg}}$ [°C]	$\mathrm{BEP_{Mg}}$ [mbar]	Mg conc. [$\mathrm{cm^{-3}}$]	sample number
0	0		201006; 220806
205	1.0×10^{-11}	below lim.	110407
225	3.0×10^{-11}	below lim.	190207
240	6.5×10^{-11}	below lim.	161207
260	1.7×10^{-10}	3.8×10^{19}	241006
285	6.0×10^{-10}	4.6×10^{19}	091006
300	1.2×10^{-9}		111006
320	3.5×10^{-9}	1.2×10^{20}	101006; 010906
355	2.0×10^{-8}	4.0×10^{20}	280806

mass spectrometer and a channeltron. The SIMS detection limit was at approx. 7×10^{18} $\mathrm{cm^{-3}}$.

The dependence of the Mg concentration in the Mg-doped NWs as a function of the $\mathrm{BEP_{Mg}}$ during growth is shown in **Fig. 4.7**. A Mg concentration of $4 \times 10^{20}\mathrm{cm^{-3}}$ was achieved for the highest Mg flux ($\mathrm{T_{Mg}} = 355$°C). The respective effusion cell temperatures, $\mathrm{BEP_{Mg}}$ values, and measured Mg concentrations are summarized in **Table 4.2**.

For Mg doping we have observed a decrease in the NW length and an increase of the NW diameter with increasing $\mathrm{BEP_{Mg}}$, the latter being more pronounced than in the case of Si doping (**Fig. 4.8**). As in the case of Si doping, we observed a change of the NW top surface crystal plane for high Mg dopand concentrations. $(10\bar{1}\mathrm{n})$ planes with mainly $\mathrm{n} = 1, 2$ were identified by analyzing the angles in side-view SEM images and TEM images (**Fig. 4.10b**).

The influence of Mg on the NW growth mechanism appears to be different compared to Si incorporation, as it does not change the prismatic NW shape. In order to clarify whether the observed effects are caused by a change in nucleation size or by an increased radial growth rate, we grew compound NW test structures (**Fig. 4.9**) and compared the axial and lateral dimensions. These compound structures were realized by 45 min growth of undoped GaN on top of a Mg-doped NW (sample A, $\mathrm{BEP_{Mg}} = 4 \times 10^{-9}$ mbar, growth time 45 min) as well as a structure grown in inverted order (sample B). For comparison, undoped (C) and Mg-doped

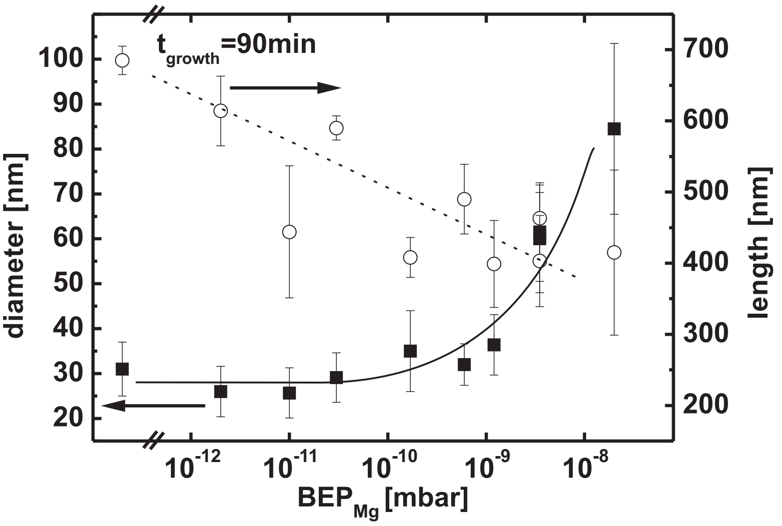

Figure 4.8: *Dependence of the nanowire diameter (left axis) and length (right axis) on the* BEP_{Mg}.

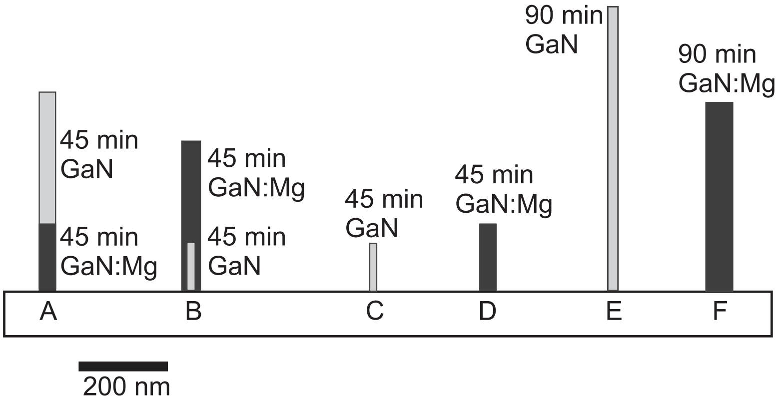

Figure 4.9: *Test structures to study the effect of Mg on nanowire growth.*

(D) reference samples were grown for 45 min and 90 min (E,F), respectively. The results summarized in **Table 4.3** allow the following conclusions:

(i) The axial growth rate is reduced due to the presence of Mg. An axial growth rate of (6.4 ± 2.2) nm/min is calculated for Mg-doped GaN (samples D and F), while a growth rate of (8.8 ± 2.2) nm/min is obtained for undoped NWs (samples C and E).

(ii) The nucleation time is decreased in the presence of Mg, as evaluated by comparison of sample C and D. This also explains that the estimated NW volume for a fixed growth time remains constant up to a $\mathrm{BEP_{Mg}}$ of 2×10^{-9} mbar and increases for higher Mg fluxes.

(iii) Further structural information was obtained by the analysis of the composite NWs: No difference in diameter was found for sample A, sample B, and

Table 4.3: *Growth conditions and NW dimensions of reference samples and compound nanowires to analyze the effect of Mg doping on the growth mechanism (cf. Fig. 4.9).*

Sample	Growth duration [min]	Length [nm]	Diameter [nm]
A (GaN on GaN:Mg)	$45 + 45$	455 ± 50	39 ± 5
B (GaN:Mg on GaN)	$45 + 45$	345 ± 60	41 ± 10
C (GaN)	45	110 ± 20	17 ± 3
D (GaN:Mg)	45	155 ± 35	36 ± 5
E (GaN)	90	640 ± 30	23 ± 5
F (GaN:Mg)	90	435 ± 65	62 ± 10

reference sample D. This is explained by a higher radial growth rate in the presence of Mg rather than by an increased nucleation diameter. The radial growth rate extracted from samples D and F is (0.5 ± 0.1) nm/min. This proves that the presence of Mg enhances growth on nonpolar surfaces. Similar results have been obtained for GaN growth by metal organic vapor phase epitaxy [Bea98]. This latter finding also demonstrates that the low radial growth rate of undoped GaN NWs is due to the different adatom kinetics on the NW sidewalls rather than being caused by the limited availability of active nitrogen [Son07]. The presence of Mg increases the probability of Ga adatoms to be incorporated in nonpolar surfaces.

4.2.1. TEM analysis of highly Mg-doped NWs

The incorporation of Mg does not only affect the NW morphology, but has also an impact on the crystal structure. The analysis of highly Mg-doped samples by cross-sectional transmission electron microscopy (XTEM) showed the formation of twins and the presence of stacking faults also in regions which are far away from the substrate/NW interface. Generally, undoped GaN NWs grown on Si(111) exhibit only one epitaxial relationship. This epitaxial relationship of the n.i.d. GaN NWs with respect to the Si(111) surface is $(0002)[0\bar{1}10]$GaN $\parallel$ $(111)[\overline{11}2]$Si. In contrast, SAED patterns of heavily Mg-doped NWs ($T_{\mathrm{Mg}} = 355°\mathrm{C}$) revealed a second contribution(1). The additional relationship for high Mg doping is $(0002)[1\bar{2}10]$GaN $\parallel$ $(111)[\overline{11}2]$Si. This corresponds to a rotation of 30° around the *c-axis* compared to

---

(1) TEM analysis performed by J. Arbiol *et al.*. Further images and corresponding SAED pattern can be found in [Arb09].

Table 4.4: *Density of stacking faults along the growth direction for different Mg fluxes.*

T_{Mg} [°C]	BEPMg [mbar]	SF [cm^{-1}]
260	1.7×10^{-10}	2×10^{7}
320	3.5×10^{-8}	8×10^{8}
355	2×10^{-8}	2×10^{10}

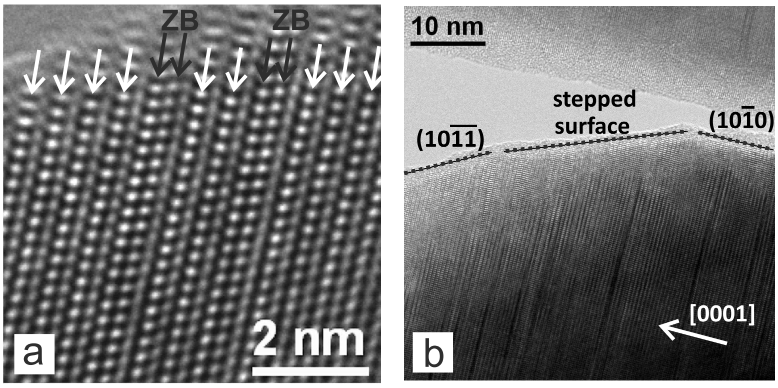

Figure 4.10: *HRTEM images of GaN:Mg NWs grown at $T_{Mg} = 355°C$. (a) Detail showing the alternating wurtzite and zincblende stacking (ZB planes marked with black arrows). (b) Detail of region near the NW top. The NW forms a tip by a stepped surface and a $(10\bar{1}\bar{1})$ surface.*

the original relationship. The nanowire can be regarded as a rotational twin crystal with additional C stacking planes to the wurtzite A-B stacking. Since A-B-C stacking forms the cubic zincblende structure, the crystal has cubic inclusions (see p. 9). Such ZB inclusions are shown in **Fig. 4.10a**. The stacking faults are found throughout the NW length without any preferential region. Their density (listed in **Tab. 4.4**) increases dramatically with the Mg flux.

Additionally, energy loss spectra (EELS) with high spatial resolution (0.1 nm probe size) were recorded on wurtzite and zincblende planes in these NWs [Arb09]. They revealed a change in the band-to-band electronic transition energy from 3.4 eV for the WZ regions to 3.2 eV for the twinned (ZB) regions. The results are in good agreement both with atomistic simulations (cf. [Arb09] for details) and PL results (cf. next chapter).

5. Optical properties of doped and undoped GaN NWs

In this chapter, the optical properties of undoped and doped GaN NWs are investigated by photoluminescence and Raman spectroscopy. Sharp near band edge emission is recorded at 4K. For undoped or slightly Si-doped material the emission is dominated by the narrow D^0X recombination at 3.4715 eV with a full width at half maximum of 1.5 meV. Point defects due to the N-rich growth conditions are discussed as the origin of the emission band at 3.45 eV. Recombination at coalescence boundaries were identified as the origin of an emission band at 3.21 eV. The luminescence properties at 3.27 eV and below in highly Mg-doped samples are shown to be affected by the presence of cubic inclusions in the otherwise wurtzite nanowires. For moderate Mg fluxes the acceptor-bound exciton recombination was detected at 3.4665 eV. Additionally, the influence of the III-V ratio on PL emission in undoped NWs is analyzed. Furthermore, Raman scattering revealed that the nanowires are strain-free, irrespective of Si or Mg doping.

The same samples as in the previous chapter are analyzed here. For the Si-doped (Mg-doped) samples, a list with effusion cell temperatures, BEPs, and corresponding sample numbers is given in **Tab. 4.1** on p. 63 (**Tab. 4.2** on p. 67).

5.1. Raman scattering

The E_2 Raman line of undoped GaN NWs was detected at $(567.1 \pm 0.2)\,\mathrm{cm}^{-1}$, in agreement with the reported value of unstrained GaN [Per92]. No changes were observed with the incorporation of Si and Mg for all investigated samples (**Fig. 5.1**). This is in strong contrast to the behavior of continuous Si-doped GaN films, where a shift from compressive to tensile stress was reported for increasing concentration of Si [Chi06]. In that report, a shift of the E_2 Raman line from $569.3\,\mathrm{cm}^{-1}$ to $566.8\,\mathrm{cm}^{-1}$ was observed when increasing the Si doping corresponding to a free carrier concentration of $2\times10^{17}\,\mathrm{cm}^{-3}$ to $9\times10^{18}\,\mathrm{cm}^{-3}$.

By using a biaxial pressure coefficient of $(2.4 \pm 0.6)\,\mathrm{cm}^{-1}\,\mathrm{GPa}^{-1}$, as reported for PAMBE-grown GaN layers on Si in Ref. [Dem04], the maximum possible strain in

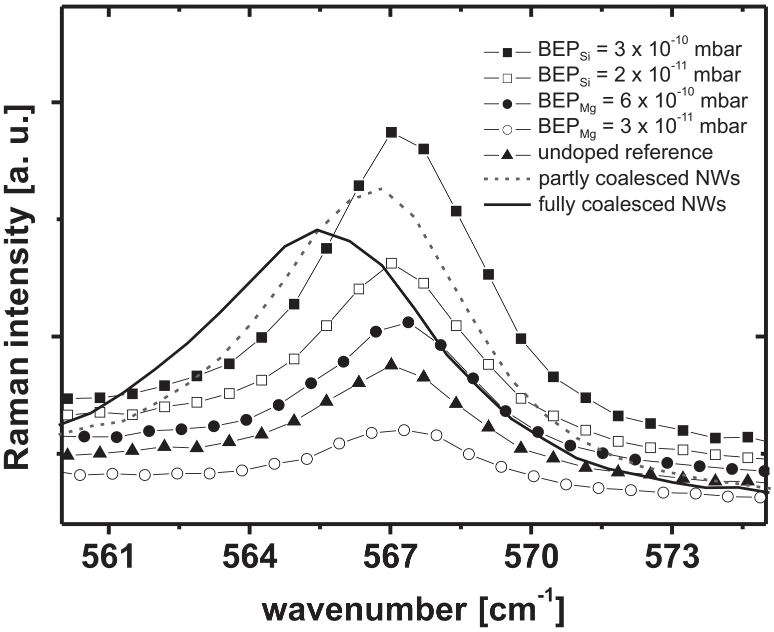

Figure 5.1: *E_2 Raman line for undoped, Si-doped, and Mg-doped GaN nanowires as well as for two undoped GaN nanowires with higher degree of coalescence. A strain-induced shift was only observed for coalescing samples. A SEM image of the fully coalesced sample (solid line) is shown in* ***Fig. 5.5d***.

the NWs within our experimental uncertainty (0.2 cm^{-1}) is 0.5 GPa. However, for an almost coalesced layer the E$_2$ Raman line is found at 565.4 cm^{-1} (**Fig. 5.1**, solid line), corresponding to a tensile strain of 3.9 GPa. GaN nanowires are confirmed to be strain-free, as it has been reported in Refs. [Wan05, Seo06] for undoped GaN NWs. Hence, they are a suitable model system to study the optical properties of doped, unstrained GaN, as it was demonstrated for thick GaN layers grown by hydride vapor phase epitaxy (HVPE) [Mon02]. The FWHM of the E$_2$ Raman line ranges from (3.4 ± 0.2) cm^{-1} for undoped, Mg-doped or weakly Si-doped samples to (3.8 ± 0.2) cm^{-1} for highly Si-doped samples. This is comparable to a FWHMs of 3.15 cm^{-1} to 4.15 cm^{-1}, which were recently reported for n.i.d. and Mg-doped GaN NWs [Lim10].

5.2. Low-temperature PL

The recorded PL spectra can be divided into three regions (**Fig. 5.2**) which are discussed separately: the near band edge regime, a region below 3.4 eV, dominated by the recombination at 3.27 eV, and the deep (yellow) luminescence.

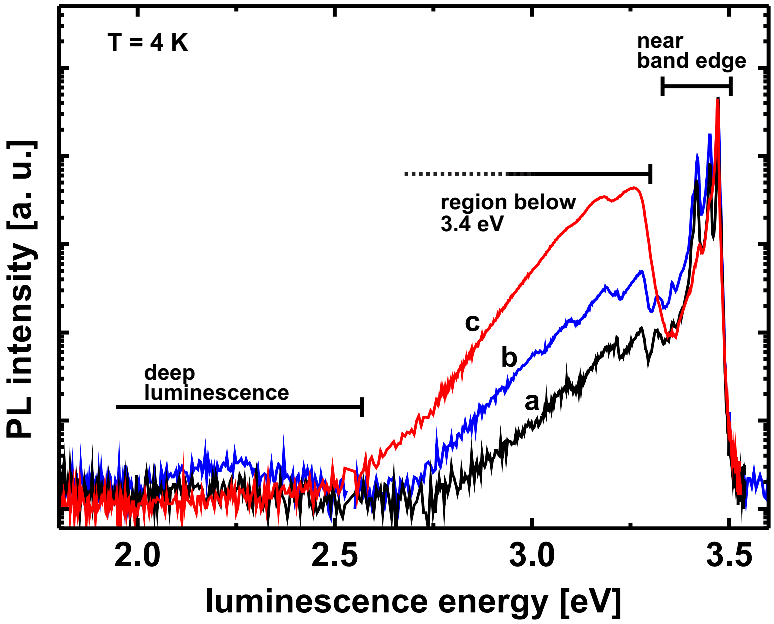

Figure 5.2: *PL survey spectra indicating the three energy regions. (Sample a: undoped GaN NW; b: BEP*$_{\mathrm{Si}} = 2 \times 10^{-11}$ *mbar; c: BEP*$_{\mathrm{Mg}} = 3 \times 10^{-11}$ *mbar).*

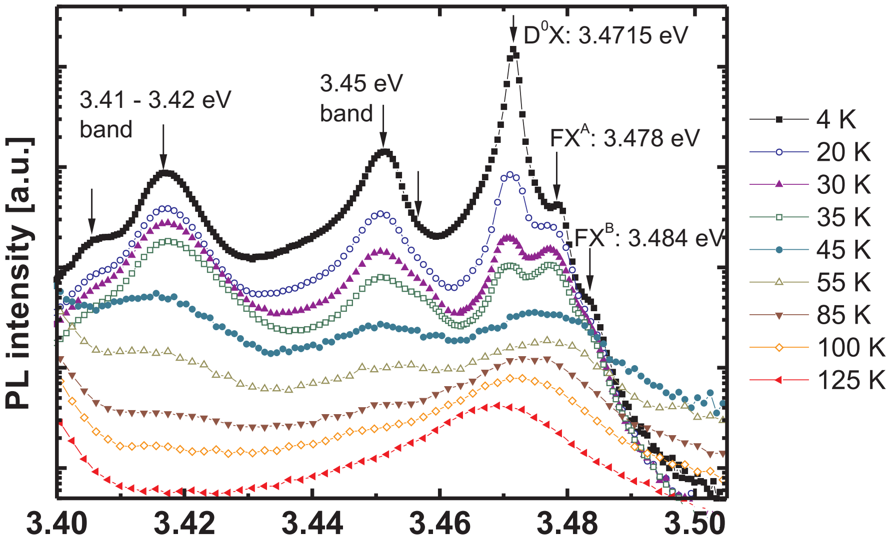

Figure 5.3: *Temperature-dependent PL spectrum of the near band edge regime of undoped GaN NWs, exhibiting three bands at 3.41 eV-3.42 eV, 3.45 eV, and 3.47 eV, respectively. Curves are vertically shifted for clarity.*

5.2.1. Near band edge PL for undoped and Si-doped samples

The near band edge luminescence (3.40 eV – 3.50 eV) of nominally undoped GaN NWs consists of three bands (**Fig. 5.3**). In the following, these contributions are discussed individually.

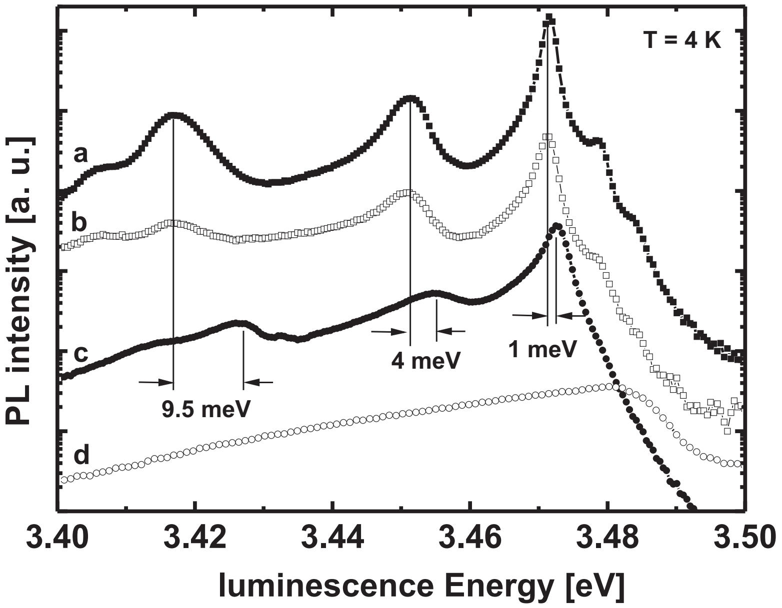

Figure 5.4: *Low temperature PL-spectra of undoped (sample a) and Si-doped GaN NW samples (sample b: BEP*$_{\mathrm{Si}} = 4\times10^{-12}$ *mbar; c: BEP*$_{\mathrm{Si}} = 9\times10^{-11}$ *mbar; d: BEP*$_{\mathrm{Si}} = 3\times10^{-10}$ *mbar). For BEP*$_{\mathrm{Si}} = 3\times10^{-10}$ *mbar the three band structure is no longer resolved.*

Luminescence between 3.47 eV and 3.50 eV

The luminescence between 3.47 eV and 3.50 eV is of excitonic origin. The strongest emission at (3.4715 ± 0.0004) eV, with a FWHM of 1.5 meV is assigned to a donor-bound exciton (D^0X) [Cal00, Mon02, Bun99, Pau98]. The observed FWHM of the D^0X line is smaller than in earlier reports on GaN NWs (2 meV in Ref. [Cal00], 6-8 meV in Ref. [Che01], 6-10 meV in Ref. [Tch07], or 5 meV for single NWs in Ref. [Sch06]). It increases continuously with Si flux up to 3.6 meV for the sample grown at $\mathrm{BEP_{Si}} = 9 \times 10^{-11}$ mbar. This emission is assigned to Si and O donors in accordance with measurements performed on unstrained HVPE GaN [Mon02]. The respective emission lines are separated by only 1 meV [Mon02, Fre05], which was not possible to resolve in our measurements. However, the increasing asymmetry of the emission peak with increasing [Si] (broadening of the low-energy side, **Fig. 5.4**) indicates that Si is causing the contribution at lower energy, as also suggested in Ref. [Mon02]. For low and moderate Si fluxes, the energetic position of the D^0X-transition remains unchanged, in contrast to the strain-induced red-shift in continuous GaN layers, which is most likely due the formation of structural defects and Si incorporation at dislocations [Chi06, Gra98]. For a Si flux of $\mathrm{BEP_{Si}} = 9 \times 10^{-11}$ mbar a blue-shift of 1 meV is observed, which we attribute to donor band formation, possibly in combination with band-filling effects (Burstein-

Moss shift), as it has been reported for homoepitaxial GaN layers [Pry98]. Uncoalesced NWs exhibit the smallest FWHM (**Fig. 5.5**). With increasing degree of coalescence the FWHM rises gradually from 1.8 meV (sample a) to 2.8 meV, 2.7 meV, and 4.0 meV for samples b,c, and d, respectively.

The free exciton emission lines at 3.478 eV (FX^A) and 3.484 eV (FX^B) indicate an exciton localization energy of 6.5 meV and a splitting between A and B valence bands of 6 meV [Cal97].

For Si-doped homoepitaxial layers, an emission at 3.466 eV has been reported, which increased in intensity with increasing Si doping level. It was assigned to an exciton bound to a shallow silicon-related acceptor [Fre05, Gra98], suggested as Si_N (i.e. a Si atom on a lattice position normally occupied by nitrogen) in [Fre05]. In the present study the emission was neither observed in the undoped nor the Si-doped samples. This supports the assignment to the formation of Si_N as this is not very probable under the N-rich growth conditions applied here.

Luminescence band at 3.45 eV

The emission band at 3.45 eV is typically observed in GaN nanowires [Cal00]. Emission at this energy in thick freestanding GaN layers has been assigned to a two electron satellite (TES) of the D^0X recombination [Wys03], based on magnetic field-dependent PL measurements. Our observations contradict this. First, the thermal quenching in comparison to the D^0X emission is less pronounced (cf. **Fig. 5.3**, most clearly visible when comparing 4K to 30K) and second, the influence of doping is different in comparison to the D^0X emission (see below of Si-doped samples, and Sec. 5.2.2 for Mg-doped samples).

Strong emission at 3.45 eV has been reported for samples with a low density of NWs protruding from a GaN wetting layer [Cal00]. We observed this emission in samples without wetting layer. It consists of at least two convoluted peaks and is centered at 3.451 eV for undoped samples at a temperature of 4K. With increasing degree of coalescence, the intensity decreases and a slight blue-shift is observed (**Fig. 5.5**). For an almost coalesced layer (sample *d* in **Fig. 5.5**) the 3.45 eV emission was only detectable as a low energy shoulder of the D^0X emission. Due to its evolution with temperature it was assigned to excitonic recombination [Cal00]. This is supported by the observation of a second contribution with less pronounced temperature-induced quenching at 7 meV higher energy, which can be observed at temperatures around 30 K (**Fig. 5.3**). For very high [Si], a blue-shift is found (4 meV for $BEP_{Si} = 9 \times 10^{-11}$ mbar, cf. **Fig. 5.4**).

In earlier work this emission has been assigned to the recombination of acceptor-bound excitons (Ref. [Cal97] and references herein) or to Ga_I (i.e. Ga interstitial),

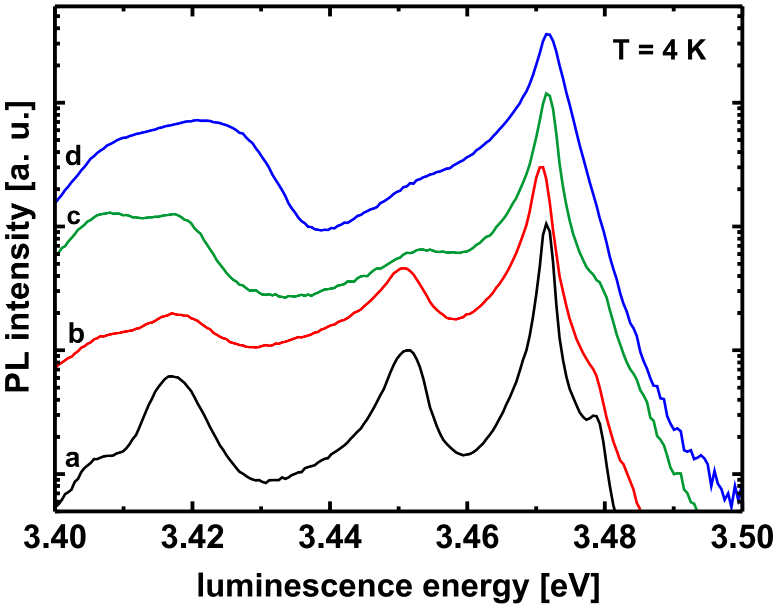

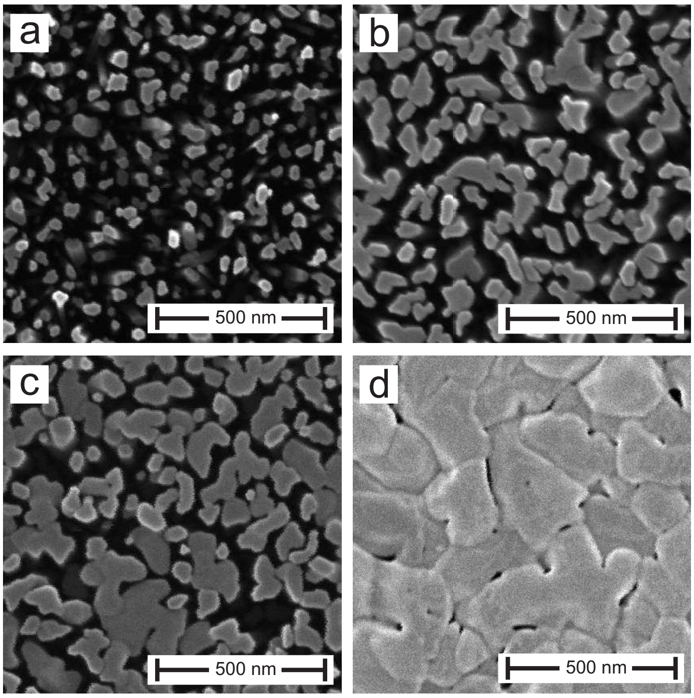

Figure 5.5: *PL spectra of four undoped GaN NW samples with increasing degree of coalescence from a to d ($T = 4K$) and their and corresponding top view SEM micrographs. Sample a is the undoped reference from Fig. 5.3. The FWHM of the 3.47 eV emission increases with rising degree of coalescence from 1.8 meV over 2.8 meV and 2.7 meV to 4.0 meV for sample a to d, respectively.*

if a local accumulation of Ga is assumed to initiate the nucleation of GaN NWs [Cal00]. As we found the same relative intensity compared to the D^0X emission for NWs with a length of 500 nm and 2400 nm (**Fig. 5.6**), we assign this emission to the volume of the NWs rather than to the NW/substrate interface, ruling out the attribution to interfacial Ga_I [Cal00]. More probably it is related to a point-defect caused by the N-rich growth conditions. These growth conditions have also been used for the samples analyzed in Ref. [Cal97], where a similar emission was reported. The Ga vacancy (V_{Ga}) was suggested in Refs. [Neu94, Mat97] as an acceptor-like defect with a low formation energy. N-rich growth conditions favor the formation of this defect in particular on the NW sidewalls, which could lead to a localization of excitons that give rise to the 3.45 eV emission.

This assignment is further confirmed by the results shown in **Fig. 5.5**, which show that a gradual transition to stoichiometric growth conditions leads to a decrease in emission intensity. Comparison of **Fig. 5.5** and **Fig. 5.7** reveals that the same trend is observed upon an increase of the Mg flux. In accordance with the arguments outlined above, this agrees with calculations in Refs. [Neu94, Mat97], where the formation of the V_{Ga} was predicted to be most probable in n-type samples with the Fermi level being far above mid-gap.

Luminescence band at 3.41 eV – 3.42 eV

The emission band around 3.41 eV consists of two peaks at 3.406 eV and 3.417 eV for undoped NWs. In Ref. [Cal97] this band has been observed as one peak with a strong sample-to-sample variation of its energetic position in compact layers. The samples investigated here show an increase in intensity of the 3.406 eV component with increasing degree of coalescence (from sample *a* to *c* in **Fig. 5.5**). For a coalesced layer (sample *d* in **Fig. 5.5**) the emission broadens and shows an increased intensity at higher energies.

The 3.41 eV emission band has been attributed to defects at the GaN/Si interface using cathodoluminescence (CL) measurements [Cal00], confirmed by CL mapping [SP02]. In the latter work, regions with strong 3.41 eV-3.42 eV emission had a rather weak emission in the excitonic regime. For the samples studied in this work, a relative decrease by about a factor of 3 of the 3.41 eV intensity compared to the D^0X emission intensity was found when the NW length was increased from 600 nm to 2400 nm (**Fig. 5.6**). The peak position remained constant. This confirms the assignment to defects in the lower section of the NWs, as concluded in Ref. [Che01].

By direct comparison of TEM and CL images of *a-plane* GaN thin films [Liu05] it was concluded that basal plane stacking faults (stacking faults along the *c-axis*)

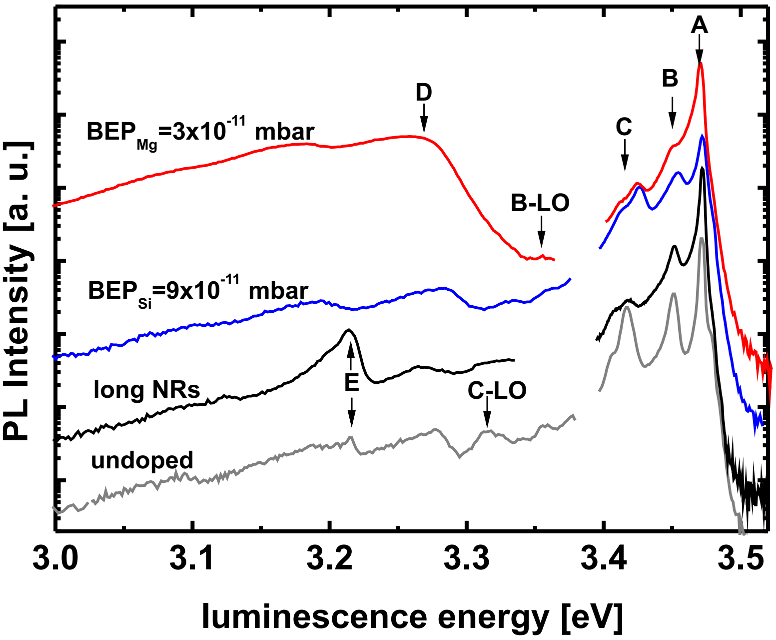

Figure 5.6: *PL spectra of an undoped reference sample (NW length 500 nm), a sample with long NWs (2400 nm) grown at BEP$_{Si}$ = 4 × 10^{-12} mbar, a Si-doped sample and a Mg-doped sample. Arrows indicate (A) the D^{0}X transition at 3.47 eV, (B) the 3.45 eV band, (C) the 3.41 eV-3.42 eV band, (D) the DAP band at 3.27 eV, and (E) the 3.21 eV emission. The LO phonon energy (92 meV) is given to mark replica of peaks (B) and (C). Curves are vertically shifted for clarity.*

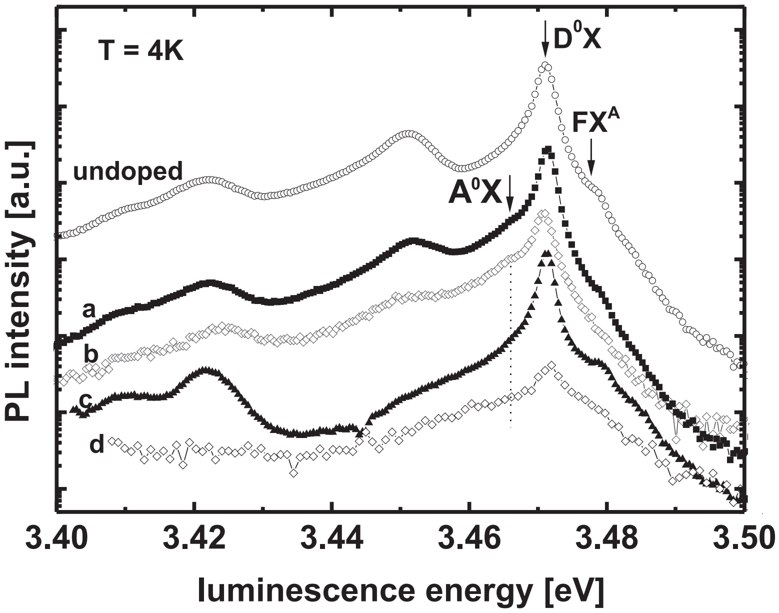

Figure 5.7: *Low temperature PL spectrum of Mg-doped GaN NWs compared to an undoped reference. The BEP$_{Mg}$ is increased from a to d (Sample a: BEP$_{Mg}$ = 1 × 10^{-11} mbar; b: BEP$_{Mg}$ = 3 × 10^{-11} mbar; c: BEP$_{Mg}$ = 1.7 × 10^{-10} mbar; d: BEP$_{Mg}$ = 6 × 10^{-10} mbar). For weak Mg doping (Samples a and b) the emission of acceptor-bound excitons (A^{0}X) can be observed at 3.4655 eV.*

are responsible for the 3.41 eV emission line. Regions with strong 3.41 eV emission were found dark in the 3.47 eV images. In a similar study on GaN NWs this emission was also assigned with stacking faults, which were formed in vicinity of boundary dislocations within the coalescence region [Con09]. The origin of this emission is ascribed to excitons bound to stacking faults [Sal99]. For our samples the presence of stacking faults was observed in TEM images at low density at the NW/substrate interface but not in the upper part of the NWs.

With rising Si flux both components of this emission are continuously blue-shifted ($+\,9.5$ meV at $\mathrm{BEP_{Si}} = 3 \times 10^{-10}$ mbar). This Si-induced shift is more pronounced than the shifts of the other two bands, confirming its different origin. In a μ-PL investigation of dispersed NWs, the 3.41 eV emission is present in coalesced NW bundles but not in uncoalesced individual NWs [Rig10a]. Thus, the relationship between this emission and the formation of coalescence defects is confirmed.

The three-band spectrum of the near band edge emission discussed in this section is clearly resolvable for Si fluxes up to $\mathrm{BEP_{Si}} = 9 \times 10^{-11}$ mbar (**Fig. 5.4**). LO phonon replica of the 3.45 eV and 3.41 eV bands with a LO phonon energy of 92 meV [Cal97, Res05] are observed at 3.36 eV and 3.32 eV, respectively (**Fig. 5.6**). For very high Si fluxes (sample *d* in **Fig. 5.4**), only one broad emission centered at 3.482 eV with a FWHM of 36 meV is observed. The morphology of these NWs differs strongly from those of n.i.d. NWs: Whereas for lower Si fluxes, the NWs exhibit a prismatic shape and a homogeneous aspect ratio, NWs grown at a high Si-concentration exhibit a cone-like shape (see **Fig. 4.1**, p. 62).

5.2.2. Near band edge regime in Mg-doped samples

For Mg-doped NWs, the intensity of the three-band spectrum discussed above is reduced compared to undoped or Si-doped samples. For doping with low and intermediate Mg fluxes the evolution of a shoulder at $3.4665\,\mathrm{eV} \pm 0.0008\,\mathrm{eV}$ is observed on the low energy side of the $\mathrm{D^0X}$-emission (**Fig. 5.7**). We assign this emission to the recombination of an exciton bound to a neutral acceptor, $\mathrm{A^0X}$. In Ref. [Mon02], $\mathrm{A^0X}$ recombination has been suggested as the origin of an emission observed between 3.466 eV and 3.480 eV. The variation in emission energy was explained by different strain states of the investigated samples. As Raman analysis of the samples investigated here did not reveal either tensile or compressive strain (see Sec. 5.1, p. 71), we attribute the emission at 3.4665 eV to the recombination of a neutral acceptor bound exciton in partially compensated, unstrained GaN nanowires.

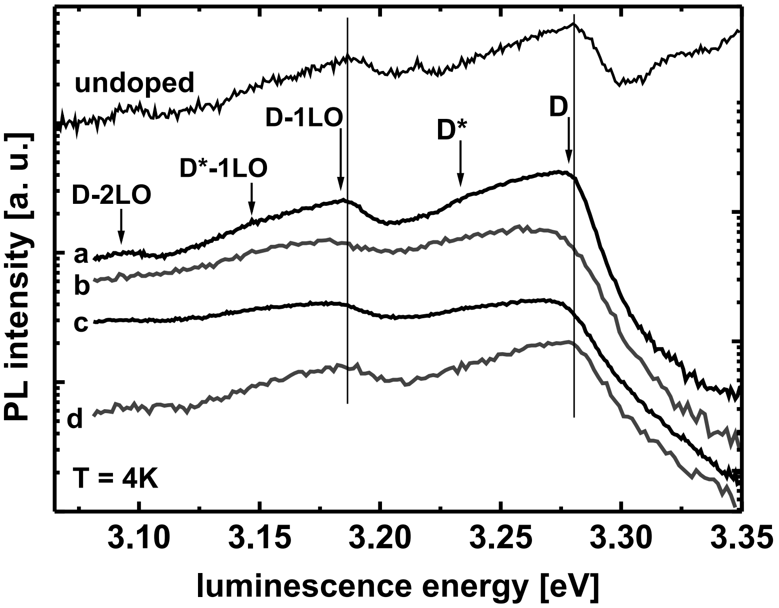

Figure 5.8: *PL in the DAP region for an undoped and four Mg-doped samples. The BEP$_{Mg}$ is increased from sample* a *to* d *(same samples as in* ***Fig. 5.7****).*

5.2.3. DAP region (below 3.4 eV)

For undoped or Si-doped samples, the intensity of emissions bands with energies below the excitonic regime was more than 2 orders of magnitude lower than the D^0X emission. In contrast, the presence of Mg enhanced the emission in this region already for the sample grown at the lowest BEP$_{\mathrm{Mg}}$, as shown in **Fig. 5.6** for a sample grown at BEP$_{\mathrm{Mg}}$ $= 3 \times 10^{-11}$ mbar. Simultaneously, the overall intensity of the near band edge regime was reduced. The energetic position of the D^0X-recombination remained constant.

3.27 eV DAP region and its replica

The strong increase of the 3.27 eV emission even for weak Mg doping (sample *a* in **Fig. 5.8**) is attributed to a donor-acceptor-pair recombination (DAP) and has been discussed in detail for Mg-doped GaN thin films [Ler99, Nar04, Mon04]. However, an increase of the BEP$_{\mathrm{Mg}}$ leads to a more complex behavior (**Fig. 5.8**). For undoped samples, only one weak emission centered at 3.279 eV with steeper high energy decay is found. In the case of weak Mg doping, this emission can be deconvoluted into two components with the main emission at 3.275 eV and a weaker contribution at approximately 40 meV lower energy (3.235 eV), labeled with *D* and *D** in **Fig. 5.8** respectively. First and second order LO phonon replica of both contributions are observed *(D-1LO, D*-1LO, D-2LO)*, red-shifted by the respective phonon energy of 92 meV. The emission at *D* was assigned to the en-

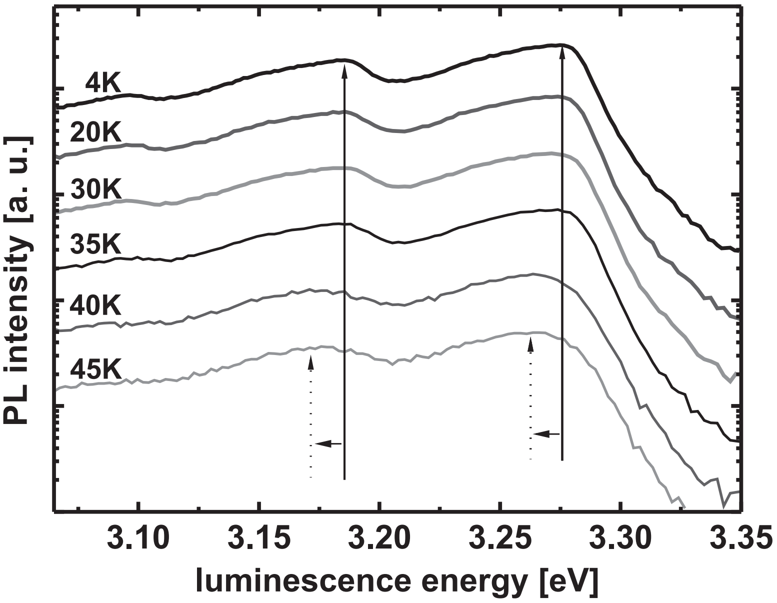

Figure 5.9: *Temperature-dependent PL spectra of Mg-doped NWs grown at* $BEP_{Mg} = 1 \times 10^{-11}$ *mbar (same sample as in curve* a *in* ***Figs. 5.7 and 5.8****).*

hanced DAP transition mentioned above, whereas the origin of the emission at D^{*} could not be clarified. The temperature-dependent measurements for the two samples with the lowest Mg flux (**Fig. 5.9**) demonstrate the redshift with increasing temperature of the dominant D emission. The same temperature dependence has also been reported for MBE-grown GaN:Mg nanowires by Park *et al.* [Par06].

Further increase of the Mg flux (samples b, c in **Fig. 5.8**) causes a red-shift of the main emission to 3.260 eV and simultaneous broadening. In addition, the emission band around 3.18 eV gains in relative intensity and even exceeds the red-shifted main emission (sample c). Hence, it can not be entirely explained as a LO phonon replica of the D emission. This contradicts the results obtained for GaN:Mg layers grown by MBE with Mg concentrations up to $1 \times 10^{19}\,\mathrm{cm}^{-3}$ on GaN templates synthesized by metal organic vapor phase epitaxy [Nar04]. In that work, the intensity ratios remained constant and an increase in total luminescence intensity with rising Mg concentration was reported. Furthermore, the peak position was reported to be unchanged. On the other hand, the results presented in Ref. [Par06] on Mg-doped GaN NWs grown under N-rich growth conditions confirm our observation that the 3.18 eV emission does not come from LO phonon replica only.

TEM analysis of the samples grown at high Mg fluxes ($\mathrm{BEP_{Mg}} \geq 3.5\times10^{-9}$ mbar) revealed stacking faults in the wurtzite lattice, which give rise to inclusions of cubic GaN (see Sec. 4.2.1, p.69, or [Arb09]). Accordingly, we attribute the observed evolution of the photoluminescence with increasing [Mg] to the presence of zincblende GaN with a lower bandgap of 3.27 eV in a wurtzite GaN matrix, which leads to enhanced recombination in the cubic inclusions even if the volume-ratio is small. Therefore, the red-shift in luminescence can be attributed to excitonic emission in cubic GaN, containing contributions of both donor-bound and free excitons [Mon04, Wu00, Men96]. The broad emission at 3.17 eV can be attributed to a superposition of the LO-phonon replica of the excitonic emission and a DAP transition that was observed in n.i.d. cubic GaN [Wu00, Men96]. A phase transition from wurtzite to zincblende was reported for PAMBE-grown N-face GaN films for Mg doping [Mon04].

3.21 eV emission

A relatively narrow transition at 3.21 eV (labeled with E in **Fig. 5.6**), also mentioned in Ref. [Mon02], was observed in undoped samples. This emission is suppressed in Si-doped samples with $\mathrm{BEP}_{\mathrm{Si}} > 1.8 \times 10^{-11}$ mbar and cannot be found in Mg-doped samples (where it is possibly masked by the broad intense emission at 3.27 eV). For long NWs (2400 nm), this transition is enhanced (**Fig. 5.6**), as it was also observed by Chen *et al.* [Che01]. The 3.21 eV emission has been attributed to excitons trapped at dislocations at the boundaries of coalesced NWs [Che01], or to disorder at the Si/GaN interface [SP02]. Our results support the first explanation as the long NWs exhibited a higher degree of coalescence. The presence of Si leads to a reduction of NW coalescence (see Sec. 4.1). However, if the NWs were grown under less N-rich conditions, the intensity of the 3.21 eV emission decreases whereas its FWHM increases (**Fig. 5.10**). In combination, this suggests that only coalescence under relatively high tilt angles, which happens often close to the substrate (see Fig. 3.11, p. 45), gives rise to this emission whereas the mechanism of coalescence towards layer formation promoted by less N-rich conditions (which lead to higher NW diameters and enhanced lateral growth) is different and does not enhance this emission.

5.2.4. Deep yellow luminescence

For undoped samples a broad emission band is detected at 2.2 eV (the yellow defect luminescence [Res05]). The intensity is more than four orders of magnitude lower than the intensity in the excitonic regime, indicating a low defect density. The emission intensity remains low for Si-doped samples. In the case of high Mg doping a broad emission for luminescence energies above 2.0 eV is found (centered around

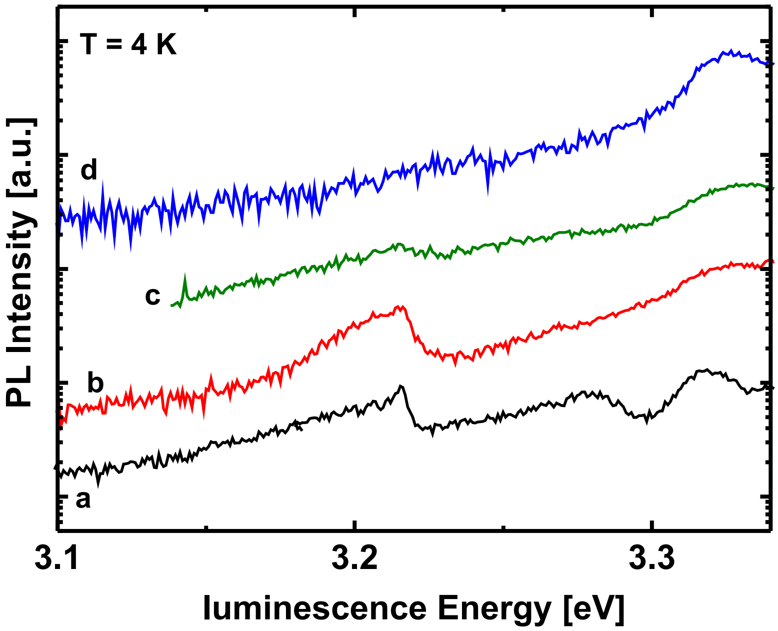

Figure 5.10: *Evolution of the 3.21 eV emission with increasing degree of coalescence (from* a *to* d*, same samples as in* ***Fig. 5.5****). The emission at 3.325 eV is the first LO phonon replica of the 3.41 eV emission.*

2.5 eV). Its intensity is about 2% of the intensity of the 3.27 eV emission for a sample with $\mathrm{BEP}_{\mathrm{Mg}} = 6 \times 10^{-10}$ mbar.

5.3. Conclusions

The NWs were found strain-free, independent of the dopant concentration. For Si doping, sharp and intense PL emission peaks are found as long as the prismatic morphology of the NWs is preserved. In the region of the strongest PL intensity (3.47 eV – 3.50 eV), free and donor-bound excitons were identified. The 3.450 eV emission was assigned to the enhanced formation of Ga vacancies (V_{Ga}) due to the N-rich growth conditions. The 3.41 eV – 3.42 eV emission band originates from the substrate interface. The addition of Mg quenches the band edge emission intensity, whereas the intensity in the region below 3.4 eV is strongly enhanced. The main emission at 3.27 eV is attributed to a combination of cubic inclusions and DAP transitions and shows a red-shift with rising Mg flux.

6. Electrical properties of GaN NWs

In this chapter, the results of electrical measurements on single GaN:Si nanowires are presented. Contacting single NWs is technologically challenging. The experimental methods are shown in detail and the results for photolithography and e-beam lithography processing are compared. To facilitate contacting, highly doped end regions (base and top part of the NW) were used. The *I*-*V* characteristics are found to depend on both the contact design and processing method. Therefore, the results should be interpreted carefully. However, a clear increase in conductivity with doping level over several orders of magnitude was observed. For undoped NWs the current is space-charge-limited. For low and moderate doping levels, a strong current enhancement by above bandgap illumination is found, as also reported by [Cal05, San10].

6.1. Surface band bending

The large surface-to-volume ratio makes NWs highly sensitive to surface effects. Surface states lead to a pinning of the Fermi level and to band bending [Cal05]. The bands are bent upwards at the GaN NW sidewalls, leading to a reduction of the free carrier density towards the surface and, therefore, a depletion zone is formed (see **Fig. 6.1**). Depending on the doping level and the NW diameter, the NW can be fully depleted or exhibit a conductive channel in its center. For nominally undoped NWs this depletion zone can be larger than the NW radius leading to a full depletion of the NWs. According to [Cal05] a critical diameter of 85 nm below that the NW is fully depleted was found by comparing single NW *I*-*V* measurements with the NW diameter. With increased doping level the width of the depletion region is reduced. Recently it was reported that the surface band bending (SBB) in depleted GaN NWs is quite small (of the order of a few 10meV) [Pfü10]. For GaN NWs with a diameter of 30 nm and a Si doping level of $10^{17}\,\mathrm{cm}^{-3}$, the SBB was estimated to 30 meV, leading to lateral electrical fields as low as $20\,\mathrm{kV\,cm}^{-1}$ [Teu11]. In that work it is also shown that the lateral

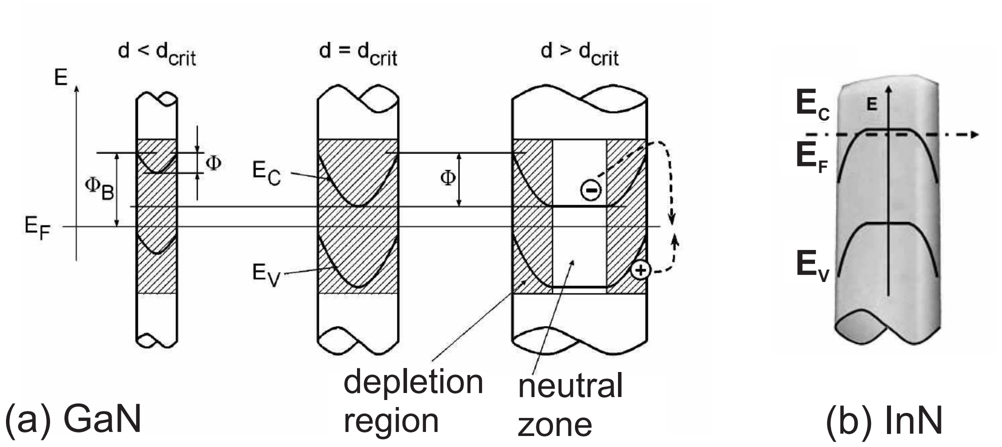

Figure 6.1: *(a) Dependence of depletion region (shaded), shape of conduction (E_C) and valence band edges (E_V), and recombination barrier on the nanowire diameter. The relative energetic positions of E_C, E_V, and E_F are not true to scale. For NW diameters below d_{crit}, the NWs are fully depleted. Image from [Cal05]. (b) Band positions for InN NWs. Image from [Cal07a].*

band profile inside fully depleted GaN NWs remains almost unchanged under the variation of the surface potential.

For InN NWs the situation is opposite. Here, the bands bend downwards and electrons accumulate at the surface [Cal07a]. Narrow bandgap semiconductors such as InAs and InSb usually show an accumulation layer due to pinning of the Fermi level above the conduction band edge. The free electrons move to the surface and form an accumulation layer. A high conductivity of InN NWs even with small diameters (86 nm – 47 nm) in contrast to GaN NWs has been reported [Cal07a].

A fully depleted NW acts as an insulator. According to the theory of space charge limited current, a $I \propto U^m$ relation with $m = 2 \ldots 3$ is found (**Fig. 6.2**). For a perfect insulator m equals 2, while traps lead to higher exponents [Ros55].

6.2. Sample preparation

For single NW measurements, the NWs were removed from their growth substrate by scratching and ultrasonic agitation while immersed in acetone. Drops of this suspension were transferred onto a insulating substrate. The NWs were then contacted by photolithography or e-beam lithography. A detailed step-by-step description is given in the Appendix (p. 147).

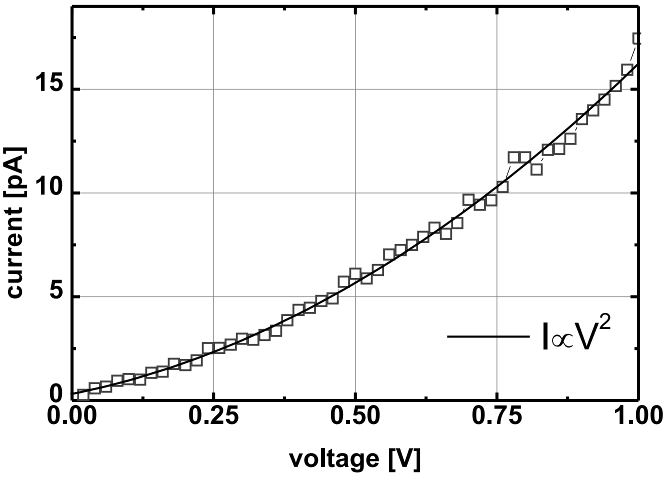

Figure 6.2: *I-V curve of a single GaN NW homogeneously doped with* T_{Si}*=1015°C (300507) after annealing at 660°C for 5 min. The data can be well reproduced by a* $I \propto U^2$ *fit (solid line).*

Ohmic Contacts For electrical measurements or applications, ohmic contacts to the semiconductor material are necessary. This often proves technologically challenging, especially for nanowires. Ohmic contacts can be seen as a special case of Schottky contacts with a low barrier height and thin space charge region. The barrier height is determined by choosing a suitable contact metal. If the space charge region is sufficiently thin, charge carriers can tunnel through the barrier. The transmission coefficient exhibits an exponential dependence of the barrier height and thickness. The tunneling current J_t is given by [Sze81]:

$$J_t \propto \exp\left(-\frac{2\Phi_{Bn}}{\hbar}\sqrt{\frac{\epsilon_s m^*}{N_D}}\right) \tag{6.1}$$

where Φ_{Bn} is the barrier height, m^* is the effective carrier mass, and ϵ_s the dielectric constant. Consequently, the tunneling current is increased with higher doping N_D.

Different approaches for reliable low resistive contacts on *n-type* GaN thin films are described in the literature:

- Ni/Au [Mot02, Sun02]
- Al/Ti [Lin94]
- Ti/Ag [Guo96]
- Ti/Al/Ti-W [Fer07]
- Ti/Al/Ti/Au [Mot03]
- Ti/Al/Ni/Ti [Fan96]
- Ni/Cr/Au [Kim97]

In all cases thermal annealing is needed after deposition. Following these considerations, first Ti/Al contacts and later Ti/Pt/Au contacts were used in this work. Ti results in a low barrier height. The Au top layer allows for low resistivity contact lines since Au has a higher specific conductivity than Ti. Furthermore, Au pads can be contacted using a gold wire bonder. Ti oxidizes easily e.g. during annealing even at low residual oxygen concentrations present in the vacuum annealing oven. Hence, a protective cap layer is necessary. The additional Pt layer is used as a diffusion barrier to avoid intermixing of Ti and Au during high temperature annealing. The maximum annealing temperature was set to 600°C, as a conductive layer was formed on the sample surface for temperatures at or above 680°C. This could either be due to melting or evaporation and redeposition of metal. On samples with photolithographically defined contact pads, layers of Ti/Pt/Au were evaporated with a thickness of the individual layers of 20 nm/20 nm/70 nm, respectively. Processing details and the mask layouts are listed in the Appendix (p. 147).

The width of the contact lines is 1 μm, and their maximal length 262 μm (the actual length depends on the position of the individual NW). This yields a maximum resistance of the Au layer alone ($\rho_{\mathrm{Au}} = 2.21 \times 10^{-8}$ Ωm) of 82 Ω. If the parallel resistances of the Ti layer of 6.41 kΩ ($\rho_{\mathrm{Ti}} = 4.27 \times 10^{-7}$ Ωm) and the Pt layer of 1.55 kΩ ($\rho_{\mathrm{Pt}} = 1.04 \times 10^{-7}$ Ωm) are also taken into account, the contact resistance is $\leq 77\,\Omega$. This value can be neglected in comparison to the NW resistance.

6.3. Si-doped GaN NWs for single wire measurements

For the measurements presented in this chapter relatively long NWs (typical lengths 2 μm) were grown to facilitate contacting. Different strategies were used to optimize the contact quality and reproducibility. Four different concepts were employed (**Fig. 6.3**), which are described in the following:

- **Homogeneously doped NWs:** For homogeneously doped NWs, two doping levels were investigated: low doping with $T_{\mathrm{Si}} = 900$°C ($\mathrm{BEP}_{\mathrm{Si}} = 4.6 \times 10^{-13}$ mbar; sample No. 181006), and moderate doping with $T_{\mathrm{Si}} = 1050$°C ($\mathrm{BEP}_{\mathrm{Si}} = 4.9 \times 10^{-11}$ mbar; sample No. 300507). The resulting *I*-*V* curves showed only low conductivity and were often asymmetric (diode-like). The sample-to-sample variations were larger than a possible trend with doping level. The current depended on the annealing procedure (duration and temperature).

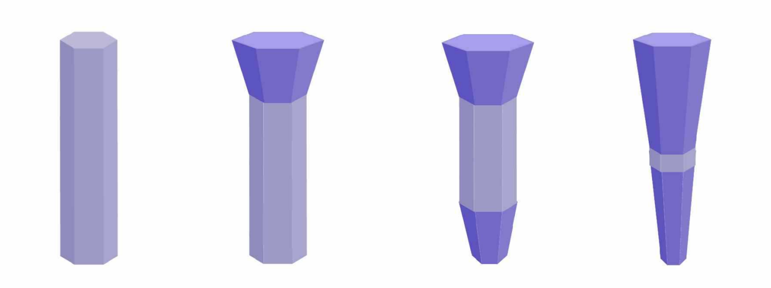

Figure 6.3: *Schematic drawing of the GaN NW structures. Heavily Si-doped regions are depicted as widening cones. The widening angle is exaggerated for clarity.*

- **Highly doped top end:** According to EELS spectroscopy on undoped NWs, the base part of the NWs is unintentionally Si-doped due to diffusion from the substrate as presented in **Fig. 3.9** (p. 43). Following the assumption that diode-like *I*-*V* curves could originate from this unintentional doping, NWs with a highly doped top end were grown. However, no improvement was achieved.
- **Both ends highly doped:** Since the approach above was insufficient, NWs with short highly doped regions at both ends (length approx. 250 nm) were grown.
- **Long highly doped ends:** Nanowires with longer contact regions were employed to guarantee a proper contact to the metal contact lines (width 1 µm, spacing 1 µm) without contacting the center region. The overall NW length was kept constant.

In the following, results from the two last strategies are discussed in detail.

6.3.1. NWs with short contact regions

All samples of this series exhibited highly doped end regions on both sides with $T_{\mathrm{Si}} = 1160°\mathrm{C}$ ($\mathrm{BEP}_{\mathrm{Si}} = 8.0 \times 10^{-10}$ mbar). The doping level in the center part of the NWs was varied (**Tab. 6.1**). Growth duration for all samples was 345 min, of which 50 min were used for the base part (“foot”) and 40 min for the top part (“head”). The base part growth duration was longer to account for the nucleation duration. In the following typical *I*-*V* curves are discussed. The measurements were performed at room temperature using a *Keithley 6517* voltage source and current meter. In the semi-logarithmic plots, the absolute value of the current is displayed.

NWs with a nominally undoped center part (sample 040408) exhibited diode-like behavior (**Fig. 6.4**). After annealing at 600°C in vacuum, the current was

Table 6.1: *Sample numbers, Si doping level given in BEP and effusion cell temperature, and NW lengths.*

Sample	Center doping BEP_{Si} $[10^{-11}]$ mbar	T_{Si} [°C]	NW length [µm]
040408	n.i.d.	–	2.26 ± 0.06
070408	2.2	980	1.70 ± 0.06
100408	7.0	1040	1.46 ± 0.05
140408	50	1120	1.91 ± 0.1

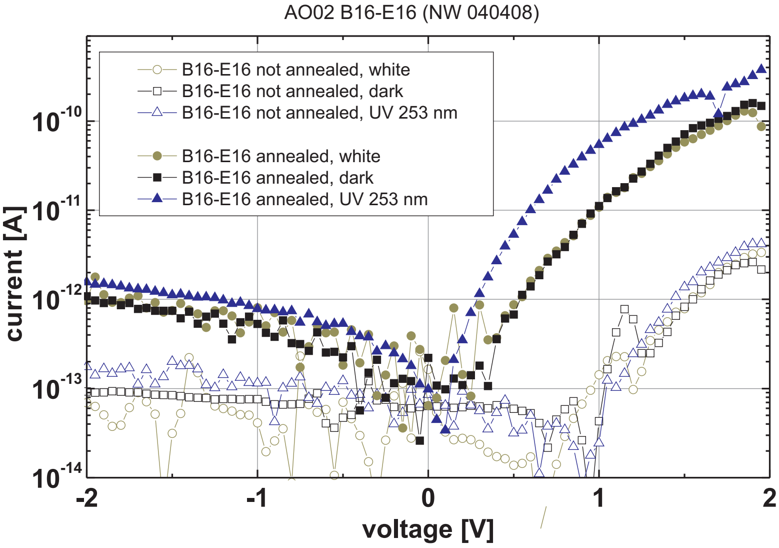

Figure 6.4: *I-V curves of a n.i.d. NW before and after annealing under different illumination conditions. The shift of the non-annealed curves is due to charging effects.*

increased by more than one order of magnitude. The curves were measured in dark, under white light (halogen lamp), and under UV illumination (253 nm = 4.9 eV, i.e. above the GaN bandgap), respectively. The current was clearly enhanced under UV illumination. Asymmetric *U-I* curves were observed.

For the first doping level (sample 070408) no increase in current was observed. At a doping level of $BEP_{Si} = 7 \times 10^{-11}$ mbar (sample 100408), the "forward" current was significantly increased. However, the diode-like asymmetry remained (**Fig. 6.5**). Illumination with UV light enhanced the current by about one order of magnitude.

Further increase of the doping level (sample 140408) lead to both a strong increase in current and a more symmetric curve. A high dark current was present, which was only slightly increased by UV illumination (**Fig. 6.6**). On a linear scale (inset), still a slight deviation from linear (ohmic) behavior was found. For higher

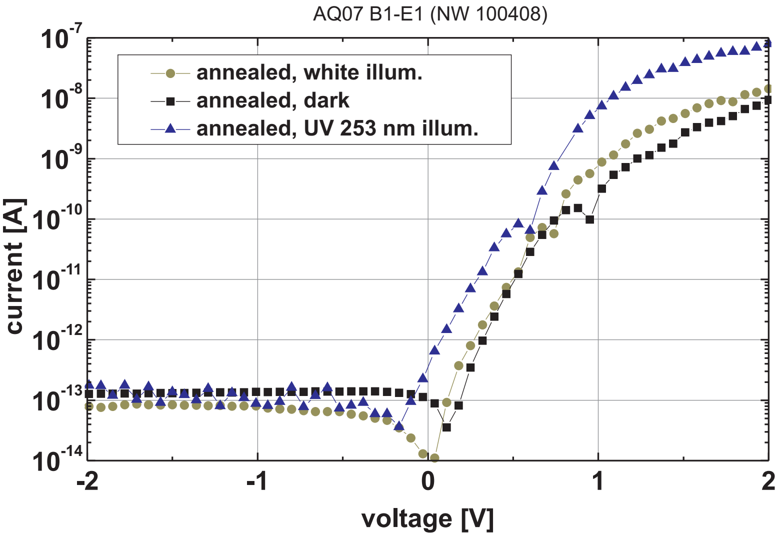

Figure 6.5: *I-V curve of a Si-doped NW (100408) after annealing under different illumination conditions.*

voltages the current increases stronger due to a reduction of the Schottky barrier height by the applied electrical field. With a contact distance of 1 µm and a potential of 2 V, the applied field is 20 kV/cm. Hence, the current density inside the NW is high: Under the assumption of a cylindrical wire with 100 nm diameter (cross sectional area $A = 7.5 \times 10^{-15}\,\mathrm{m}^2$) and the measured current of 0.45 mA at 2V, the current density is $j = 5.7\ \mathrm{MA/cm}^2$. This is considerably higher than technologically relevant current densities. For example, the first InGaN/GaN/AlGaN-based laser diodes demonstrated by Nakamura *et. al.* in 1998 had a lasing threshold current of 7 kA/cm^2 [Nak98]. For such high current densities, self-heating and heat dissipation become important. However, no damage or irreproducibility for repeated measurements on the same NW was observed.

The measured current values scattered over several orders of magnitude within one batch of samples processed simultaneously. Thus, reliable statements should only be given after statistical analysis of many NWs. However, despite the sample-to-sample variations, different regimes can be clearly discerned by comparison of the current at 1 V for single NWs with short contact regions(1) (see **Tab. 6.1**) of different doping levels (**Fig. 6.7**). For n.i.d. (040408, eight individual NWs were measured) and low Si-doped samples (070408, eight individual NWs were measured), the forward currents were in the range of $I = 1 \times 10^{-13}$ A to $I = 2 \times 10^{-11}$ A. The asymmetry factor (forward current divided by reverse current, both measured at 1 V) was in the range of 4 to 1000.

---

(1) As mentioned above, self-heating effects at the relatively high currents must be kept in mind. However, analyzing the currents at considerably lower voltages (e.g. 100 mV) was not feasible due to large differences in contact barrier height between individual NWs from one batch.

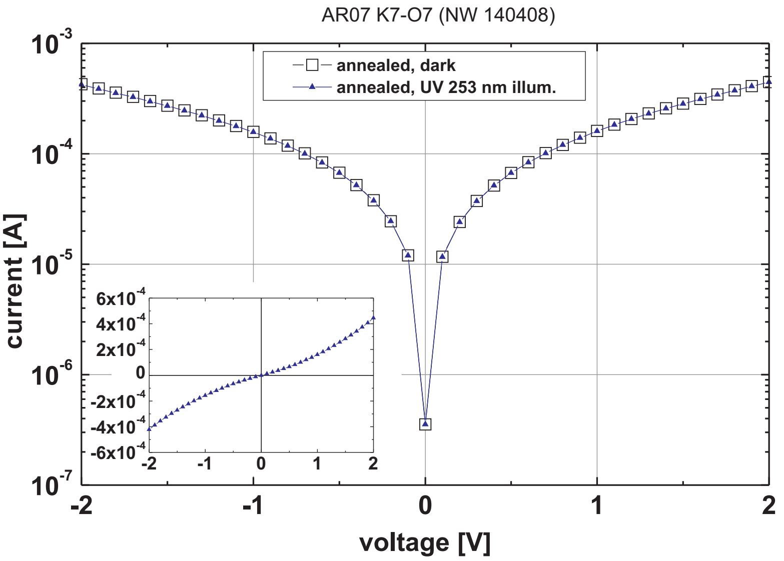

Figure 6.6: *I-V curve of a highly Si-doped NW (140408) after annealing under different illumination conditions. Inset: I-V curve under UV illumination on a linear scale.*

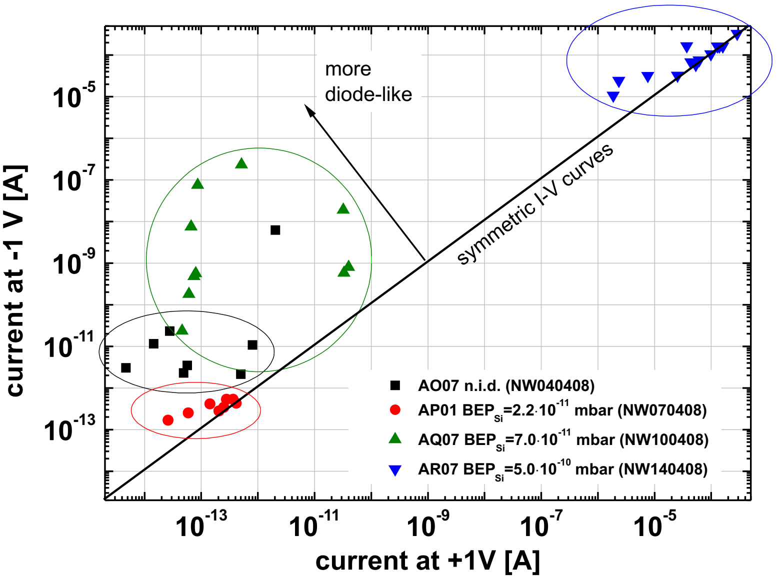

Figure 6.7: *Forward and reverse currents at ±1 V of several individual NWs with four different doping levels measured under white illumination at room temperature.*

Table 6.2: *Average dark current (I_{dark}) and current increase under UV illumination (photocurrent, $I_{UV} - I_{dark}$) measured at +1 V as function of doping.*

Sample No.	Center doping BEP$_{\mathrm{Si}}$ [10^{-11} mbar]	T$_{\mathrm{Si}}$ [°C]	Dark current [A]	Photocurrent [A]
040408	n.i.d.	-	$(7\pm18)\times10^{-10}$	$(2.4\pm1.1)\times10^{-11}$
070408	2.2	980	$(3.9\pm1.4)\times10^{-13}$	$(1.3\pm1.7)\times10^{-11}$
100408	7.0	1040	$(2.1\pm6.0)\times10^{-8}$	$(3.4\pm7.5)\times10^{-8}$
140408	50	1120	$(1.1\pm1)\times10^{-4}$	$(3.4\pm3.0)\times10^{-6}$

For moderately doped samples (100408, ten individual NWs were measured) the currents were in the range of $I = 2\times10^{-11}$ A to $I = 3\times10^{-7}$ A. The asymmetry factor was between 10 and 7×10^5. For highly doped samples (140408, thirteen individual NWs were measured) the currents were in the range of $I = 2\times10^{-6}$ A to $I = 4\times10^{-4}$ A. The asymmetry factor was between 1 and 10, i.e. these structures exhibited a relatively symmetric behavior. These results show that by doping the NW conductivity can be modified within eight orders of magnitude.

For all doping levels – except the highest – the current was increased under UV (253 nm) illumination typically by a factor between 2 and 40 compared to the current in darkness (**Fig. 6.8**). For the highest doping level only a weak photo-induced relative current increase of 2.2% ± 1.1% was recorded. However, the dark current in these samples was already at least two orders of magnitude higher than for the best conducting samples of smaller doping level. The average dark current and UV-induced current increase ($I_{UV} - I_{dark}$) for the different doping levels is listed it **Tab. 6.2**. The absolute value of the photocurrent was stronger in higher doped samples. However, due to the increased dark current, the relative increase is lower.

Spectrally resolved photocurrent Illumination with light whose energy is above the GaN bandgap generates electron-hole pairs which additionally contribute to the conductivity. In **Fig. 6.9** the spectrally resolved photocurrent of a single n.i.d. NW (040408) is shown for temperatures between 86K and room temperature. The sample was kept in vacuum ($p \leq 3\times10^{-6}$ mbar) and illuminated with the spectrally dispersed light of a xenon lamp. The photocurrent was measured by the voltage drop over the NW in lock-in technique. For that, the incoming light was chopped with a frequency of 18 Hz and the chopper signal was used as the reference for a lock-in amplifier to amplify only that signal compo-

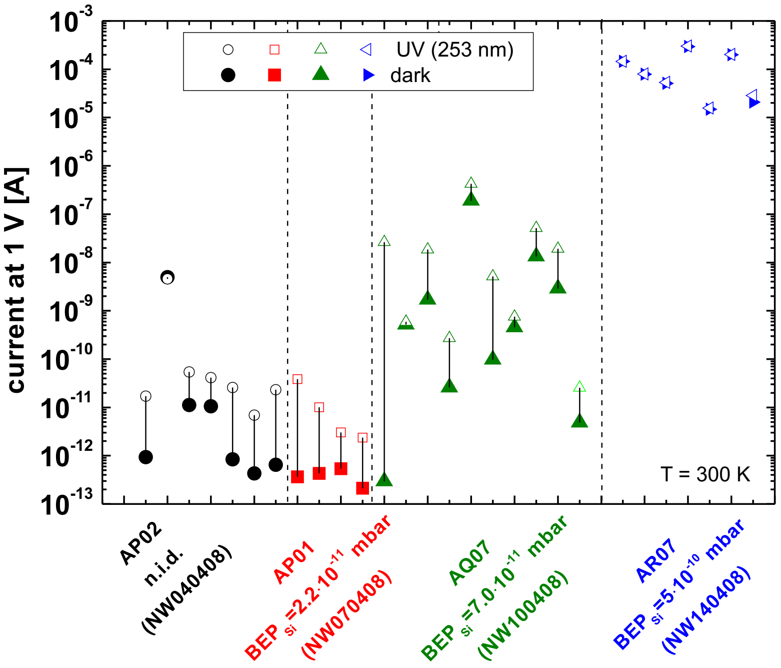

Figure 6.8: *Dark current (full symbols) and current under UV illumination (open symbols) for different nanowire doping levels. (Same samples as in* ***Fig. 6.7****.)*

nent which varies with the chopper frequency. Therefore, only the light-induced current is recorded and the constant dark current background is suppressed.

A sharp onset of the photocurrent was observed at 3.45 eV, the bandgap of GaN, proving that this current is generated by the photo-generation of charge carriers inside the NWs. For lower energies, the signal intensity lies within the noise level. In this spectral range, the phase signal fluctuated strongly, proving that no real signal was measured. Whereas in the rage of 86K to 150K the magnitude of the photocurent stayed constant, it was reduced for increasing temperature due to enhanced electron-hole recombination. The density of photogenerated carriers (i.e. the intensity of the photocurrent) is inversely proportional to the recombination rate. Using a thermally activated recombination rate, the photocurrent is proportional to $1 - \exp\left(\frac{E_a}{k_b T}\right)$. An activation energy of $E_a = 33\,\mathrm{meV}$ could be extracted (**Fig. 6.9b**).

Model for diode-like behavior In spite of the fact that both ends of the NW were highly doped, most of the I-V curves (except those for the highest doping level) exhibited a pronounced asymmetry. This can be explained by considering the position of the metal contact pads on the NW. If the metal is in contact with both the highly doped end and the weaker doped center part, a depletion zone may be formed under the contact area in the weaker doped part (**Fig. 6.10**). This

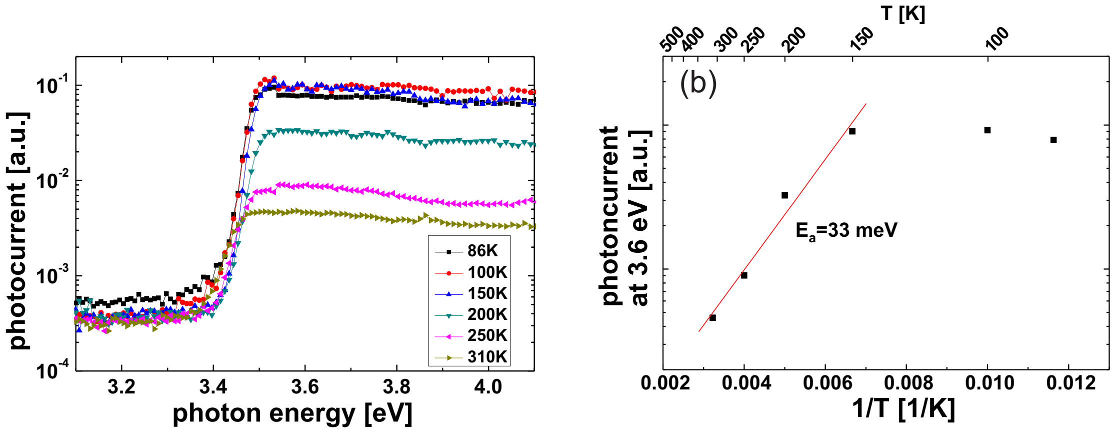

Figure 6.9: *(a) Spectrally resolved photocurrent signal for a single n.i.d. GaN NW measured at different temperatures under vacuum. (b) Photocurrent at 3.6 eV as function of inverse temperature.*

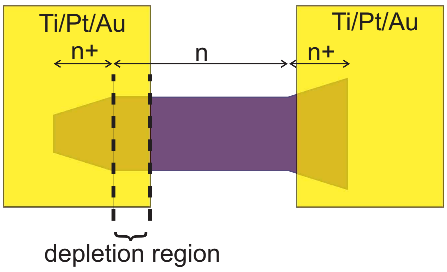

Figure 6.10: *If the weaker doped center part of the NW is also contacted, a depletion zone may be formed underneath.*

contact can act as a Schottky contact which leads to diode-like I-V characteristics. In the NWs with the highest doping level, the carrier concentration in the center part is already high enough to form an ohmic contact.

NWs with low and moderate Si doping levels exhibited interesting properties. The reverse current was relatively low and an electrical breakthrough was not observed even for high voltages up to 50 V. **Fig. 6.11** shows an I-V curve of a NW with a doping level of $\mathrm{BEP_{Si}}=7\times10^{-11}$ mbar (NW100408).

Since the gap between the two contact lines is 1 µm, an electric field of 50 MV/m is present for a voltage of 50 V. This is still well below the breakthrough field strength of GaN of 300 MV/m [BJ99]. The observed behavior could possibly be explained by a Schottky diode with a parallel current path. For undoped or weakly doped GaN NWs full depletion is assumed in the area under the metal contact. Here, the current is space-charge limited (SCL current) [Ros55, Lam56, Lam70]. In contrast to an Ohmic conductor ($I \propto U$), the current no longer increases linearly, but with $I = K_{SCL} \cdot U^m$ with a material-dependent constant K_{SCL}. When an

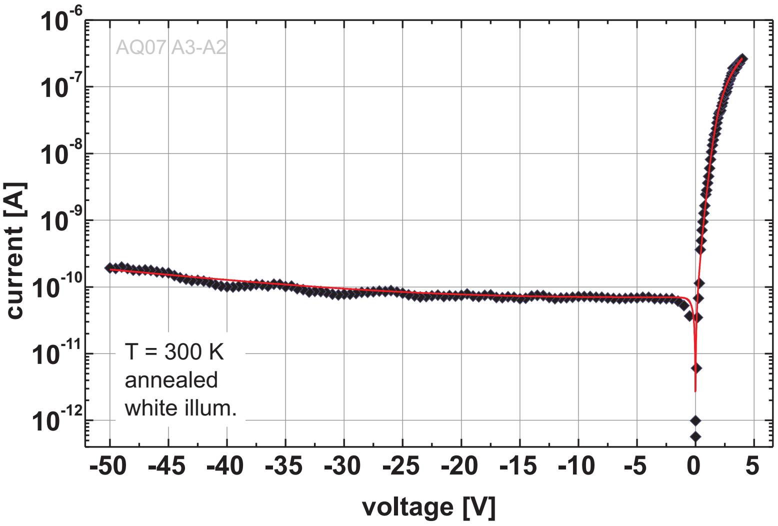

Figure 6.11: *I-V measurement (black symbols) of a NW with BEP*$_{\mathrm{Si}}$=7×10^{-11} *mbar (NW100408) under illumination with white light and a fit (red line) according to **Eq. 6.2**.*

additional voltage drop is considered at a serial resistance R_s, the current I is determined by:

$$I = I_0 \left(\exp \left(\frac{e}{nk_bT} (U - R_s I) \right) - 1 \right) + K_{SCL} (U - R_s I)^m \tag{6.2}$$

The measured data can be reproduced by this equation using an ideality factor $n = 10$, $I_0 = 7 \times 10^{-11}$ A, $K_{SCL} = 9 \times 10^{-16}$ A V^{-3}, $R_s = 7 \times 10^6\,\Omega$, and $m = 3$ (**Fig. 6.11**). The exponent $m \neq 2$ indicates the presence of traps in the bandgap or a field-dependent mobility. The large ideality factor n might possibly originate from the not abrupt border of the space charge region. The metal contacts do not fully surround the NW (no metal is below the NW) leading to an inhomogeneous depletion zone. However, the underlying mechanism could not be clarified by these measurements.

6.3.2. NWs with long contact regions

To overcome the problem discussed above, the highly doped contact regions of the NWs were extended to avoid direct contact between the center part of the NW and the metal contacts. The growth duration for base, center, and top part was 180 min, 55 min, and 110 min, respectively, resulting in the same overall growth duration as for the structures with short contact regions. The Si flux for both end regions was identical (T$_{\mathrm{Si}}$ = 1160°C, BEP$_{\mathrm{Si}}$ = 8.0×10^{-10} mbar). Sample numbers and doping levels are summarized in **Tab. 6.3**.

Table 6.3: *Sample numbers, Si doping levels given as BEP and effusion cell temperature, and NW lengths for the samples with long contact regions.*

Sample No.	Center doping BEP_{Si} [10^{-11} mbar]	T_{Si} [°C]	NW length [μm]
180708	-		1.65 ± 0.08
180608	2.2	980	1.51 ± 0.09
130508	7.0	1040	1.81 ± 0.08

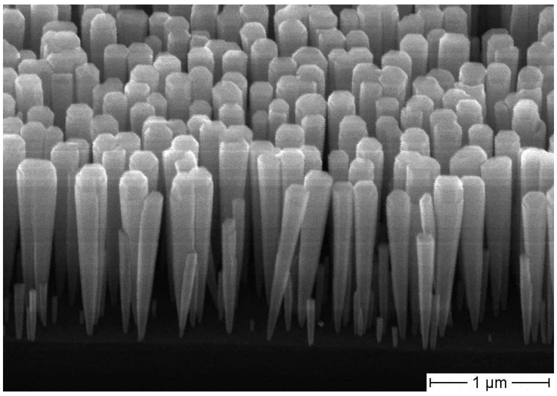

Figure 6.12: *SEM image of a cleaved edge of sample 130508 recorded at 45° inclination.*

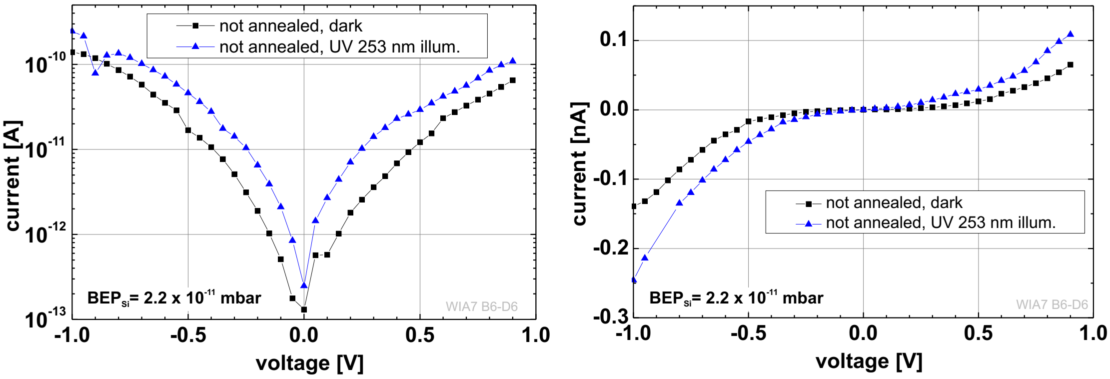

Figure 6.13: *I-V curves of a weakly doped single NW (sample 180608) measured in darkness and under UV illumination (253 nm wavelength), in logarithmic scale (left) and linear scale (right).*

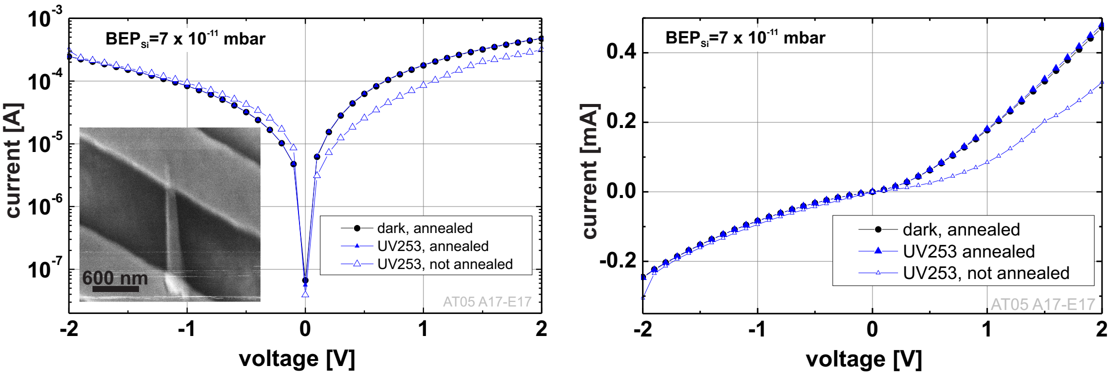

Figure 6.14: *I-V curves of a single strongly doped NW (sample 130508) measured in darkness and under UV illumination, logarithmic scale (left). The inset shows a SEM micrograph of the contacted wire. Right: Linear scale.*

Generally, high Si fluxes lead to a morphological change of the NWs from the prismatic shape to widening cones accompanied by a reduction of the axial growth rate (see Section 4.1 and Fig. 4.3, p. 64). Therefore, the average NW length compared to NWs with short contacts is reduced. To avoid a high degree of coalescence due to the widening of the NW diameter, the nucleation density was reduced. For that, a relatively high substrate temperature of 790°C was chosen (the same as for the short contact NWs) to achieve a delayed NW nucleation (see Section 3.2.2). After 40 min, the substrate temperature was increased by 15°C to prevent further nucleation. A SEM image of the as-grown NWs is shown in **Fig. 6.12**.

Typical *I-V* curves are compared for a weakly doped NW (**Fig. 6.13**) and a highly Si-doped NW (**Fig. 6.14**). In contrast to NWs with short contacts, no annealing was necessary for most samples, as annealing did not increase the current. As for the weakly doped samples with short contact regions, the current was increased under UV illumination.

The asymmetry of the *I-V* curves could be significantly reduced employing long contact regions. The strongest improvement was achieved for NWs with undoped or weakly doped center part (**Fig. 6.15**). For undoped NWs, the asymmetry factor was between 1 (symmetric) and 350. For the doped samples, the asymmetry factors were lower (maximum of 30, average around 4).

6.4. E-beam assisted contacting

For this work, NWs were not only contacted by photolithography, but also by e-beam assisted platinum deposition. This technique allows to contact individual NWs which were dispersed on Si wafers with a SiO_2 insulating layer. Details of the sample preparation are described in the Appendix (p. 147). The samples

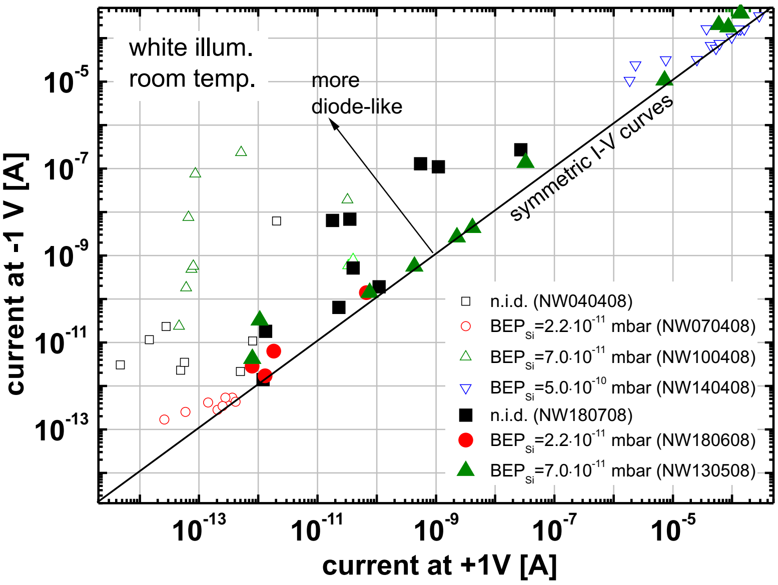

Figure 6.15: *Forward and reverse currents for NWs with short contact regions (open symbols, same data as in* ***Fig. 6.7****) in comparison to NWs with long contact regions (full symbols) with the same doping levels in the center part.*

were transferred into a SEM system with an add-on that allows to introduce a metal-organic Pt compound gas through a thin nozzle which can be placed in close vicinity to the sample surface (Manufacturer: *Carl Zeiss*). The e-beam dissociates the gas and metallic Pt is deposited on the desired spots on the sample (**Fig. 6.16**). Each contact has to be written individually for each NW limiting the overall throughput. In this setup, only a Pt precursor could be used. Generally, due to its work function, Pt forms Schottky contacts on n-type GaN. The recorded *I*-*V* curves clearly reveal this Schottky barrier behavior (**Fig. 6.16**). Typical *I*-*V* curves for a highly and moderately doped NW are shown in **Fig. 6.16** and **Fig. 6.17**, respectively.

A comparison of reverse and forward currents for NWs which were contacted by photolithography as well as by e-beam-assisted Pt deposition is shown in **Fig. 6.18**. Only NWs with short end regions were used. The reverse current at -1 V is plotted as a function of the forward current at +1 V. For the higher doped samples, the current at 1 V in the e-beam-assisted NWs is systematically smaller than in the photolithographically contacted NWs. This is due to the Schottky barrier behavior of the Pt contacts. For higher voltages, the difference is less pronounced.

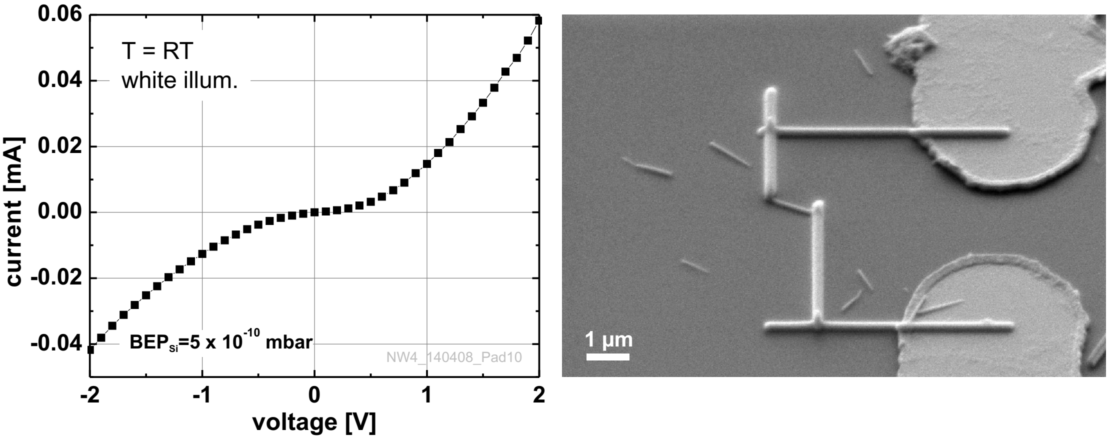

Figure 6.16: *Left: I-V measurement at a single NW with highly Si-doped center part (140408) contacted with e-beam-assisted Pt deposition. Right: Corresponding SEM image. The large contacts in the right part of the image were done photolithographically in a previous step.*

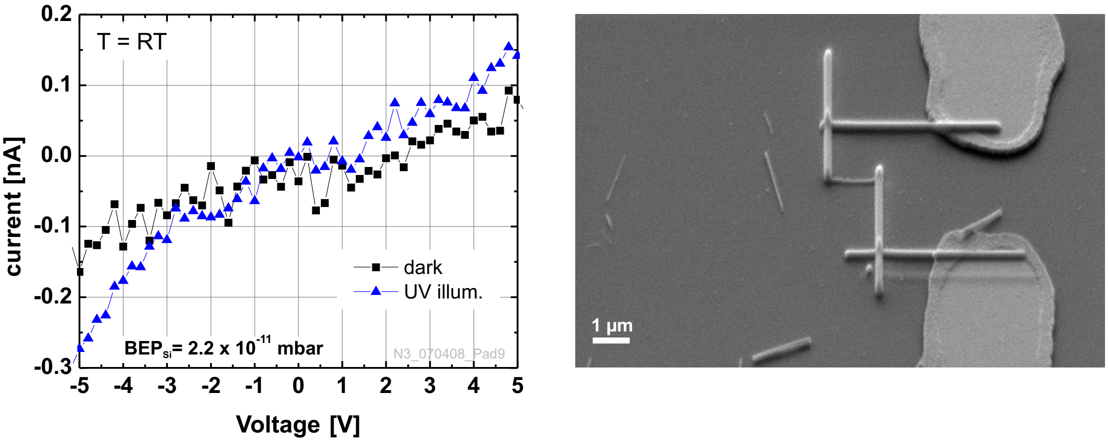

Figure 6.17: *Left: I-V measurement at a single NW with moderately Si-doped center part (070408) contacted with e-beam-assisted Pt deposition. Right: Corresponding SEM image.*

6.5. Conclusions

Contacting of single NWs is technologically highly demanding. The current technology (µ-technology) does not prove to be suitable for nanowires. Photolithograpy – the standard semiconductor manufacturing technology – does not provide sufficient reproducibility and yield. Also e-beam or FIB (focused ion beam) technology needs specific improvement. New approaches like dielectrophoretic alingment (self-alignment of NWs that are dispersed in liquids using AC electric fields) need to be investigated [Hua01, Hua05]. The dielectrophoretic alignment procedure and results obtained with the NWs presented in this work are shown in [Sta08].

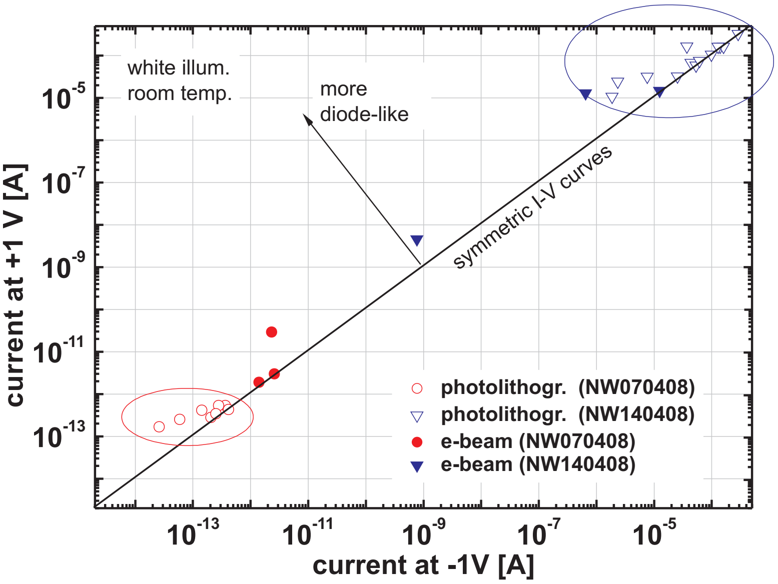

Figure 6.18: *Comparison of forward and reverse current for NWs contacted by photolithography (open symbols, same data as in **Fig. 6.7**), and similar NWs contacted with e-beam-assisted Pt deposition (full symbols).*

Additionally the NWs have to be tailored appropriately with respect to size and doping levels. In this work it could be demonstrated that the metal-NW contacts can be improved by highly doped contact regions.

The large variance between individual NWs even from one growth sample is not only critical for possible applications, but also impairs the interpretation of the results presented here. Especially the diode-like behavior in these purely n-type doped structures is not satisfactorily understood. Nevertheless, it was proven by individually contacted NWs with different Si doping levels that the conductivity can be varied within several orders of magnitude. At the highest currents self-heating effects due to the high current density must be kept in mind. The measured currents were in the range of 10^{-12} A to 10^{-4} A at 1 V.

7. GaN nanodisks embedded in AlGaN/GaN NWs

Nanodisks (NDs) in NWs can be seen as an analogy to quantum wells in thin films. During thin film growth, a quantum well can be formed in a stack of layers by a sufficiently thin layer (a few nm) of the material with lower bandgap energy (E_{Gap}) in between two layers of the higher bandgap material (barrier). Accordingly, the insertion of a material with lower E_{Gap} during NW growth forms a nanodisk. Whereas the axial dimension can be controlled by the growth duration of the ND on a single monolayer (ML) level, the lateral dimension is defined by the NW diameter which is typically in the range of 15 nm to 100 nm for the NWs presented here. The difference in strain and strain relaxation mechanisms as well as the exposure of the ND sidewall leads to different properties compared to thin films.

This chapter focuses on the structural and optical characteristics of GaN/AlGaN nanowire heterostructures (NWHs). GaN/Al(Ga)N NWHs with embedded GaN nanodisks were fabricated using the same techniques as the GaN NWs presented in the previous chapters.

By changing the composition of the $Al_xGa_{x-1}N$ barrier or the thickness of the GaN ND, the PL emission energy is modified. For low and moderate Al concentrations, the emission energies increase with increasing Al content due to better confinement. The temperature stability improves and becomes comparable to that of quantum dots, which are known to be superior to quantum wells [Gui06]. This makes these structures usable as optical sensors for gas detection at room temperature or elevated temperatures, exploiting the higher sensitivity of nanowire heterostructures compared to thin films for gases like oxygen [Teu11]. Surface treatments e.g. covering the NWs with a thin Pt layer can be used to change the response selectively to hydrogen.

However, for high Al concentrations (above 30% – 35%) the emission energy decreases again mainly due to internal electric fields (quantum-confined Stark effect). Furthermore, the temperature stability decreases.

Generally, the emission properties are strongly affected by the strain state of

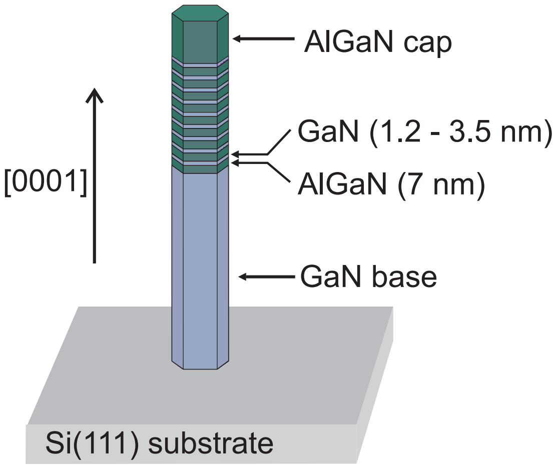

Figure 7.1: *Schematic drawing of GaN nanodisks embedded in a GaN/*$Al_xGa_{x-1}N$ *nanowire.*

the structures. Lateral growth of the barrier material for samples with AlN or $Al_xGa_{x-1}N$ with high Al content leads to the formation of a shell. Its thickness decreases from the bottom to the top part of a multi-nanodisk structure. Due to shading effects between adjacent NWs the shells are not perfectly homogeneous from wire to wire. Additionally, the results from three-dimensional numerical simulations using the actual nanodisk dimensions are presented and compared with measurements.

7.1. Sample design

For the formation of nanodisks, a base region of GaN nanowires with a length of 350 nm to 400 nm was grown on Si(111), directly followed by the growth of the quantum well structure (ND region). The resulting diameters of the individual NWs are distributed in the range of 25 nm – 50 nm. A nine-fold GaN nanodisk stack (i.e. multi quantum well, MQW) with the same nominal thickness for each ND in the stack was formed between barriers (spacers) of 7 nm AlN or $Al_xGa_{x-1}N$ in different compositions (**Fig. 7.1**). The ND thickness was varied in the range of 1.2 nm – 3.5 nm. The growth was finished with a 20 nm cap layer of the barrier material. The respective dimensions were determined by HRTEM analysis(1).

A constant substrate temperature of 775°C was used for the whole NW heterostructure. The substrate temperature was optimized for GaN NW growth (see Sec. 3.1). The temperature of the Ga effusion cell was kept constant at 1012°C

---

(1) TEM analysis shown in this chapter was done at the University of Barcelona (Dept. Electrònica) by the groups of Prof. Joan Ramon Morante and Prof. Jordi Arbiol

Table 7.1: *Al effusion cell temperatures, corresponding beam equivalent pressure (BEP), and Al content x. The Al content x was determined by $x = BEP_{Al} / (BEP_{Al} + BEP_{Ga})$ with $BEP_{Ga} = 3.9 \times 10^{-7}$ mbar for all samples. Additionally, the PL peak emission energy (at 4K) and the corresponding Al content of the reference samples without NDs is given.*

T_{Al} [°C]	BEP_{Al} [mbar]	x from BEP ratio	PL peak energy [eV]	x from PL peak position
1020	1.40×10^{-8}	0.03	3.52	0.03
1030	1.66×10^{-8}	0.04		
1056	3.30×10^{-8}	0.08	3.60	0.08
1074	4.70×10^{-8}	0.11		
1092	6.50×10^{-8}	0.14	3.67	0.13
1110	9.70×10^{-8}	0.20		
1130	1.40×10^{-7}	0.26	3.99	0.28
1150	2.00×10^{-7}	0.34		
1160	2.30×10^{-7}	0.37		
1170	2.70×10^{-7}	0.41		

($BEP_{Ga} = 3.9 \times 10^{-7}$ mbar) in both the GaN regions and in the AlGaN barriers. For the formation of AlN barriers, the Al cell was operated at a temperature of 1185°C ($BEP_{Al} = 1.5 \times 10^{-7}$ mbar). For the AlGaN samples, Al was additionally supplied to the Ga flux at cell temperatures between 1056°C and 1170°C. The BEPs (beam equivalent pressures), corresponding Al concentrations x, and sample numbers are listed in **Tab. 7.1** and **Tab. 7.2**, respectively.

The Al content was determined by two methods: First, the ratio of the BEP_{Al} to BEP_{Ga} was measured by a Bayard–Alpert flux gauge which was positioned directly under the wafer inside the MBE chamber (see Sec. 2.2, p. 22). Second, by evaluating the PL spectrum of reference samples. For this purpose, additional NW heterostructures with 100 nm AlGaN on top of the GaN base part instead of the MQW structure were grown. The Al content was then calculated from the position of the AlGaN PL peak using Eq. 1.1 (p. 11) assuming a bowing parameter of b = 1.3 eV [Ang97]. In the following, the Al concentrations x according to the BEP ratio are used (**Tab. 7.1**), which are in good agreement with the optical measurements.

Low Ga flux samples To realize a reduced Al(Ga)N shell thickness for high Al concentrations, one set of samples was grown with the Ga flux reduced to 40% of the previous value. For this, the Ga effusion cell temperature was reduced

Table 7.2: *List of samples discussed in this chapter. See also* **Tab. 7.1**.

T_{Al} [°C]	x from BEP ratio	sample No. ND-sample	sample No. ref. sample
1020	0.03		010207
1056	0.08	250908	050207
1074	0.11	290808	
1092	0.14	050908	270207 270808 220908
1110	0.20	110908	
1130	0.26	120908	250609
1150	0.34	021008	
1170	0.41	011008	

from T_{Ga}= 1012°C to T_{Ga}= 965°C during growth of the ND part, resulting in a reduction of the total metal flux and, thereby, reducing the lateral growth. The obtained structures allow us to discriminate between effects of the shell, the ND thickness, and the variation in the barrier concentration.

7.2. Structural characterization

Lateral growth For samples with AlN or AlGaN barriers of high Al content, radial growth of an AlN or AlGaN shell was observed. This has already been reported in Refs. [Ris05a] and [Tch08] for samples with AlN barriers. In our case the radial growth rate was 11% of the axial growth for AlN (see **Fig. 7.2a-c**) and (5 ± 2) % for $Al_{0.41}Ga_{0.59}N$ (see **Fig. 7.2d**). Due to the resulting increase in NW diameter, the diameters of the following NDs in the stack were gradually increased, whereas the thickness of the individual NDs remained constant. The lateral growth rate depends on the growth details (e.g. it was 35% in Ref. [Tch08]). In contrast to Ref. [Tch08], no indication of lateral GaN growth was found. It could be efficiently suppressed by the high growth temperatures applied in this work.

If the growth conditions for the nanodisk stack are modified by reducing the total metal flux as described above, the lateral growth is reduced, shown in **Figs. 7.2e and f** for a sample with an estimated Al concentration(1) of $x = 0.72$ (T_{Al} = 1160°C) and a ND thickness of 2.5 nm (250110). The radial growth rate was 5% of the axial rate, which is equal to the rate observed already at $x = 0.41$

---

(1) See p. 110 for an explanation how the Al content has been estimated.

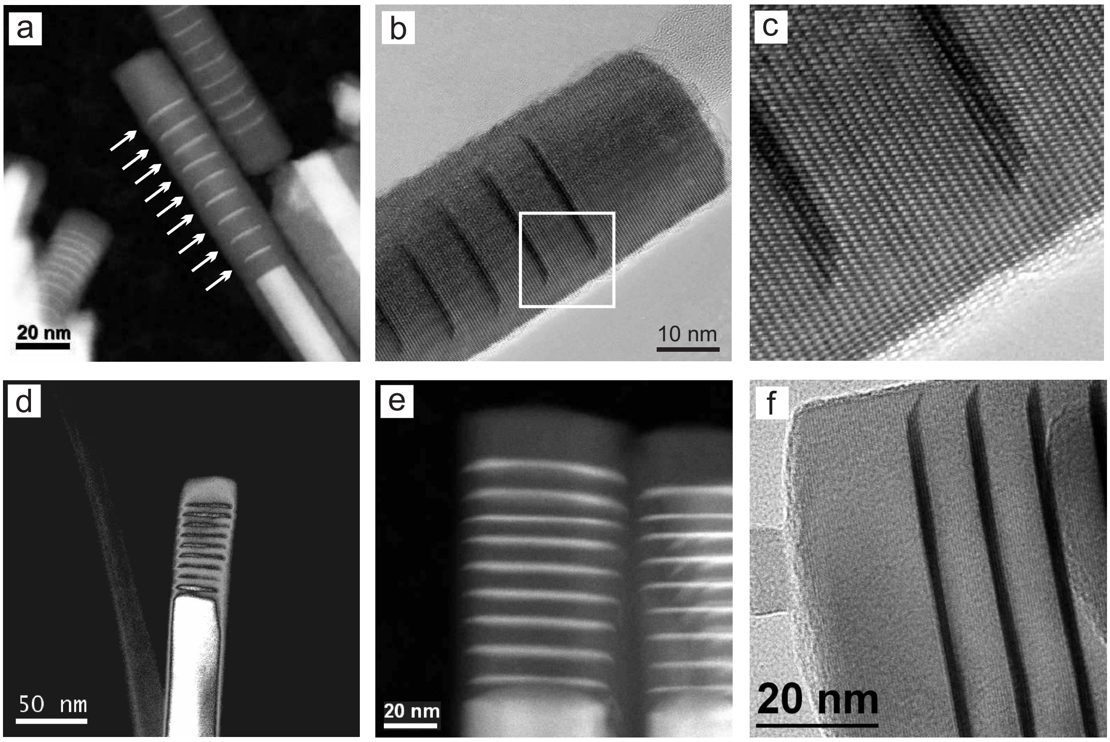

Figure 7.2: *(a) HAADF (high angle annular dark field) TEM image of nanowires with 9-fold 1.7 nm thick GaN nanodisks embedded in AlN barriers. The GaN appears bright, the surrounding AlN dark. (b) HRTEM image (bright field) of the same sample. The ND diameter increases towards the top. (c) Detail view of b. (d) HAADF contrast-enhanced image of a NW with 41% Al in the barrier. (e) HAADF image of a sample with an Al content of approx. 72% grown with reduced Ga flux. (f) HRTEM detail image of the sample from image e.*

for those samples grown at regular metal flux, showing that the lateral growth was efficiently reduced. However, for samples grown at $T_{\mathrm{Al}} = 1202°\mathrm{C}$ abrupt widening was observed, demonstrating that N-rich conditions are crucial to maintain the NW morphology.

From the results described above it is not certain whether the shell consists of pure AlN or AlGaN with the same composition as in the barriers. No contrast difference between the barriers and the shell was observed by TEM, giving evidence that there is no (strong) difference in composition. However, due to the high sticking coefficient of Al and a high Ga adatom mobility and desorption, Al enrichment is not unlikely.

While the GaN core exhibits the shape of a hexagonal prism with $\{10\bar{1}0\}$ planes (*m-planes*) as lateral facets, the AlN shell shows a rounded cross-section (**Fig. 7.3**). The difference in the cross-section of the prismatic GaN NW core and the cylindrical AlN shell directly reflects the difference in surface diffusivity. Accordingly,

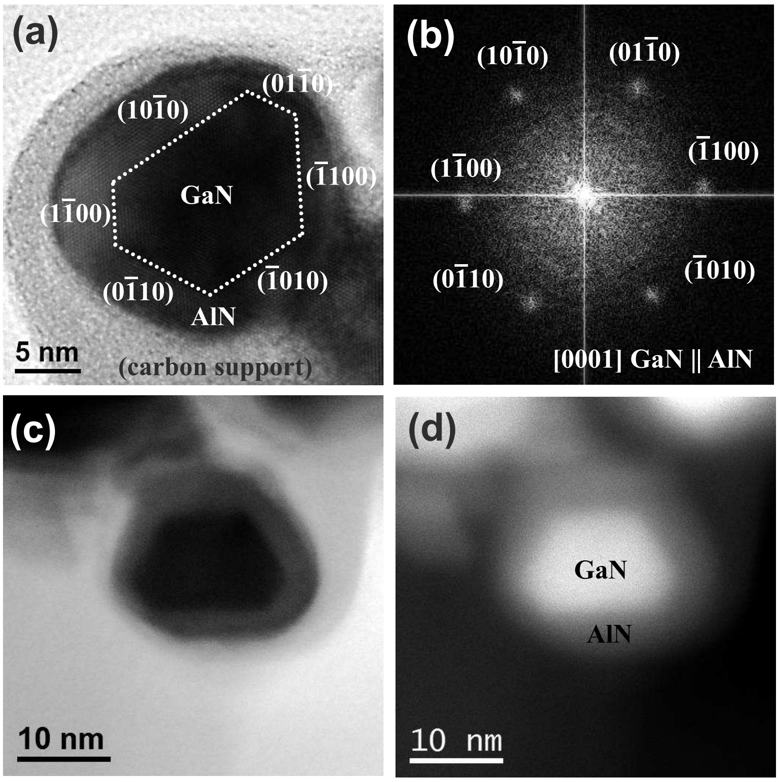

Figure 7.3: *TEM cross-section of a GaN NW with AlN shell (sample 100708). (a) The GaN core forms a hexagonal prism with* $\{10\bar{1}0\}$ *planes (m-planes) as lateral facets. The surrounding AlN shell is more cylindrical with rounded facets. (b) Corresponding SAED pattern, proving that the sidewalls are m planes; (c) Bright field TEM image; (d) corresponding HAADF TEM image.*

the mobile Ga adatoms either desorb or are incorporated on those crystal facets which allow minimization of the surface energy under the present growth conditions. In the present case this facet is the *c-plane*, since no lateral GaN growth was observed. The surface thermodynamics were found to be anisotropic for Ga adatoms (see also Sec. 3.5, esp. 58). Contrarily, Al adatoms exhibit a high sticking coefficient and a low mobility at the growth temperatures applied here and are therefore incorporated on the spot where they impinge.

Nanodisk shape The GaN/Al(Ga)N interfaces were sharp without signs of Ga-Al interdiffusion, except for fluctuations on the single monolayer scale. On the outer edges the disks were slightly faceted. The same facets were observed for the Al(Ga)N cap layer (**Fig. 7.2b,c**). According to the inclination angles determined from TEM images, these facets were attributed to $\{10\bar{1}n\}$ facets with mainly $n = 2$ (angle towards GaN $\{10\bar{1}0\}$ plane: 46.8°) and in some cases (see AlN cap in **Fig. 7.2b**) also $n = 3$ (angle towards $10\bar{1}0$: 58.0°). Faceting has also sometimes been observed at the top of pure GaN NWs in samples analyzed in this work. The shape of the ND stack follows the shape (i.e. the faceting) of the NW base part. Nanodisk faceting has also been mentioned in Ref. [Ris05a], where it was referred to as “lateral layer bending” without giving further details or assignment to specific crystallographic planes.

Nanodisk and spacer heights The ND and spacer (barrier) heights in the AlGaN series were determined by high angle annular dark field (HAADF) images. Since the Ga flux was kept constant throughout the growth and Al was additionally supplied for barrier growth, an increasing barrier thickness with increasing Al concentration was expected. For the highest Al concentration ($x = 0.41$), the additional flux should cause an increase of 3 nm to 4 nm in barrier thickness compared to the sample with the lowest Al concentration. However, a well-to-well distance of 7.4 ± 0.5 nm was found, which, within the measurement uncertainty, is equal to the samples with T_{Al} = 1092°C and 1130°C (8.5 ± 0.6 nm and 8.7 ± 0.6 nm, respectively). The absence of a higher axial growth rate might be explained by lateral growth which is present for the AlGaN part in the T_{Al} = 1170°C sample.

As an effect of the lateral growth, a constant decrease in spacer height was observed for the GaN/AlN samples from bottom to top of the ND stack. For sample 100708 (**Fig. 7.2a**) the spacer height was 7.4 nm between GaN base and ND 1, and 6.0 nm between ND 8 and ND 9, which equals a reduction of 19%. The average spacer height was 6.5 nm. For the $Al_{0.72}Ga_{0.28}N$ sample grown under reduced flux (250110), this effect was less pronounced (**Fig. 7.2e**). The spacer height was reduced by 9% from 7.1 nm (bottom of ND stack) to 6.5 nm (top of ND stack), with an average spacer height of 6.8 nm.

This indicates diffusion of Al adatoms from the sidewalls to contribute to the axial growth rate. This effect decreases for larger NW diameters since the NW sidewalls area scales with the NW radius r, while the top surface scales with r^2 (assuming a cylindrical wire), leading to a reduced axial growth rate for thicker NWs. Accordingly, diffusing adatoms from the sidewall are distributed on a larger top surface. In contrast to Ga adatoms, it is unlikely for Al adatoms to desorb, due to their high sticking coefficient. Thus, they can be either be incorporated on the spot where they impinge, or diffuse to the top or to lower parts of the sidewall.

For those samples grown at a reduced Ga flux, the GaN ND growth duration was adjusted by the ratio between the standard and reduced Ga flux (1 : 0.4). For sample 250110, a ND height of 3.5 nm was expected for 70 sec of ND growth. However, the measured ND height was (2.0 ± 0.2) nm, which is only 57% of the expected value. This gives evidence for significant desorption, which is a function of substrate temperature rather than the impinging flux. (For the samples grown at standard Ga flux, the relative influence of desorption is lower. Therefore it is understandable that no significant differences between the Al content calculated by flux ratios and the Al content evaluated by PL measurements at reference samples is found.) For the samples grown at the standard Ga flux ($T_{Ga} = 1012°C$), the GaN growth rate was 7.5 nm/min, but only 1.7 nm/min for the low Ga flux samples. Under the assumption that the growth rate depends linearly on the Ga flux (justified by N-rich growth conditions), the effective Ga flux is $1.7/7.5 = 0.23$. This means that only 23% of the Ga flux compared to the standard conditions were present, although the impinging Ga flux was still 40% of the standard flux. For the low Ga flux samples the effective Ga flux is therefore 3.9×10^{-7} mbar $\cdot\, 0.23 = 0.88\times 10^{-7}$ mbar. For the samples grown at $BEP_{Al} = 2.3\times10^{-7}$ mbar (T_{Al}=1160°C), the Al content is calculated to $2.3/(2.3+0.88)=$ 72%. PL Measurements on a reference sample with thick AlGaN part did not show any AlGaN-related luminescence. Since the employed setup illuminates the sample at 244 nm (5.1 eV), corresponding to the bandgap of $Al_xGa_{x-1}N$ with x=0.7, an Al concentration above 70% must be assumed which is in agreement with the desorption-corrected calculations above.

Strain distribution Partial strain relaxation of the NDs by formation of misfit dislocations could be observed in Fourier-filtered HRTEM images (**Fig. 7.4**). Some of these dislocations are compensated, i.e. a dislocation where two crystal lattice planes merge into one is accompanied by a second dislocation nearby at the same GaN/AlN interface where one crystal plane is split into two. However, some dislocations remain uncompensated. The difference in the lattice parameter *a* of GaN and AlN is 2.4% (see **Tab. 1.1**, p. 9). Hence, the length of 42 lattice planes of GaN is almost equal to the length of 43 lattice planes of AlN ($1-43/42 = 0.0238$). In **Fig. 7.4** an example is shown, where 42 lattice planes of GaN are matched to 43 lattice planes of AlN, indicating an almost complete strain relaxation. However, not all GaN/AlN interfaces exhibited this degree of relaxation. The formation of dislocations was enhanced for the samples with larger NDs (150908, 080908) compared to the sample with 1.2 nm thick NDs (160908), where no dislocations were observed and completely pseudomorphic growth occurs.

Additionally, contrast changes in bright field STEM images reveal the presence of strain inside the GaN base region (**Fig. 7.5**). Corresponding electron energy loss spectrum (EELS) line scans were recorded along the NW growth axis. The intensity of the Al signal rises from the NW base to the top. The amount differs between individual NWs. Typically, very little Al is found in the lowest 100 nm. The inhomogeneous shell thickness results in an inhomogeneous strain distribution

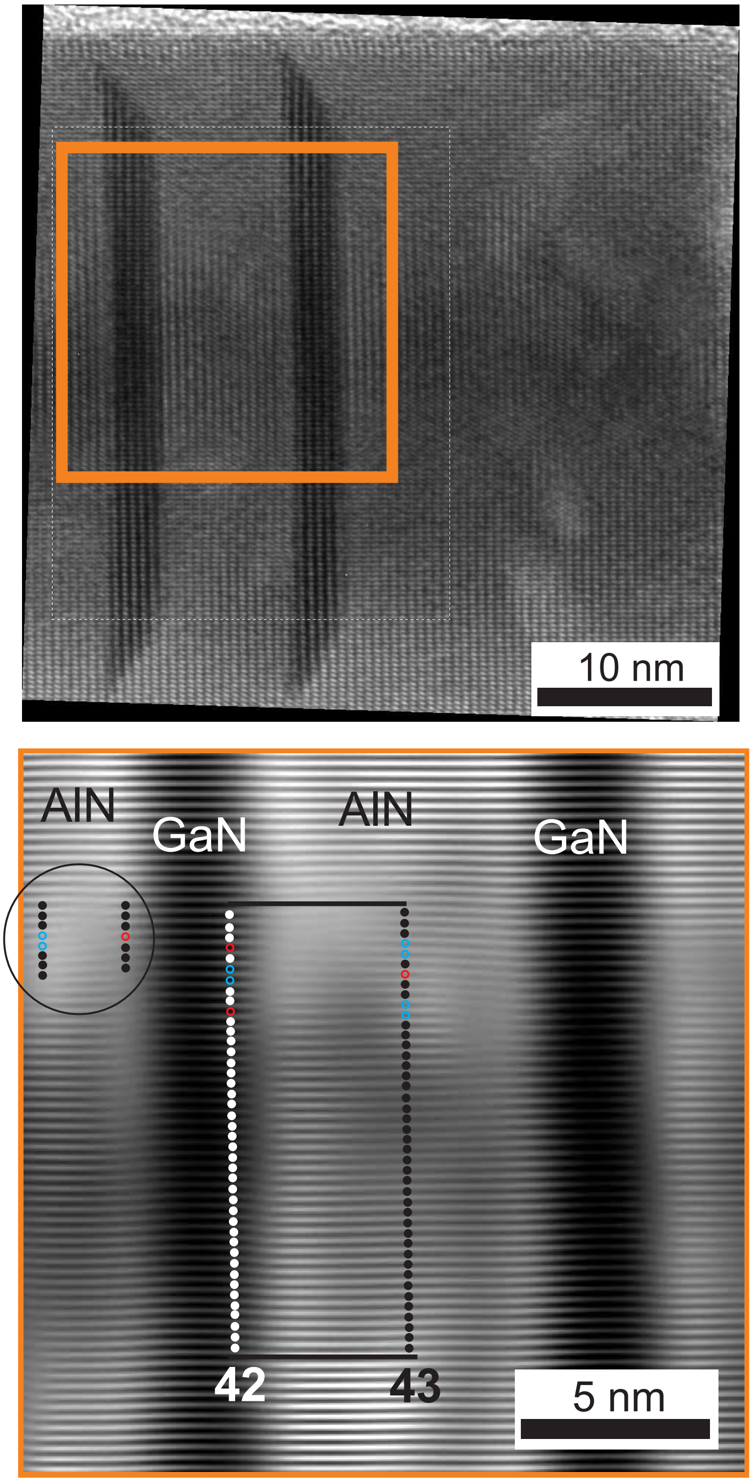

Figure 7.4: *Top: HRTEM image of the two topmost GaN NDs of a 9-fold ND stack embedded in AlN barriers (sample 180908). Bottom: Fourier-filtered detail from left image which highlights the* $(1\bar{1}00)$ *planes. Misfit dislocations are marked with open colored circles, planes that continue regularly over the GaN/AlN interface are marked with solid black (inside AlN part) and white (inside GaN part) circles. For 42 marked GaN planes, one additional AlN plane is inserted.*

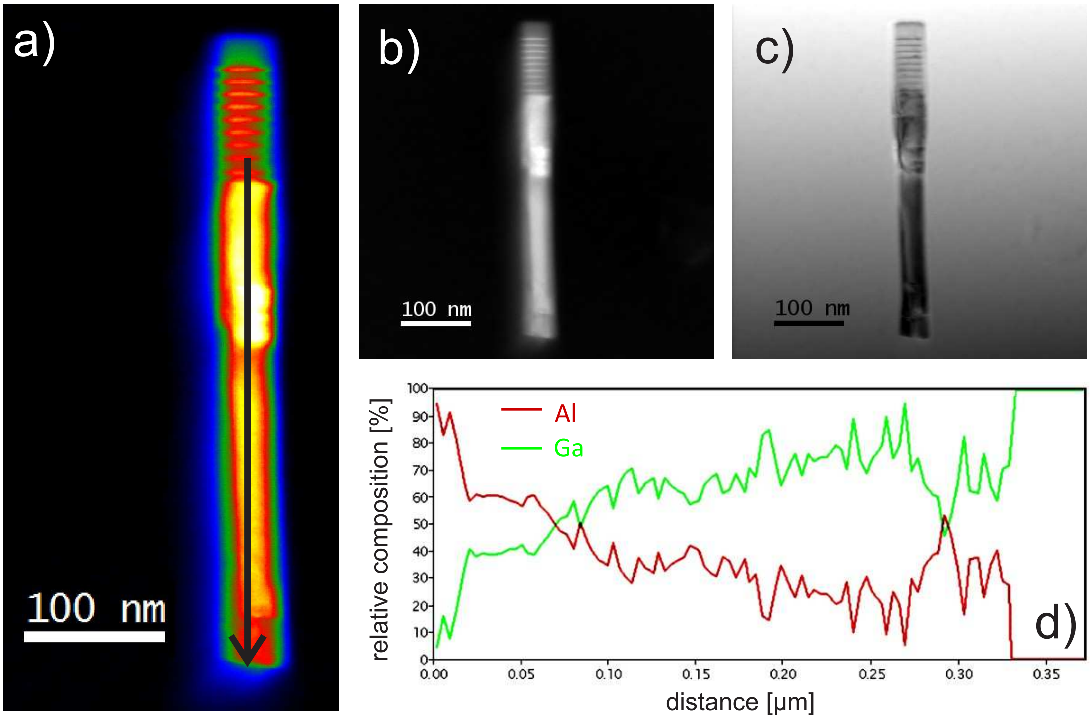

Figure 7.5: *(a) False color HAADF image of a GaN/AlN NW with 2.5 nm thick NDs (sample 150908). (b) Corresponding HAADF image (AlN: bright; GaN: dark) and (c) BF STEM image (GaN: bright; AlN: dark). (d) Al/Ga relative concentration along the line highlighted in (a) using EELS. The Al signal decreases along the NW base from top to bottom. However, there is still Al present even at the lower end of the NW.*

in the GaN base, which is also reflected in emission broadening in ensemble PL measurements (see Sec. 7.3).

Geometrical model for shell formation and lateral growth Thickness inhomogeneities of the AlN shell can be understood by purely geometrical reasons as explained by Foxon *et al.* [Fox09]: When the growth of the Al(Ga)N-containing ND part is initiated, a dense "forest" of about 310 nm to 380 nm high GaN NWs is already present. The typical gap between two NWs is approx. 50 nm (as determined from top-view SEM images). Due to the design of the MBE chamber, the adatoms impinge under an angle tilted by 30° from the substrate normal (the angle of the effusion cells towards the substrate normal). For the above mentioned NW dimensions and spacings (NW height of 350 nm, wire-to-wire spacing 50 nm), this angle had to be lower than 10° for the adatoms to reach the substrate. At 30° impinging angle, on the average only the topmost 100 nm of the NW are directly reached by the impinging beam. Taking the high sticking coefficient and low mobility of Al adatoms into account, this explains the partial absence of an

Table 7.3: *Nanodisk thicknesses and sample numbers. The actual ND thicknesses were measured by HAADF TEM imaging.*

nominal ND thickness [nm]	actual ND thickness [nm]	sample No. $Al_{0.14}Ga_{0.86}N$ barriers	sample No. AlN barriers
1.5	1.2	050509	160908
2	1.7	050908	080908
3	2.5	190908	150908
4	3.5	260908	180908

Al(Ga)N shell in the lowest part of the NWs and an increase of the Al(Ga)N shell thickness towards the NW top. However, a certain degree of Al adatom mobility was observed by (i) the presence of the shell also in the lower NW part (even though with reduced thickness), (ii) a reduced barrier growth rate when the NW diameter is enlarged (see p. 109).

Following these geometrical considerations [Fox09], a lateral growth rate of 18% is evaluated (cylindrical wire, 30° impinging angle, rotated sample, no desorption, no diffusion between top and side walls included). Considering a partial shielding of the sidewall by neighboring NWs and/or some degree of diffusion along the sidewall, this lateral growth rate is lowered and therefore the above mentioned lateral growth rate (11% of the axial rate) can be explained by geometrical effects. Foxon *et al.* additionally pointed out that, due to the fact that Ga and N are usually supplied from different directions, Ga adatoms at the sidewall might not meet nitrogen atoms directly and can therefore diffuse or desorb before being incorporated. At the top surface, both species are present simultaneously.

7.3. Optical characterization

In this section, the photoluminescence properties of GaN/AlGaN ND structures are discussed regarding the influence of well thickness and Al concentration in the barrier. An overview of the samples analyzed in this section is given in **Tab. 7.3** for samples with varied ND height and in **Tab. 7.2** for samples with varied Al content in the barrier.

7.3.1. Influence of nanodisk thickness

Samples with $Al_{0.14}Ga_{0.86}N$ barriers The low-temperature PL emission has two main contributions:

- The emission band around 3.4 eV and 3.5 eV originates from the GaN base part. The emission peak is broadened compared to pure GaN NWs.
- The ND-related peak. Its intensity exceeds the bulk GaN emission by about one order of magnitude.

This ND-related peak was blueshifted from 3.53 eV to 3.64 eV with decreasing well thickness from 3.5 nm to 1.2 nm (**Fig. 7.6**). Due to quantum confinement effects the excitonic emission is blueshifted compared to the emission in bulk GaN.

The FWHMs of the ND peak were in the range of 30 meV to 39 meV for the three thicker NDs, and 51 meV for the 1.2 nm NDs. For the latter sample, the effect of monolayer thickness fluctuations is more pronounced and can possibly explain the broadening. The different contributions of the bulk GaN near band edge emission (see Sec. 5.2.1, p. 73) could not clearly be separated. The FWHMs of the composite emission peak were in the range 54 meV to 62 meV. In comparison, a FWHM of 2 meV was found for pure (strain free) GaN NWs (see Sec. 5.2.1, p. 74). This highlights the effect of strain inhomogeneities in these heterostructures already on the emission of the GaN base part.

A decrease of emission intensity with decreasing well width for samples with 28% Al in the barrier has been reported by Ristić *et al.* [Ris05a]. In our samples with 14% Al no significant change of the intensity with changing ND thickness was found.

Samples with AlN barriers In the low-temperature PL spectra of ND samples with AlN barriers a much stronger shift of the emission peak with varied ND height compared to the $Al_xGa_{x-1}N$ (x=0.14) samples is observed (**Fig. 7.7**). Contributions from the GaN base region (that do not shift with the well thickness) at 3.47 eV and around 3.27 eV could be identified. Additionally, there is a weak broad contribution around 2.38 eV, which is present also in n.i.d. GaN. Due to the relatively weak ND emission compared to samples with low Al content it seems more pronounced here. This so-called yellow or green luminescence (YL, GL, depending on the actual peak center) is most likely due to point defects (like a V_{Ga} - O_N complex) [Res05].

The energetic position of the ND-related emission redshifts with increasing well width from 3.97 eV to 2.71 eV (0.76 eV below the band edge of bulk GaN), showing that a relatively wide energy range can be covered with the GaN/AlGaN system.

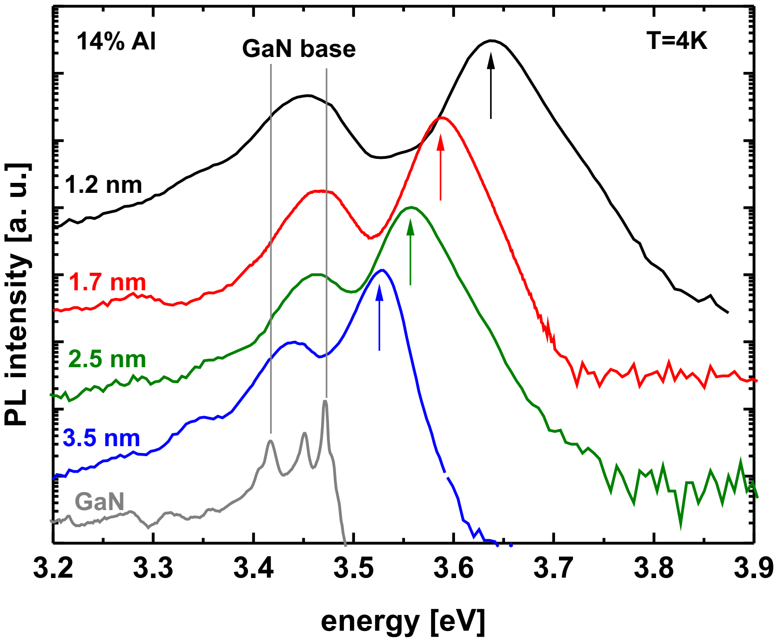

Figure 7.6: *PL of four GaN/*$Al_xGa_{1-x}N$ *(x = 0.14) NWs with different well thicknesses. For comparison, also the emission of pure n.i.d. GaN NWs is shown. Curves are vertically shifted for clarity.*

The energy of the ND emission peak as a function of the ND thickness is compared in **Fig. 7.8** for the set of samples containing pure AlN barriers (samples from **Fig. 7.7**) to those containing $Al_xGa_{x-1}N$ (x = 0.14) barriers (samples from **Fig. 7.6**). For both barrier types, the energy constantly shifts towards lower energies with rising well thickness. Whereas for the AlGaN barrier samples the emission energy is always above the GaN bandgap, this is only valid for thin NDs (1.2 nm and 1.7 nm) in the case of AlN barriers. For thicker NDs (2.5 nm and 3.5 nm) the emission energy is below the GaN bandgap, indicating the presence of the quantum-confined Stark effect (QCSE). These results are in agreement with those published by Renard *et al.* [Ren09]. Small deviations from our results could be caused by the differences in the sample structure (single GaN ND with 10 nm AlN barriers in Ref. [Ren09]). The redshift in GaN/AlN ND structures was found to be less pronounced than in GaN/AlN quantum well layers [Ade03] indicating that internal electric fields inside the NDs are lower than inside quantum wells of the same thickness.

Comparison with a 2D quantum well We compare the data with calculated results for a standard quantum well (box potential with finite barrier height), disregarding any strain or polarization effects (solid lines in **Fig. 7.8**). It must be pointed out that this does not mirror the real ND structure which needs a full 3D

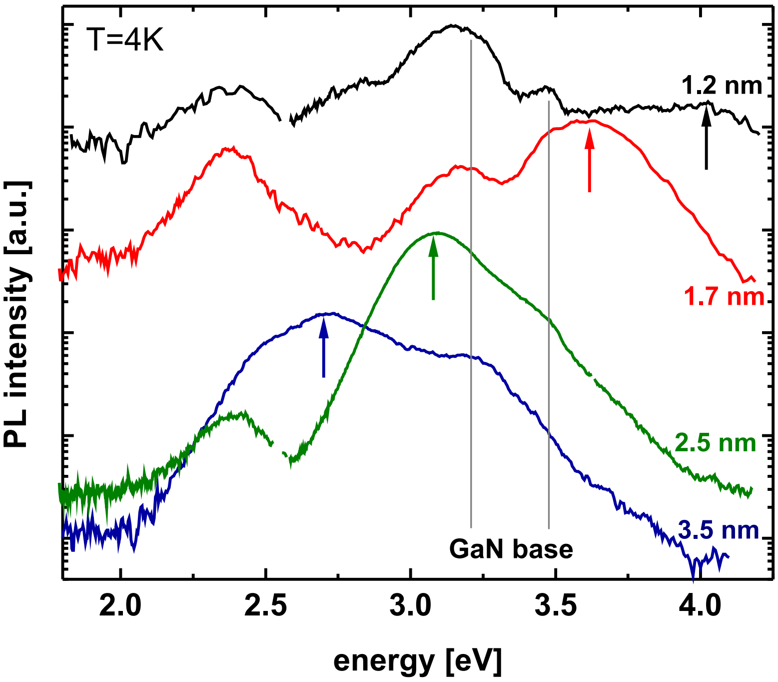

Figure 7.7: *PL of four GaN/AlN NWs with different well thicknesses as given in the plot. The nanodisks related emission is indicated by arrows. The vertical lines at 3.47 eV and 3.2 eV mark emission from the GaN base. Curves are shifted vertically for clarity.*

simulation. However, it allows comparison with a well-known model system and fitting of the data with an effective electrical field as the only parameter.

The energy eigenstates can be calculated by numerically solving the equation

$$\frac{\sqrt{S-y^2}}{y} = \tan(y) \tag{7.1}$$

with the dimensionless variables

$$S = -\frac{2m_e^* V_0 L}{4\hbar^2} \qquad \text{and} \qquad y = \frac{q \cdot L}{2} \tag{7.2}$$

with m_e^* the effective electron mass ($m_{e,GaN}^* = 0.2 \cdot m_0$), V_0 the depth and L the length (i.e. ND height) of the potential well [Fli00]. The wave vector q for the bound state is connected with the ground state energy by the following relation

$$E_0 = \frac{\hbar^2 q^2}{2m_e^*} \tag{7.3}$$

For calculating the electron (and hole) wave functions one has to know the band alignment, i.e. the bandgap discontinuities between the conductions (va-

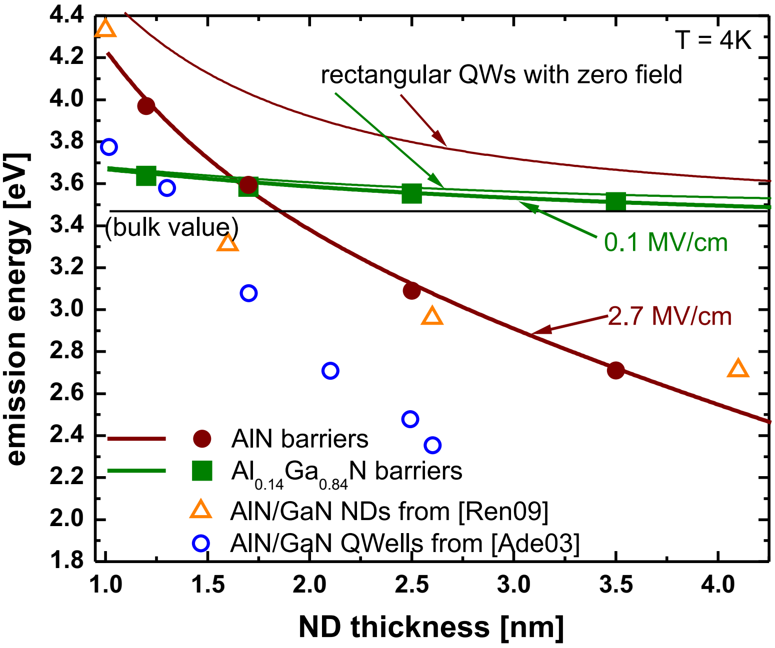

Figure 7.8: *Evolution of emission energy with well thickness for samples with AlN barriers (full circles) and* $Al_xGa_{x-1}N$ *(x = 0.14) barriers (full squares). Thin lines are calculations for rectangular quantum wells, and thick lines for the same wells with additional electrical field present. For comparison, also data of GaN NDs inside AlN barriers from Ref. [Ren09] (open triangles) and from AlN/GaN quantum well layers [Ade03] (open circles) is shown.*

lence) bands. A conduction (valence) band discontinuity of 75% (25%) of the GaN to AlGaN bandgap difference was selected [Kin98, Mar96, Wes06]. The ground state energy is given by the GaN bandgap plus the energies of the first bound state in the conduction and valence band quantum well. Additionally an effective electrical field V_{eff} was assumed ($E_{0,\text{field}} = E_0 - V_{\text{eff}} \cdot L$) and its value fitted to the PL data points.

For our AlN samples, the PL data could be reproduced with an effective field of 2.7 MV/cm, showing that polarization effects (either due to strain or the difference in spontaneous polarization between AlN and GaN) play an important role in this case. The data for the $Al_xGa_{x-1}N$ (x = 0.14) samples, however, could be well reproduced without an electric field. For comparison, the calculation for an effective field of 0.1 MV/cm is also shown. For GaN/AlGaN thin film quantum well layers with x = 0.17, Grandjean *et al.* [Gra99] reported a much stronger built-in electric field of 0.71 MV/cm. An apparent reduction of the electric field in NWs compared to thin films is also reported in Ref. [Zam05], where for NDs embedded in $Al_xGa_{x-1}N$ (x = 0.28) barriers, an electric field of 0.4 MV/cm was extracted, which is only one third of the value that has been calculated for pseudomorphically grown GaN/AlGaN quantum well layers with the same Al concentration [Fio99].

7.3.2. Influence of barrier composition

The PL emission energy from the NDs can also be influenced by variation of the Al content in the barrier, i.e. the Al flux during growth (see **Fig. 7.9**). An increase of the Al concentration from 8% to 34% resulted in an increase of the emission energy from 3.53 eV to 3.73 eV, which is due to a stronger confinement. The emission intensity exceeded the emission from the GaN NW itself (3.40 eV – 3.47 eV) by a factor of 7 ± 2 for the samples up to $x = 0.34$.

However, a further increase of the Al concentration lead to a decrease of the emission energy to 3.66 eV for the sample with 41% Al and 3.63 eV for the sample with AlN barriers, respectively. For these Al concentrations, the ND emission intensity was strongly reduced. This is caused by the quantum-confined Stark effect (QCSE) and shows the presence of large electric fields which originate from the differences in the spontaneous polarization between well and barrier material and the piezoelectric polarization due to strain. The QCSE also leads to a spatial separation of photo-generated holes and electrons, quenching the light emission intensity.

A steady increase of the full width at half maximum (FHWM) throughout the whole composition range was observed (open symbols in **Fig. 7.10**). The FWHM was as low as 18 meV (at 4K) for the sample with the smallest Al concentration and increased with increasing Al concentration up to 100 meV (**Fig. 7.10**) for the sample with $x = 0.34$. For the AlGaN sample with the highest Al concentration investigated ($x = 0.41$), a more pronounced increase of the FWHM to 180 meV was found. The FWHM of the AlN barrier sample was 260 meV.

Measurements on single NWs (or a bundle of a few coalesced NWs) exhibit several narrow lines distributed over an energy interval that corresponds to emission distribution of the ensemble measurements [Rig10d, Rig10c, Rig10b]. These lines can be attributed to the emission of individual NDs within one NW. For comparison, reference samples containing only one ND instead of the 9-fold multi ND stack were grown. Only one sharp ND-related PL emission line is recorded for a single NW (**Fig. 7.11**).

7.3.3. Temperature dependence

For samples with low Al content, the emission intensity strongly decreases when increasing the temperature from 4K to RT. However, the temperature stability

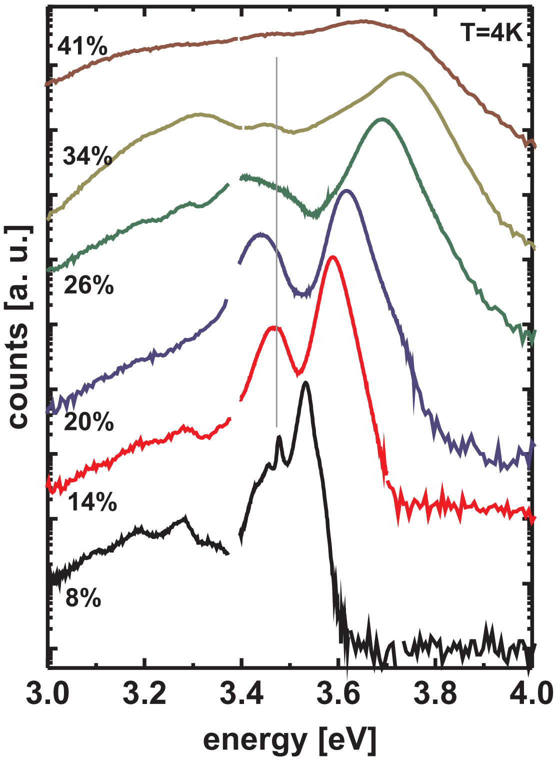

Figure 7.9: *PL spectra (at 4K) of samples with AlGaN barriers with Al content varying from 8% to 41%. The vertical line at 3.47 eV marks the position of the excitonic recombination in pure GaN NWs. Curves are shifted vertically for clarity.*

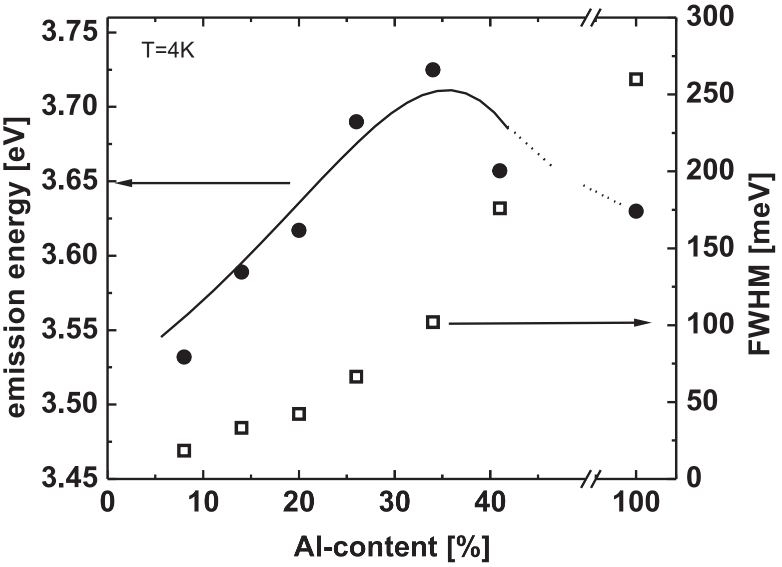

Figure 7.10: *PL peak position and corresponding FHWM of the nanodisk peak as a function of the Al content in the barrier in samples with 1.7 nm thick GaN NDs (**Fig. 7.9**).*

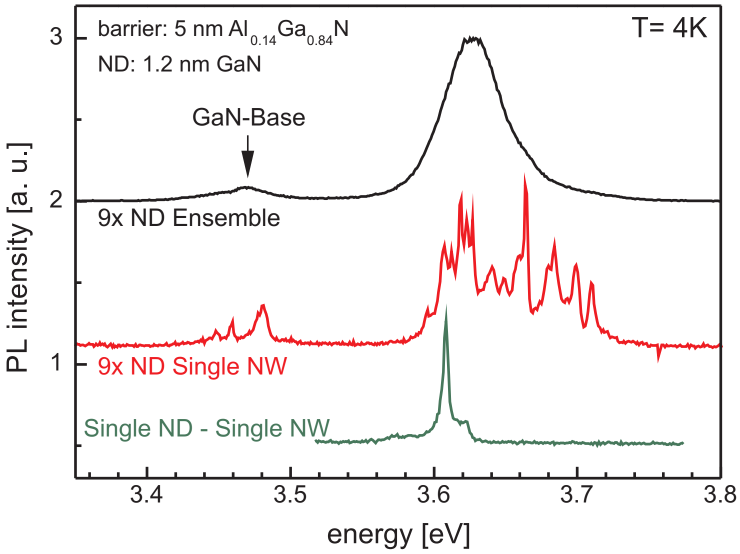

Figure 7.11: *PL spectra of a NW ensemble (black line) and a single NW (red line) from the same sample. The green line corresponds to a single NW with only one ND grown at the same parameters [Rig10d]. Only one sharp emission line is recorded (FWHM 7 meV).*

continuously increases with increased Al content up to $x = 0.26$ (**Fig. 7.12**). The room temperature (300 K) intensity of the sample with $x = 0.26$ ($x = 0.14$) was 23% (0.3%) of the 3.3 K intensity, respectively. Whereas for the $x = 0.14$ sample the temperature dependence is comparable to GaN quantum wells in thin AlN films, it is comparable to GaN quantum dots in AlN matrix [Gui06] for the sample with $x = 0.26$.

7.4. Discussion and comparison with 3D simulations

The key factor to understand the observed behavior is the presence of the Al(Ga)N shell. It influences the strain state of the individual NDs. To simulate the structures(1), the axial and lateral dimensions obtained from TEM analysis were used as input parameters for a 3-dimensional simulation using NextNano(2). **Fig. 7.13a** shows the strain distribution (e_{zz} component of the strain tensor) within a 9-fold GaN ND stack embedded in AlGaN barriers. Due to lateral barrier growth, the thickness of the AlN shell increases from the topmost to the lowest ND. Therefore the strain state of the individual NDs exhibits a strong variation withing the ND

---

(1) The simulations were performed by Dr. Jörg Teubert at the University of Gießen

(2) See www.nextnano.de for information and tutorials

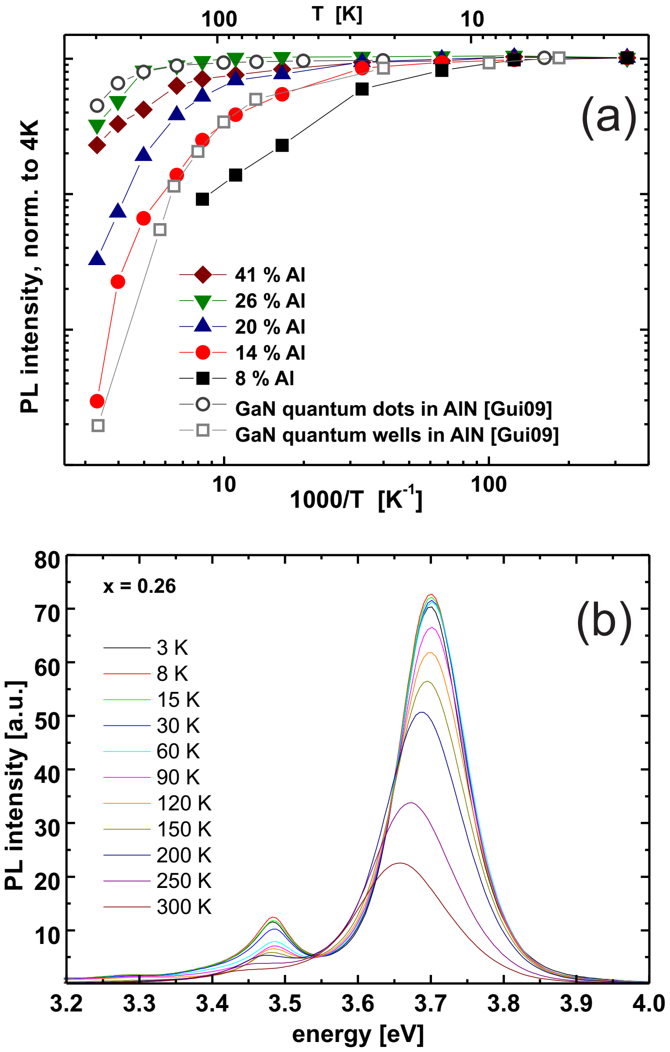

Figure 7.12: *(a) Normalized PL emission intensity as function of the temperature for ND samples with different Al content in the barriers. Comparison with quantum dots and quantum wells according to Ref. [Gui06]. (b) PL curves for the x=0.26 sample.*

stack. While the first ND (close to the base part) is strongly influenced by the GaN base part and a thick AlN shell, resulting in moderate in-plane compressive strain, the top ND is highly compressively strained due to the AlN cap layer combined with a small shell thickness. **Fig. 7.13b** shows the e_{zz} strain component along the NW growth axis for four different Al contents in the barrier. The higher the Al content, the more pronounced is the strain variation. In particular, the c-lattice parameter in the GaN base decreases considerably due to the vertical compression induced by the surrounding shell. This can be regarded as the main reason for the GaN PL emission broadening with increasing [Al], i.e. with increasing shell thickness (compare **Fig. 7.10**).

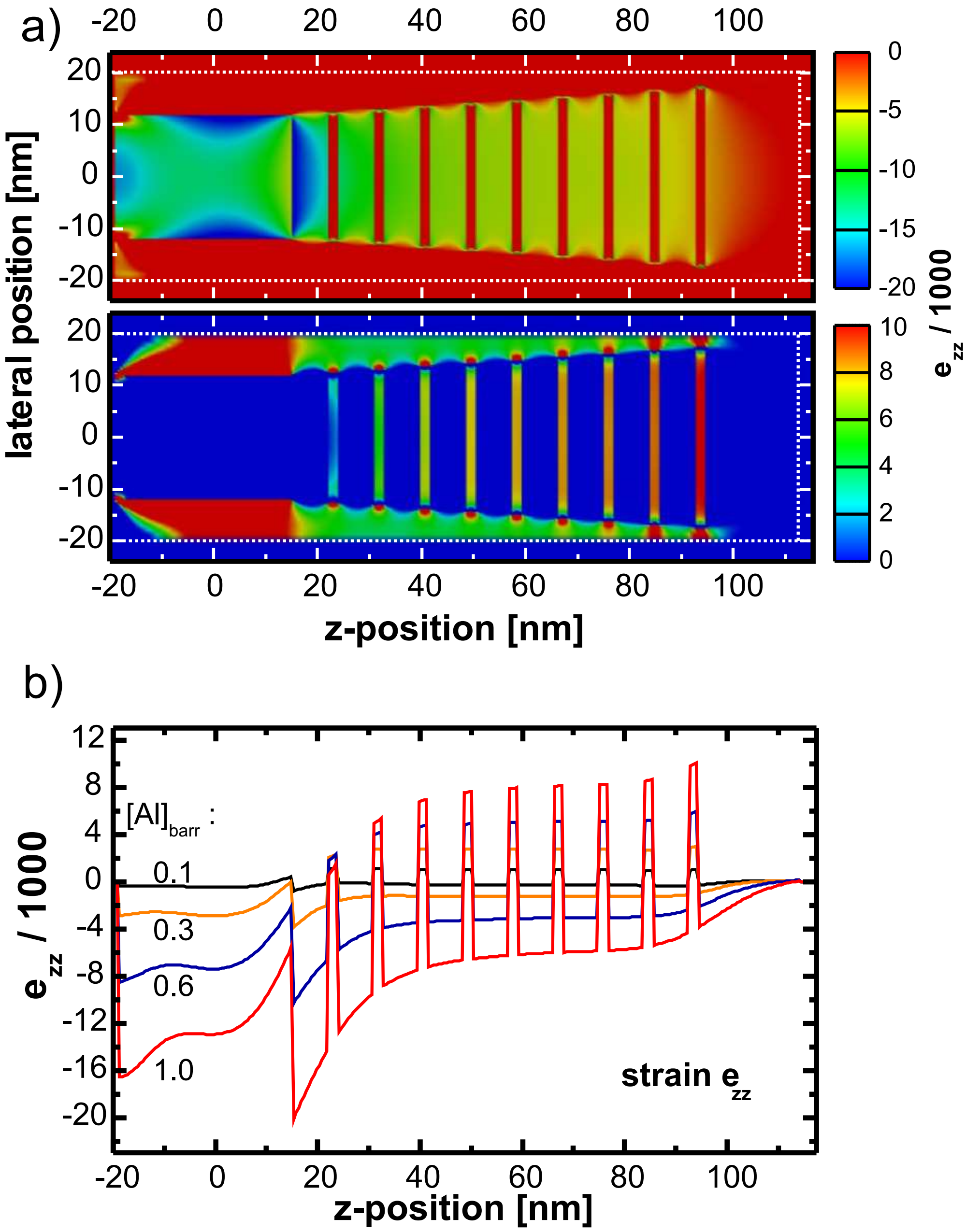

Figure 7.13: **(a)** *Cross-sectional view of the e_{zz} component of the strain tensor for a NW with AlN barriers (z axis ∥ growth direction). Both parts of the image show the same data set. For contrast enhancement, the color scale in each part was restricted to show the negative (upper part) and positive (lower part) values of e_{zz}, respectively. White dotted lines indicate the outer boundaries of the NW.* **(b)** *Distribution of the e_{zz} component of the strain tensor along the NW growth axis for four different [Al] in the barrier.*

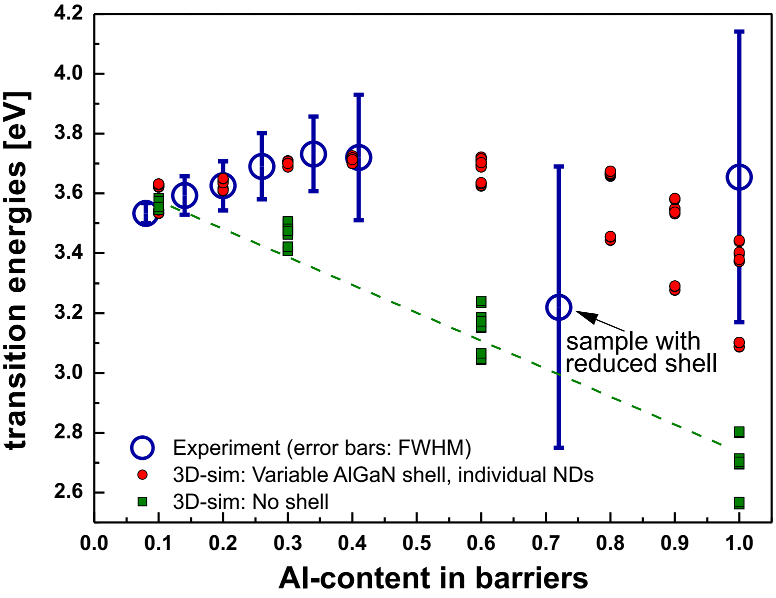

Figure 7.14: *Comparison of the PL emission energy (open circles) and FWHMs (error bars) of the GaN/AlGaN ND samples with 3-dimensional simulations with (full circles) or without (full squares) shell. The eigenstates for several disks in the 9-fold nanodisk stack (disk number 2, 5, 7, and 9) were calculated, showing that the individual disks emit at different energies.*

Additionally to strain effects, the surface band bending at the GaN sidewalls (see Sec. 6.1, p. 85) is altered due to the Al(Ga)N shell. While for a thin lateral shell ([Al] $<$ 0.3) the lateral confinement potential for electrons shows a minimum at the NW center [Riv07, Fur11], the curvature becomes non-monotonous for higher [Al] with a ring-shaped minimum relatively close to the NW sidewall (see [Fur11] for further details, esp. Fig. 8 therein). This band bending leads to a lateral field gradient inside the NDs. Earlier publications took a lateral strain gradient into account ("strain confinement"), however no shell was considered [Ris05b, Riv07].

The variation of the PL emission energy with Al content could be well reproduced (**Fig. 7.14**). The calculations were performed for several NDs in the 9-fold ND stack (number 2,5,7,9). The higher the Al content, the stronger were the differences between the individual NDs, explaining the continuous increase of the FWHM of the PL emission. The emission energy maximum was found at $x = 0.35 - 0.4$, which is in good agreement with the PL data. For this Al concentration, the lateral strain gradient is minimized, leading to almost flat-band conditions. Furthermore, the dispersion along the NW axis is minimized. This leads to an ideal overlap of the electron and hole wave function not only for one individual ND, but for all NDs within the multi ND stack.

In contrast to this, calculations for structures without shell revealed a continuous decrease of the PL emission energy with rising Al content (full squares in **Fig. 7.14**). For a sample with reduced shell and x = 0.72 (see p. 105), a PL emission energy of 3.22 eV was found. This is close to the calculated value for a sample without shell.

7.5. Conclusions

In conclusion, we have successfully grown GaN/AlGaN and GaN/AlN nanowires with embedded GaN nanodisks. Lateral growth of the AlN part (and AlGaN with high Al content) was observed, leading to the formation of core-shell wires, whereas there was no lateral GaN growth. This directly reflects the different adatom kinetics between Ga and Al. Thickness inhomogeneities of this Al(Ga)N shell (mainly caused by shadowing effects due to the high NW density) give rise to strain inhomogeneities which are the most likely the reason for PL emission line broadening. The presence of the shell strongly influences the strain and the emission properties. The emission energy can be controlled by the nanodisk thickness or the Al concentration in the barriers. It could be shown that for low Al content in the barrier ($x \leq 0.34$) the ND emission energy rises with increasing Al content, showing that the energetic position is dominated by the confinement, whereas for higher Al content the ND emission energy decreases, indicating the influence of the quantum-confined Stark effect (QCSE). Samples with an Al content around x = 0.26 exhibited the highest temperature stability of the PL emission, which is similar to GaN quantum dots. For this Al concentration, the simulations revealed practically flat-band conditions and thereby an optimum overlap between electron and hole wave functions.

8. InGaN nanodisks embedded in GaN NWs

In this chapter the growth conditions for InGaN/GaN nanowire heterostructures are evaluated and results from structural (TEM, SEM) and optical (PL) characterizations are discussed. The structures were designed in analogy to the GaN/AlGaN heterostructures (cf. Chapter 7). Changing the active material from GaN to InGaN allows a reduction of PL emission and excitation energies. This is favored for the application of these structures as a DOTSENSE sensor as it avoids the need for deep UV excitation sources, which still suffer from low output power, limited lifetime, and high costs$^{(1)}$.

The structures were mainly grown on Si(111). Additional samples were grown on Si-buffered sapphire wafers (cf. Sec. 3.3, p. 45) to allow illumination and emission detection from the backside for compliance with the DOTSENSE specifications (p. 15).

Reports on MBE growth of GaN/InGaN nanowires with embedded NDs and their emission properties were to our knowledge first presented by the group of K. Kishino, which has shown NWs with tunable emission in the range of 530 nm to 645 nm (2.34 eV – 1.92 eV) [Kik04]. A more recent publication [Kik06] demonstrates that the accessible wavelength regime can be expanded from 436 nm (2.85 eV, blue) to 614 nm (2.02 eV, red). Additionally, InGaN NDs with high In content emitting in the infrared range of 1500 nm to 1920 nm (0.83 eV – 0.65 eV) were reported [Kou06]. However, in all these reports no structural characterization was presented, leaving the question of the actual shape of the InGaN inclusions unanswered.

Before 2002, a value for the InN bandgap of 1.8 eV was generally accepted. However, later it could be shown that the measured bandgap in thin films depends

---

(1) Commercially available 245 nm LEDs cost around 360 EUR (optical output power 0.07 mW at 150 mW electrical power consumption, typical lifetime 50 h). Compare this with 375 nm LEDs (32 EUR, optical output power 200 mW, electrical power consumption 1 W, lifetime of more than 10’000 h) or 440 nm LEDs (12 EUR, optical output power 380 mW, electrical power consumption 1 W). Prices and data from Roithner Laser (www.roithner-laser.com), as of Aug. 2013.

strongly on the carrier concentration. This is due to the low electron effective mass leading to rapid filling of the conduction band (low density of states) for high charge carrier concentrations which are often present in InN due to defects [Dav02]. Additionally, structural characterization of InN/InGaN by TEM is difficult since typically used e-beam intensities already induce damage (like Indium clustering) in the material [Sme03, Sme06].

There is also a tendency for phase separation (limited miscibility) for $\mathrm{In_xGa_{x-1}N}$ during growth or at a later annealing step [Ho96, Sin97, Gan08] or interdiffusion at the GaN/InGaN interface, which was also observed in the samples in this work (cf. Sec. 8.2.2). These effects depend strongly on the applied growth conditions (substrate temperature, fluxes) and make it difficult to control the In content and the homogeneity of the samples.

8.1. Design of the samples and growth parameters

The main challenge for the growth of GaN/InGaN heterostructures is the large difference in growth temperatures between the two materials. InGaN decomposition can occur at the optimum GaN nanowire growth temperature of 770°C – 780°C. For pure InN (GaN), decomposition is reported for temperatures above 630°C (850°C) [Amb96]. Therefore, the GaN base region of the structures investigated here was grown at 772°C, whereas for the nanodisk part (both for the InGaN NDs and the GaN spacers) a reduced growth temperature was chosen (see Tab. 8.1 for details). This reduction of temperature leads to degraded quality of the GaN spacers (high density of stacking faults, cf. Sec. 8.2.2).

Nanowires with multiple thin InGaN inclusions ("nanodisks"$^{(1)}$) between GaN barriers (**Fig. 8.2a**) and additional nanowires with a single thick InGaN top part were grown (**Fig. 8.2b**) as reference samples. To analyze the influence of reduced substrate temperatures on the growth of GaN, GaN NWs with a low-temperature GaN top part were also grown (**Fig. 8.2c**).

The nanodisk stack consists of nine periods of InGaN with constant nominal thickness embedded into GaN spacers (thickness 5 nm to 10 nm). The InGaN ND height was varied from 1.3 nm to 4 nm. The cap layer consisted of 20 nm GaN.

First, GaN NWs were grown as base part for the heterostructures at a substrate temperature of $T_{\mathrm{sub},1} = 772$°C for 55 min. The growth was then interrupted to re-

---

(1) We call them nanodisks in analogy to the previous chapter. However, as it is shown in the following, their shape differs from the GaN nanodisks in the GaN/AlGaN samples presented in the previous chapter.

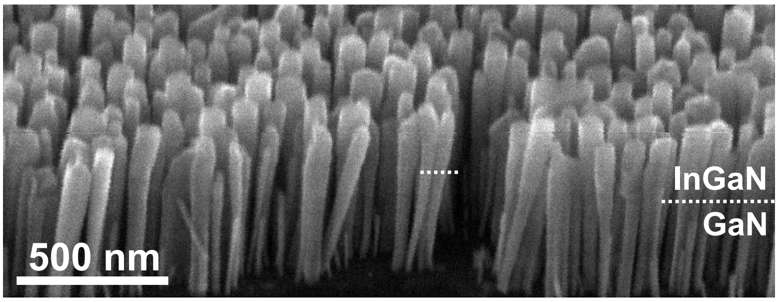

Figure 8.1: *SEM image of GaN/InGaN NWs (sample 040609) grown on Si(111) taken at 45° inclination. The transition between GaN base and InGaN part is exemplary marked with dashed lines for some NWs. The upper part (InGaN) is slightly widened.*

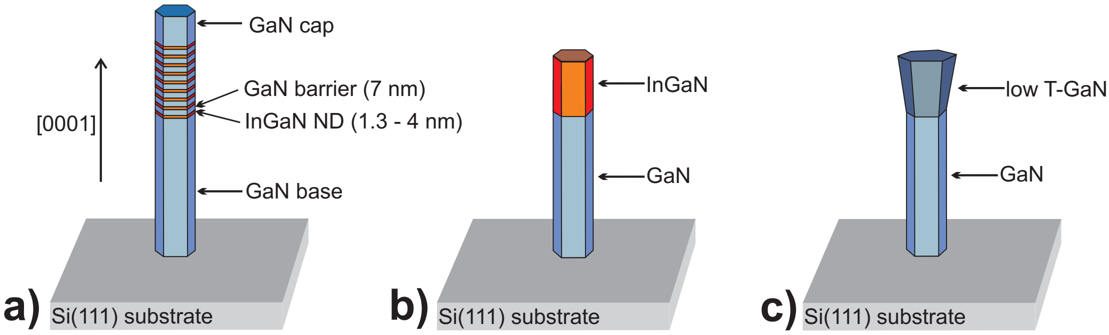

Figure 8.2: *Schematic of view the different NW designs. (a) GaN NW with InGaN nanodisks (b) GaN NW with thick InGaN top part (c) GaN NW with low-temperature top part.*

duce the substrate temperature for the heterostructure part (temperature ramp 15°C/min). The heterostructure part was grown at a constant substrate temperature of $T_{sub,2}$ which was in the range of 530°C – 595°C (see Tab. 8.1 for data of the individual samples).

Ga was supplied by a standard effusion cell operating at $T_{Ga} = 1012°C$ (beam equivalent pressure $BEP_{Ga} = 3.9 \times 10^{-7}$ mbar) both for the GaN and the InGaN regions. Nitrogen background pressure and plasma source operation power was 2.7×10^{-5} mbar and 425 W, respectively. For the InGaN regions, the In flux was additionally provided by an In effusion cell operating between $T_{In} = 660°C$ and $T_{In} = 780°C$ ($BEP_{In} = 1.1 \times 10^{-8}$ mbar to $BEP_{In} = 1.6 \times 10^{-7}$ mbar). A change of 30°C changes the In flux by a factor of 2.

Additionally, samples with reduced Ga flux were grown, since for samples grown with a relatively high In flux widening of the NW diameter at the beginning of the heterostructure part was observed (**Fig. 8.1**). Therefore, the Ga flux was reduced by a factor of two to 1.8×10^{-7} mbar during growth of the InGaN section

Table 8.1: *Growth parameters for the samples discussed in this chapter. The substrate temperature, In and Ga effusion cell temperatures during growth of the heterostructure part are given. Sample No. 100610 was grown on sapphire with Si nitride buffer, all other samples on Si(111). ND thicknesses are nominal values.*

$T_{sub,2}$ [°C]	T_{In} [°C]	$T_{Ga,2}$ [°C]	base part duration	InGaN part	sample No.
595	780	1012	75 min GaN	30 min InGaN	040609
595	750	1012	75 min GaN	30 min InGaN	090609
530	780	1012	70 min GaN	9 × 4 nm InGaN	020709
590	720	1012	40 min GaN	30 min InGaN	220909
565	692	973	55 min GaN	30 min InGaN + 9 × 2 nm InGaN	110210
565	692	973	55 min GaN	30 min InGaN	100310
565	692	973	55 min GaN	9 × 2 nm InGaN	150310
565	780	1012	55 min GaN	9 × 4 nm InGaN	010410
595	695	1012	55 min GaN	9 × 4 nm InGaN	070410
595	780	1012	55 min GaN	9 × 4 nm InGaN	090410
625	780	1012	55 min GaN	9 × 4 nm InGaN	120410
565	780	1012	55 min GaN	9 × 3 nm InGaN	150410
565	780	1012	55 min GaN	9 × 2 nm InGaN	190410
565	780	1012	55 min GaN	9 × 1.3 nm InGaN	260410
555	755	982	60 min GaN	9 × 4 nm InGaN	100610

by lowering the Ga effusion cell temperature from 1012°C to 973°C. This avoids metal-rich (or less N-rich) growth conditions. The respective growth parameters are also listed in **Tab. 8.1**.

8.2. Morphological properties

8.2.1. Morphology and defects of low-temperature GaN

To asses the influence of the lowered substrate temperature on GaN growth (i.e. the formation of stacking faults), test structures consisting of the GaN base part, followed by a low temperature GaN top were grown (**Fig. 8.2c**). They can be regarded as GaN/InGaN heterostructures without InGaN disks. These samples were analyzed by SEM and PL. The growth duration was 55 min for the base part, and 25 min for the low-temperature GaN part plus an interruption for the temperature ramp. The Ga flux and the N flux were kept constant (T_{Ga} = 1012°C,

Table 8.2: *Growth parameters for the low-temperature GaN NWs and comparable GaN/InGaN heterostructures with 9-fold InGaN NDs with 4 nm nominal thickness. The substrate temperatures (T_{sub}) and the substrate heater setpoints (T_h) are given for the base ($_{,1}$) and top part ($_{,2}$), respectively.*

$T_{sub,1}$ [°C]	$T_{sub,2}$ [°C]	$T_{h,1}$ [°C]	$T_{h,2}$ [°C]	T_{In} [°C]	sample No.
772	560	863	580	—	231110
772	595	860	630	—	021210
772	630	860	680	—	151210
772	560	859	580	780	010410
772	595	859	630	780	090410

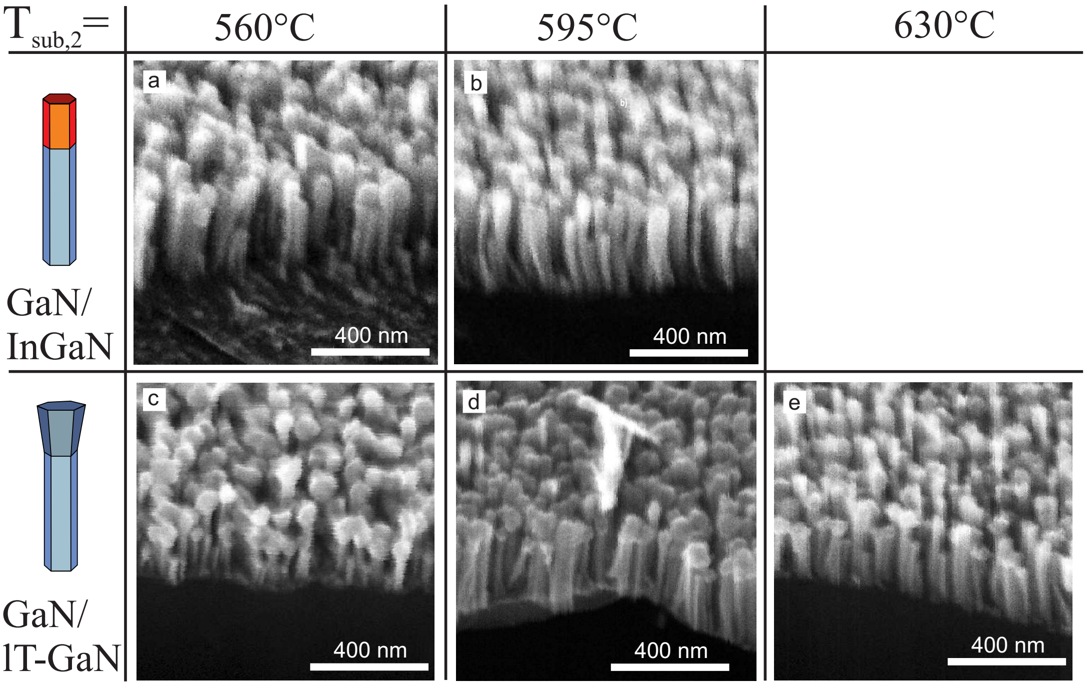

Figure 8.3: *SEM images of GaN/InGaN heterostructures (a: 010410, b: 090410) and low-temperature GaN NWs (c: 231110, d: 021210, e: 151210) taken under 45° inclination. See Table 8.2 for sample details.*

$p_{MBE} = 2.7 \times 10^{-5}$ mbar, i.e. the same values as for the GaN/InGaN samples). The growth parameters are listed in **Tab. 8.2**.

Abrupt widening of the NW diameter is observed for the GaN samples at the onset of the low-temperature region. It is more pronounced for lower $T_{sub,2}$, but still present at the highest substrate temperature of $T_{sub,2} = 630$°C (**Fig. 8.3c-e**). In contrast, the GaN/InGaN NWs exhibit a much lower degree of widening. It is only visible in the sample grown at $T_{sub,2} = 560$°C (**Fig. 8.3a**). The presence

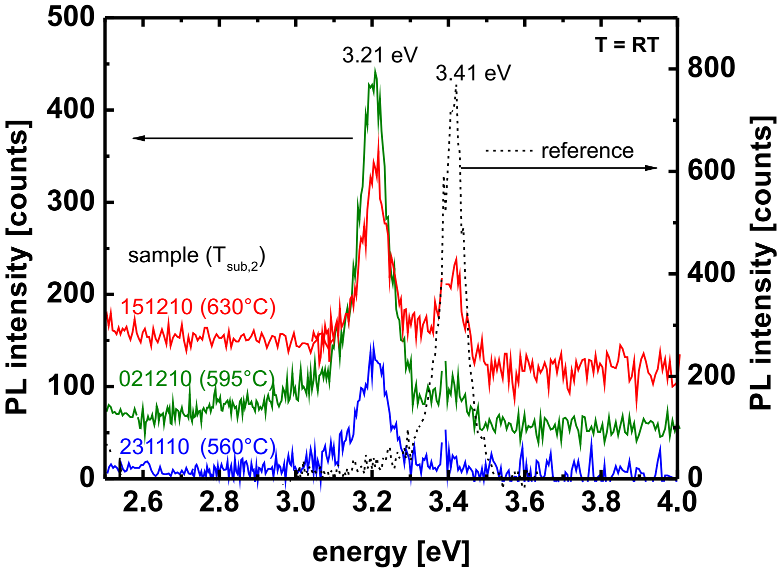

Figure 8.4: *Room-temperature PL of three GaN/low-temperature GaN NW samples (see Table 8.2) and one GaN reference sample grown under optimized conditions (010710). Curves are vertically shifted for clarity.*

of In enhances the Ga adatom mobility. This surfactant effect is described in the literature (see [Neu03] and references herein). The actual effect strongly depends on the specific growth conditions (i.e. V-III ratio, In flux, etc.). For high In flux and at N-rich conditions, an instability of the *c-plane* surface and faceting (especially the formation of In-covered GaN $\{1\bar{1}01\}$ surfaces) was calculated by first-principle methods [Neu03, Nor99]. This might explain the faceting of the InGaN nanodisks that was observed in TEM analysis (see Sec. 8.2.2).

The room-temperature PL intensity of the 3.41 eV emission increases monotonically when $T_{sub,2}$ is raised. This is accompanied by a decrease of the 3.21 eV emission. A reference sample (growth of 90 min n.i.d. GaN at $T_{sub,1}$) does not emit in this region (**Fig. 8.4**). The 3.21 eV room temperature PL emission is present in pure GaN samples when the growth is carried out at too low substrate temperatures. This energy corresponds to the bandgap of cubic GaN [Lei92, Rin08, RF94]. Basal plane stacking faults leading to cubic inclusions were observed in the GaN/InGaN samples by HRTEM (see Sec. 8.2.2). Recently, it was reported that a strong reduction of the substrate temperature from 850°C to 580°C during growth of undoped GaN NWs has promoted the change from the hexagonal phase to the cubic phase, with the two phases separated by a transition zone containing stacking faults [Ren10].

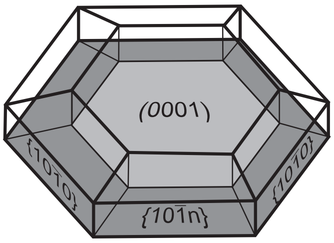

Figure 8.5: *Schematic diagram of the InGaN nanodisk shape. Filled areas: Bottom of nanodisk,* {10$\bar{1}$n} *surfaces in dark gray,* (0001) *surface in light gray. Wire frame structure: Nanodisk, the sidewalls are* {10$\bar{1}$0} *planes.*

8.2.2. Structural characterization of nanodisk samples

In the GaN/AlGaN nanostructures, flat GaN disks with sharp interfaces and constant thickness along the NW radius were observed throughout the whole $Al_xGa_{x-1}N$ concentration range with only slight faceting. The morphology of the InGaN inclusions is different. Faceted ND top surfaces lead to a truncated pyramidal shape and dome-like morphology (**Fig. 8.5**). Additionally, indium diffusion into the GaN barriers was found by EELS. A similar shape was recently reported for 7 nm high InGaN nanodisks with approx. 15% to 25% In [Cha10]. Indium distribution profiles obtained from HRTEM images from these samples revealed the formation of In-rich clusters inside the NDs.

For high In contents, the NDs could be clearly resolved by TEM (**Fig. 8.6**). The measured heights of the NWs (sample 010410) were $330 - 380$ nm, with the majority reaching a height of (356 ± 16) nm. The height of the GaN base part was (255 ± 17) nm. The NW diameter increased from the bottom (20 ± 5) nm to the top (44 ± 8) nm. The heights of the NDs and the spacers are constant throughout the 9-fold stack. The measured ND heights were (3 ± 0.7) nm, and the ND-to-ND distance (11.5 ± 0.2) nm, leading to a GaN spacer height of 8.5 nm. The cap layer was 14 nm. This is slightly lower than the nominal values given in **Tab. 8.1**. A growth rate of 6.0 nm/min was calculated for the InGaN disks (5.1 nm/min for the GaN spacer; 4.5 nm/min GaN cap) by using the measured heights and the growth durations of 30 sec for each InGaN disk (100 sec for each GaN spacer; 180 sec for the GaN cap). Since In was added to a constant Ga flux during ND growth, a higher growth rate for the NDs is expected.

Basal stacking faults (BSFs) were observed in the majority of the NWs (**Fig. 8.6c**), residing in the InGaN ND/GaN structure rather than in the GaN base part. Their typical density was $7.8 \times 10^5 \text{cm}^{-1}$. The stacking fault formation can be explained by the low growth temperature for the GaN spacers (see Sec. 8.2.1).

Based on the ELNES (energy loss near edge structure [Mai09]) spectra from

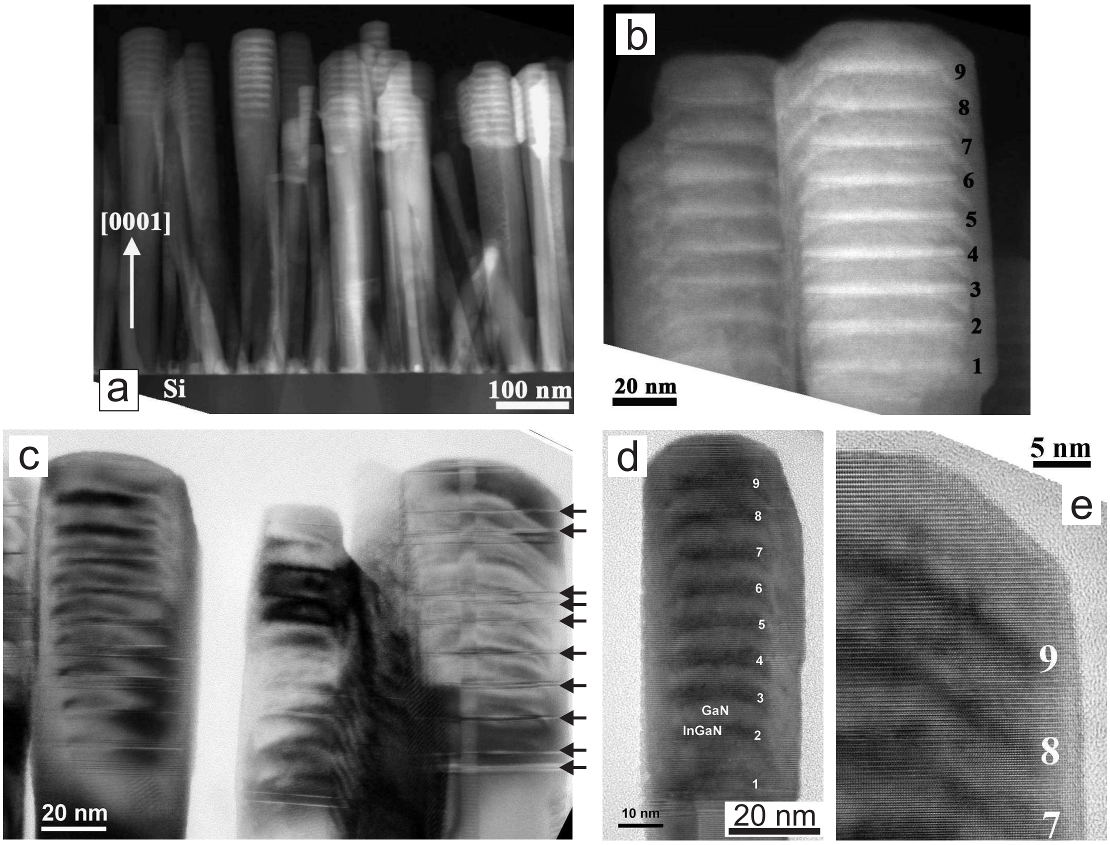

Figure 8.6: *TEM images of sample 010410 taken along the* $\left[11\bar{2}0\right]$ *GaN zone axis. (a) HAADF Z-contrast STEM showing the overall morphology with bright layers corresponding to InGaN NDs. (b) Detail view of ND region from image a. (c) Cross-section TEM showing stacking faults (some are marked with arrows). (d), (e) HRTEM images with InGaN in dark.*

the $\mathrm{C_K}$- absorption edge, $\mathrm{N_K}$-edge, $\mathrm{In_{M4,5}}$-edge, and $\mathrm{Ga_{L2,3}}$-edge of the GaN NWs, the ratio of the $\mathrm{Ga_{L2,3}/N_K}$ edge was calculated at 0.7755 ± 0.0006 indicating an indium content of 22% in the ND for sample 010410. Additionally, an analysis of the strain / interatomic distances in HRTEM images of this sample reveals an average strain of the InGaN NDs of (4.0 ± 0.7)%, taking the GaN base part as zero strain reference. No misfit dislocations were observed. This can be converted into an In content of 28%. Both techniques lead to quite good agreement.

In comparison to sample 010410, sample 090410 was grown at a higher substrate temperature ($\Delta T_{\mathrm{sub},2} = 30°\mathrm{C}$). The heterostructure part started with the first InGaN ND, whereas it started with a low-temperature GaN barrier in 010410. The omission of a first low-temperature GaN barrier might be the reason why faceting of the sidewalls is not detectable for the first ND in contrast to sample 010410 (**Fig. 8.6d**). Bulging out started after the first InGaN disk, whereas it could be detected below the first InGaN disk in sample 010410 (see **Fig. 8.6b**),

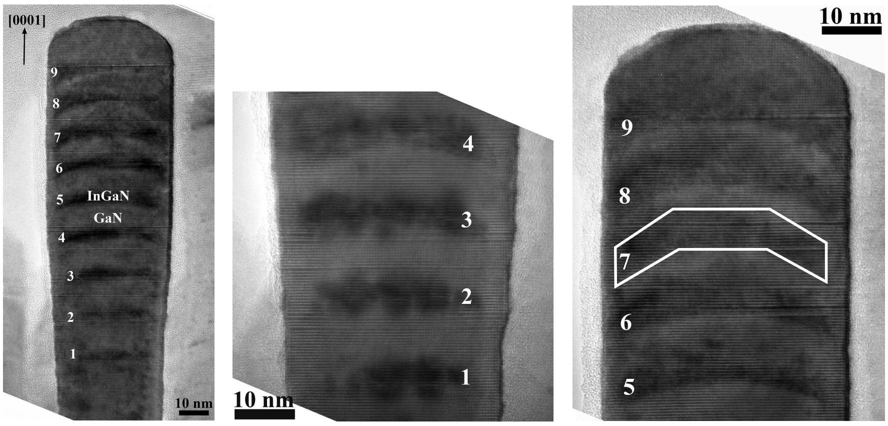

Figure 8.7: *HRTEM images of sample 090410 taken along* $\left[11\bar{2}0\right]$ *GaN zone axis.*

exactly at the beginning of the low-temperature GaN part. Undoped GaN NWs grown at a high substrate temperature (as the GaN base part) normally do not show faceted top surfaces. In sample 090410, the degree of faceting gradually increases from the lowest to the topmost ND. In the lower part of the ND stack, the nanowire diameter widens when going to the NW top. The lateral growth reduces the GaN spacer height from 14.5 nm between ND 1 and 2 (see **Fig. 8.7**) to 11 nm between ND 4 and 5. Whereas the interface between a GaN spacer and the InGaN ND above is relatively sharp, the interface between an InGaN ND and GaN spacer above is blurred. This is due to In diffusion as the effect of the substrate temperature which is too high for InGaN but relatively cold for GaN (i.e. no Ga diffusion into InGaN NDs). The diffusion is stronger than in sample 010410 which can be directly attributed to the higher substrate temperature.

A growth rate of 5.8 nm/min was calculated for the InGaN disks (5.5 nm/min for the GaN spacers; 4.6 nm/min GaN cap) by using the measured heights and the growth durations of 30 sec for each InGaN disk (100 sec for each GaN spacer; 180 sec for the GaN cap). These values are similar to those of the 010410 sample. However, they are lower compared to the GaN growth rates for the GaN/AlGaN samples (see p. 110) grown with the same Ga effusion cell temperature, but at a higher substrate temperature. This points to a contribution to the axial growth rate from diffusion, which is reduced for the InGaN/GaN samples due to a lower substrate temperature.

Samples with low In content For samples with lower In content, no NDs could be resolved in TEM analysis. Three samples grown at $T_{In} = 720°C$ and different substrate temperatures ($T_{sub,2} = 565°C - 610°C$) were examined. This can be attributed to a insufficient material contrast for this low In content. The samples,

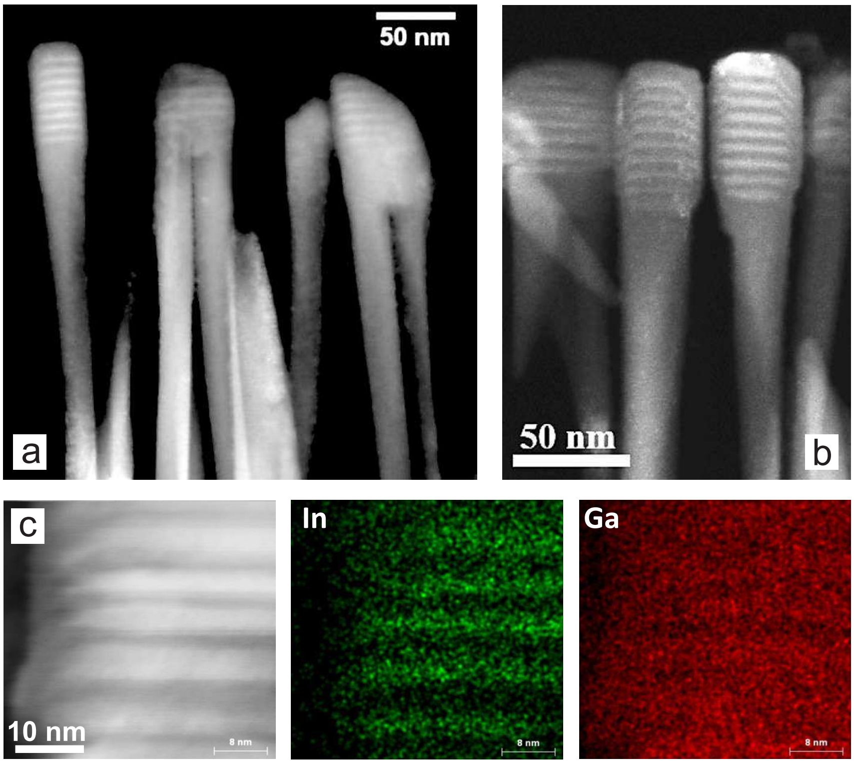

Figure 8.8: *TEM images of a sample grown at a relatively low substrate temperature of* $T_{\mathrm{sub},2} = 530°\mathrm{C}$ *(sample 020709). InGaN parts appear in bright. (a) View along the* $[1\bar{1}00]$ *GaN zone axis (b) View along the* $[11\bar{2}0]$ *GaN zone axis (c) View along the* $[1\bar{1}00]$ *GaN zone axis plus EDX maps for In and Ga. Diffusion of In into the GaN spacers is observed.*

however, exhibit InGaN-related PL emission peaked in the range of 2.4 eV to 2.5 eV at 4K. For a sample with thick InGaN part ($T_{\mathrm{sub},2} = 565°\mathrm{C}$, $T_{\mathrm{In}} = 720°\mathrm{C}$), EDX mapping proved the presence of In and allowed a quantification to approx. 3%. This sample (011209) showed intense room temperature PL emission at 2.28 eV (FWHM 230 meV). Using the standard bowing equation (Eq. 1.1, p. 11), the peak energy corresponds to an In content of 26% in thin films, pointing to the presence of In-rich clusters.

Influence of low substrate temperature For a lower substrate temperature of $T_{\mathrm{sub},2} = 530°\mathrm{C}$, abrupt widening of the NW diameter with beginning of the heterostructure part was observed (sample 020709). For this sample, the heterostructure part was started with InGaN (28 sec), followed by 60 sec GaN. This widening lead to increased coalescence (**Fig. 8.8b**). EDX analysis revealed that even at this low substrate temperature In diffusion into the GaN spacer could not be avoided (**Fig. 8.8c**). As observed before, the shape of the NDs changes from flat disks to dome-like inclusions from the lowest to the topmost ND.

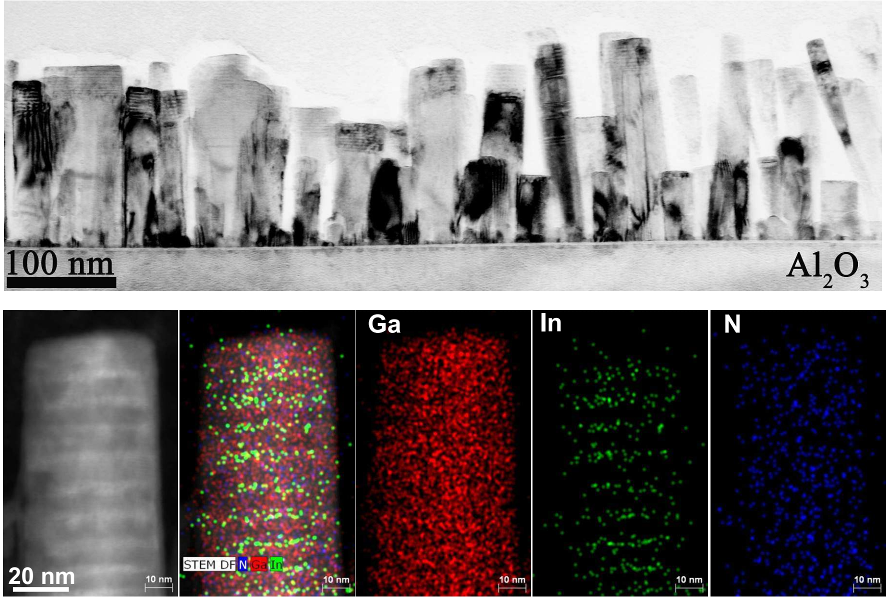

Figure 8.9: *Cross-section TEM images of a GaN/InGaN ND sample grown on c-plane sapphire taken along the GaN* $[11\bar{2}0]$ *axis. Top: Overall morphology. Bottom: EDX maps of different elements.*

GaN/InGaN NWs on sapphire A different ND morphology was observed for the GaN/InGaN NWs (sample 100610) grown on sapphire with a Si_xN_y interlayer (see Section 3.3, p. 45 for details of the substrates and the Si_xN_y interlayer)(1). TEM images revealed flat disks. Compared to the samples shown before (010410, 090410), this sample was grown at a reduced Ga flux (60% of the standard Ga flux both for the GaN base and for the heterostructure part), to suppress the tendency of coalescence which is more pronounced for growth on sapphire substrates. Accordingly, the In flux was reduced from $T_{sub} = 780°C$ to $T_{sub} = 755°C$ to keep the impinging flux ratio constant. As for the other samples, In diffusion into the GaN spacers was observed (**Fig. 8.9**). The ND height is 1.85 nm, the ND-to-ND distance 5.5 nm, leading to a growth rate of 3.7 nm/min (2.2 nm/min) for the InGaN NDs (GaN spacer). The average NW diameter is in the range of 50 nm to 90 nm, which is larger than for NWs on Si(111). Possibly, the lower metal flux rate (i.e. a higher III-V ratio, since the N flux was kept constant) avoids the formation of inclined side facets. However, more structural analysis is needed for clarification.

---

(1) Note that due to the radiation heating of the substrates during growth (see Section 2.2, p. 22) the substrate temperatures differ between different substrate materials due to different heat absorption. The substrate heater temperature was raised by 20°C during growth of the GaN base part of sample 100610 to compensate fot the lower thermal absorption of sapphire compared to Si, however it is not guaranteed that this was sufficient.

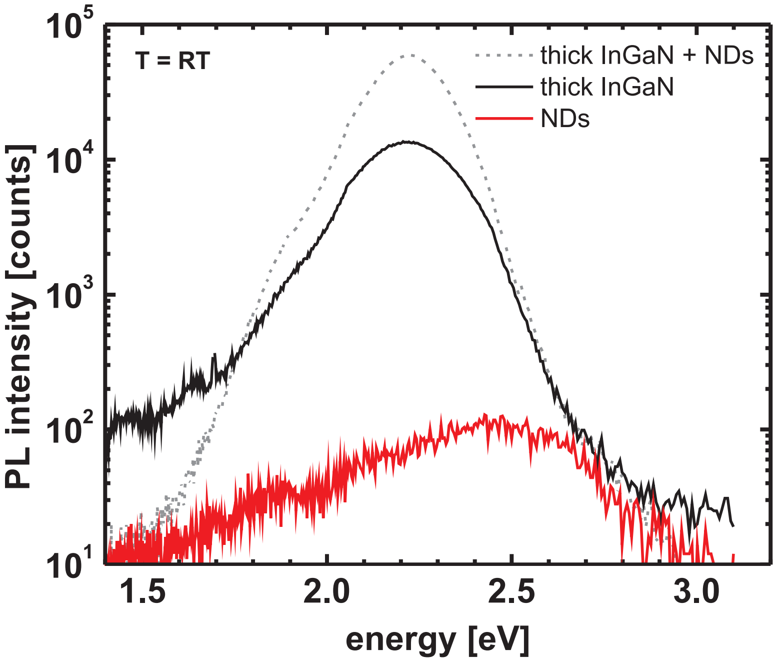

Figure 8.10: *Room-temperature PL spectra of samples grown at the same In flux and substrate temperature, but with different sample designs (samples 110210, 100310, 150310).*

8.3. Optical investigation

Single heterostructures vs. nanodisks Intense RT PL emission was observed for samples with a single thick InGaN top part (i.e. without NDs). The emission intensity exceeded that of similar samples with InGaN NDs by two orders of magnitude. Samples with thick InGaN part plus ND part exhibited similar PL properties in peak position and intensity compared to the samples with thick InGaN only, showing that this part dominates the emission properties in compound structures (**Fig. 8.10**).

PL emission of heterostructures with single long InGaN part In the 4K PL spectra of a InGaN/GaN heterostructure sample without NDs (220909), several bands could be identified. At 3.42 eV the near band edge contribution of the GaN base is visible. Its intensity is strongly suppressed compared to pure GaN NWs (**Fig. 8.11**).

The intensity of the region around 3.0 eV to 3.3 eV is higher than those of the near band edge. In contrast to the GaN reference, there is not only the 3.27 eV DAP peak plus its LO phonon replica (with redshift of 92 meV, see Sec. 5.2.3, p. 80) visible, but also a second contribution. This peak is centered at 3.16 eV and exhibits a higher intensity than the 3.26 eV emission, which rules out that it

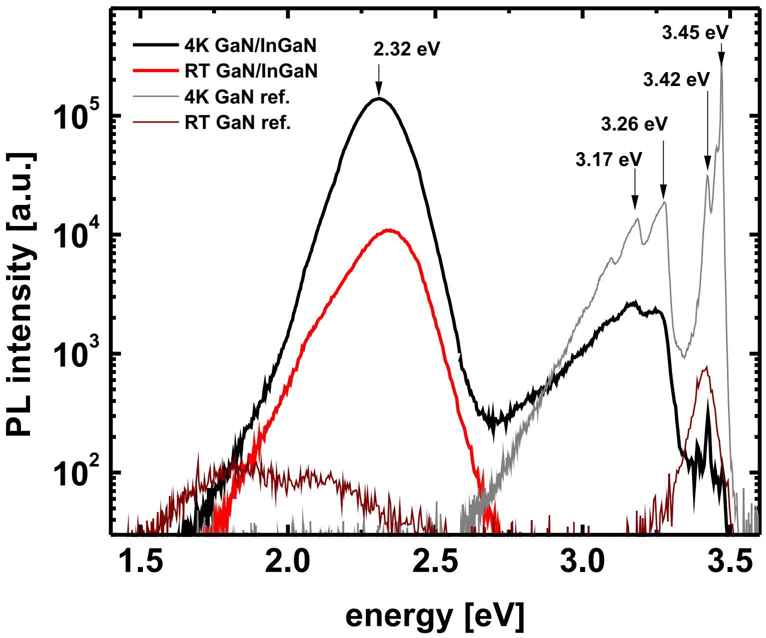

Figure 8.11: *PL spectra of a InGaN/GaN NW heterostructure (single thick InGaN part, sample No. 220909) compared to reference GaN NWs (010710).*

arises from a phonon replica alone. These emissions were found in all InGaN/GaN heterostructure samples, both with thick InGaN as well as with NDs. The position did not shift with In content. It could not be detected in the room temperature spectra. The InGaN-related emission is found at 2.32 eV (FWHM 190 meV) at 4K. This emission exhibits a high temperature stability. The GaN reference has no emission in this region.

The emission energy of the InGaN-related emission can be lowered by increasing the In flux. In **Fig. 8.12**, the PL spectrum of the above mentioned sample is compared to two other samples grown with the same conditions except a higher In flux. The position of the emission peak is shifted from 2.32 eV to 1.78 eV by increasing the In flux by a factor of 3.2. The peak positions allow to calculate the In concentration by using Eq. 1.1 (p. 11). A bowing parameter of $b = 2.5\,\text{eV}$, and bandgap energies of $E_{\text{gap}}(\text{In}) = 0.7\,\text{eV}$ and $E_{\text{gap}}(\text{Ga}) = 3.478\,\text{eV}$ were used. The results compared with an estimation of the In concentration via the Ga/In flux ratio

$$[\text{In}] = \frac{\text{BEP}_{\text{In}}}{\text{BEP}_{\text{In}} + \text{BEP}_{\text{Ga}}}$$

are presented in **Tab. 8.3**. The emission peak energy decreases monotonically with increased In flux. However, the resulting In concentrations are systematically higher than those calculated by the flux ratios.

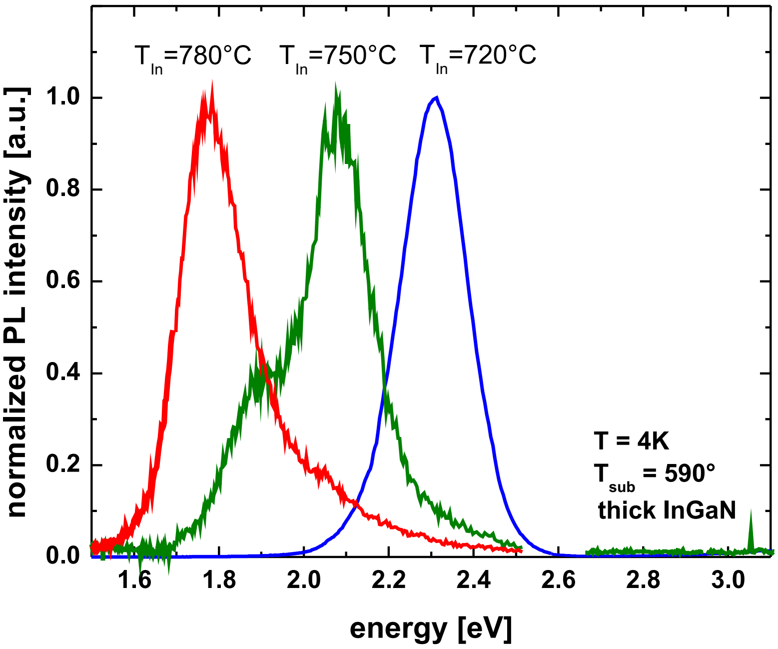

Figure 8.12: *Normalized PL spectra (measured at 4K) of InGaN/GaN NW heterostructures with single InGaN top part grown with different In fluxes (samples 040609, 090609, 220909).*

Table 8.3: *Comparison of 4K PL peak position and In flux for NW samples with thick InGaN top part.* BEP_{Ga} *is* 3.9×10^{-7} *mbar for all samples.*

T_{In} [°C]	PL peak pos. [eV]	BEP_{In} [mbar]	[In] from PL	[In] from flux ratio	sample No.
720	2.32	5×10^{-8}	0.25	0.11	220909
750	2.09	9×10^{-8}	0.31	0.18	090609
780	1.78	1.6×10^{-7}	0.40	0.29	040609

Influence of the substrate temperature The PL emission peak energy varies not only with the Indium flux, but also with the substrate temperature during growth of the InGaN part. A higher substrate temperature leads to higher In desorption and therefore to a reduced In content.

Room temperature PL spectra of three different NW samples with InGaN NDs (nominal thickness 4 nm) grown at different substrate temperatures $T_{sub,2}$ and the same In flux of 1.7×10^{-7} mbar (T_{In}=780°C) are compared in **Fig. 8.13**. An increase of the substrate temperature leads to an increase of the emission peak energy. For the sample grown at $T_{sub,2}$ = 565°C, the emission peak is centered at 2.32 eV (534 nm) with a full width at half maximum (FWHM) of 440 meV. The emission was blueshifted to 2.54 eV (488 nm) (FWHM 390 meV) when the

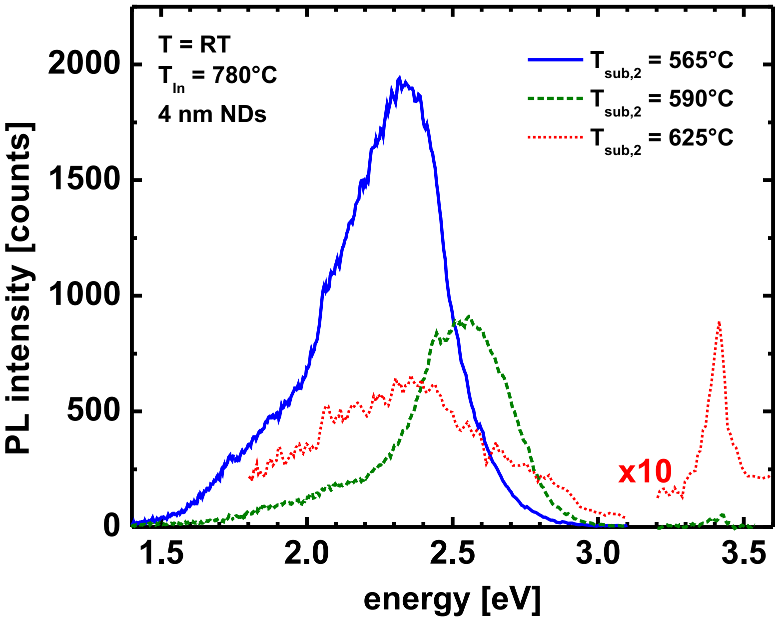

Figure 8.13: *Room temperature PL spectra for three samples containing nine nominal 4 nm thick NDs grown at the same In cell temperature (T_{In} = 780°C) but different substrate temperatures (010410, 090410, 120410). The intensity of the sample with the highest $T_{\mathrm{sub},2}$ was multiplied by 10 for better visibility. The peak at 3.41 eV originates from the GaN base part. See Figs. 8.6 and 8.7 for TEM images of sample 010410 and 090410, respectively.*

substrate temperature was increased by 35°C. For both samples, a shoulder was observed on the low energy side in the range of 2.0 eV to 1.7 eV (2.2 eV to 1.8 eV) for the first (the latter) sample. This can be interpreted as a sign of phase separation with the formation of In-rich regions. This effect becomes more pronounced for the sample with the highest substrate temperature, where only a weak and broad emission centered at 2.37 eV was detected. However, a faint high energy contribution at 2.78 eV is still present. The overall intensity was decreasing with increased substrate temperature.

Influence of ND thickness When reducing the ND thickness from 4 nm to 2 nm, the emission energy at RT is raised from 2.32 eV (543 nm) to 2.42 eV (512 nm) and the FWHM is reduced from 420 meV to 240 meV (**Fig. 8.14**). For the sample with the thinnest NDs (1.3 nm) the peak energy is further increased to 2.44 eV (508 nm). The FWHM increases again to 390 nm, which can be attributed to the pronounced relative influence of monolayer thickness fluctuations for such thin NDs. The spectra are broadened on the low energy side which could originate from phase separation but also from strain inhomogeneities. TEM images (cf. **Fig. 8.7** and **Fig. 8.8**) suggest a different In concentration between the top and the bottom

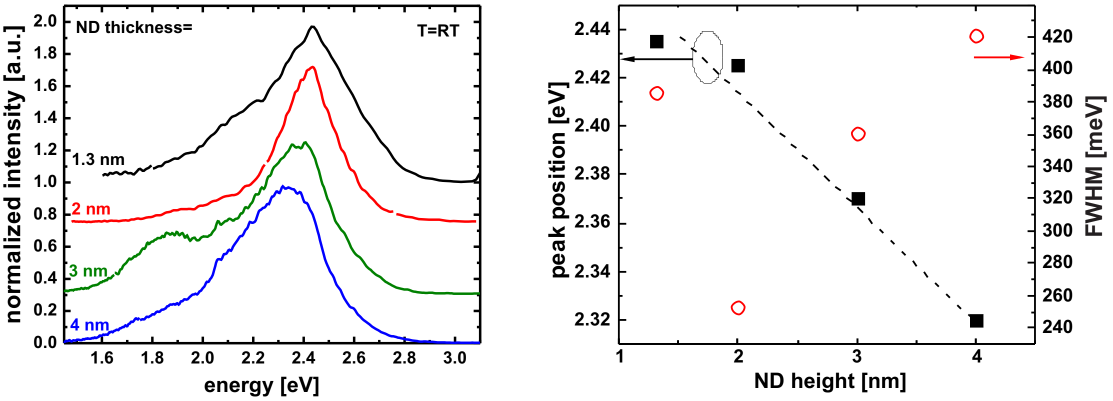

Figure 8.14: *Left: PL spectra (at RT) for four samples with different ND heights grown at* $T_{\text{sub},2}$ = *565°C (sample No. 260410, 190410, 150410, 010410). Right: Corresponding emission peak positions and FWHMs.*

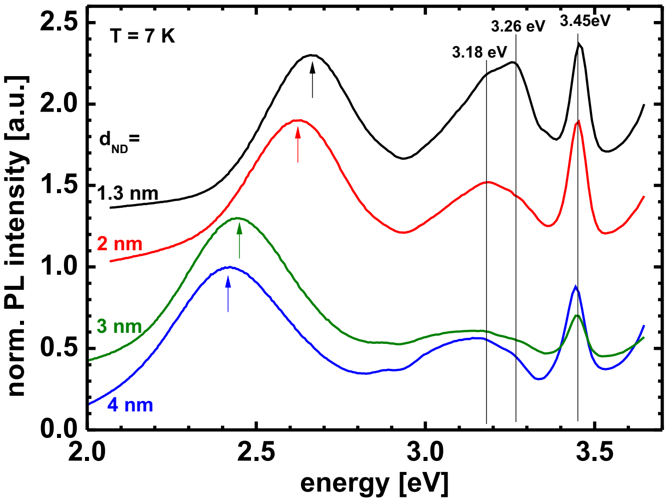

Figure 8.15: *PL spectra (at 7K) for four different samples (same as in Fig. 8.14) with different ND heights grown at* $T_{\text{sub},2}$ = *565°C. Measurements were performed at the JLU Gießen.*

of the NDs. PL spectra recorded at 7K are presented in **Fig. 8.15**. Here, the same trend for the influence of the ND thickness is observed. Additionally, the 3.45 eV emission originating from the GaN base part and the 3.18 eV/3.27 eV emission band is detected. These contributions show a pronounced quenching with raised temperature and are, therefore, not detectable in the RT measurements.

The energy shift is less pronounced than it is expected for quantum wells along the polar direction, where normally a strong influence of the quantum-confined Stark effect is expected. For comparable InGaN/GaN nanowire structures with single quantum wells with thicknesses between 2 nm and 9 nm, no evidence for QCSE was recently reported [Arm10]. Time-resolved PL on ensemble and single InGaN quantum disks also indicated the absence of an internal electric field [Bar09].

Temperature dependence For the sample with 4 nm NDs (010410), the temperature dependence of the emission is shown in **Fig. 8.16**. When raising the temperature from 7 K to room temperature, the emission peak is redshifted by 100 meV. This trend is followed monotonically for temperatures from 50K to room temperature without the often observed S-shape behavior, which is a sign for alloy fluctuations and carrier localization (see e.g. Ref. [Hol00] for MBE and MOCVD grown InGaN quantum wells). The emission intensity exhibits a high temperature stability: at 200 K (300 K), the intensity of the ND peak is still 25% (8%) of the 7 K value, which does give evidence for localization effects. The activation energy (determined in the temperature range of 150K to 300K) is 45 ± 4 meV. A similar monotonous temperature dependence was recently reported by Chang *et al.* [Cha10] for comparable samples with 7 nm high InGaN nanodisks.

This temperature behavior is significantly different for samples with a single thick InGaN part (**Fig. 8.16**). Here, first a blueshift of 28 meV with increasing temperature from 10 K up to 200 K was found. Further increase of the temperature results in a redshift. However, the peak position at 300 K is still blueshifted by 20 meV compared to the 10 K value. The inhomogeneity of the peak shape (broadening at the high energy side) points to several contributions that differ in their temperature behavior.

The peak intensity at 200 K (300 K) is 20% (8%) of the 10 K intensity, giving these structures a temperature stability which is comparable to the intentionally grown NDs. One possible explanation for this behavior is the formation of In-rich clusters due to alloy fluctuations in the InGaN base part. Spontaneous formation of In rich clusters or quantum dot-like inclusions was reported in the literature: In Ref. [Nis00] quantum dot formation (sizes in the range of 1.5 nm to 3 nm) in InGaN films with 22% In by HRTEM is shown and attributed to a phase separation process. However, it is not clear whether these clusters were generated during TEM observation, since the high intensity electron beam of a TEM is known to introduce In clustering [Sme06]. Local strain inhomogeneities are proposed as a different process that can lead to exciton localization in InGaN films [Sou07]. The activation energy (determined in the temperature range of 120K to 300K) is 25 ± 4 meV, which is lower than for the ND sample.

Samples on sapphire In general, InGaN/GaN NWs grown on sapphire exhibited a weaker PL intensity. This is mainly caused by the not fully optimized buffer

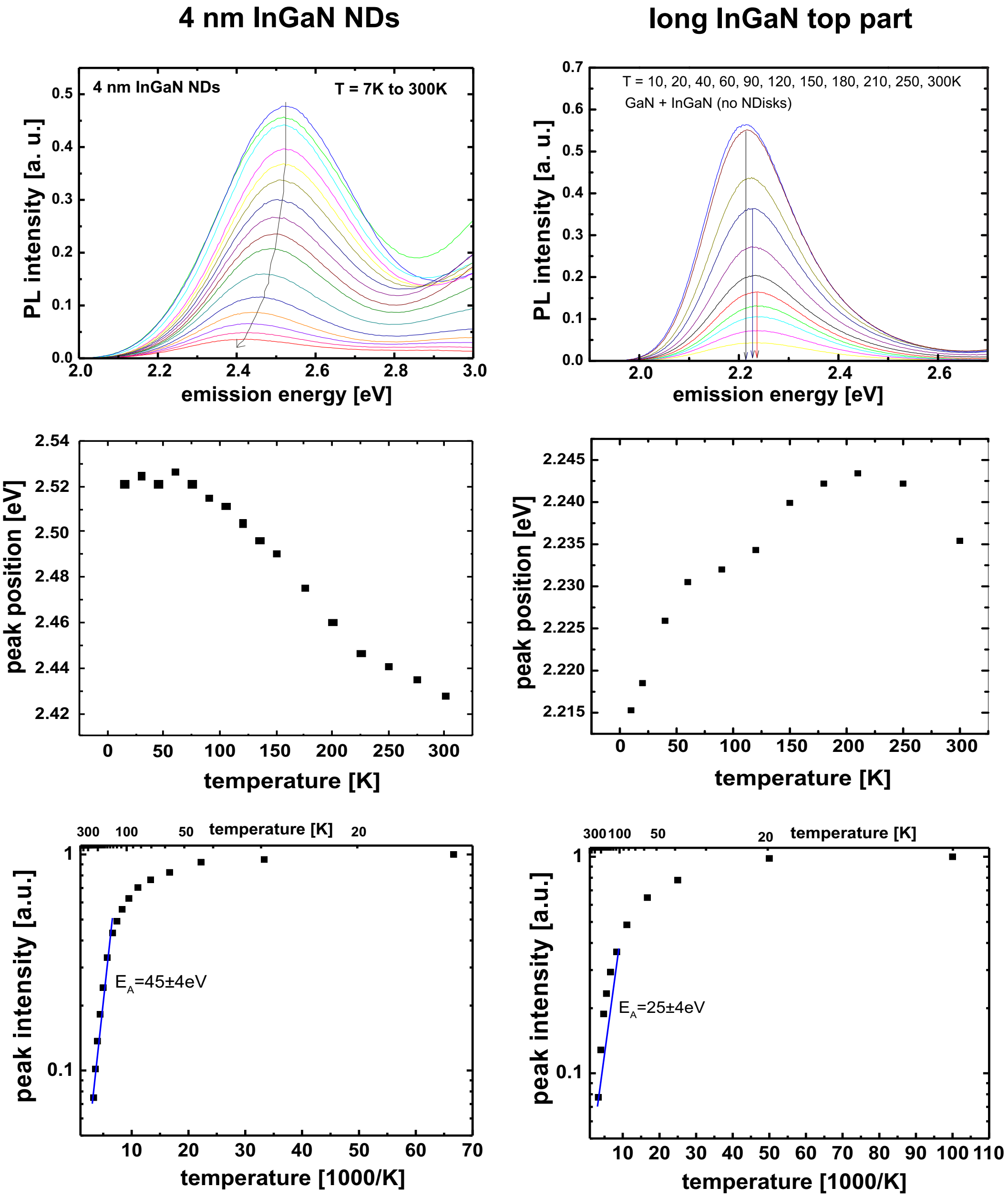

Figure 8.16: *Temperature-dependent PL measurements of two InGaN/GaN samples. Left column: sample with 4 nm thick NDs (010410). Right column: sample with long InGaN top part (100310). From top to bottom row: PL curves, peak position as a function of temperature, peak intensity as a function of temperature. Whereas the peak position decreases monotonically with temperature for the ND sample, there is an increase for temperatures up to 200K for the sample with a long InGaN part. The reduction of intensity between 15K and 300K is similar for both samples, however, as also indicated by the different activation energies, the ND sample exhibits a higher temperature stability for temperatures up to 250K.*

layer and substrate temperatures. Due to the less effective heating of the sapphire substrates compared to Si substrates during growth (see Section 3.3, p. 45 for details), the NWs on sapphire suffer from a high density of basal plane stacking faults (BSFs). These BSFs drastically reduce the luminescence intensity.

Most suitable for utilization as DOTSENSE sensors were GaN/InGaN NW samples with thick InGaN top part, since they exhibit a higher PL emission intensity than the nanodisk samples. These samples were grown on 2" sapphire wafers with a nitridated Si interlayer as described on p. 49. The substrate temperature for the GaN part was 695°C as measured by pyrometer, which is equivalent to a substrate heater temperature of 888°C. Low-temperature PL spectroscopy of later grown GaN NWs on sapphire (see **Fig. 3.18**, p. 53) shows a clear increase of the near band edge (NBE) emission intensity with substrate temperature. Only the sample grown at the highest investigated heater temperature of 1000°C exhibits emission properties comparable to GaN NWs on Si.

In **Fig. 8.17**, the room temperature photoluminescence of four GaN/InGaN single heterostructure samples grown on sapphire is presented. These samples were grown at different In fluxes and substrate temperatures for the In top part as indicated in the graph. The PL peak emission energy exhibited the same dependence on the In flux and the substrate temperature which were found for the samples grown on Si(111) substrates. An emission range of 1.8 eV – 2.7 eV (690 nm – 460 nm) can be covered with these samples. The maximum intensity was achieved around 2.2 eV (565 nm), as observed in the case of NWs grown on Si(111).

8.4. Conclusions

In summary, GaN/InGaN nanowire heterostructures were grown on Si(111) and sapphire wafers. Two concepts for the active InGaN region, one comprising of thin InGaN nanodisks separated by GaN barriers, the other comprising of a single thick InGaN top part were analyzed. The peak position of the PL emission is influenced by the substrate temperature and the In flux. The optimum in emission intensity was achieved around 2.2 eV – 2.4 eV (565 nm – 515 nm). This energy range is in agreement with the results recently presented in Ref. [Wöl12].

Both nanowire designs exhibited a high temperature stability of the PL emission, which can be attributed to localization effects. The PL emission energy is redshifted with increased ND height. However, the decrease of PL emission peak position with increasing ND thickness is relatively small, which rules out a

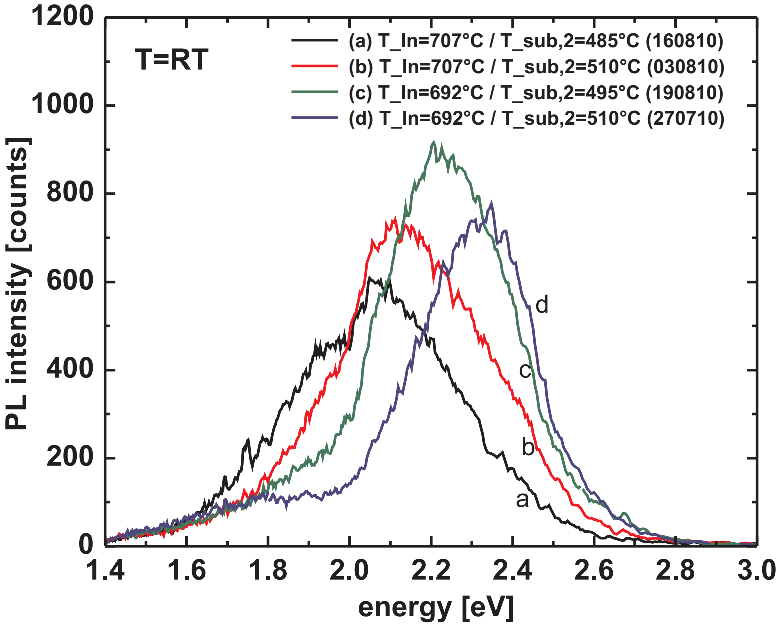

Figure 8.17: *Room temperature photoluminescence of four GaN/InGaN single heterostructure samples grown on sapphire with different In fluxes and substrate temperatures* $T_sub, 2$ *for the In top part. The substrate temperature for the GaN NW base part was 695°C for all samples.*

strong influence of electrical fields in these polar structures. HRTEM observations exhibited the formation of dot-like nanodisks with faceted sidewalls.

The strongest PL emission intensity was recorded for GaN/InGaN single heterostructure nanowires without intentionally grown NDs. The temperature dependence, i.e. high temperature stability and the "S-shaped" behavior of the PL peak position point to the formation of In-rich clusters inside these nanowires.

Growth of GaN/InGaN nanowires on sapphire was achieved using a thin Si interlayer (5 nm – 20 nm), which is practically transparent ensuring their applicability as sensors in the DOTSENSE device.

Diffusion of In into the GaN spacer above was observed for all substrate temperatures, leading to a blurred upper interface of each ND, whereas the lower interface was relatively sharp. The effect became more pronounced for higher substrate temperatures. The NW diameter increased at the beginning of the heterostructure part. This effect was more pronounced for high In fluxes and low substrate temperatures. The comparison with samples with low-temperature GaN top part instead of InGaN showed that this widening is strongly enhanced for lower substrate temperatures, and reduced by the presence of In. In atoms were shown to have a surfactant effect for InGaN growth.

9. Conclusions

What makes nitride nanowires fascinating is the fact that they are both an ideal system for fundamental research concerning the group III-nitride growth and material properties as well as that they are promising for various applications.

The nucleation and growth of GaN nanowires by MBE was studied in detail. The main focus was put on Si(111) as the substrate material. Under optimized parameters, GaN NWs with high structural quality and no wetting layer could be grown. These structures provide sharp and intense near band edge PL emission with a typical FWHM of 1.5 meV at 4K for n.i.d. NWs. High Mg doping levels lead to the formation of stacking faults. These were independently detected by PL and HRTEM. No sign for lateral growth was present for n.i.d. GaN NWs, whereas the NW morphology is characteristically changed upon doping with Si or Mg.

The growth process was transferred to other substrates than Si(111), namely sapphire and diamond. By employing a thin Si buffer layer, GaN NWs can be grown on sapphire in similar quality as on Si(111). Sapphire is of great interest for sensing applications since it allows PL excitation and readout through the substrate making these structures suitable for operation in harsh environments.

Nanowire heterostructures (NWHs) containing GaN nanodisks embedded in AlGaN and AlN NWs were grown. The PL emission wavelength could be controlled by the ND thickness and Al concentration. For Al concentrations in the range of 25% - 35% a high temperature stability of the emission intensity was observed. The difference in adatom kinetics between Ga and Al was directly reflected by the formation of an Al(Ga)N shell for GaN/Al(Ga)N NWs. The characteristics of this shell were shown to have strong influence on the PL emission properties of these GaN NDs. Additionally GaN/InGaN NWHs were grown and analyzed with respect to their PL emission and morphological properties.

By combining the observations made regarding axial/lateral growth rates and NW morphology within the different NWs and nanowire heterostructures, additional insight in the growth kinetics was provided (see Section 3.5, p. 57 for details). A superposition of adatom desorption, diffusion and geometrical effects is present, its quantification depending on the type of adatom, the impurity concentration and on the growth temperature.

Single NWs were electrically contacted by photolithography and e-beam-assisted Pt deposition. Special masks for photolithography were developed to allow contacting random-oriented NWs. The conductivity can be adjusted over several orders of magnitude by controlling the doping level. However, it is currently technologically not feasible to contact individual NWs in a reproducible and efficient way. The utilization of single NWs in electronic devices needs the development of a specific new technology.

In this work, several questions about nucleation and growth of GaN NWs and the formation of nanodisks could be resolved. However, there is plenty of room for future research. The parameters for NW growth on sapphire and diamond need further optimization.

Especially for InGaN, many issues like defect formation, In segregation, the range of achievable and controllable In content needs further studies. InGaN is the ternary III-nitride compound with the largest commercial relevance since it is used for white LEDs.

The idea of Nanowire LEDs seems quite obvious [Kik06]. However, a comparison to conventional LEDs or a proof of advantages of nanowire LEDs is still missing [Waa11]. Electrical contacting will remain a big problem. Devices where individual contacts to the NWs are necessary are difficult to realize. More promising seems the utilization of NWs as sensors with purely optical detection of changes in photoluminescence as shown in the DOTSENSE project. For commercialization, questions like the long term stability need to be answered.

A. Appendix

A.1. Sample processing for single NW contacts

In the following, the procedure to contact NWs individually as presented in Chapter 6 is explained step-by-step.

Steps for photolithographic contacts:

Nanowire suspension As first step, a suspension of the NWs in a solvent is made. A 5 mm × 5 mm piece of the as-grown sample is put in a beaker together with 15 ml of acetone. The NWs are removed from the substrate by ultrasonic agitation and (if necessary) scratching with a single-use glass pipette. The suspension is bottled and can be stored for further use.

Substrates An insulating substrate is needed. In most cases, sapphire wafers (*c-plane*, single-sided polished) were used. Additionally, also Si wafers with 100 nm thermal oxide were used. Pieces of 8 mm × 8 mm were cleaved and cleaned with a Q-tip under acetone, followed by two further cleaning steps with acetone and isopropanol in the ultrasonic bath. The samples are blown dry by nitrogen.

Dispersion of NW suspension The bottled NW suspension is put shortly into an ultrasonic bath. With a single-use glass pipette typically 2 to 3 drops are put onto one substrate. Each drop is allowed to dry before the next one is applied. If the solvent does not fully evaporate, the sample is blown dry using nitrogen.

The samples are then cleaned on a photo-resist spinner to remove unwanted debris. The NW adhesion is strong enough to prevent their unintentional removal. The used parameter are: Ramp acceleration 1, rotation speed 4000 rpm, duration 40 sec, ramp decelerating 0. During the rotation, the samples are uninterruptedly sprinkled with acetone and isopropanol, and then blown dry.

Fig. A.1a to f show images of the different steps that will be explained in the following.

Spin-on photoresist The sample is not removed from the spinner. While not rotating, the photoresist *Shipley Microposit S1805* is dropped on the sample. This photoresist is designed to produce an approx. 0.5 µm thick layer (hence the 05 in the name) and is capable of a minimum structure size of 0.48 µm according to the manufacturer. Rotation parameters are the same as above. To improve the contact between substrate and mask during the exposure, the photoresist can be removed at the edges of the substrate. (The photoresist can form bulges at the substrate edges which hinder a close contact to the mask and reduce the quality (sharpness) of the exposure.) With a piece of lint-free cloth coiled around a Q-tip and soaked with acetone the substrate edges are carefully wiped clean. A softbake in the oven at 90°C for 45 min is performed to prepare the resist for exposure.

Mask exposure and developing The samples are transferred to the mask-aligner (*Karl Suss MJB3*) and put in position under the mask. The mask layout is shown in **Fig. A.2**. The mask-to-substrate surface distance must be carefully adjusted to achieve a sharp image. Exposure is done in contact-mode for typ. 2.8 sec for sapphire substrates or 3.3 sec for Si substrates. The actual exposure time has to be tested since it varies with the lamp power (typ. 330 W) and completed operating hours (lamp service life).

Developing is done in the diluted developer (5 parts DI-water : 1 part developer) at room temperature for typ. 5.5 sec for Si substrates and 7.5 sec for sapphire substrates. The developing process is stopped by putting the samples in DI water. The quality is checked under a optical microscope.

Metallization and Lift-off The samples are glued on to an object glass plate with a small amount of photoresist *Shipley Microposit S1818* and baked by 90°C for 30 min. Alternatively the samples can be glued on a copper plate for better heat dissipation during evaporation. This can facilitate lift-off when evaporating metals at high temperature (e.g. Pt), since the photoresist polymerizes when exposed to high temperatures. The photoresist is then hard to remove.

Metals are evaporated using a e-beam evaporator: The metalization scheme is 20 nm Ti, followed by 20 nm Pt and 70 nm Au. Titanium is the most suitable metal to form ohmic contacts on n-type GaN, gold has a high conductivity to allow thin low-resistivity circuit paths. The platinum intermediate layer was introduced to prevent Au and Ti intermixing during annealing.

The excess metal and the photoresist is removed under acetone in the ultrasonic bath. The ultrasonic bath is driven with a low voltage (typ. 70 V to 90 V instead of 230 V) to prevent damage of the structures.

The samples are now ready for measurement. However, in most cases annealing is necessary to achieve good contacts. For that, the samples are heated under vacuum as stated in the respective measurement section.

Steps for e-beam-assisted Pt deposition:

For this work, NWs were not only contacted by photolithography, but also by e-beam-assisted platinum deposition. This technique allows to contact individual NWs which were dispersed on Si wafers with a 100 nm SiO_2 insulating layer.

Since it would be too time-consuming to write all contacts including the large contact pads with the e-beam system a special photolithography mask with contact pads and open contact terminals is used (see **Fig. A.3**). The processing steps are the same as for the photolithographically contacted NWs with the difference that the NW suspension is applied onto the samples *after* the lithography and metalization process.

The samples were transferred into a scanning electron microscope (SEM) and focused ion beam (FIB) system (manufacturer: *Carl Zeiss*; model: Gemini, NVision 40) system with an add-on that allows to introduce a metal-organic Pt compound gas trough a thin nozzle which can be placed in close vicinity to the sample surface. The e-beam(1) dissociates the gas and metallic Pt is deposited on the desired spots on the sample. Individual contacts have to be drawn for each NW limiting the overall throughput. The percentage of successfully contacted wires was between 30% and 40%.

---

(1) An alternative attempt of contacting NWs by focused Ga ion beam (FIB)-assisted Pt deposition proved unsuccessful since leakage current paths through the SiO_2 insulating layer were introduced. Consequently, the recorded I-V curves were determined by current through the Si substrate, which was much higher than through the individual NWs.

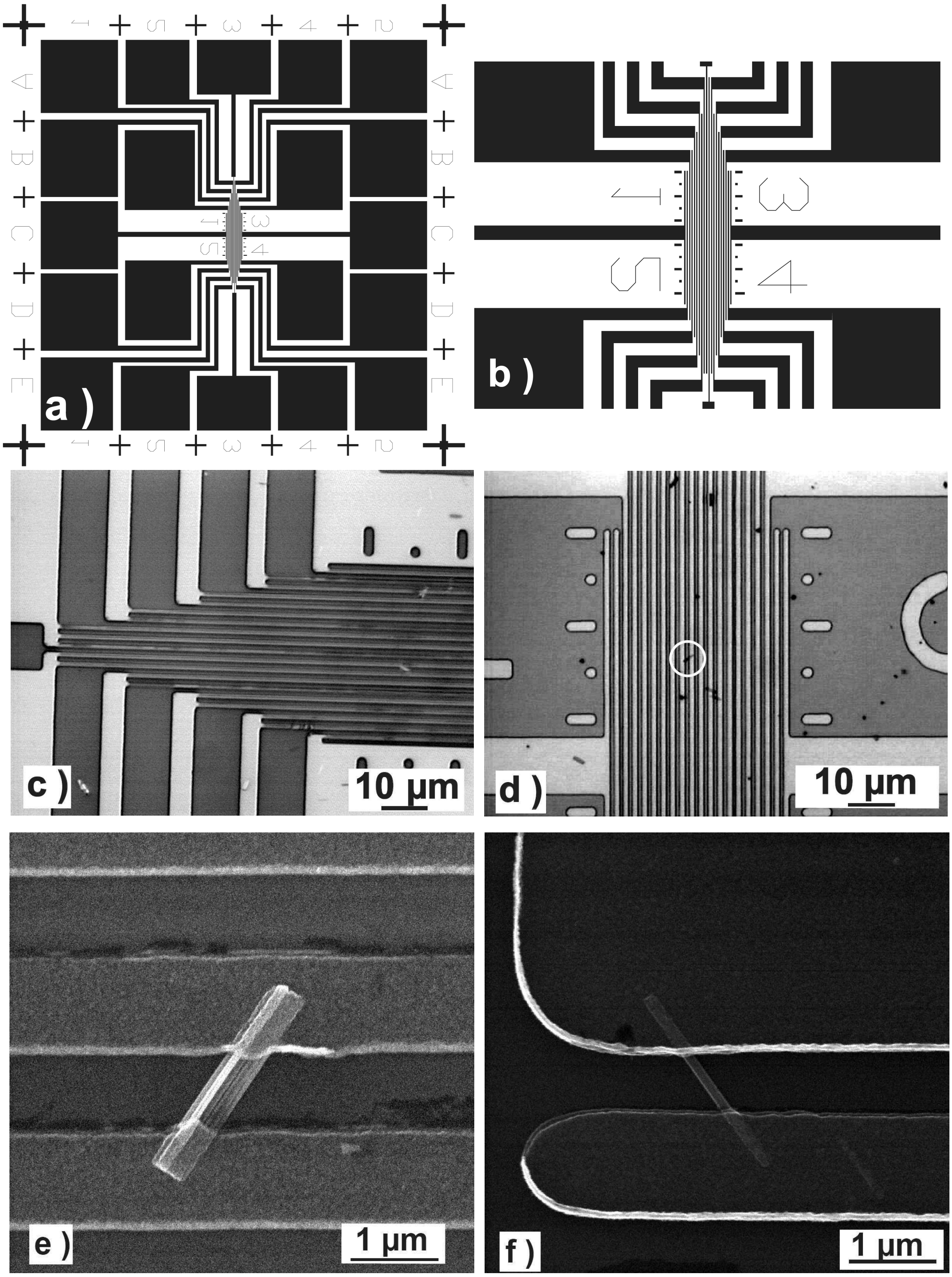

Figure A.1: *(a) Photolithography mask for contacting single NWs. 1 mm by 1 mm crop (measured form the centers of the big alignment crosses at the edges). The whole mask layout is shown in Fig. A.2. (b) Detail from (a) showing the 1 µm wide terminals in the center. (c) and (d) Optical microscope images: (c) Developed structure. (d) Sample after metalization and lift-off. One NW is marked with a circle. (e) SEM image of NW bundle and (f) a single NW.*

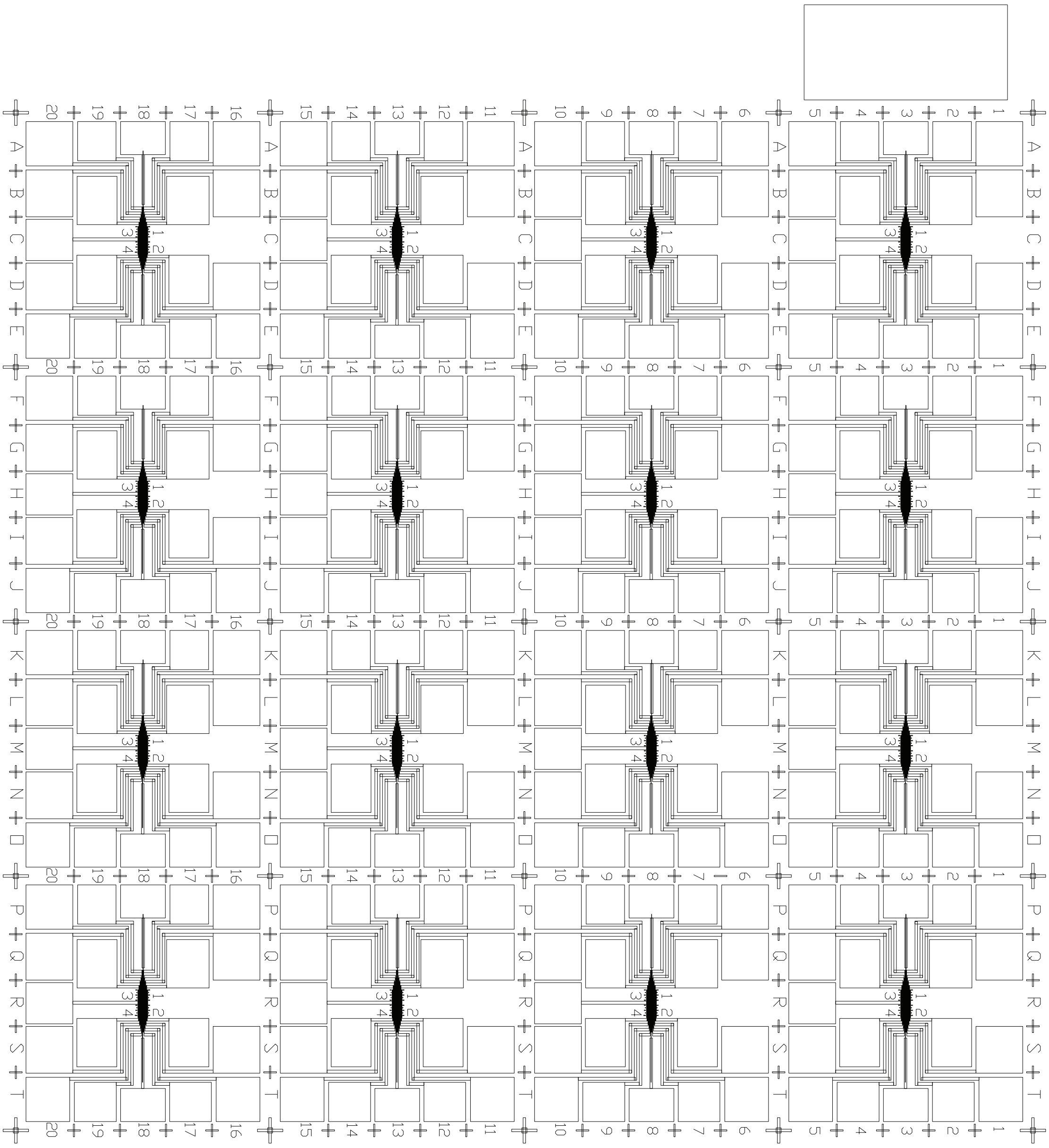

Figure A.2: *Photolithography mask layout for contacting single NW by photolithography only. The whole area is 4 mm by 4 mm (excluding the big rectangle in the upper right that determines the mask orientation). Sixteen equal areas with 19 contact pads each are present, allowing a high number of NWs to be addressed on one sample. Every contact pad can be identified by the row and column number grid. Compare also* ***Fig. A.1***.

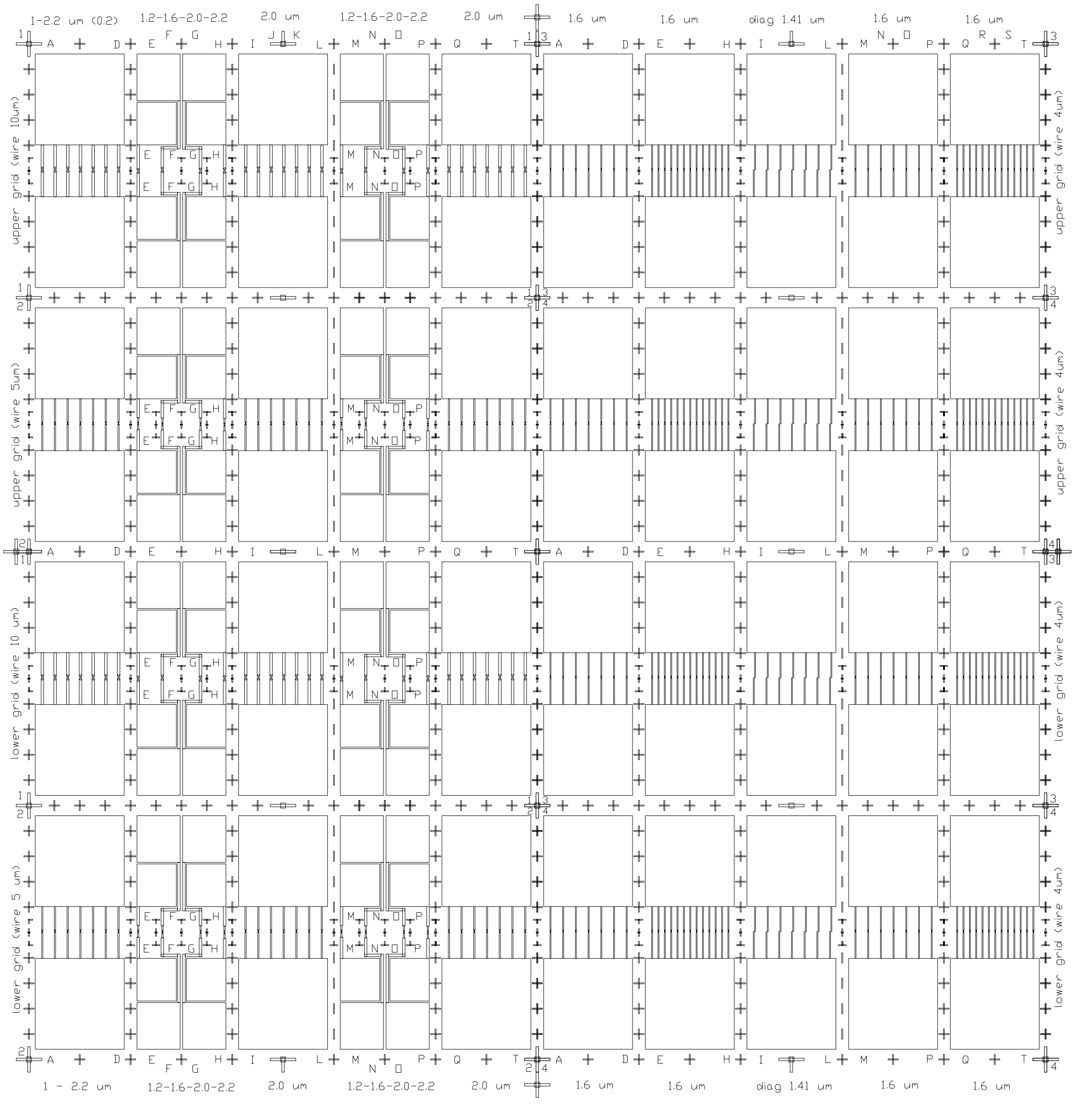

Figure A.3: *Photolithography mask layout for contacting single NW in a later e-beam-assisted step. Here, the contact terminals are brought close together leaving gaps between 1 µm and 2.2 µm (see inscription in the topmost or lowest line of the mask). This gap will be bridged by a single NW plus contacts that will be written by e-beam-assisted Pt deposition in a later step. The whole area is 4 mm by 4 mm (measured from the centers of the four large alignment crosses in the corners. Note: This mask was initially designed for dielectrophoretic alignment of NWs as presented in [Sta08] but proved useful for e-beam-assisted contacting too.*

Bibliography

[Ade03] C. Adelmann, E. Sarigiannidou, D. Jalabert, Y. Hori, J.-L. Rouviere, B. Daudin, S. Fanget, C. Bru-Chevallier, T. Shibata and M. Tanaka: *Growth and optical properties of GaN/AlN quantum wells*, Applied Physics Letters **82**, 4154 (2003).

[Amb96] O. Ambacher, M. S. Brandt, R. Dimitrov, T. Metzger, M. Stutzmann, R. A. Fischer, A. Miehr, A. Bergmaier and G. Dollinger: *Thermal stability and desorption of group III nitrides prepared by metal organic chemical vapor deposition*, Journal of Vacuum Science & Technology B: Microelectronics and Nanometer Structures **14**, 3532 (1996).

[Amb98] O. Ambacher: *Growth and applications of group III-nitrides*, J. Phys. D: Appl. Phys. **31**, 2653 (1998).

[Amb99] O. Ambacher, J. Smart, J. R. Shealy, N. G. Weimann, K. Chu, M. Murphy, W. J. Schaff, L. F. Eastman, R. Dimitrov, L. Wittmer, M. Stutzmann, W. Rieger and J. Hilsenbeck: *Two-dimensional electron gases induced by spontaneous and piezoelectric polarization charges in N- and Ga-face AlGaN/GaN heterostructures*, Journal of Applied Physics **85**, 3222 (1999).

[Amb03] O. Ambacher, M. Eickhoff, A. Link, M. Hermann, M. Stutzmann, F. Bernardini, V. Fiorentini, Y. Smorchkova, J. Speck, U. Mishra, W. Schaff, V. Tilak and L. F. Eastman: *Electronics and sensors based on pyroelectric AlGaN/GaN heterostructures*, physica status solidi (c) **0**, 1878 (2003).

[Ang97] H. Angerer, D. Brunner, F. Freudenberg, O. Ambacher, M. Stutzmann, R. Höpler, T. Metzger, E. Born, G. Dollinger, A. Bergmaier, S. Karsch and H.-J. Körner: *Determination of the Al mole fraction and the band gap bowing of epitaxial* $Al_xGa_{1-x}N$ *films*, Applied Physics Letters **71**, 1504 (1997).

[Arb09] J. Arbiol, S. Estradé, J. D. Prades, A. Cirera, F. Furtmayr, C. Stark, A. Laufer, M. Stutzmann, M. Eickhoff, M. H. Gass, A. L. Bleloch, F. Peiró and J. R. Morante: *Triple-twin domains in Mg doped GaN wurtzite nanowires: structural and electronic properties of this zinc-blende-like stacking*, Nanotechnology **20**, 145704 (2009).

[Arm10] R. Armitage and K. Tsubaki: *Multicolour luminescence from InGaN quantum wells grown over GaN nanowire arrays by molecular-beam epitaxy*, Nanotechnology **21**, 195202 (2010).

[Asc09] T. Aschenbrenner, C. Kruse, G. Kunert, S. Figge, K. Sebald, J. Kalden, T. Voss, J. Gutowski and D. Hommel: *Highly ordered catalyst-free and mask-free GaN nanorods on r-plane sapphire*, Nanotechnology **20**, 075604 (2009).

[Bar09] R. Bardoux, A. Kaneta, M. Funato, Y. Kawakami, A. Kikuchi and K. Kishino: *Positive binding energy of a biexciton confined in a localization center formed in a single* $In_xGa_{1-x}N/GaN$ *quantum disk*, Phys. Rev. B **79**, 155307 (2009).

[Bay50] R. T. Bayard and D. Alpert: *Extension of the low pressure range of the ionization gauge*, Review of Scientific Instruments **21**, 571 (1950).

[Bea98] B. Beaumont, S. Haffouz and P. Gibart: *Magnesium induced changes in the selective growth of GaN by metalorganic vapor phase epitaxy*, Applied Physics Letters **72**, 921 (1998).

[Bel11] A. Belabbes, L. C. de Carvalho, A. Schleife and F. Bechstedt: *Cubic inclusions in hexagonal AlN, GaN, and InN: Electronic states*, Phys. Rev. B **84**, 125108 (2011).

[Ben01] L. A. Bendersky and F. W. Gayle: *Electron diffraction using transmission electron microscopy*, Journal of Research of the National Institute of Standards and Technology **106**, 997 (2001).

[Ber06a] K. Bertness, A. Roshko, N. Sanford, J. Barker and A. Davydov: *Spontaneously grown GaN and AlGaN nanowires*, Journal of Crystal Growth **287**, 522 (2006).

[Ber06b] K. Bertness, N. Sanford, J. Barker, J. Schlager, A. Roshko, A. Davydov and I. Levin: *Catalyst-free growth of GaN nanowires*, Journal of Electronic Materials **35**, 576 (2006).

[Ber07] K. Bertness, A. Roshko, L. Mansfield, T. Harvey and N. Sanford: *Nucleation conditions for catalyst-free GaN nanowires*, Journal of Crystal Growth **300**, 94 , first International Symposium on Growth of Nitrides - ISGN-1 (2007).

[Ber08] K. Bertness, A. Roshko, L. Mansfield, T. Harvey and N. Sanford: *Mechanism for spontaneous growth of GaN nanowires with molecular beam epitaxy*, Journal of Crystal Growth **310**, 3154 (2008).

[BJ99] A. A. Burk Jr., M. J. O'Loughlin, R. R. Siergiej, A. K. Agarwal, S. Sriram, R. C. Clarke, M. F. MacMillan, V. Balakrishna and C. D. Brandt: *SiC and GaN wide bandgap semiconductor materials and devices*, Solid-State Electronics **43**, 1459 (1999).

[Bru97] D. Brunner, H. Angerer, E. Bustarret, F. Freudenberg, R. Hopler, R. Dimitrov, O. Ambacher and M. Stutzmann: *Optical constants of epitaxial AlGaN films and their temperature dependence*, Journal of Applied Physics **82**, 5090 (1997).

[Bun99] G. E. Bunea, W. D. Herzog, M. S. Ünlü, B. B. Goldberg and R. J. Molnar: *Time-resolved photoluminescence studies of free and donor-bound exciton in GaN grown by hydride vapor phase epitaxy*, Applied Physics Letters **75**, 838 (1999).

[Cal97] F. Calle, F. J. Sánchez, J. M. G. Tijero, M. A. Sánchez-García, E. Calleja and R. Beresford: *Exciton and donor - acceptor recombination in undoped GaN on Si(111)*, Semiconductor Science and Technology **12**, 1396 (1997).

[Cal99] E. Calleja, M. A. Sánchez-Gárcia, F. J. Sánchez, F. Calle, F. B. Naranjo, E. Muñoz, S. I. Molina, A. M. Sánchez, F. J. Pacheco and R. García: *Growth of III-nitrides on Si(111) by molecular beam epitaxy doping, optical, and electrical properties*, Journal of Crystal Growth **201-202**, 296 (1999).

[Cal00] E. Calleja, M. A. Sánchez-García, F. J. Sánchez, F. Calle, F. B. Naranjo, E. Muñoz, U. Jahn and K. Ploog: *Luminescence properties and defects in GaN nanocolumns grown by molecular beam epitaxy*, Phys. Rev. B **62**, 16826 (2000).

[Cal05] R. Calarco, M. Marso, T. Richter, A. I. Aykanat, R. Meijers, A. v.d. Hart, T. Stoica and H. Luth: *Size-dependent photoconductivity in MBE-grown GaN-nanowires*, Nano Letters **5**, 981 (2005).

[Cal07a] R. Calarco and M. Marso: *GaN and InN nanowires grown by MBE: A comparison*, Applied Physics A: Materials Science & Processing **87**, 499 (2007).

[Cal07b] E. Calleja, J. Ristić, S. Fernández-Garrido, L. Cerutti, M. A. Sánchez-García, J. Grandal, A. Trampert, U. Jahn, G. Sánchez, A. Griol and B. Sánchez: *Growth, morphology, and structural properties of group-III-nitride nanocolumns and nanodisks*, physica status solidi (b) **244**, 2816 (2007).

[Chè10] C. Chèze, L. Geelhaar, O. Brandt, W. Weber, H. Riechert, S. Münch, R. Rothemund, S. Reitzenstein, A. Forchel, T. Kehagias, P. Komninou, G. Dimitrakopulos and T. Karakostas: *Direct comparison of catalyst-free and catalyst-induced GaN nanowires*, Nano Research **3**, 528 (2010).

[Cha10] Y.-L. Chang, J. L. Wang, F. Li and Z. Mi: *High efficiency green, yellow, and amber emission from InGaN/GaN dot-in-a-wire heterostructures on Si(111)*, Applied Physics Letters **96**, 013106 (2010).

[Che01] C.-C. Chen, C.-C. Yeh, C.-H. Chen, M.-Y. Yu, H.-L. Liu, J.-J. Wu, K.-H. Chen, L.-C. Chen, J.-Y. Peng and Y.-F. Chen: *Catalytic growth and characterization of Gallium Nitride nanowires*, Journal of the American Chemical Society **123**, 2791 (2001).

[Che08] D. Cherns, L. Meshi, I. Griffiths, S. Khongphetsak, S. V. Novikov, N. Farley, R. P. Campion and C. T. Foxon: *Defect reduction in GaN/(0001)sapphire films grown by molecular beam epitaxy using nanocolumn intermediate layers*, Applied Physics Letters **92**, 121902 (2008).

[Chi06] Z. Chine, A. Rebey, H. Touati, E. Goovaerts, M. Oueslati, B. E. Jani and S. Laugt: *Stress and density of defects in Si-doped GaN*, physica status solidi (a) **203**, 1954 (2006).

[Con09] V. Consonni, M. Knelangen, U. Jahn, A. Trampert, L. Geelhaar and H. Riechert: *Effects of nanowire coalescence on their structural and optical properties on a local scale*, Applied Physics Letters **95**, 241910 (2009).

[Con10] V. Consonni, M. Knelangen, L. Geelhaar, A. Trampert and H. Riechert: *Nucleation mechanisms of epitaxial GaN nanowires: Origin of their self-induced formation and initial radius*, Phys. Rev. B **81**, 085310 (2010).

[Dav02] V. Davydov, A. Klochikhin, V. Emtsev, S. Ivanov, V. Vekshin, F. Bechstedt, J. Furthmüller, H. Harima, A. Mudryi, A. Hashimoto, A. Yamamoto, J. Aderhold, J. Graul and E. Haller: *Band gap of InN and In-rich* $In_xGa_{1-x}N$ *alloys* $(0.36 < x < 1)$, phys. stat. sol. (b) **230**, R4 (2002).

[Deb07] R. K. Debnath, R. Meijers, T. Richter, T. Stoica, R. Calarco and H. Lüth: *Mechanism of molecular beam epitaxy growth of GaN nanowires on Si(111)*, Applied Physics Letters **90**, 123117 (2007).

[Dem04] F. Demangeot, J. Frandon, P. Baules, F. Natali, F. Semond and J. Massies: *Phonon deformation potentials in hexagonal GaN*, Phys. Rev. B **69**, 155215 (2004).

[Dim00] R. Dimitrov, M. Murphy, J. Smart, W. Schaff, J. R. Shealy, L. F. Eastman, O. Ambacher and M. Stutzmann: *Two-dimensional electron gases in Ga-face and N-face AlGaN/GaN heterostructures grown by plasma-induced molecular beam epitaxy and metalorganic chemical vapor deposition on sapphire*, Journal of Applied Physics **87**, 3375 (2000).

[Ege09] R. F. Egerton: *Electron energy-loss spectroscopy in the TEM*, Reports on Progress in Physics **72**, 016502 (2009).

[Eic03] M. Eickhoff, J. Schalwig, G. Steinhoff, O. Weidemann, L. Görgens, R. Neuberger, M. Hermann, B. Baur, G. Müller, O. Ambacher and

M. Stutzmann: *Electronics and sensors based on pyroelectric AlGaN/GaN heterostructures - Part B: Sensor applications*, physica status solidi (c) **0**, 1908 (2003).

[Fan96] Z. Fan, S. N. Mohammad, W. Kim, O. Aktas, A. E. Botchkarev and H. Morkoc: *Very low resistance multilayer ohmic contact to n-GaN*, Applied Physics Letters **68**, 1672 (1996).

[Fel98] R. D. Felice and J. E. Northrup: *Energetics of AlN thin films on the* Al_2O_3 *(1000) surface*, Applied Physics Letters **73**, 936 (1998).

[Fer07] S. Fernández, R. Peña, M. T. Rodrigo, J. Plaza, M. Verdú, F. J. Sánchez and M. T. Montojo: *Low resistance Ti/Al/Ti-W/Au ohmic contact to n-GaN for high temperature applications*, Applied Physics Letters **90**, 083504 (2007).

[Fio99] V. Fiorentini, F. Bernardini, F. Della Sala, A. Di Carlo and P. Lugli: *Effects of macroscopic polarization in III-V nitride multiple quantum wells*, Phys. Rev. B **60**, 8849 (1999).

[Fli00] T. Fließbach: *Quantenmechanik*, Lehrbuch zur Theoretischen Physik, Spektrum Akademischer Verlag, Heidelberg, 2000, Third edn., ISBN-10: 3-8274-0996-9.

[Fox09] C. Foxon, S. Novikov, J. Hall, R. Campion, D. Cherns, I. Griffiths and S. Khongphetsak: *A complementary geometric model for the growth of GaN nanocolumns prepared by plasma-assisted molecular beam epitaxy*, Journal of Crystal Growth **311**, 3423 (2009).

[Fre85] J. K. Fremerey: *The spinning rotor gauge*, Journal of Vacuum Science & Technology A: Vacuum, Surfaces, and Films **3**, 1715 (1985).

[Fre05] J. A. Freitas, Jr: *Optical studies of bulk and homoepitaxial films of III-V nitride semiconductors*, Journal of Crystal Growth **281**, 168 (2005).

[Fur08a] F. Furtmayr, M. Vielemeyer, M. Stutzmann, J. Arbiol, S. Estradé, F. Peirò, J. R. Morante and M. Eickhoff: *Nucleation and growth of GaN nanorods on Si (111) surfaces by plasma-assisted molecular beam epitaxy - the influence of Si- and Mg-doping*, Journal of Applied Physics **104**, 034309 (2008).

[Fur08b] F. Furtmayr, M. Vielemeyer, M. Stutzmann, A. Laufer, B. K. Meyer and M. Eickhoff: *Optical properties of Si- and Mg-doped gallium nitride nanowires grown by plasma-assisted molecular beam epitaxy*, Journal of Applied Physics **104**, 074309 (2008).

[Fur11] F. Furtmayr, J. Teubert, P. Becker, S. Conesa-Boj, J. R. Morante, A. Chernikov, S. Schäfer, S. Chatterjee, J. Arbiol and M. Eickhoff: *Carrier confinement in* $GaN/Al_xGa_{1-x}N$ *nanowire heterostructures (*$0 < x \leq 1$*)*, Phys. Rev. B **84**, 205303 (2011).

[Gan08] M. G. Ganchenkova, V. A. Borodin, K. Laaksonen and R. M. Nieminen: *Modeling the compositional instability in wurtzite*, Phys. Rev. B **77**, 075207 (2008).

[Gee07] L. Geelhaar, C. Chèze, W. M. Weber, R. Averbeck, H. Riechert, T. Kehagias, P. Komninou, G. P. Dimitrakopulos and T. Karakostas: *Axial and radial growth of Ni-induced GaN nanowires*, Applied Physics Letters **91**, 093113 (2007).

[Geo01] A. Georgakilas, S. Mikroulis, V. Cimalla, M. Zervos, A. Kostopoulos, P. Komninou, T. Kehagias and T. Karakostas: *Effects of the sapphire nitridation on the polarity and structural properties of GaN layers grown by plasma-assisted MBE*, phys. stat. sol. (a) **188**, 567 (2001).

[Gol01] Y. Goldberg: *Properties of Advanced Semiconductor Materials: GaN, AlN, InN, BN, SiC, SiGe*, John Wiley & Sons, Inc., New York, 2001.

[Gra98] N. Grandjean, J. Massies, M. Leroux and P. Lorenzini: *Ultraviolet GaN light-emitting diodes grown by molecular beam epitaxy using* NH_3, Applied Physics Letters **72**, 82 (1998).

[Gra99] N. Grandjean, B. Damilano, S. Dalmasso, M. Leroux, M. Laugt and J. Massies: *Built-in electric-field effects in wurtzite AlGaN/GaN quantum wells*, Journal of Applied Physics **86**, 3714 (1999).

[Gud02] M. S. Gudiksen, L. J. Lauhon, J. Wang, D. C. Smith and C. M. Lieber: *Growth of nanowire superlattice structures for nanoscale photonics and electronics*, Nature **415**, 617 (2002).

[Gui06] F. Guillot, E. Bellet-Amalric, E. Monroy, M. Tchernycheva, L. Nevou, L. Doyennette, F. H. Julien, L. S. Dang, T. Remmele, M. Albrecht, T. Shibata and M. Tanaka: *Si-doped GaN/AlN quantum dot superlattices for optoelectronics at telecommunication wavelengths*, Journal of Applied Physics **100**, 044326 (2006).

[Guo94] Q. Guo and A. Yoshida: *Temperature dependence of band gap change in InN and AlN*, Japanese Journal of Applied Physics **33**, 2453 (1994).

[Guo96] J. D. Guo, C. I. Lin, M. S. Feng, F. M. Pan, G. C. Chi and C. T. Lee: *A bilayer Ti/Ag ohmic contact for highly doped n-type GaN films*, Applied Physics Letters **68**, 235 (1996).

[Her89] M. Herman and H. Sitter: *Molecular beam epitaxy*, Springer, Berlin, 1989, ISBN-13: 978-3-540-19075-2.

[Her06] S. D. Hersee, X. Sun and X. Wang: *The controlled growth of GaN nanowires*, Nano Letters **6**, 1808 (2006).

[Her09] M. Hermann: *Epitaktische AlN-Schichten auf Saphir und Diamant*, Ph.D. thesis, Technische Universität München; Physik-Department (2009).

[Hes11] K. Hestroffer, C. Leclere, C. Bougerol, H. Renevier and B. Daudin: *Polarity of GaN nanowires grown by plasma-assisted molecular beam epitaxy on Si(111)*, Phys. Rev. B **84**, 245302 (2011).

[Ho96] I. Ho and G. B. Stringfellow: *Solid phase immiscibility in GaInN*, Applied Physics Letters **69**, 2701 (1996).

[Hol00] J. Holst, A. Kaschner, U. Gfug, A. Hoffmann, C. Thomsen, F. Bertram, T. Riemann, D. Rudloff, P. Fischer, J. Christen, R. Averbeck, H. Riechert, M. Heuken, M. Schwambera and O. Schön: *Comparison of the mechanism of optical amplification in InGaN/GaN heterostructures grown by Molecular Beam Epitaxy and MOCVD*, physica status solidi (a) **180**, 327 (2000).

[Höp97] R. Höpler: *Hochaufgelöste Röntgenbeugung an epitaktischen Schichten und Heterostrukturen aus Gruppe-III-Nitriden*, Ph.D. thesis, Technische Universität München; Physik-Department (1997).

[Hua01] Y. Huang, X. Duan, Q. Wei and C. M. Lieber: *Directed assembly of one-dimensional nanostructures into functional networks*, Science **291**, 630 (2001).

[Hua05] Y. Huang, X. Duan and C. Lieber: *Nanowires for integrated multicolor nanophotonics*, Small **1**, 142 (2005).

[Ima12] M. Imade, K. Murakami, D. Matsuo, H. Imabayashi, H. Takazawa, Y. Todoroki, A. Kitamoto, M. Maruyama, M. Yoshimura and Y. Mori: *Centimeter-sized bulk GaN single crystals grown by the Na-flux method with a necking technique*, Crystal Growth & Design **12**, 3799 (2012).

[Jel06] F. Jelezko and J. Wrachtrup: *Single defect centres in diamond: A review*, physica status solidi (a) **203**, 3207 (2006).

[Joh05] J. Johansson, C. P. T. Svensson, T. Mårtensson, L. Samuelson and W. Seifert: *Mass transport model for semiconductor nanowire growth*, The Journal of Physical Chemistry B **109**, 13567 (2005).

[Joh06] J. Johansson, B. A. Wacaser, K. A. Dick and W. Seifert: *Growth related aspects of epitaxial nanowires*, Nanotechnology **17**, S355 (2006).

[Jun08] H. S. Jung, Y. J. Hong, Y. Li, J. Cho, Y.-J. Kim and G.-C. Yi: *Photocatalysis using GaN nanowires*, ACS Nano **2**, 637 (2008).

[Kaz98] A. Kazimirov, G. Scherb, J. Zegenhagen, T.-L. Lee, M. J. Bedzyk, M. K. Kelly, H. Angerer and O. Ambacher: *Polarity determination of a GaN thin film on sapphire (0001) with x-ray standing waves*, Journal of Applied Physics **84**, 1703 (1998).

[Keh08] T. Kehagias, P. Komninou, G. P. Dimitrakopulos, C. Chèze, L. Geelhaar, H. Riechert and T. Karakostas: *Atomic-scale configuration of catalyst particles on GaN nanowires*, physica status solidi (c) **5**, 3716 (2008).

[Kik04] A. Kikuchi, M. Kawai, M. Tada and K. Kishino: *InGaN/GaN multiple quantum disk nanocolumn light-emitting diodes grown on (111) Si substrate*, Japanese Journal of Applied Physics **43**, L1524 (2004).

[Kik06] A. Kikuchi, M. Tada, K. Miwa and K. Kishino: *Growth and characterization of InGaN/GaN nanocolumn LED*, Proceedings of SPIE - Quantum Dots, Particles, and Nanoclusters III **6129**, 612905 (2006).

[Kim97] T. Kim, M. C. Yoo and G. T. Taeil Kim: *Cr/Ni/Au ohmic contacts to the moderately doped p- and n-GaN*, Materials Research Society Symposium Proceedings **449**, 1061 (1997).

[Kin98] S. W. King, C. Ronning, R. F. Davis, M. C. Benjamin and R. J. Nemanich: *Dependence of (0001) GaN/AlN valence band discontinuity on growth temperature and surface reconstruction*, Journal of Applied Physics **84**, 2086 (1998).

[Kis08] K. Kishino, T. Hoshino, S. Ishizawa and A. Kikuchi: *Selective-area growth of GaN nanocolumns on titanium-mask-patterned silicon (111) substrates by RF-plasma-assisted molecular-beam epitaxy.*, Electronics Letters **44**, 819 (2008).

[Kle90] W. Kleber: *Einführung in die Kristallographie*, Verlag Technik GmbH Berlin, 1990, 17th edn..

[Kne10] M. Knelangen, V. Consonni, A. Trampert and H. Riechert: *In situ analysis of strain relaxation during catalyst-free nucleation and growth of GaN nanowires*, Nanotechnology **21**, 245705 (2010).

[Koe10] R. Koester, J. S. Hwang, C. Durand, D. L. S. Dang and J. Eymery: *Self-assembled growth of catalyst-free GaN wires by metal-organic vapour phase epitaxy*, Nanotechnology **21**, 015602 (2010).

[Kou06] T. Kouno, A. Kikuchi and K. Kishino: *Growth of high-In-content InGaN multiple quantum disk nanocolumns on Si(111) by RF plasma-assisted molecular-beam epitaxy*, physica status solidi (b) **243**, 1481 (2006).

[Lam56] M. A. Lampert: *Simplified theory of space-charge-limited currents in an insulator with traps*, Physical Review **103**, 1648 (1956).

[Lam70] M. A. Lampert and P. Mark: *Current Injection in solids*, Academic Press, New York, 1970, ISBN-13: 0-12-435350-9.

[Lan09] O. Landré, C. Bougerol, H. Renevier and B. Daudin: *Nucleation mechanism of GaN nanowires grown on (111) Si by molecular beam epitaxy*, Nanotechnology **20**, 415602 (2009).

[Lar08] L. Largeau, D. L. Dheeraj, M. Tchernycheva, G. E. Cirlin and J. C. Harmand: *Facet and in-plane crystallographic orientations of GaN nanowires grown on Si(111)*, Nanotechnology **19**, 155704 (2008).

[Lei92] T. Lei, T. D. Moustakas, R. J. Graham, Y. He and S. J. Berkowitz: *Epitaxial growth and characterization of zinc-blende gallium nitride on (001) silicon*, Journal of Applied Physics **71**, 4933 (1992).

[Ler99] M. Leroux, N. Grandjean, B. Beaumont, G. Nataf, F. Semond, J. Massies and P. Gibart: *Temperature quenching of photoluminescence intensities in undoped and doped GaN*, Journal of Applied Physics **86**, 3721 (1999).

[Les94] M. Leszczynski, T. Suski, H. Teisseyre, P. Perlin, I. Grzegory, J. Jun, S. Porowski and T. D. Moustakas: *Thermal expansion of gallium nitride*, Journal of Applied Physics **76**, 4909 (1994).

[Li06] H. Li, A. Chin and M. Sunkara: *Direction-dependent homoepitaxial growth of GaN nanowires*, Advanced Materials **18**, 216 (2006).

[Li12] S. Li and A. Waag: *GaN based nanorods for solid state lighting*, Journal of Applied Physics **111**, 071101 (2012).

[Lim10] F. Limbach, E. O. Schaefer-Nolte, R. Caterino, T. Gotschke, T. Stoica, E. Sutter and R. Calarco: *Morphology and optical properties of Mg doped GaN nanowires in dependence of growth temperature*, Journal of Optoelectronics and Advanced Materials **12**, 1433 (2010).

[Lin94] M. E. Lin, Z. Ma, F. Y. Huang, Z. F. Fan, L. H. Allen and H. Morkoc: *Low resistance ohmic contacts on wide band-gap GaN*, Applied Physics Letters **64**, 1003 (1994).

[Liu02] L. Liu and J. H. Edgar: *Substrates for gallium nitride epitaxy*, Materials Science and Engineering: R: Reports **37**, 61 (2002).

[Liu05] R. Liu, A. Bell, F. A. Ponce, C. Q. Chen, J. W. Yang and M. A. Khan: *Luminescence from stacking faults in gallium nitride*, Applied Physics Letters **86**, 021908 (2005).

[Lym09] L. Lymperakis and J. Neugebauer: *Large anisotropic adatom kinetics on nonpolar GaN surfaces: Consequences for surface morphologies and nanowire growth*, Physical Review B (Condensed Matter and Materials Physics) **79**, 241308 (2009).

[Mai09] A. Maigné and R. D. Twesten: *Review of recent advances in spectrum imaging and its extension to reciprocal space*, Journal of Electron Microscopy **58**, 99 (2009).

[Mar96] G. Martin, A. Botchkarev, A. Rockett and H. Morkoc: *Valence-band discontinuities of wurtzite GaN, AlN, and InN heterojunctions measured by x-ray photoemission spectroscopy*, Applied Physics Letters **68**, 2541 (1996).

[Mat97] T. Mattila and R. M. Nieminen: *Point-defect complexes and broadband luminescence in GaN and AlN*, Phys. Rev. B **55**, 9571 (1997).

[Mat12] M. de la Mata, C. Magen, J. Gazquez, M. I. B. Utama, M. Heiss, S. Lopatin, F. Furtmayr, C. J. Fernández-Rojas, B. Peng, J. R. Morante, R. Rurali, M. Eickhoff, A. Fontcuberta i Morral, Q. Xiong and J. Arbiol: *Polarity assignment in ZnTe, GaAs, ZnO, and GaN-AlN nanowires from direct dumbbell analysis*, Nano Letters **12**, 2579 (2012).

[Mei06] R. Meijers, T. Richter, R. Calarco, T. Stoica, H.-P. Bochem, M. Marso and H. Lüth: *GaN-nanowhiskers: MBE-growth conditions and optical properties*, Journal of Crystal Growth **289**, 381 (2006).

[Men96] J. Menniger, U. Jahn, O. Brandt, H. Yang and K. Ploog: *Identification of optical transitions in cubic and hexagonal GaN by spatially resolved cathodoluminescence*, Phys. Rev. B **53**, 1881 (1996).

[Met97] T. Metzger: *Strukturelle Charakterisierung von Gruppe-III Nitriden*, Ph.D. thesis, Technische Universität München; Physik-Department (1997).

[MG97] J. Martin-Gil, F. J. Martin-Gil, M. Sarikaya, M. Qian, M. Jose-Yacaman and A. Rubio: *Evidence of a low compressibility carbon nitride with defect-zincblende structure*, Journal of Applied Physics **81**, 2555 (1997).

[Mis03] C. R. Miskys, J. A. Garrido, C. E. Nebel, M. Hermann, O. Ambacher, M. Eickhoff and M. Stutzmann: *AlN/diamond heterojunction diodes*, Applied Physics Letters **82**, 290 (2003).

[Mon02] B. Monemar, P. P. Paskov, T. Paskova, J. P. Bergman, G. Pozina, W. M. Chen, P. N. Hai, I. A. Buyanova, H. Amano and I. Akasaki: *Optical characterization of III-nitrides*, Materials Science and Engineering B **93**, 112 (2002).

[Mon04] E. Monroy, M. Hermann, E. Sarigiannidou, T. Andreev, P. Holliger, S. Monnoye, H. Mank, B. Daudin and M. Eickhoff: *Polytype transition of N-face GaN:Mg from wurtzite to zinc-blende*, Journal of Applied Physics **96**, 3709 (2004).

[Mor09] M. Moret, B. Gil, S. Ruffenach, O. Briot, C. Giesen, M. Heuken, S. Rushworth, T. Leese and M. Succi: *Optical, structural investigations and band-gap bowing parameter of GaInN alloys*, Journal of Crystal Growth **311**, 2795 , proceedings of the 2nd International Symposium on Growth of III Nitrides (2009).

[Mot02] A. Motayed, A. V. Davydov, L. A. Bendersky, M. C. Wood, M. A. Derenge, D. F. Wang, K. A. Jones and S. N. Mohammad: *High-transparency Ni/Au bilayer contacts to n-type GaN*, Journal of Applied Physics **92**, 5218 (2002).

[Mot03] A. Motayed, R. Bathe, M. C. Wood, O. S. Diouf, R. D. Vispute and S. N. Mohammad: *Electrical, thermal, and microstructural characteristics of Ti/Al/Ti/Au multilayer ohmic contacts to n-type GaN*, Journal of Applied Physics **93**, 1087 (2003).

[Mou01] T. D. Moustakas, E. Iliopoulos, A. V. Sampath, H. M. Ng, D. Doppalapudi, M. Misra, D. Korakakis and R. Singh: *Growth and device applications of III-nitrides by MBE*, J. Cryst. Growth **227-228**, 13 (2001).

[Mur94] M. Murayama and T. Nakayama: *Chemical trend of band offsets at wurtzite/zinc-blende heterocrystalline semiconductor interfaces*, Phys. Rev. B **49**, 4710 (1994).

[Nak98] S. Nakamura, M. Senoh, S. Nagahama, N. Iwasa, T. Yamada, T. Matsushita, H. Kiyoku, Y. Sugimoto, T. Kozaki, H. Umemoto, M. Sano and K. Chocho: *Continuous-wave operation of InGaN/GaN/AlGaN-based laser diodes grown on GaN substrates*, Applied Physics Letters **72**, 2014 (1998).

[Nar04] F. Naranjo, E. Calleja, Z. Bougrioua, A. Trampert, X. Kong and K. Ploog: *Efficiency optimization of p-type doping in GaN:Mg layers grown by molecular-beam epitaxy*, Journal of Crystal Growth **270**, 542 (2004).

[Neu94] J. Neugebauer and C. G. Van de Walle: *Atomic geometry and electronic structure of native defects in GaN*, Phys. Rev. B **50**, 8067 (1994).

[Neu03] J. Neugebauer: *Surfactants and antisurfactants on group-III-nitride surfaces*, physica status solidi (c) **0**, 1651 (2003).

[Nis00] L. Nistor, H. Bender, A. Vantomme, M. F. Wu, J. V. Landuyt, K. P. O'Donnell, R. Martin, K. Jacobs and I. Moerman: *Direct evidence of spontaneous quantum dot formation in a thick InGaN epilayer*, Applied Physics Letters **77**, 507 (2000).

[Niu93] C. Niu, Y. Z. Lu and C. M. Lieber: *Experimental realization of the covalent solid carbon nitride*, Science **261**, 334 (1993).

[Nor99] J. E. Northrup and J. Neugebauer: *Indium-induced changes in GaN(0001) surface morphology*, Phys. Rev. B **60**, R8473 (1999).

[Nos06] J. V. Nostrand, K. Averett, R. Cortez, J. Boeckl, C. Stutz, N. Sanford, A. Davydov and J. Albrecht: *Molecular beam epitaxial growth of high-quality GaN nanocolumns*, Journal of Crystal Growth **287**, 500 (2006).

[Pal00] T. Palacios, F. Calle, M. Varela, C. Ballesteros, E. Monroy, F. B. Naranjo, M. A. Sánchez-García, E. Calleja and E. Muñoz: *Wet etching of GaN grown by molecular beam epitaxy on Si(111)*, Semiconductor Science and Technology **15**, 996 (2000).

[Par06] Y. S. Park, J. H. Na, R. A. Taylor, C. M. Park, K. H. Lee and T. W. Kang: *The recombination mechanism of Mg-doped GaN nanorods grown by plasma-assisted molecular-beam epitaxy*, Nanotechnology **17**, 913 (2006).

[Pau98] S. Pau, Z. X. Liu, J. Kuhl, J. Ringling, H. T. Grahn, M. A. Khan, C. J. Sun, O. Ambacher and M. Stutzmann: *Time-resolved photoluminescence study of excitons in hexagonal GaN layers grown on sapphire*, Phys. Rev. B **57**, 7066 (1998).

[Pau12] S. Paul, A. Helwig, G. Müller, F. Furtmayr, J. Teubert and M. Eickhoff: *Opto-chemical sensor system for the detection of H_2 and hydrocarbons based on InGaN/GaN nanowires*, Sensors and Actuators B: Chemical **173**, 120 (2012).

[Per92] P. Perlin, C. Jauberthie-Carillon, J. P. Itie, A. San Miguel, I. Grzegory and A. Polian: *Raman scattering and x-ray-absorption spectroscopy in gallium nitride under high pressure*, Phys. Rev. B **45**, 83 (1992).

[Pfü10] C. Pfüller, O. Brandt, F. Grosse, T. Flissikowski, C. Chèze, V. Consonni, L. Geelhaar, H. T. Grahn and H. Riechert: *Unpinning the Fermi level of GaN nanowires by ultraviolet radiation*, Phys. Rev. B **82**, 045320 (2010).

[Pry98] P. Prystawko, M. Leszczynski, B. Beaumont, P. Gibart, E. Frayssinet, W. Knap, P. Wisniewski, M. Bockowski, T. Suski and S. Porowski: *Doping of homoepitaxial GaN layers*, physica status solidi (b) **210**, 437 (1998).

[Ren09] J. Renard, R. Songmuang, G. Tourbot, C. Bougerol, B. Daudin and B. Gayral: *Evidence for quantum-confined stark effect in GaN/AlN quantum dots in nanowires*, Physical Review B (Condensed Matter and Materials Physics) **80**, 121305 (2009).

[Ren10] J. Renard, G. Tourbot, D. Sam-Giao, C. Bougerol, B. Daudin and B. Gayral: *Optical spectroscopy of cubic GaN in nanowires*, Applied Physics Letters **97**, 081910 (2010).

[Res05] M. A. Reshchikov and H. Morkoc: *Luminescence properties of defects in GaN*, Journal of Applied Physics **97**, 061301 (2005).

[RF94] G. Ramírez-Flores, H. Navarro-Contreras, A. Lastras-Martínez, R. C. Powell and J. E. Greene: *Temperature-dependent optical band gap of the metastable zinc-blende structure β-GaN*, Phys. Rev. B **50**, 8433 (1994).

[Rig10a] L. Rigutti, F. Fortuna, M. Tchernycheva, A. D. L. Bugallo, G. Jacopin, F. H. Julien, S. T. Chou, Y. T. Lin, L. W. Tu and J.-C. Harmand: *Optical properties of GaN and GaN/AlN nanowires: the effect of doping and structural defects*, physica status solidi (c) **7**, 2233 (2010).

[Rig10b] L. Rigutti, F. Fortuna, M. Tchernycheva, A. D. L. Bugallo, G. Jacopin, F. H. Julien, F. Furtmayr, M. Stutzmann and M. Eickhoff: *Optical characterization of AlGaN/GaN quantum disc structures in single nanowires*, physica status solidi (c) **7**, 2243 (2010).

[Rig10c] L. Rigutti, M. Tchernycheva, A. De Luna Bugallo, G. Jacopin, F. H. Julien, F. Furtmayr, M. Stutzmann, M. Eickhoff, R. Songmuang and F. Fortuna: *Photoluminescence polarization properties of single GaN nanowires containing* $Al_xGa_{1-x}N/GaN$ *quantum discs*, Phys. Rev. B **81**, 045411 (2010).

[Rig10d] L. Rigutti, J. Teubert, G. Jacopin, F. Fortuna, M. Tchernycheva, A. De Luna Bugallo, F. H. Julien, F. Furtmayr, M. Stutzmann and M. Eickhoff: *Origin of energy dispersion in* $Al_xGa_{1-x}N/GaN$ *nanowire quantum discs with low Al content*, Phys. Rev. B **82**, 235308 (2010).

[Rin08] P. Rinke, M. Winkelnkemper, A. Qteish, D. Bimberg, J. Neugebauer and M. Scheffler: *Consistent set of band parameters for the group-III nitrides AlN, GaN, and InN*, Phys. Rev. B **77**, 075202 (2008).

[Ris02] J. Ristić, M. Sánchez-García, J. Ulloa, E. Calleja, J. Sanchez-Páramo, J. Calleja, U. Jahn, A. Trampert and K. Ploog: *AlGaN nanocolumns and AlGaN/GaN/AlGaN nanostructures grown by molecular beam epitaxy*, physica status solidi (b) **234**, 717 (2002).

[Ris05a] J. Ristić, E. Calleja, A. Trampert, S. Fernández-Garrido, C. Rivera, U. Jahn and K. H. Ploog: *Columnar AlGaN/GaN nanocavities with AlN/GaN Bragg reflectors grown by molecular beam epitaxy on Si(111)*, Phys. Rev. Lett. **94**, 146102 (2005).

[Ris05b] J. Ristić, C. Rivera, E. Calleja, S. Fernández-Garrido, M. Povoloskyi and A. Di Carlo: *Carrier-confinement effects in nanocolumnar GaN /* $Al_xGa_{1-x}N$ *quantum disks grown by molecular-beam epitaxy*, Phys. Rev. B **72**, 085330 (2005).

[Ris08] J. Ristic, E. Calleja, S. Fernández-Garrido, L. Cerutti, A. Trampert, U. Jahn and K. H. Ploog: *On the mechanisms of spontaneous growth of III-nitride nanocolumns by plasma-assisted molecular beam epitaxy*, Journal of Crystal Growth **310**, 4035 (2008).

[Riv07] C. Rivera, U. Jahn, T. Flissikowski, J. L. Pau, E. Muñoz and H. T. Grahn: *Strain-confinement mechanism in mesoscopic quantum disks based on piezoelectric materials*, Physical Review B (Condensed Matter and Materials Physics) **75**, 045316 (2007).

[Ros55] A. Rose: *Space-charge-limited currents in solids*, Phys. Rev. **97**, 1538 (1955).

[Ros02] A. L. Rosa, J. Neugebauer, J. E. Northrup, C.-D. Lee and R. M. Feenstra: *Adsorption and incorporation of silicon at GaN(0001) surfaces*, Applied Physics Letters **80**, 2008 (2002).

[Sal99] G. Salviati, M. Albrecht, C. Zanotti-Fregonara, N. Armani, M. Mayer, Y. Shreter, M. Guzzi, Y. V. Melnik, K. Vassilevski, V. A. Dmitriev and H. P. Strunk: *Cathodoluminescence and transmission electron microscopy study of the influence of crystal defects on optical transitions in GaN*, physica status solidi (a) **171**, 325 (1999).

[San05] N. A. Sanford, L. H. Robins, M. H. Gray, Y.-S. Kang, J. E. V. Nostrand, C. Stutz, R. Cortez, A. V. Davydov, A. Shapiro, I. Levin and A. Roshko: *Fabrication and analysis of GaN nanorods grown by MBE*, physica status solidi (c) **2**, 2357 (2005).

[San10] N. A. Sanford, P. T. Blanchard, K. A. Bertness, L. Mansfield, J. B. Schlager, A. W. Sanders, A. Roshko, B. B. Burton and S. M. George: *Steady-state and transient photoconductivity in c-axis GaN nanowires grown by nitrogen-plasma-assisted molecular beam epitaxy*, Journal of Applied Physics **107**, 034318 (2010).

[Sch02a] J. Schalwig: *Feldeffekt-Gassensoren und ihre Anwendung in Abgasnachbehandlungssystemen*, Ph.D. thesis, Technische Universität München; Physik-Department (2002).

[Sch02b] J. Schalwig, G. Müller, M. Eickhoff, O. Ambacher and M. Stutzmann: *Gas sensitive GaN/AlGaN-heterostructures*, Sensors and Actuators B: Chemical **87**, 425 (2002).

[Sch06] J. B. Schlager, N. A. Sanford, K. A. Bertness, J. M. Barker, A. Roshko and P. T. Blanchard: *Polarization-resolved photoluminescence study of individual GaN nanowires grown by catalyst-free molecular beam epitaxy*, Applied Physics Letters **88**, 213106 (2006).

[Sch11] T. Schumann, T. Gotschke, F. Limbach, T. Stoica and R. Calarco: *Selective-area catalyst-free MBE growth of GaN nanowires using a patterned oxide layer*, Nanotechnology **22**, 095603 (2011).

[Sek08a] H. Sekiguchi, K. Kato, J. Tanaka, A. Kikuchi and K. Kishino: *Ultraviolet GaN-based nanocolumn light-emitting diodes grown on n-(111) Si substrates by rf-plasma-assisted molecular beam epitaxy*, physica status solidi A **205**, 1067 (2008).

[Sek08b] H. Sekiguchi, K. Kishino and A. Kikuchi: *Ti-mask selective-area growth of GaN by RF-plasma-assisted molecular-beam epitaxy for fabricating regularly arranged InGaN/GaN nanocolumns*, Applied Physics Express **1**, 124002 (2008).

[Seo06] H. W. Seo, Q. Y. Chen, M. N. Iliev, L. W. Tu, C. L. Hsiao, J. K. Mean and W.-K. Chu: *Epitaxial GaN nanorods free from strain and luminescent defects*, Applied Physics Letters **88**, 153124 (2006).

[SG98] M. A. Sanchez-Garcia, E. Calleja, E. Monroy, F. J. Sanchez, F. Calle, E. Munoz and R. Beresford: *The effect of the III/V ratio and substrate temperature on the morphology and properties of GaN- and AlN-layers grown by molecular beam epitaxy on Si(1 1 1)*, Journal of Crystal Growth **183**, 23 (1998).

[Sin97] R. Singh, D. Doppalapudi, T. D. Moustakas and L. T. Romano: *Phase separation in InGaN thick films and formation of InGaN/GaN double heterostructures in the entire alloy composition*, Applied Physics Letters **70**, 1089 (1997).

[Sme03] T. M. Smeeton, M. J. Kappers, J. S. Barnard, M. E. Vickers and C. J. Humphreys: *Electron-beam-induced strain within InGaN quantum wells: False indium "cluster" detection in the transmission electron microscope*, Applied Physics Letters **83**, 5419 (2003).

[Sme06] T. Smeeton, C. Humphreys, J. Barnard and M. Kappers: *The impact of electron beam damage on the detection of indium-rich localisation centres in InGaN quantum wells using transmission electron microscopy*, Journal of Materials Science **41**, 2729 (2006).

[Son07] R. Songmuang, O. Landré and B. Daudin: *From nucleation to growth of catalyst-free GaN nanowires on thin AlN buffer layer*, Applied Physics Letters **91**, 251902 (2007).

[Sou07] S. d. Sousa Pereira, K. O'Donnell and E. da Costa Alves: *Role of nanoscale strain inhomogeneity on the light emission from InGaN epilayers*, Advanced Functional Materials **17**, 37 (2007).

[SP02] J. Sanchez-Paramo, J. M. Calleja, M. A. Sanchez-Garcia, E. Calleja and U. Jahn: *Structural and optical characterization of intrinsic GaN nanocolumns*, Physica E: Low-dimensional Systems and Nanostructures **13**, 1070 (2002).

[Sta08] C. Stark: *Elektrische Eigenschaften von III-Nitrid Nanostrukturen*, Diplomarbeit, Technische Universität München; Physik-Department; Lehrstuhl E25 (2008).

[Stu01] M. Stutzmann, O. Ambacher, M. Eickhoff, U. Karrer, A. Lima Pimenta, R. Neuberger, J. Schalwig, R. Dimitrov, P. Schuck and R. Grober: *Playing with polarity*, phys. stat. sol. (b) **228**, 505 (2001).

[Sun02] Y. Sun, X. M. Shen, J. Wang, D. G. Zhao, G. Feng, Y. Fu, S. M. Zhang, Z. H. Zhang, Z. H. Feng, Y. X. Bai and H. Yang: *Thermal annealing behaviour of Ni/Au on n-GaN Schottky contacts*, Journal of Physics D: Applied Physics **35**, 2648 (2002).

[Sze81] S. M. Sze: *Physics of Semiconductor Devices*, Wiley & Sons, New York, 1981, second Edition, ISBN-10: 0-471-05661-8.

[Tan06] H. Tang, S. Haffouz and J. A. Bardwell: *Si (111) substrates as highly effective pseudomasks for selective growth of GaN material and devices by ammonia-molecular-beam epitaxy*, Applied Physics Letters **88**, 172110 (2006).

[Tch07] M. Tchernycheva, C. Sartel, G. Cirlin, L. Travers, G. Patriarche, J.-C. Harmand, L. S. Dang, J. Renard, B. Gayral, L. Nevou and F. Julien: *Growth of GaN free-standing nanowires by plasma-assisted molecular beam epitaxy: structural and optical characterization*, Nanotechnology **18**, 385306 (7pp) (2007).

[Tch08] M. Tchernycheva, C. Sartel, G. Cirlin, L. Travers, G. Patriarche, L. Largeau, O. Mauguin, J.-C. Harmand, L. S. Dang, J. Renard, B. Gayral, L. Nevou and F. Julien: *GaN/AlN free-standing nanowires grown by molecular beam epitaxy*, physica status solidi (c) **5**, 1556 (2008).

[Teu11] J. Teubert, P. Becker, F. Furtmayr and M. Eickhoff: *GaN nanodiscs embedded in nanowires as optochemical transducers*, Nanotechnology **22**, 275505 (2011).

[Umr] D. W. Umrath: *Grundlagen der Vakuumtechnik*, Oerlikon Leybold Vacuum.

[Vur01] I. Vurgaftman, J. R. Meyer and L. R. Ram-Mohan: *Band parameters for III–V compound semiconductors and their alloys*, Journal of Applied Physics **89**, 5815 (2001).

[Vur03] I. Vurgaftman and J. R. Meyer: *Band parameters for nitrogen-containing semiconductors*, Journal of Applied Physics **94**, 3675 (2003).

[Waa11] A. Waag, X. Wang, S. Fündling, J. Ledig, M. Erenburg, R. Neumann, M. Al Suleiman, S. Merzsch, J. Wei, S. Li, H. H. Wehmann, W. Bergbauer, M. Straßburg, A. Trampert, U. Jahn and H. Riechert: *The nanorod approach: GaN NanoLEDs for solid state lighting*, physica status solidi (c) **8**, 2296 (2011).

[Wag64] R. S. Wagner and W. C. Ellis: *Vapor-liquid-solid mechanism of single crystal growth*, Applied Physics Letters **4**, 89 (1964).

[Wal12a] J. Wallys, S. Hoffmann, F. Furtmayr, J. Teubert and M. Eickhoff: *Electrochemical properties of GaN nanowire electrodes - influence of doping and control by external bias*, Nanotechnology **23**, 165701 (2012).

[Wal12b] J. Wallys, J. Teubert, F. Furtmayr, D. M. Hofmann and M. Eickhoff: *Bias-enhanced optical pH response of group III-Nitride nanowires*, Nano Letters **12**, 6180 (2012).

[Wan05] D. Wang, C. C. Tin, J. R. Williams, M. Park, Y. S. Park, C. M. Park, T. W. Kang and W. C. Yang: *Raman characterization of electronic properties of self-assembled GaN nanorods grown by plasma-assisted molecular-beam epitaxy*, Applied Physics Letters **87**, 242105 (2005).

[Was] T. Wassner and B. Laumer: *(private communication)*.

[Wei09] O. Weidemann, P. K. Kandaswamy, E. Monroy, G. Jegert, M. Stutzmann and M. Eickhoff: *GaN quantum dots as optical transducers for chemical sensors*, Applied Physics Letters **94**, 113108 (2009).

[Wei12] O. Weidemann: *Interfaces in nitride devices*, Ph.D. thesis, Technische Universität München; Physik-Department (2012).

[Wes06] A. N. Westmeyer, S. Mahajan, K. K. Bajaj, J. Y. Lin, H. X. Jiang, D. D. Koleske and R. T. Senger: *Determination of energy-band offsets between GaN and AlN using excitonic luminescence transition in AlGaN alloys*, Journal of Applied Physics **99**, 013705 (2006).

[Wöl12] M. Wölz, J. Lähnemann, O. Brandt, V. M. Kaganer, M. Ramsteiner, C. Pfüller, C. Hauswald, C. N. Huang, L. Geelhaar and H. Riechert: *Correlation between In content and emission wavelength of $In_xGa_{1-x}N$/GaN nanowire heterostructures*, Nanotechnology **23**, 455203 (2012).

[Wra10] J. Wrachtrup: *Defect center room-temperature quantum processors*, Proceedings of the National Academy of Sciences **107**, 9479 (2010).

[Wu00] J. Wu, H. Yaguchi, B. Zhang, Y. Segawa, K. Onabe and Y. Shiraki: *Optical properties of cubic GaN grown on 3C-SiC (100) substrates by metalorganic vapor phase epitaxy*, physica status solidi (a) **180**, 403 (2000).

[Wu03] J. Wu, W. Walukiewicz, K. M. Yu, J. W. Ager, S. X. Li, E. E. Haller, H. Lu and W. J. Schaff: *Universal bandgap bowing in group-III nitride alloys*, Solid State Communications **127**, 411 (2003).

[Wys03] A. Wysmolek, M. Potemski, R. Stepniewski, J. M. Baranowski, D. C. Look, S. K. Lee and J. Y. Han: *Resonant interaction of LO phonons with excited donor states in GaN*, physica status solidi (b) **235**, 36 (2003).

[Yam79] H. Yamashita, K. Fukui, S. Misawa and S. Yoshida: *Optical properties of AlN epitaxial thin films in the vacuum ultraviolet region*, Journal of Applied Physics **50**, 896 (1979).

[Yos97] M. Yoshizawa, A. Kikuchi, M. Mori, N. Fujita and K. Kishino: *Growth of self-organized GaN nanostructures on Al_2O_3 (0001) by RF-radical source molecular beam epitaxy*, Jpn. J. Appl. Phys. **36**, L459 (1997).

[Yos98] M. Yoshizawa, A. Kikuchi, N. Fujita, K. Kushi, H. Sasamoto and K. Kishino: *Self-organization of GaN/$Al_{0.18}Ga_{0.82}N$ multi-layer nanocolumns on (0001) Al_2O_3 by RF molecular beam epitaxy for fabricating GaN quantum disks*, Journal of Crystal Growth **189/190**, 138 (1998).

[Zam05] M. Zamfirescu, M. Gurioli, A. Vinattieri, J. Ristić and E. Calleja: *Study of piezoelectric field in GaN quantum discs embedded in AlGaN nanocolumns*, physica status solidi (c) **2**, 3847 (2005).

[Zub01] A. Zubrilov: *Properties of Advanced Semiconductor Materials: GaN, AlN, InN, BN, SiC, SiGe*, John Wiley & Sons, Inc., New York, 2001.

List of publications

The following articles were published in peer-reviewed journals during this thesis:

As first author

- F. Furtmayr, M. Vielemeyer, M. Stutzmann, J. Arbiol, S. Estradé, F. Peirò, J. R. Morante, and M. Eickhoff: *Nucleation and growth of GaN nanorods on Si (111) surfaces by plasma-assisted molecular beam epitaxy - the influence of Si- and Mg-doping*, Journal of Applied Physics **104**, 034309 (2008).
- F. Furtmayr, M. Vielemeyer, M. Stutzmann, A. Laufer, B. K. Meyer, and M. Eickhoff: *Optical properties of Si- and Mg-doped gallium nitride nanowires grown by plasma-assisted molecular beam epitaxy*, Journal of Applied Physics **104**, 074309 (2008).
- F. Furtmayr, J. Teubert, P. Becker, S. Conesa-Boj, J. R. Morante, A. Chernikov, S. Schäfer, S. Chatterjee, J. Arbiol, and M. Eickhoff: *Carrier confinement in* $GaN/Al_xGa_{1-x}N$ *nanowire heterostructures* ($0 < x \leq 1$), Phys. Rev. B **84**, 205303 (2011).

As co-author

- J. Arbiol, S. Estradé, J. D. Prades, A. Cirera, F. Furtmayr, C. Stark, A. Laufer, M. Stutzmann, M. Eickhoff, M. H. Gass, A. L. Bleloch, F. Peiró, and J. R. Morante: *Triple-twin domains in Mg doped GaN wurtzite nanowires: structural and electronic properties of this zinc-blende-like stacking*, Nanotechnology **20**, 145704 (2009).
- M. Röppischer, R. Goldhahn, C. Buchheim, F. Furtmayr, T. Wassner, M. Eickhoff, C. Cobet, and N. Esser: *Analysis of polarization-dependent photoreflectance studies for c-plane GaN films grown on a-plane sapphire*, physica status solidi (a) **206**, 773 (2009).
- L. Rigutti, F. Fortuna, M. Tchernycheva, A. D. L. Bugallo, G. Jacopin, F. H. Julien, F. Furtmayr, M. Stutzmann, and M. Eickhoff: *Optical characterization of AlGaN/GaN quantum disc structures in single nanowires*, physica status solidi (c) **7**, 2243 (2010).
- L. Rigutti, F. Fortuna, M. Tchernycheva, A. D. L. Bugallo, G. Jacopin, F. H. Julien, S. T. Chou, Y. T. Lin, L. W. Tu, and J.-C. Harmand: *Optical properties of GaN and GaN/AlN nanowires: the effect of doping and structural defects*, physica status solidi (c) **7**, 2233 (2010).

- L. Rigutti, M. Tchernycheva, A. De Luna Bugallo, G. Jacopin, F. H. Julien, F. Furtmayr, M. Stutzmann, M. Eickhoff, R. Songmuang, and F. Fortuna: *Photoluminescence polarization properties of single GaN nanowires containing* $Al_xGa_{1-x}N/GaN$ *quantum discs*, Phys. Rev. B **81**, 045411 (2010).

- L. Rigutti, J. Teubert, G. Jacopin, F. Fortuna, M. Tchernycheva, A. De Luna Bugallo, F. H. Julien, F. Furtmayr, M. Stutzmann, and M. Eickhoff: *Origin of energy dispersion in* $Al_xGa_{1-x}N/GaN$ *nanowire quantum discs with low Al content*, Phys. Rev. B **82**, 235308 (2010).

- G. Jacopin, L. Rigutti, L. Largeau, F. Fortuna, F. Furtmayr, F. H. Julien, M. Eickhoff, and M. Tchernycheva: *Optical properties of wurtzite/zinc-blende heterostructures in GaN nanowires*, Journal of Applied Physics **110**, 064313 (2011).

- J. Teubert, P. Becker, F. Furtmayr, and M. Eickhoff: *GaN nanodiscs embedded in nanowires as optochemical transducers*, Nanotechnology **22**, 275505 (2011).

- M. de la Mata, C. Magen, J. Gazquez, M. I. B. Utama, M. Heiss, S. Lopatin, F. Furtmayr, C. J. Fernández-Rojas, B. Peng, J. R. Morante, R. Rurali, M. Eickhoff, A. Fontcuberta i Morral, Q. Xiong, and J. Arbiol: *Polarity assignment in ZnTe, GaAs, ZnO, and GaN-AlN nanowires from direct dumbbell analysis*, Nano Letters **12**, 2579 (2012).

- F. Schuster, F. Furtmayr, R. Zamani, C. Magén, J. R. Morante, J. Arbiol, J. A. Garrido, and M. Stutzmann: *Self-assembled GaN nanowires on diamond*, Nano Letters **12**, 2199 (2012).

- S. Paul, A. Helwig, G. Müller, F. Furtmayr, J. Teubert, and M. Eickhoff: *Opto-chemical sensor system for the detection of* H_2 *and hydrocarbons based on InGaN/GaN nanowires*, Sensors and Actuators B: Chemical **173**, 120 (2012).

- J. Wallys, J. Teubert, F. Furtmayr, D. M. Hofmann, and M. Eickhoff: *Bias-enhanced optical pH response of group III-Nitride nanowires*, Nano Letters **12**, 6180 (2012).

- J. Wallys, S. Hoffmann, F. Furtmayr, J. Teubert, and M. Eickhoff: *Electrochemical properties of GaN nanowire electrodes - influence of doping and control by external bias*, Nanotechnology **23**, 165701 (2012).

- M. d. l. Mata, X. Zhou, F. Furtmayr, J. Teubert, S. Gradecak, M. Eickhoff, A. Fontcuberta i Morral, and J. Arbiol: *A review of MBE grown 0D, 1D and 2D quantum structures in a nanowire*, J. Mater. Chem. C, (2013).
- G. Jacopin, L. Rigutti, J. Teubert, F. H. Julien, F. Furtmayr, P. Komninou, T. Kehagias, M. Eickhoff, and M. Tchernycheva: *Optical properties of GaN-based nanowires containing a single* $Al_{0.14}Ga_{0.86}N/GaN$ *quantum disc*, Nanotechnology **24**, 125201 (2013).
- T. Kehagias, G. P. Dimitrakopulos, I. Häeusler, A. Chernikov, P. Becker, S. Chatterjee, J. Kioseoglou, T. Karakostas, F. Furtmayr, T. Koukoula, H.-M. Solowan, U. T. Schwarz, M. Eickhoff, and P. Komninou: *Nanostructure and strain in InGaN/GaN superlattices grown in GaN nanowires*, Nanotechnology **24**, 435702 (2013).

Acknowledgements

Auch wenn unter dem Titel dieser Arbeit nur mein Name steht, so wäre sie doch nie zustande gekommen ohne die Unterstützung vieler Anderer. Ich darf mich an dieser Stelle herzlich bedanken bei:

Prof. Dr. Martin Stutzmann für die Möglichkeit, an seinem Lehrstuhl selbstverantwortlich und mit dem Zugang zu vielfältigem Equipment arbeiten zu können. Er eröffnete mir einen breiteren Blickwinkel auf das Thema und lehrte mich, vieles zu hinterfragen.

Prof. Dr. Martin Eickhoff, dem „Vater“ des DOTSENSE-Projektes, der mich immer wieder anspornte, es noch besser zu machen und der nach seinem Weggang nach Gießen weiter meine Fernbetreuung und Fernfinanzierung übernahm.

Meinen beiden Diplomanden **Martin Vielemeyer** und **Christoph Stark** für ihr tatkräftiges Mitforschen.

Meinem Vorgänger an der MBE **Martin Hermann**, der mich in die vielfältigen Eigenheiten und Geheimnisse der MBE eingeweiht hatte.

Den weiteren Mitgliedern meiner Arbeitsgruppe: **Barbara Baur, Olaf Weidemann, Tom Wasser** und **Bernhard Laumer**.

Meinem Nachfolger an der MBE **Fabian Schuster**.

Meinen Bürokollegen im S304: **Marco Höb**, **Christoph Bihler**, **Benedikt Stoib**, **Lukas Dreher** für eine sowohl sehr spaßige als auch produktive Atmosphäre.

Sowie allen meinen Mit-Doktoranden, insbesondere **Felix Buth** für Diamantsubstrate und gemeinsame Laufrunden, **John Howgate** for keeping the MBEs' erratic liquid nitrogen system working while avoiding electrical interference with the even more erratic XPS system attached to it, **Susanne Schäfer** für das Korrekturlesen dieser Arbeit, **Sebastian Schöll** und **Tobias Antesberger**

Den Technikern am WSI, ohne die eine solche experimentelle Arbeit nicht möglich wäre, namentlich:
Sonja Matich für sorgfältige und ausdauernde Unterstützung bei der e-beam Lithographie, den Chemikerinnen **Angelika Stumpf** und **Claudia Paulus** für die Einführung in die Bedienung und ihre Wartung der Metall-Aufdampfanlage und Unterstützung bei allen nasschemischen Prozessen, sowie **Hubert Riedl** für die Einführung in die RIE und Tipps zur MBE-Wartung, **Wolfgang Bendak** für das Schweißen der leckgeschlagenen MBE-Hauptkammer, **Fritz Sedlmeir, Michi Fischer, Bernhard Kratzer, Max Bichler**.

Den Sekretärinnen **Veronika Enter** und **Joana Figueiredo**.

Dem gesamten E25 für eine menschlich großartige Zeit.

Dem Lehrstuhl E10, namentlich **Prof. Dirk Grundler** und **Paul Berberich** für die Erlaubnis, ihr Rasterelektronenmikroskop ausgiebig nutzen zu dürfen.

Unseren Kooperationspartnern bei EADS:
Dr. Andreas Helwig und **Sumit Paul**

Den Kooperationspartnern von anderen Universitäten und Instituten:
Ein großes Dankeschön / thank you / Merci! / Grazie! / ¡Gracias! / Gràcies! / Ευχαριστω goes to

Dr. Jörg Teubert (Universität Gießen)
Dr. Eva Monroy (CEA Grenoble)
Dr. Lorenzo Rigutti (Université Paris Sud)

Prof. Dr. Jordi Arbiol and his group at the Univ. of Barcelona and to
Prof. Dr. Philomela Komninou and her group at the Univ. of Thessaloniki for a huge number of fantastic TEM images and their hospitality when I visited them at their sites.

Und schließlich meinem Vater **Peter Furtmayr** für seine immerwährende Unterstützung und Motivierung, über all die Jahre an dieser Arbeit dranzubleiben.